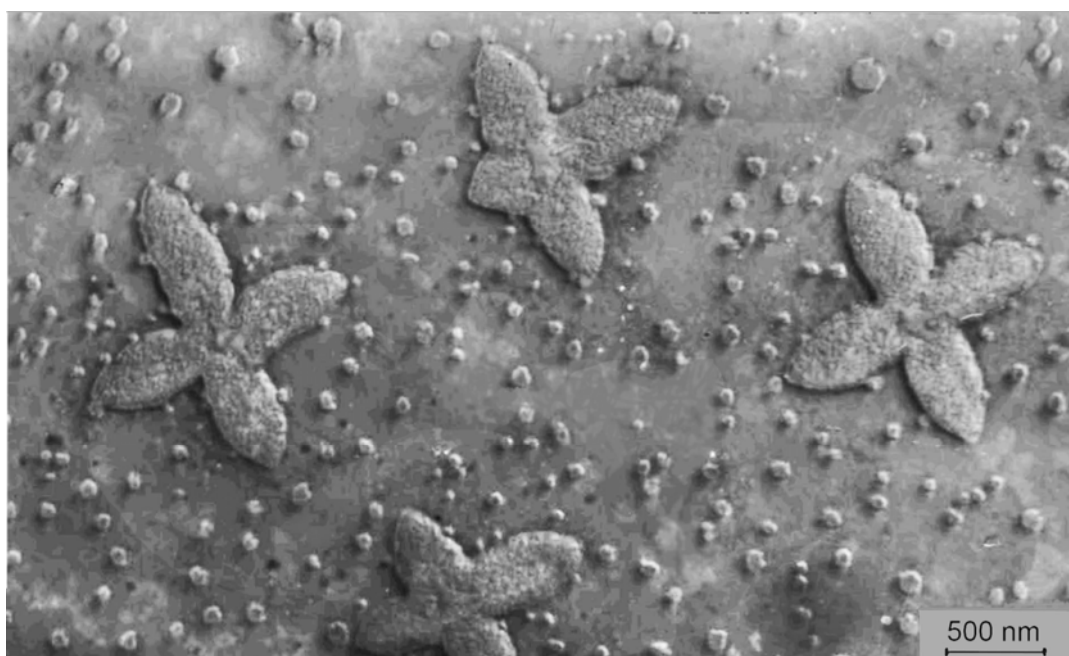


**RUSSIAN ACADEMY OF SCIENCES  
RUSSIAN FOUNDATION FOR BASIC RESEARCH  
YAROSLAVL BRANCH OF THE INSTITUTE  
OF PHYSICS AND TECHNOLOGY  
YAROSLAVL DEMIDOV STATE UNIVERSITY  
SCIENTIFIC EDUCATIONAL CENTER  
“NANOTECHNOLOGY AND INNOVATIONS”  
CENTER FOR COLLECTIVE USE  
“DIAGNOSTICS OF MICRO- AND NANOSTRUCTURES”**

**INTERNATIONAL CONFERENCE  
ON**

**MODERN PROBLEMS IN PHYSICS  
OF SURFACES AND NANOSTRUCTURES**



**BOOK OF ABSTRACTS**



**YAROSLAVL, RUSSIA  
2010**

### **International Advisory Board:**

Alexander Orlikovsky, director of IPT RAS\*, Moscow, Russia  
Alexander Rusakov, rector of the Yaroslavl Demidov State University, Yaroslavl, Russia  
Vladimir Lukichev, deputy director of IPT RAS\*, Moscow, Russia  
Tapio Ala-Nissial, Helsinki University of Technology, Helsinki, Finland  
See-Chen Ying, Brown University, Providence, USA  
Talat Rahman, University of Central Florida, Orlando, USA  
Enzo Granato, Institute of Space Research, San Jose dos Campos, Brasil  
Oleg Trushin, YB IPT RAS\*\*, Yaroslavl, Russia  
Ildar Amirov, deputy head of YB IPT RAS\*\*, Yaroslavl, Russia

### **The Local Organizing Committee:**

Arkady Berdnikov (head of organizing committee), head of YB IPT RAS\*\*, Yaroslavl, Russia  
Oleg Trushin (dep. head of organizing committee), senior researcher, YB IPT RAS\*\*, Yaroslavl, Russia  
Valery Rudakov (dep. head of organizing committee), head of laboratory, YB IPT RAS\*\*, Yaroslavl, Russia  
Ildar Amirov, deputy head of YB IPT RAS\*\*, Yaroslavl, Russia  
Alexander Rudy, Yaroslavl Demidov State University, Yaroslavl, Russia  
Irina Kuznetsova, Yaroslavl Demidov State University, Yaroslavl, Russia

\* - Institute of Physics and Technology, Russian Academy of Sciences

\*\* - Yaroslavl Branch of the Institute of Physics and Technology, Russian Academy of Sciences

Cover: Scanning Electron Microscope image of Gd-Co thin film surface.

# CONTENTS

<b>1. Properties of nano-objects and selective nanochemistry at semiconductor surfaces and interfaces</b>	
<u>P.G.Soukiassian</u> .....	L1-1
<b>2. Nano-plasmonics: mega-fields and nano-guides</b>	
<u>I.P.Radko</u> .....	L1-2
<b>3. Surface reactions in plasma etching for nanoelectronics</b>	
<u>D.Shamiryan</u> .....	L1-3
<b>4. Mechanism of photochemical reactions and photophysical processes during UV curing of organosilicate films with low dielectric constant</b>	
<u>M.R.Baklanov</u> .....	L1-4
<b>5. Mechanisms of chemical deposition from supercritical fluids for advanced microelectronics applications</b>	
<u>E.Kondoh</u> , K.Tamai, N.Fukasawa, K.Kotaka, and M.Matsubara.....	L1-5
<b>6. The morphology-dependent acoustic resonance in thin films</b>	
<u>M.Samoylovich</u> , A.Belyanin, N.Tcherniega, P.Pashchenko.....	O1-1
<b>7. Effectiveness enhancement of plasmonic photovoltaic elements by surface nanostructuring</b>	
A.A.Mironenko, V.A.Paporkov, N.A.Rud, A.S.Rudy, E.I.Vaganova, <u>A.V.Prokaznikov</u> .....	O1-2
<b>8. Spectra and mechanisms of ultraviolet photoluminescence from nanostructured 3C-SiC/Si heterocompositions grown in vacuum from hydrides and hydrocarbon mixture</b>	
<u>L.K.Orlov</u> , Yu.N.Drozдов, E.A.Shteiman, V.I.Vdovin, M.L.Orlov, A.Pod'yacheva, T.N.Smyslova, N.L.Ivina, A.S.Dondarenko.....	O1-3
<b>10. The W/HfO<sub>2</sub>/Si (100) structures fabricated by the RF magnetron sputtering</b>	
<u>E.Bogoyavlenskaya</u> , Yu.Denisenko, V.Naumov, V.Rudakov.....	O1-4
<b>11. Electron tomography and STEM investigation of amorphous and nanocrystalline materials CoW-CoNiW systems in external action</b>	
<u>O.Voitenko</u> , E.Modin, A.Gluhov, E.Pustovalov, S.Dolzhikov, V.Plotnikov, S.Grabchikov, L.Sosnovskaya.....	O1-5
<b>12. Structure investigation of electrodeposited CoP-CoNiP amorphous alloys under thermal impact</b>	
<u>E.Modin</u> , O.Voitenko, A.Gluhov, E.Pustovalov, S.Dolzhikov, B.Grudin, V.Plotnikov, S.Grabchikov.....	O1-6
<b>13. Application of the phase-field crystal model for materials modeling: metals and colloids</b>	
<u>T.Ala-Nissilä</u> .....	L2-1
<b>14. Phase-field-crystal model for pinning and sliding of adsorbed layers</b>	
<u>E.Granato</u> .....	L2-2
<b>15. Diffusion of adatom clusters on metal surfaces: periphery diffusion or concerted motion?</b>	
<u>T.S.Rahman</u> .....	L2-3
<b>16. Ordering of 2D binary system with Interaction to next nearest neighbors - CCMF method</b>	
<u>Z.Chvoj</u> .....	L2-4
<b>17. Multiscale study of submonolayer growth for Fe/Mo(110)</b>	
<u>M.Mašín</u> , M.O.Jahma, T.Ala-Nissilä and M.Kotrla.....	O2-1

18.	<b>Effect of misfit dislocation on surface diffusion</b> O.Trushin, M.Aminpour, T.S.Rahman.....	O2-2
19.	<b>Multiagent approach to adsorption processes modeling by the method of likelihood cellular automat</b> N.A.Rud, A.A.Astapkov, P.G.Morozov.....	O2-3
20.	<b>Toroidal moment and current induced transitions in the triangular molecular magnet V<sub>15</sub></b> V.V.Kostyuchenko.....	O2-4
21.	<b>Magnetic properties and structure of cobalt films and Cu/Co/Cu/Si heterostructures</b> A.P.Glukhov, E.V.Pustovalov, B.N.Grudin, V.S.Plotnikov, K.S.Ermakov.....	O2-5
22.	<b>Optimization of spin-valve structures for GMR sensor applications</b> O.S.Trushin, V.V.Naumov, E.Yu.Buchin, V.F.Bochkarev.....	O2-6
23.	<b>The possibilities of Mossbauer spectroscopy at research of iron compound in nanostructure (On examples of objects from «natural laboratories» the Earth and Mars)</b> A.A.Zalutskii, R.N.Kuzmin.....	O2-7
24.	<b>Investigation of surface morphology and magnetoresistance of the granular Co-Cu films deposited by ion-plasmic method</b> E.Yu.Buchin, V.F.Bochkarev, D.A.Kokanov, and V.V.Naumov.....	O2-8
25.	<b>Surface modification of oxides by low-energy Ar<sup>+</sup> and O<sub>2</sub><sup>+</sup> ion beams</b> N.Alov.....	O3-1
26.	<b>Ion-beam two-dimensional patterning of silicon subsurface region</b> M.Yu.Barabanenkov, A.F.Vyatkin, A.I.Il'in, V.I.Zinenko.....	O3-2
27.	<b>Redistribution of constituent elements during Co silicidation process in Ti/Co/Ti/Si (100) systems</b> Yu.Denisenko, V.Naumov, S.Simakin, V.Rudakov.....	O3-3
28.	<b>Etching of high aspect ratio Si nanostructures in the fluorinated plasma</b> I.I.Amirov, E.N.Zhikharev, V.A.Kalnov, V.F.Lukichev.....	O3-4
29.	<b>Mid infrared tunable whispering gallery modes lasers</b> V.V.Sherstnev, E.A.Grebenshchikova, M.I.Larchenkov, A.M.Monakhov, A.N.Imenkov, A.N.Baranov and Yu.P.Yakovlev.....	O3-5
30.	<b>Nanoscale storage elements based on the TiZrPb<sub>2</sub>O<sub>3</sub> films using the atomic force microscopy methods</b> A.Avachev, K.Mitrofanov, N.Klimov.....	O3-6
31.	<b>Simulation of the 100-40 nm transistor gate formation process by EB lithography for 950K PMMA – Si substrate system</b> M.Alexandrova.....	O3-7
32.	<b>Synthesis of Cu nanoparticles in solutions and its studies with X-ray absorption spectroscopy and X-ray photoelectron spectroscopy</b> S.Saykova, S.Vorobyev, Y.Mikhlin, A.Romanchenko, M.Likhatski.....	O3-8
33.	<b>Investigations of morphological and structural properties of porous nanostructured lead chalcogenide films fabricated with the variation of anodic electrochemical treatment conditions</b> S.P.Zimin, V.M.Vasin, E.S.Gorlachev, V.V.Naumov, E.Yu.Buchin.....	O3-9
34.	<b>Mechanical pressure influence on sulfide zinc nanocrystalline films structure</b> P.N.Krylov, E.A.Romanov, I.V.Fedotova.....	O3-10



<b>35. Forming methods of island structures</b>	
Yu.V.Panfilov, S.V.Sidorova.....	O3-11
<b>36. Effect of arsenic molecular form (As<sub>2</sub> or As<sub>4</sub>) on the composition of solid solutions GaP<sub>x</sub>As<sub>1-x</sub>, GaSb<sub>x</sub>As<sub>1-x</sub> during the molecular-beam epitaxy</b>	
E.Emelyanov, M.Putyato, B.Semyagin, A.Vasilenko, V.Preobrazhenskii.....	O3-12
<b>37. Local composition analysis of Ge:Mn, Si:Mn и Si:Co magnetic semiconductor thin films by XPS and SAM</b>	
D.Nikolitchev, E.Demidov, V.Podolskii, V.Lesnikov, A.Boryakov, A.Vihorev, S.Zubkov, S.Levchuk.....	O3-13
<b>38. Self-organization of atoms into nanosystems</b>	
D.B.Titorov.....	O3-14
<b>39. Development of the atomic force microscopy research technique for the nanostructures on the vertical edge of thin insulating film</b>	
E.S.Gorlachev, V.M.Mordvintsev, V.L.Levin.....	O3-15
<b>40. The scalable up process production of carbon nanotube CNT by means of catalytic pyrolysis ethanol on heterogeneous catalyst</b>	
N.Savinski, M.Gitlin, A.Rusakov, V.Naumov.....	O3-16
<b>41. SOI doping and its influence on a wafer temperature during RTA</b>	
V.Prigara, V.Ovcharov, V.Rudakov.....	O3-17
<b>42. Switching conductivity effect is promising direction of non-volatile memory devices creation</b>	
A.Berdnikov, A.Popov, V.Alekseev, A.Perminov.....	O3-18
<b>43. Technology for obtaining nanocrystalline inclusions in the matrix SiO<sub>2</sub></b>	
A.A.Dedyukhin, V.F.Kobzev, P.N.Krylov, I.V.Fedotova.....	P2-1
<b>44. Study of the amorphization effects in silicon surface layer at PAI step for process of ultra shallow boron doping</b>	
V.Boyadzhi, A.Starosek, and K.Rudenko.....	P2-2
<b>45. Photoluminescence and photoexcitation transport in silicon-rich nitride films with <math>\alpha</math>-Si nanoclusters</b>	
V.Stuchinsky, T.Korchagina, V.Volodin, A.Popov, M.Vergnat.....	P2-3
<b>46. Magneto-optical investigation of exchange interacting in Py/Cu/Co structure</b>	
E.Fedorov, V.Naumov, V.Paporkov, N.Zvezdin.....	P2-4
<b>47. Micromagnetic simulations of spin-valve structure</b>	
O.S.Trushin, N.Barabanova, V.P.Alexeev.....	P2-5
<b>48. Influence of filler size on the mechanical failure of a polymer nanocomposite</b>	
A.Kutvonen, G.Rossi, T.Ala-Nissilä.....	P2-6
<b>49. Eighth order fitting method for the phase field crystal model</b>	
A.Jaatinen, C.V.Achim, T.Ala-Nissilä, K.R.Elder.....	P2-7
<b>50. Path integral hyperdynamics for systems with internal degrees of freedom – Kramers escape problem for polymers</b>	
T.Ikonen, J.Shin, M.Khandkar, T.Ala-Nissilä, S.-C.Ying, W.Sung.....	P2-8
<b>51. A data bank approach to multiscale modelling of microstructure formation in polymer casting</b>	
T.Pitkänen, M.Majaniemi, T.Ala-Nissilä.....	P2-9
<b>52. Cutting ice: regelation at the nanoscale</b>	
V.Heinonen, T.Hynninen, C.L.Dias, T.Ala-Nissilä, A.S.Foster and M.Karttunen.....	P2-10

<b>53. Modeling close-packed metallic interfaces with amplitude expansion of the phase-field crystal model</b>	
P.T.Kanerva, J.Jalkanen, G.Rossi, K.R.Elder, T.Ala-Nissilä.....	P2-11
<b>54. Nonlinear microrheology of dense colloidal suspensions</b>	
I.Gazuz, A.M.Puertas and M.Fuchs.....	P2-12
<b>55. Lattice-Boltzmann simulations of colloidal hydrodynamics</b>	
S.T.T.Ollila, C.J.Smith and C.Denniston.....	P2-13
<b>56. XPS depth profiling of SiO<sub>2</sub> / HfO<sub>2</sub> / Si thin layers</b>	
A.V.Boryakov, A.S.Vihorev, A.V.Ershov, S.Yu.Zubkov, V.V.Karzanov.....	P2-14
<b>57. Three-dimensional modeling of dynamic processes in the crystalline matrix</b>	
V.V.Kostin, N.A.Rud.....	P2-15
<b>58. Formation of nanostructured silicon films on glass substrates using femtosecond laser pulse annealings</b>	
V.A.Volodin, T.T.Korchagina, A.S.Kachko, A.Kh.Antonenko, G.N.Kamaev.....	P2-16
<b>59. Optical properties of silicon nanoclusters formed in SiN<sub>x</sub> films: effect of pressure annealing</b>	
V.A.Volodin, K.O.Bugaev, A.A.Popov, and A.Misiuk.....	P2-17
<b>60. Switch conductivity effect in dielectric films with different incorporated clusters</b>	
A.E.Berdnikov, A.A.Popov, A.A.Mironenko, V.D.Chernomordick, A.V.Perminov, V.N.Gusev.....	P3-1
<b>61. Studying of current flow mechanism in structures with conductivity switching effect</b>	
A.V.Prokaznikov, A.A.Popov, A.A.Mironenko, A.V.Perminov, A.E.Berdnikov, V.D.Chernomordick.....	P3-2
<b>62. Self-formation of microstructures at the deep quartz etching in high density fluorocarbon plasma</b>	
M.Izumov, I.Amirov.....	P3-3
<b>63. Cantilever eigenfrequencies control</b>	
M.Lokhanin, A.Nikolaev.....	P3-4
<b>64. Characterization of electrostatically-actuated metal microbeams</b>	
A.V.Postnikov, I.V.Uvarov, I.I.Amirov.....	P3-5
<b>65. Growth of carbon nanotubes on multilayers films surface</b>	
N.Savinski, M.Gitlin, A.Rusakov, V.Naumov, V.Orlov.....	P3-6
<b>66. The microwave polyol nano-reactors synthesis of metallic nanoparticles</b>	
N.Savinski, V.Naumov.....	P3-7
<b>67. Solution combustion synthesis of nano oxide catalysts for growth carbon nano tube and nano wire</b>	
N.Savinski, V.Naumov.....	P3-8
<b>68. Template synthesis of water soluble PANI</b>	
N.Savinski.....	P3-9
<b>69. Nano particle Ag has been prepared by photo - polyol methods</b>	
N.Savinski, V.Naumov.....	P3-10
<b>70. Carbon nanotube emitter matrixs based autoemission devices</b>	
N.Savinski, M.Gitlin, A.Shornikov.....	P3-11
<b>71. Potential applications of low-frequency noise spectroscopy to the development of flicker-noise gas microsensor</b>	
M.I.Makoviychuk.....	P3-12
<b>72. Adsorption-desorption flicker noise spectroscopy</b>	

	M.I.Makoviychuk.....	P3-13
<b>73.</b>	<b>Development of 3D-formation on the surface of SIMOX-structure of flicker-noise gas sensor</b>	
	M.K.Aminov, M.I.Makoviychuk, E.O.Parshin.....	P3-14
<b>74.</b>	<b>Annealing temperature dependence of the photo-emf in silicon p-n-junctions with SiO<sub>x</sub>B<sub>y</sub> nanoclusters</b>	
	S.A.Krivelevich, R.V.Selyukov.....	P3-15
<b>75.</b>	<b>Diffusion simulation during RTA of plasma immersion ion implanted boron in SOI structure</b>	
	V.Ovcharov, V.Rudakov, A.Kurennya, S.Simakin.....	P3-16
<b>76.</b>	<b>Plasma molding in deep silicon reactive ion etching</b>	
	O.Morozov.....	P3-17
<b>77.</b>	<b>The test bench for study of dynamic characteristics of MEMS</b>	
	A.V.Postnikov, I.A.Kozin.....	P3-18
<b>78.</b>	<b>Electron-hole plasma in a one-dimensional parallel wires system</b>	
	V.Stepanov, A.Churilov.....	P3-19

# Properties of nano-objects and selective nanochemistry at semiconductor surfaces and interfaces

P.G.Soukiassian

*Commissariat à l'Energie Atomique, Centre d'Etudes de Saclay 91191 Gif sur Yvette Cedex, France and  
Département de Physique, Université Paris-Sud, 91405 Orsay, Orsay, France,  
patrick.soukiassian@cea.fr*

Nanostructures at SiC and epitaxial graphene/SiC surfaces/interfaces, and nanochemistry are investigated by synchrotron radiation-based photoemission spectroscopy (VB-PES and CL-PES), scanning tunneling microscopy/spectroscopy (STM/STS), infrared absorption spectroscopies (IRAS), and *ab-initio* theoretical calculations. Silicon carbide (SiC) and graphene are advanced semiconductors having figures of merit scaling well above those of well-established semiconductors. The main characteristics of SiC include i) a wide band gap (2.4 to 3.3 eV depending on polytype), ii) biocompatibility, iii) excellent mechanical properties, and iv) high resistance to radiation damages. Strain/stress minimization is the driving force in SiC surface/interface organization leading to complex surface atomic structures and to massively parallel passive/active nano-lines/nano-wires self-organizing at SiC surfaces [1,2]. Another interesting feature is to have SiC as a very suitable substrate for epitaxial graphene growth. Graphene, a single atomic layer of graphite, could be exfoliated or epitaxially grown on a substrate [3-5]. It exhibits outstanding transport properties, with carriers moving at zero mass and constant velocity just like photons, leading to linear valence band dispersion forming Dirac cones [6,7] and unsurpassed mobility up-to  $250.000 \text{ cm}^2/\text{V}^{-1}$  at room temperature for epitaxial graphene [8]. Graphene also has the highest mechanical resistance ever measured [9]. Among some important features, a special emphasis will be put on the following:

- The 1st example of H-induced semiconductor surface metallization on a SiC surface, also taking place on a pre-oxidized surface, with an amazing isotopic effect using D [10].
- Initial oxygen interaction and subsequent insulating thin film formation
- Monitoring the band-gap of epitaxial/exfoliated graphene by oxidation or hydrogenation [11]
- Atomic crack defects developing at surfaces [12].
- Nano-objects forming mesas with steep sides suggestive of C nanotubes at graphene/SiC interface, triggering interface states possibly detrimental to carrier mobility, and graphene layer going deep into nano-cracks at SiC surface with no disruption and no resulting electronic interface states [13].

The different mechanisms at the origin of these features will be discussed. The results directly impact engineering semiconductor surface/interface properties. It also allows to achieve on the same surface two opposite functions, metallization and passivation, which is especially interesting for interfacing with biology.

## References

1. P. Soukiassian, F. Semond, A. Mayne and G. Dujardin, *Phys. Rev. Lett.* **79**, 2498 (1997)
2. M. Silly, F. Charra and P. Soukiassian, *Appl. Phys. Lett.* **91**, 223111 (2007)
3. K.S. Novoselov *et al.*, *Science* **306**, 666 (2004); J.C. Meyer *et al.*, *Nature* **446**, 60 (2007)
4. C. Berger *et al.*, *J. Phys. Chem. B* **108**, 19912 (2004); C. Berger *et al.*, *Science* **312**, 1191 (2006)
5. V.Yu. Aristov *et al.*, *Nano Lett.* **10**, 992 (2010); H. Fukidome *et al.*, *Jpn. J. Appl. Phys.* **49** 01AH03 (2010)
6. M. Sprinkle, P. Soukiassian, W.A de Heer, C. Berger, E.H Conrad, *PSS-RRL* **3**, *Expert Opinion*, A91 (2009)
7. M. Sprinkle, D. Siegel, Y. Hu, J. Hicks, A. Tejeda, A. Taleb-Ibrahimi, P. Le Fevre, F. Bertran, S. Vizzini, H. Enriquez, S. Chiang, P. Soukiassian, C. Berger, W.A. de Heer, A. Lanzara, E.H. Conrad, *Phys. Rev. Lett.* **103**, 226803 (2009)
8. M. Orlita *et al.*, *Phys. Rev. Lett.* **101**, 267601 (2008); D.L. Miller *et al.*, *Science* **324**, 924 (2009)
9. Changgu Lee, Xiaoding Wei, Jeffrey W. Kysar, James Hone, *Science* **321**, 385 (2008)
10. V. Derycke, P. Soukiassian, F. Amy, Y.J. Chabal, M. D'angelo, H. Enriquez, M.G. Silly, *Nature Mat.* **2**, 253 (2003); M. Silly *et al.* *Appl. Phys. Lett.* **85**, 4893 (2004); J. Roy *et al.* **89**, 042114 *ibid* (2006)
11. Xiaosong Wu *et al.* *Phys. Rev. Lett.* **101**, 026801 (2008); D.C. Elias *et al.*, *Science* **323**, 610 (2009); D.L. Miller *et al.*, *Science* **324**, 934 (2009); A. Bostwick *et al.*, *Phys. Rev. Lett.* **103**, 056404 (2009)
12. F. Amy, P. Soukiassian, C. Brylinski, *Appl. Phys. Lett.* **85**, 926 (2004); P. Soukiassian *et al.*, *Mat. Sci. For.* **556**, 481 (2007)
13. S. Vizzini, H. Enriquez, S. Chiang, H. Oughaddou and P. Soukiassian, arXiv-0911.2143

# Nano-plasmonics: mega-fields and nano-guides

I.P.Radko

*Institute of Sensors, Signals and Electrotechnics (SENSE), University of Southern Denmark, Odense, Denmark,  
ilr@sense.sdu.dk*

The explosive progress in nanoscience has led to uncovering and exploring numerous physical phenomena occurring at nanoscale. One of the main research directions in nano-optics is the search for configurations that efficiently interconvert propagating ( $\mu\text{m}$ -sized) and highly localized (nm-sized) optical fields resulting hereby in strongly enhanced local fields, which are indispensable for optical characterization, sensing and manipulation at nanoscale.

Another effort is directed into miniaturization of integrated-optics functional elements, where classical approach has already reached its limit. Indeed, photonic components are superior to electronic ones in terms of operational bandwidth but suffer from the diffraction limit that constitutes a major problem on the way towards miniaturization and high-density integration of optical circuits. The degree of light confinement in dielectric structures, including those based on the photonic band-gap effect, is fundamentally limited by the light wavelength in the exploited dielectric. The main approach to circumvent this problem is to take advantage of hybrid nature of *surface plasmons* (SPs) whose subwavelength confinement is achieved due to very short (nm-long) penetration of light in metals.

After briefly reviewing the general properties of SPs, the results of our investigations of subwavelength photonic components utilizing SP modes propagating along channels cut into gold films are overviewed, demonstrating first examples of ultracompact plasmonic components that pave a way for a new class of integrated optical circuits. Regarding the search for local-field enhancing structures, a novel route exploiting retardation-based resonances involving (slow) surface plasmons supported by metal nanostructures is considered in detail. It is argued that the suggested configuration can be advantageously used in order to realize strong and robust field enhancement effects.

1. T. Ebbesen, C. Genet, and S. I. Bozhevolnyi, "Surface-plasmon circuitry," *Physics Today*, **May**, pp.44-50, 2008.
2. I. P. Radko, V. S. Volkov, J. Beermann, A. B. Evlyukhin, T. Søndergaard, A. E. Boltasseva, and S. I. Bozhevolnyi, "Plasmonic metasurfaces for waveguiding and field enhancement," *Laser & Photonics Reviews* **3**, pp.575-590, 2009.
3. D. K. Gramotnev and S. I. Bozhevolnyi, "Plasmonics beyond the diffraction limit," *Nature Photonics* **4**, pp.83-91, 2010.

# Surface reactions in plasma etching for nanoelectronics

D. Shamiryan

*IMEC, Leuven, Belgium, E-mail: shamir@imec.be*

Continuous miniaturization is a major driving force behind the progress in microelectronics. The miniaturization follows so-called Moore's law that states that the number of transistors that can be inexpensively placed on an integrated circuit is increasing exponentially, doubling approximately every two years [1].

One of the critical steps in integrated circuit manufacturing is pattern transfer using plasma etching. For years, miniaturization of integrated circuits demanded just reduction of the feature sizes. However, as downscaling progressed, it turned out that the conventional materials start to reach their limits and must be replaced by novel materials. That poses an enormous challenge for plasma etching as almost all plasma etch steps in semiconductor manufacturing must be redeveloped.

As gate dielectric was thinned down to several nanometers, increased gate leakage made transistor operation impossible. In order to overcome the high leakage the gate dielectric thickness must be increased, but it contradicts the downscaling requirements. To solve the problem  $\text{SiO}_2$  was replaced by dielectrics with higher dielectric constant  $k$ , so-called "high- $k$ " dielectrics. The range of materials that could be used as high- $k$  dielectrics is quite wide. One can find reports on using  $\text{HfO}_2$ ,  $\text{ZrO}_2$ ,  $\text{Al}_2\text{O}_3$ ,  $\text{Dy}_2\text{O}_3$ ,  $\text{La}_2\text{O}_3$ ,  $\text{Sc}_2\text{O}_3$ ,  $\text{Y}_2\text{O}_3$ ,  $\text{Ta}_2\text{O}_5$ ,  $\text{TiO}_2$ ,  $\text{Gd}_2\text{O}_3$  and their combinations as gate dielectrics. Plasma etching of those material poses a significant challenge, [2] especially taking into account the fact that many of those elements do not form volatile compounds.

Si gates, in turn, cannot be scaled down further due to gate depletion problem. In order to alleviate gate depletion, Si is being replaced by metals or metallic compounds like nitrides or carbides. Many materials (Ru, Mo, TiN, TaN, TaC etc.) are screened as potential candidates for gate material, but the final choice has not been made yet. Additional complication of the metal gate approach is the fact that an integrated circuit should contains gate materials with two different work functions aligned to the conductance and the valence bands of Si. That makes plasma etching extremely challenging as two different materials must be etched simultaneously with similar etch rates.

In the metallization part of an integrated circuit both metal and intermetal dielectric must be replaced. An electric signal propagating through a circuit experiences delay that is a product of resistance and capacitance, known as RC delay. As resistance is inversely proportional to a wire cross-section and capacitance is inversely proportional to the distance between wires, they both increase as the dimensions of the circuit decrease. At some point the RC delay becomes higher than the switching time of transistors rendering the high-speed devices useless. In order to decrease the RC delay, both resistance and capacitance must be decreased. Since the geometry of the circuit cannot be changed, the change is made in the materials. Al is replaced by Cu that has lower resistivity, while  $\text{SiO}_2$  is replaced by materials with low dielectric constant, so-called "low- $k$  dielectrics" [3] – usually porous materials of SiOCH composition. Not only materials, but the whole metallization scheme must be changed. Unlike Al, Cu is very difficult to etch by plasma since it doesn't form volatile etch products. As a results, a so-called "damascene" scheme is used where low- $k$  dielectric is etched first and then the trenches are filled with Cu. The excess of Cu is removed by chemical-mechanical polishing.

One of the major issues in the low- $k$  patterning is plasma damage. Low- $k$  materials are intentionally hydrophobic since water with dielectric constant of 80 easily gets adsorbed inside the porous structure that ruins all advantages of those materials. However, as the low- $k$  film is exposed to etching and stripping plasma, the hydrophobic groups (usually  $\text{Si-CH}_3$ ) could be removed making the film hydrophilic and totally unsuitable as a low- $k$  dielectric. The demand of low plasma damage significantly restricts the range of plasmas that could be used for low- $k$  dielectrics patterning.

Another challenge for plasma etching is 3D device manufacturing. On the device level, 3D architecture is used to improve device performance. A so-called “finFET” is used where the channel is located perpendicular to the wafers surface while a gate is applied on the both sides. If the width of the fin is around 20 nm, the electric field applied from two sides can completely shut off the channel significantly improving device performance. The greatest challenge of finFET for plasma etching is its high topography. As fin height is usually in the range of 50 nm – 100 nm, the gates that are running over the fins are extremely difficult to pattern. As the gate etch is highly anisotropic, the amount of material to be etched right next to the fin can be several times higher as compared to large flat areas. To make things more complicated, finFETs are often combined with high-*k* dielectrics and metal gates.

On the integration level, 3D architecture is used to increase integration density. Usually, several planar circuits are made, then the substrates are thinned down, contacts are made through the substrates and the substrates are stacked to obtain a 3D integrated circuit. From plasma etching this approach demands manufacturing of the contact holes that runs through the wafer. Even though the substrate is thinned, contact hole up to 100  $\mu\text{m}$  deep are required. At the same time, the diameter of the contact holes should not exceed several micrometers that results in etching the holes with aspect ratio up to 1:100.

As microelectronics enters the nano-era, there are many challenges that lie ahead. Carbon nanotubes, semiconductor nanowires, graphene (a sheet of graphite of one atomic layer thickness) etc. – all these structures might require plasma processing tomorrow.

All those challenges require significantly deeper understanding of surface reactions taking place during plasma etching. If some time ago the feature dimensions as well as layer thicknesses were in order of hundreds of nanometers, now the feature dimensions can be as small as 10 nm and a layer to be etched can be as thin as one monolayer. In other words, the etched features are now comparable with the surface reaction layer thicknesses. As a result even small changes in the surface reaction layer can bring substantial changes to the etched profiles or selectivity over the substrate.

The present work will review the role of surface reactions in tackling the recent plasma etching challenges including etch of modern gate stacks comprising high-*k* dielectrics and metal gates, intermetal low-*k* dielectrics with focus on the plasma damage.

## REFERENCES

1. E. Moore // *Electronics*. **V. 38**. P. 114, 1965
2. D. Shamiryan, M. Baklanov, M. Claes, W. Boullart, and V. Paraschiv // *Chem. Eng. Comm.* **V. 196**, P. 1475, 2009
3. K. Maex, M. R. Baklanov, D. Shamiryan, F. Iacopi, S. Brongersma and Z. S. Yanovitskaya // *J. Appl. Phys.*, **V. 93**, P. 8793, 2003

# Mechanism of photochemical reactions and photophysical processes during UV curing of organosilicate films with low dielectric constant

M.R.Baklanov

*IMEC, Leuven, Belgium, E-mail: baklanov@imec.be*

The intrinsic speed limit of an integrated circuit is determined by the frequency at which its transistors can be turned “on” and “off”. Since smaller transistors have inherently higher clock frequencies, advances in IC speed historically have been achieved by downward scaling of feature size. Currently, however, the speed limit of advanced ICs is set by the delay in signal propagation in the metal interconnect lines, which is determined by the time constant of the line. The time constant is the product of the resistance ( $R$ ) between the line and the capacitance ( $C$ ) between the line and all adjusted lines :

$$RC = 2\rho k \varepsilon_0 L^2 \left( \frac{4}{P^2} + \frac{1}{T^2} \right)$$

Therefore, the time constant of the conductive lines with thickness ( $T$ ), pitch ( $P$ ) and length ( $L$ ) depends on the metal resistivity and dielectric constant of interline dielectric ( $k$ ). This is the reason why traditional aluminum based metallisation and  $\text{SiO}_2$  that have been the materials of choice during the last few decades are replaced to copper and dielectric materials with the reduced dielectric constant (in comparison with  $\text{SiO}_2$ ). Reduction of dielectric constant is achieved by selecting chemical compounds with low polarizability and introducing porosity. Presently popular organosilicate (OSG) low- $k$  films have a structure similar to  $\text{SiO}_2$  but some oxygen atoms in silica tetraeder are replaced by alkyl groups (mostly  $\text{CH}_3$ ) having low polarisability and hydrophobic properties. To synthesize such films the  $\text{SiCOH}$  matrix material (alkyl derivatives of silane) is co-deposited together with organic porogen that afterwards is decomposed and removed, creating the pores. To remove the porogen, thermal annealing, irradiation by UV light or electron beam can be applied. If to compare different curing approaches the thermal curing is too slow, e-beam curing damaged low- $k$  materials. Therefore, UV curing is considered as a most suitable approach [1].

Interaction of UV light with low- $k$  matrix and porogen has a quite complicated mechanism. This is the reason why in recent years significant effort has been invested in studies of UV-cures, in terms of curing light wavelength, mechanisms of photochemical and photophysical processes and the resulting changes to the material. The most important effects of these cures, besides the porogen removal, are the photochemical changes to the material followed by densification and shrinkage. The UV light promotes cross-linking of the matrix and reorganizes the Si-O-Si skeleton towards a more stable network structure. Upon the UV irradiation, an important part of the low- $k$  films, the  $-\text{CH}_3$  groups, responsible for hydrophobic properties and low dielectric constant can be partially removed and replaced by Si-H bonds. This process is much stronger for high-energetic photons with energies above 6.5 eV (wavelengths below 190 nm), because of the threshold energy, necessary to break the Si- $\text{CH}_3$  bond. The carbon depletion and increase of the Si-H bond concentration is also responsible for reduced chemical and plasma damage resistance, important for successful integration into industrial process conditions. On the other hand, the porogen polymer is destructed by UV light and form volatile hydrocarbons that are removed during the curing and non-volatile carbon rich residues. These residues have properties similar to amorphous carbon and therefore drastically increase the leakage current and decrease the breakdown voltage of low- $k$  materials. Amount of porogen residue also depends on the wavelength of UV light.

In this presentation we will report the results obtained during the UV curing of  $\text{SiCOH}$  low- $k$  dielectric films. The films were deposited by Plasma Enhanced Chemical Vapour Deposition (PECVD) together with an organic porogen. The target values of dielectric constant of the major materials were 2.5 and 2.3 and porosity higher than 25%. For exclusion of any oxygen to avoid oxidation of methyl groups, the irradiation treatment at high temperature was carried out at vacuum conditions or by flushing the irradiation chamber by nitrogen of high purity at various pressures. UV radiation was generated by excimer lamps with max intensity at  $\lambda = 172$  nm and 220 nm or a Hg low pressure lamp ( $\lambda_1 = 185$  nm,  $\lambda_2 = 254$  nm). Broadband UV source with  $\lambda > 200$  nm was also used for certain comparative experiments. The oxygen concentration in the nitrogen inlet gas of the vacuum chamber was below 1.5 ppm. Various techniques like FTIR, XPS, TOF-SIMS, Ellipsometric Porosimetry, UV ellipsometry were used to evaluate the effects of the UV curing. Nitrogen purged UV ellipsometry (Sopra) allowed evaluation of optical characteristics of low- $k$  films in



VIS-UV region and these data have been used for analysis UV curing mechanisms[2]. The results of material evaluation were compared with electrical characteristics. Quantum-chemical calculations were used to understand mechanism of photochemical reactions.

The major results can be summarized as following:

1. There is an energy threshold in modification of low-k materials. Using Quantum-chemical calculations it was shown that the photon energy sufficient to break Si-CH<sub>3</sub> bonds is located between 190-200 nm (depends on type of low-k matrix material)[3]. The UV light with wavelengths shorter than 190 nm efficiently increases Young Modulus but decreases concentration of CH<sub>3</sub> groups, densifies low-k material, makes low-k material hydrophilic and increases the k-value.
2. The porogen used in this research has maximum absorption at wavelengths close to 200-220 nm while the film matrix is transparent in this area. Therefore, the light source with wavelength >200 nm allows selective removal of porogen without degradation of low-k matrix. It is interesting that the reduction of ≡Si-CH<sub>3</sub> groups concentration always lead to formation of ≡Si-H groups. The ≡Si-CH<sub>3</sub> and ≡Si-H concentrations are inversely proportional each to another.
3. Wavelength > 200 nm is more efficient for porogen removal because of less formation of porogen residue. More energetic photons are not able to provide complete porogen removal because some part of porogen (10-15%) are degraded forming non-volatile amorphous carbon like residue on pores sidewall. However, throughput of the curing process with the light > 200 nm is smaller because needs much longer time.
4. Although the chemical and plasma resistance of ≡Si-H free low-k films is not pronounced, the wavelength with λ>200 nm provides more uniform curing from top to bottom of the film because of low absorption coefficient. It is shown that single wave length source can generate complicated gradients of Young Modulus because of formation of standing waves. This negative effect can be avoided by using multiwave length sources or by special design of the curing chamber. For instance by using several bulbs, resulting in a wide range of incident angles of curing light.

Mechanism of UV curing of SiCOH based low-k materials will be discussed using original experimental results and the data published in literature.

1. K. Maex, M. R. Baklanov, D. Shamiryan, F. Iacopi, S. H. Brongersma, and Z. S. Yanovitskaya, "Low dielectric constant materials for microelectronics" J. Appl. Phys. **93**, 8793-8841, 2003.
2. P. Marsik, P. Verdonck, D. De Roest, M. R. Baklanov. "Porogen residues detection in optical properties of low-k dielectrics cured by UV radiation", Thin Solid Films, 2010.
- L. Prager, P. Marsik, J. W. Gerlach, M. R. Baklanov, S. Naumov, L. Pistol, D. Schneider, L. Wennrich, P. Verdonck, M. R. Baklanov, "Effect of pressure on efficiency of UV curing of CVD-derived low-k material at different wavelengths", Microelectronic Engineering **85**, 2094-2097, 2008.

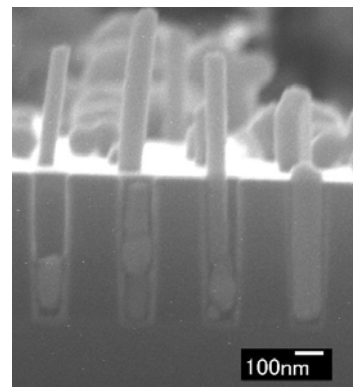
# Mechanisms of chemical deposition from supercritical fluids for advanced microelectronics applications

E.Kondoh, K.Tamai, N.Fukasawa, K.Kotaka, and M.Matsubara

*Interdisciplinary Graduate School and Medicine and Engineering, University of Yamanashi, Kofu 400-0016, Japan*

A supercritical fluid is a high-pressure fluid that possesses properties of both liquids and gases. The critical point of CO<sub>2</sub> is 73.8 MPa and 31°C; above this temperature, CO<sub>2</sub> is a supercritical fluid. Supercritical fluids have zero surface tension and are able to penetrate deep into small features. Supercritical fluids function as an ideal medium for delivering a dissolved substance into such features, because they have moderately high diffusivity and density and thus a high diffusion flux—the diffusion flux of a substance in a medium is proportional to the product of the diffusivity and (the gradient of) the density. Thin metal films can be deposited in supercritical fluids using an organometallic compound (precursor). Previous studies have reported that thin film deposition in supercritical CO<sub>2</sub> occur usually in a very conformal manner [2]. However, for very narrow features below approximately 50 nm, it has been reported that deposition proceeds without forming seams or voids from ULSI vias to carbon nanotubes [3–6]. This somehow defies our belief in thin film deposition chemistry, because the conformal deposition usually ends up with the formation of seam or void in narrow features due to mass flux crowding at the edge of a feature portal.

One interesting preferential growth of Cu nanorods in a narrower concave topography, namely topography-sensitive growth (see Figure). Cu was deposited via hydrogen reduction of an organometallic Cu precursor that was dissolved in a supercritical CO<sub>2</sub> fluid. It was found that the growth occurred in narrow capillaries and corners that have a small curvature. Residues containing carbon, oxygen, and copper, presumably unreacted precursors, were found at some of these locations. From supporting experiments using a window view cell, the formation of the residue at these locations was believed to occur in a supercritical solution that is nearly saturated with a precursor having a low solubility to the solution. The Cu grains were presumably single-crystalline, and grew in an anisotropic manner leading to a rodlike shape. This behavior suggests that the topography-sensitive growth is a dynamic process. In principle, the topography-sensitive growth mode proceeds better in the narrower features, which can be a key to solve the limit of continued downscaling in micro and nano device processing.



One finding obtained from the above observations is that sorption process in supercritical CO<sub>2</sub> can proceed anomalously. We have studied surface reaction kinetics of Cu thin film growth in supercritical CO<sub>2</sub> from a  $\beta$ -diketonate complex [7]. Generally, growth rate increased as the Cu precursor and H<sub>2</sub> concentration increased. At a low deposition temperature, the growth rate became zero order at higher precursor and H<sub>2</sub> concentrations, whereas no significant saturation was observed at a higher temperature. These results were discussed with a surface reaction mechanism of adsorbed species, and an empirical overall rate equation was obtained, taking into account the temperature dependencies of adsorption equilibrium constants and the rate constant of the rate-determining reaction (Langmuir-Hinshelwood model). In this model, the Cu precursor was supposed to adsorb nondissociatively, contrarily to our general belief. Moreover, it was found that the Langmuir-isotherm does not stand and the observed deposition kinetics followed the BJH-type multilayer sorption when the precursor concentration was high.

1. E. Kondoh, H. Kato, *Microelectron. Eng.* 64 (2002) 495.2
2. A. Cabañas, J.M. Blackburn, J.J. Watkins, *Microelectron. Eng.* 64 (2002) 53.
3. X.-R. Ye, Y. Lin, C. Wang, C.M. Wai, *Adv. Mater.* 15 (2003) 316.
4. H. Uchida, A. Otsubo, K. Itatani, S. Koda, *Jpn. J. Appl. Phys.* 44 (2005) 1901.
5. E. Kondoh, *Jpn. J. Appl. Phys.* 43 (2004) 3928.
6. T.A. Crowley, K.J. Ziegler, D.M. Lyons, D. Ertz, H. Olin, M.A. Morris, J.D. Holmes, *Chem. Mater.* 15 (2003) 3518.
7. M. Matsubara and E. Kondoh, *J. Electrochem. Soc.* 156 (2009) H443.

# The morphology-dependent acoustic resonance in thin films

M.Samoylovich<sup>1</sup>, A.Belyanin<sup>1</sup>, N.Tcherniega<sup>2</sup>, P.Pashchenko<sup>3</sup>

1. Central Research Technological Institute «TECHNOMASH», Moscow, Russia,

E-mail: samoylovich@technomash.ru.

2. Physical Institute of the Russian Academy of Sciences, Moscow, Russia.

3. Lomonosov Moscow State University Skobeltsyn Institute of Nuclear Physics (MSU SINP), Moscow, Russia

In all cases, as has been previously shown [1, 2], formation of polycrystalline systems occurs in thin films (with various texture degree) as a result of flat surfaces forming under condition of morphological instability (boundary growth forms), when morphological hierarchy appears as domains, plates, fibers and other types followed by elastic volume energy transfer in interphase energy. For example, formation of crystallites – nanoclusters of sputtered phase with area of coherent scattering not more than 0,5–1  $\mu\text{m}$  retain crystal type (point group) being characteristic for crystals of the phase under consideration, but cannot be described as a crystalline phase with the corresponding Fedorov group due to disturbance of translational equivalence (for the corresponding sizes). Excitation is localized in large domains in continuum, thereby all nanoclusters located in area under question with dimensions greater than the length of electromagnetic waves absorb light energy with the same rate. In a dispersion media, i.e. in fractal composites, excitation is localized in small domains – local area ( $r$ ), while the volume of local area is determined by the parameter  $r^d$  ( $d$  – dimension). The nature of observed effects of morphologically dependent resonances for acoustic vibrations is close to the same phenomena for electromagnetic waves in optical fields [3].

The experimental investigations of the interaction of pulsed laser radiation with different types of thin films are presented. High efficiency inelastic scattering of light due to optoacoustic interaction was registered. Spectral features of the scattered light are defined by the morphology of samples. Like electromagnetic waves acoustic waves demonstrate number of novel phenomena while propagating in medium consisting of morphological inhomogeneities with dimensions of the order of the acoustic wavelength [4]. For typical size of the morphologically defined inhomogeneities (rods, globules and so on) of several hundred nanometers the acoustic wavelength corresponds to hypersound. The optical scheme of the experimental setup for spectral characteristics of the scattered light measurement is shown in Fig. 1. Ruby laser giant pulses ( $\lambda = 694,3 \text{ nm}$ ,  $\tau = 20 \text{ ns}$ ,  $E_{\text{max}} = 0,3 \text{ J}$ ) were used as the source of excitation. Exciting light has been focused into the material by lenses with different focal lengths (50, 90, and 150 mm). It allowed us to vary the power density at the entrance of the sample and field distribution inside the sample. Fabri-Perot interferometers were used for spectral structure investigations: the range of dispersion was changed from 0,42 to 1,67  $\text{cm}^{-1}$ .

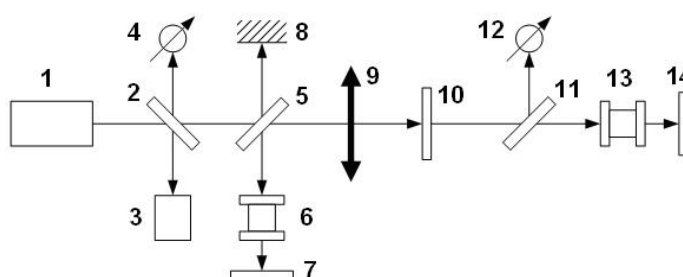


Fig. 1. Optical scheme for stimulated scattering studies: 1 – ruby laser; 2, 5, 11 – glass plates; 3 – system for laser parameters control; 4, 12 – system for measuring the scattered light energy in backward and forward directions; 6, 13 – Fabri-Perot interferometers; 7, 14 – systems of spectra registration; 8 – mirror; 9 – lens; 10 – sample.

The experimental data are presented in the table and include all observed Stokes components, but the following calculations were proceeded for the first component. Measurements were carried out for aluminum nitride (AlN) and indium tin oxide (ITO) films on substrates of quartz glass, and also for polycluster diamond (PCD) films, lattice packing nanosphere films (LPS), silica films (Fig. 2). Data obtained by scanning electron microscopy (SEM) studies in combination with measurements of coherent dispersion, calculated by X-ray diffractograms, make it possible to calculate the rates of acoustic waves in films of

various types. Under lack of data under question, but in case if acoustic wave rates of various types are available, we can solve the inverse problem and to determine the parameters of nanostructuring of the films under study.

Table. Parameters acoustics waves for different films.

№	Sample/ substrate	Threshold d GW/cm <sup>2</sup>	First Stocks component frequency shift, GHz	Design speed acoustics waves, km/sec	Average dimension of the structural inhomogeneities by the REM image, μm
1	AlN/glass	0,16	8,1	6,48	0,8
2	AlN/glass	0,16	6,0	6,2	1,0
3	ITO/glass	0,14	8,7	5,22	0,6
4	ITO/glass	0,14	6,3	5,04	0,8
5	ITO/glass	0,15	5,1	4,85	0,95
6	PCD/diamond	0,1	10,2	9,18	0,9
7	PCD/diamond	0,12	7,2	9,0	1,25
8	LPS/glass	0,2	0,2	1,8	0,23

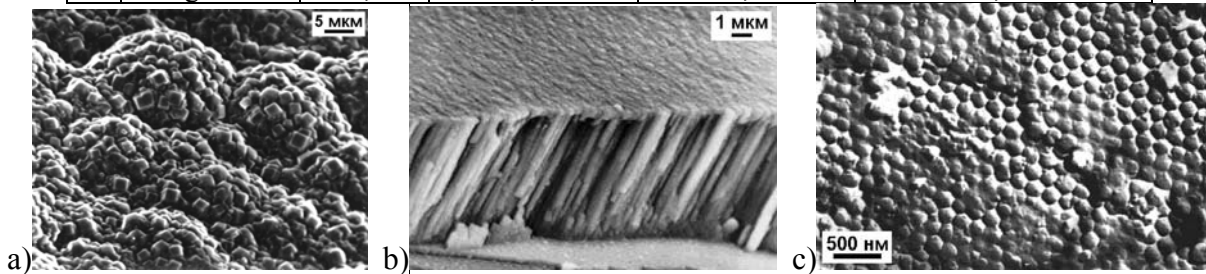


Fig. 2. SEM image of polyclusters diamond film on diamond monocrystal (a), AlN thin film grown by reactive magnetron sputtering grown on glass substrate (b), the films of lattice packings nanospheres SiO<sub>2</sub> on glass substrate (c)

As discussed metallic film systems and similar structures should be related to fractal due to self-organization processes invariant under the group of large-scale (affine) transformations. Therefore, the fractal system is not only nonlinear, but in contrast to the periodically ordered solid-state systems, associated with the method of system constructing, so that the fractal structure and the corresponding characteristic dimension are the main properties. To evaluate fractality, it is necessary to construct the test material for the films obtained under different conditions by the same method, the dependence between the frequency of the acoustic resonances and the parameter  $D^{-1}$ , where  $D$  is the linear dimensions of nanostructuring, and the difference of parameters 1 and 3 will be the characteristic value for fractality. Opal matrix with diameter range of nanospheres SiO<sub>2</sub>  $\pm 5\%$  is characterized by the parameter of fractal dimension  $d = 2,9$ .

Among the unusual characteristics of acoustic metamaterials should be mentioned the ability to focus the acoustic waves, the selectivity of possible frequencies, determined by their internal structure and the availability of new types of elastic waves, in particular, determined by the dispersion (for nanometer scale) density or elastic properties.

Financial support from RFFI (Grant № 08-02-13500; 09-02-13531) is acknowledged.

1. M.I. Samoilovich, A.F. Belyanin, A.L. Talis. Nanomaterials. I. Basic theory of symmetry nanostructured states. II. Thin films of diamond-like materials as nano-structured system. M.: Technomash, 2006, 400 pp.
2. A.F. Belyanin, M.I. Samoilovich. Nanomaterials. IV. Thin films as nano-structured system. M.: Technomash, 2008, 254 pp.
3. A.K. Sarychev, V.N. Shalaev. Electrodynamics of Metamaterials. Word Scientific, 2007, 240 pp.
4. N.V. Tcherniega, M.I. Samoilovich, A.D. Kudryavtseva, A.F. Belyanin, P.V. Pashchenko, N.N. Dzbanovski. "Stimulated scattering caused by the interaction of light with morphology-dependent acoustic resonance", Optics letters, 35, 3, 2010.

# Effectiveness enhancement of plasmonic photovoltaic elements by surface nanostructuring

A.A.Mironenko<sup>1</sup>, V.A.Paporkov<sup>2</sup>, N.A.Rud<sup>2</sup>, A.S.Rudy<sup>2</sup>, E.I.Vaganova<sup>1</sup>,  
A.V.Prokaznikov<sup>1</sup>

1. Yaroslavl Branch of the Institute of Physics and Technology, Russian Academy of Sciences, Yaroslavl, Russia, E-mail address: prokaznikov@mail.ru. 2. Yaroslavl Demidov State University, Yaroslavl, Russia, E-mail address: rudy@uniyuar.ac.ru

In the present time a special attention is paid to the properties of nano-structured systems in connection with size minimization of physical systems in modern electronics as well as unusual properties of such objects. Unique properties of objects with low dimensions are determined first of all by quantum physical regularities that come in force on these scales. Thus, one make it possible to include new unusual physical phenomena stipulating theirs entering into the regions that are based traditionally on regularities of well known systems [1].

In this work a method of nano-size objects creation is suggested which increases an effectiveness of investigated photoelectrical systems that are used to transform electromagnetic radiation energy into electrical one. This method is based on formation thin porous silicon (PS) film, which plays a role of optical window, and on formation on the base of porous structure a large number of nano-dots that can concentrate electromagnetic radiation energy and enhance sufficiently their properties due to localized plasmonic modes (see Fig. 1a). On the base of elaborated technology a special design of solar cell was suggested that used plasmonic effect which is created by metal (Ni) nano-dots (see Fig 1b) [2]. Control photovoltaic cell was done without Ni nano-dots.

As numerical evaluations of experimental data, that were obtained for both photovoltaic element of special design and control element, have shown a fill factor ( $FF$ ) of current-voltage characteristics (CVC) in both cases is approximately the same and is equal to  $FF \approx 0.25$ . Short circuit current for the structures on the base of PS with nickel (Ni) nano-dots is equal to  $I_{SC} = 5.5 \text{ mA}$  and open circuit voltage  $V_{OC} = 0.45 \text{ V}$ , while for control structures without Ni nano-dots –  $I_{SC} = 1.07 \text{ mA}$  and  $V_{OC} = 0.26 \text{ V}$  (see Fig. 1b). The photosensitivity spectra are nearly the same and they have a maximum near  $\lambda_{max} \approx 780 \text{ nm}$ . A radiation stream evaluation gives  $\Phi \approx 30 \text{ mWatt/cm}^2$  and integral capacity is equal to  $P \approx 1.5 \text{ Watt}$ . Estimation of efficiency coefficient was carried out by means of standard glow lamp which has a spectrum that differs from solar spectrum on the Earth surface. Because of this obstacle there is some reason to present only ratio of efficiency coefficients for the element based on PS with Ni nano-dots and without them so this ratio is equal to two. Thus, increasing in two times is observed for efficiency coefficient of photovoltaic element on the base of systems with Ni nano-dots.

Investigations of transverse magneto-optical Kerr effect (TMOKE) was carried out according to the method that was described in the work [3]. As TMOKE investigations have shown a value of Kerr effect  $\delta(\phi)$  with respect to the incident angle  $\phi$  and reflection coefficient  $R_p(\phi)$  testify that the main part of initial laser radiation with  $\lambda = 632 \text{ nm}$  penetrates into the system where it interacts with surrounding medium. It confirms the fact that Ni nano-dots play a role of electromagnetic energy concentrators that promote effective collection of light energy.

Theoretical imaginations of CVC behavior for silicon (Si) photo-elements is based on results of the work [4]. For CVC modeling of photovoltaic elements with Ni nanodots within the limits of investigated region of parameters more convenient model is that from the work [5]. About this fact the results of numerical evaluations testify moreover photo-stimulated current was equal to the short circuit current similarly to the

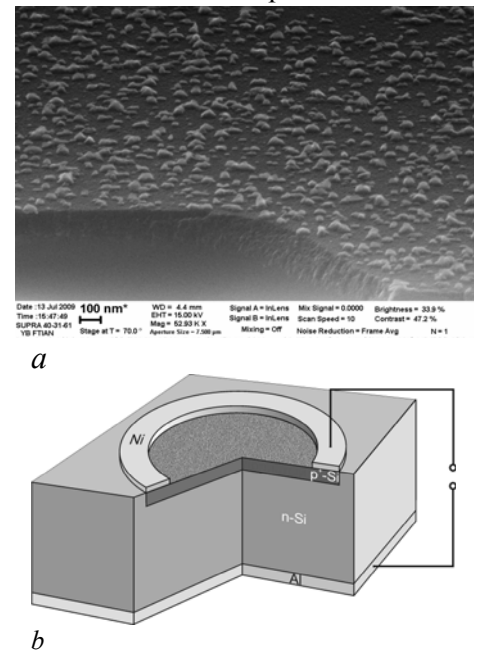


Figure 1. Structure consisted of porous silicon and Ni nano-dots (a); scheme of photovoltaic cell, which consists of porous silicon layer (with the thickness of 120 nm on Si sample surface) on the base of  $p^+-Si$ ,  $p^+-Si$  layer (with the thickness of 1  $\mu\text{m}$ ), upper nickel contact, Ni nanodots, back aluminum contact (b).

results of the work [4]. By the absence in the model shunt resistance (see [5]) one need to take ideality factor large enough for good approximation of obtained experimental results. Large enough values of ideality factor were obtained for the structures on the base of porous silicon *Me – porSi - p-Si* in the work [6] which was equal to  $n = 8 \div 14$ . In our case ideality factor is equal to  $n \sim 20$ . The authors of mentioned above work tie this fact with high enough concentration of localized electronic states on the border of *Me – porSi*. If by modeling CVC ideality factor corresponds to the values from the work [5] then a shunt resistance in the formula from [5] should be taken also large enough. Let us note that contribution in a large value of ideality factor can be connected in our case with contacts to the device. Thus, equivalent scheme of photovoltaic device with the usage of *Ni* nano-dots within the frameworks of investigated region of parameters is more closer to that suggested in the work [5] from legacy models. Generally speaking, elaboration of more detail model theory demands in our case realization of further investigations. Clear understanding of regularities of reaction for the system being created on external influence of radiation can be based on possibility of collective plasmonic modes creation [2]. Let us note that for description of observed physical picture one should take into account the possibility of charge carriers generation through the channel of collective plasmonic mode decay [7]. Theoretical aspect of the problem of collective plasmonic mode creation in nano-size objects was considered in more detail in the work [8]. In the work [8] was demonstrated that while decreasing an object sizes the probability of processes passing through the channel with assistance of plasmonic modes increases moreover there are some configurations of structures by that this probability is close to unity [8]. In the work [7] there was demonstrated experimentally that the decay of collective plasmonic mode at the presence of applied electric potential can be assisted by creation up to several dozen of electrons per plasmon. In our case the influence of PS layer as a resistance can be neglected because *Ni* penetrates into pores during electrochemical deposition and shunts it as well as *Ni* nano-dots can concentrate radiation deep under the porous silicon surface [2]. Changing a porosity one can change dielectric constant of medium surrounding *Ni* nano-dots and consequently a frequency of plasmonic resonance [2]. Depositing metal nano-dots of different shapes, sizes and elements one can optimize the work of solar cell. In this work due to the presence of metallic objects with dimensions of the order of several nanometers creation of collective plasmonic mode occurs on the borders of *Ni* nanoclusters and  $p^+$  - type *Si* moreover because of the sharp edges of *Ni* clusters splitting of edge plasmonic modes take place what make it easier theirs creation due to special dispersion feature for these modes [1, 2]. Plasmonic modes decay results in effective creation of additional charge carriers [7] that are separated from each other on *p-n* junction by usual way. All these facts result in high enough effectiveness in operation of investigated device. In this work a method is suggested how to form an effective photovoltaic cell on the base of *p-n* junction. This method is based on nano-size object formation that results in increasing of effectiveness of photoelectrical response of the systems that are used in electromagnetic radiation energy conversion into electrical one. This method is based on thin porous film formation in doped silicon that is used for creation off small metallic nano-dots on PS surface. These nano-dots play a role of light concentrators and surface plasmon sources what increases sufficiently the effectiveness of plasmon photovoltaic devices.

1. D.M. Schaadt, B. Feng, E.T. Yu, “Enhanced semiconductor optical absorption via surface plasmon excitation in metal nanoparticles”, *Appl. Phys. Letters*, v.86, 063106, 2005.
2. K.R. Catchpole, A. Polman, “Plasmonic solar cells”, *Optic Express*, v. 16, No 26, pp.21793-21800.
3. E.Yu. Buchin, E.I. Vaganova, V.V. Naumov, V.A. Paporkov, A.V. Prokaznikov, “Enhancement of the transversal magneto-optical Kerr effect in nanoperforated cobalt films”, *Technol. Phys. Letters*, v. 35, No 7, pp. 589-593, 2009.
4. V.M. Andreev, V.A. Grilihes, V.D. Rumyantsev. *Photoelektricheskoe preobrazovanie koncentririvannogo solnechnogo izlucheniya*. Nauka, Leningrad, 1989.
5. P. Schilinsky, Ch. Waldauf, J. Hauch, Ch.J. J. Brabec, “Simulation of light intensity dependent current characteristics of polymer solar cells”, *J. Appl. Phys.*, v. 95, No 5, pp. 2816-2819, 2004.
6. M. Ben-Chorin, F. Moller, F. Koch, “Band alignment and carrier injection at the porous silicon-crystalline silicon interface”, *J. Appl. Phys.*, v. 77, No 9, pp. 4482-4488, 1995.
7. A.L. Falk, F.H.L. Koppens, L.Yu. Chun, K. Kang, N. de Leon Snapp, A.V. Akimov, M.-H. Jo, M.D. Lukin, H. Park, “Near-field electrical detection of optical plasmons and single-plasmon sources”, *Nature Physics*, v. 5, pp. 475-479, 2009.
8. D.E. Chang, A.S. Sorensen, P.R. Hemmer, M.D. Lukin, “Strong coupling of single emitters to surface plasmons”, *Phys. Rev. B*, v. 76, 035420, 2007.

# **Spectra and mechanisms of ultraviolet photoluminescence from nanostructured 3C-SiC/Si heterocompositions grown in vacuum from hydrides and hydrocarbon mixture**

L.K.Orlov<sup>1</sup>, Yu.N.Drozdo<sup>1</sup>, E.A.Shteiman<sup>3</sup>, V.I.Vdovin<sup>4</sup>, M.L.Orlov<sup>1</sup>, A.Pod'yacheva<sup>2</sup>,  
T.N.Smyslova<sup>2</sup>, N.L.Ivina<sup>2</sup>, A.S.Dondarenko<sup>4</sup>

*1. Institute for Physics of Microstructures, Russian Academy of Sciences, N. Novgorod, orlov@ipm.sci-nnov.ru.*

*2. Nizhny Novgorod State Technical Alekseev University. 3. Institute of Solid State Physics, Russian Academy of Sciences, Chernogolovka. 4. St. Petersburg State University, Russia*

For last decade, the special attention is given to films of cubic silicon carbide (3SiC/Si), grown up on silicon substrates, not only, as a material of high-temperature electronics with raised power characteristics, but also in connection with the specific optoelectronic problems. Silicon carbide, thanks to the big width of the gap and high efficiency of radiating transitions in it, is considered recently among materials of a  $A_4B_4$  group as the unique competitor wideband compounds on a basis oxides and nitrides at creation of light-emitting sources from infrared [1] to ultraviolet [2] ranges of frequencies. In connection with these problems, the big interest to photoluminescent properties of carbide structures which are grown up on silicon, and to ways of updating of their crystal structure for the purpose of expansion of light-emitting elements spectral range in the spectrum area of a deep ultraviolet is observed. As the lattices mismatch of the considered SiC/Si heteropair is rather considerably, that leads to occurrence of some problems at growth of perfect monocrystal layers, so the salvation of this problem is in creation of the compositions with nanostructured polycrystalline silicon carbide layers at simultaneous achievement of high injection, temperature and radiating characteristics of formed heterotransition. The several ways of crystal structure modification for silicon carbide layers on silicon are offered, beginning from the growth, with a use of various technological methods, the composite structures with the nanometer scale crystallites [2,3] and the subsequent electrochemistry etching of samples (nanoporous silicon carbide [4,5]), and finishing the formation of low-dimensional structures with arrays of quantum dots [6] and quantum wires [7]. Experience shows that high degree of a mismatch between the silicon and silicon carbide crystal lattices, bad mutual solubility of carbon in silicon and germanium, and a growth of epitaxial layers at the lowered heteroepitaxy temperatures is exclusive for island growth mechanism, that promotes a formation of nanocrystal compositions on the basis of silicon, germanium and carbon.

In the present work the photoluminescent properties of the polycrystalline 3C-SiC layers besieged on silicon substrates with orientation Si (111) and Si (100) are studied. Films were grown up by a method of chemical epitaxy [3] from a mixture of silicon and germanium hydrides with hexane vapor in vacuum at temperature  $T_{gr} \leq 700^\circ\text{C}$ . The light-emitting properties of cubic silicon carbide films from room to helium measurement temperatures are discussed. The radiation of the helium-cadmium laser with 325 nanometers wave length (3.81 eV) was used for excitation of the electron subsystem in a SiC layer. It allowed to study the peculiarities in the photoluminescence spectra connected with a nanocrystal structure of the investigated material, in a range of waves lengths radiation since 350 nanometers and above (Fig.1a,d). The use of a low temperature in the photoluminescent experiment has allowed not only to eliminate undesirable temperature lines broadening, and to observe lines not resolved at measurements at a room temperature, but also to draw conclusions about the possible mechanisms of a light-emitting recombination in this material.

In addition, for the purpose of an establishment of mechanisms of a photoluminescence, we investigated the crystal structure, phase composition and surface morphology of a formed carbide films (Fig.1). Researches have been carried out with use of the different methods including the methods of X-ray diffraction, electronography, secondary ion mass spectrometry, optical interferometry and scanning electron microscopy. Distinctive features of a crystal structure of the SiC layers which have been grown up on silicon substrates with orientation of Si (100) and Si (111) are considered. Sharing various methods at the analysis of a crystal structure of the layers has allowed to reveal, on the one hand, nanocrystal structure of the grown up 3C-SiC layers (Fig.1c,f) which could be, according to the modern representations, responsible for observable lines in a ultraviolet photoluminescence spectra. On the other hand, on data electronography researches, the formation possibility in a structure, even in conditions of a low temperature epitaxy, along

with cubic and rhombohedral phases is not excluded, that also can give the additional contribution to formation of line structure in the photoluminescence spectra from the silicon carbide layers.

This work has been carried out at a support of the Russian basic research foundation, grant numbers 08-02-00065 и 08-02-97017p -«povolzhie».

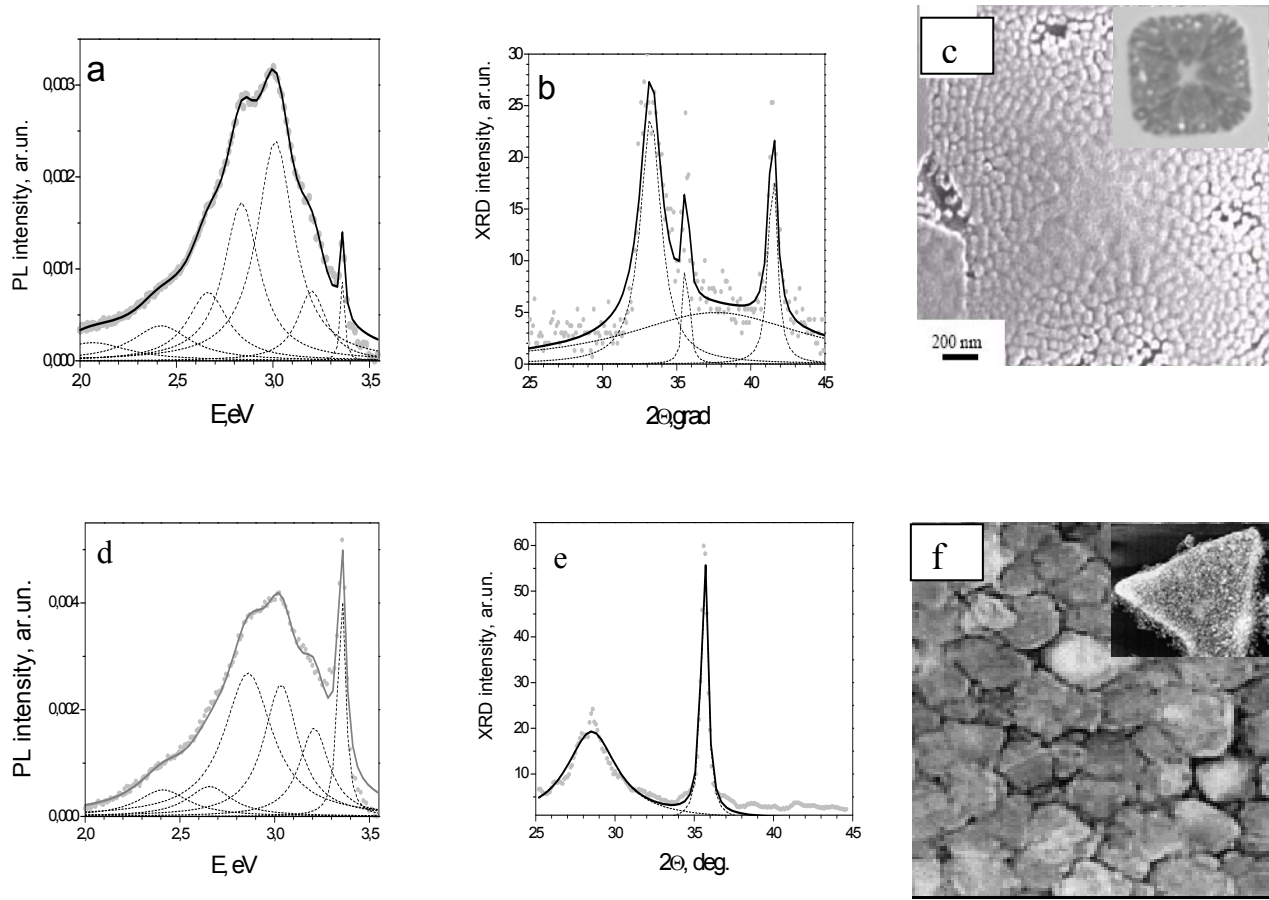


Fig.1. Photoluminescence spectra (a,d) at 10K, X-ray diffraction spectra (b,e) and electron microscopy images of a nanocrystal structure of the polycrystalline grains (c,f) for the samples 3C-SiC/Si (100) - № 810b (a-c) and 3C-SiC/Si (111) – № 808a (d-f).

- [1] W. J. Choyke, R. P. Devaty, L. L. Clemen, M. Yoganathan, G. Pensl, and Ch. Hässler, "Intense erbium-1.54- $\mu$ m photoluminescence from 2 to 525 K in ion-implanted 4H, 6H, 15R, and 3C SiC", *Appl.Phys.Lett.*, 65, pp.1668-1670, 1994.
- [2] S.J.Xu, M.B.Yu, Rusli, S.F.Yoon, and C.M.Che, "Time-resolved photoluminescence spectra of strong visible light-emitting SiC nanocrystalline films on Si deposited by electron-cyclotron-resonance chemical-vapor deposition", *Appl.Phys.Lett.*, 76, pp. 2550-2552, 2000.
- [3] L.K.Orlov, Yu.N.Drozdov, N.A.Alyabina, N.L.Ivina, V.I.Vdovin, and I.N.Dmitruk, "Structure and ultraviolet photoluminescence of 3C-SiC films grown on Si(111)", *Phys. Solid State.*, 49, pp.474-480, 2007.
- [4] L.K.Orlov, Yu.N.Drozdov, V.I.Vdovin, Yu.I.Tarasova, and T.N.Smyslova, "Specific features of morphology and the structure of nanocrystalline cubic silicon carbide films grown on a Silicon surface", 51, pp.1077-1082, 2009.
- [5] X.L.Wu, J.Y.Fan, T.Qiu, X.Yang, G.G.Siu, and P.K.Chu, "Experimental evidence for the quantum confinement effect in 3C-SiC nanocrystallites", *Phys.Rev.Lett.*, 94, pp.026102/1-3, 2005.
- [6] J.Zhu, Z.Liu, X.L.Wu, L.L.Xu, W.C.Zhang, and P.K.Chu, "Luminescent small-diameter 3C-SiC nanocrystals fabricated via a simple chemical etching method", *Nanotechnology*, 18, pp.365603/1-5, 2007.
- [7] L.Zhang, W.Yang, H.Jin, Z.Zheng, Z.Xie, H.Miao, and L.An, "Ultraviolet photoluminescence from 3C-SiC nanorods", *Appl.Phys.Lett.* 89, pp.143101/1-3, 2006.



# **The W/HfO<sub>2</sub>/Si (100) structures fabricated by the RF magnetron sputtering**

E.Bogoyavlenskaya, Yu.Denisenko, V.Naumov, V.Rudakov

*Yaroslavl Branch of the Institute of Physics and Technology, Russian Academy of Sciences, Yaroslavl, Russia,*

*E-mail address: lbhoo@yandex.ru*

Nowadays, hafnium oxide (HfO<sub>2</sub>) attracts much attention being one of the famous high dielectric (high-*k*) materials convenient for replacing oxide silicon (SiO<sub>2</sub>) as a gate dielectric in field-effect transistors (FETs) [1, 2]. It is known, that there is a dependence of the dielectric constant upon the crystal structure or crystallographic orientation in high-*k* materials [2]. Therefore, structural studies of HfO<sub>2</sub> are very important especially because this material may form some crystalline phases (monoclinic (stable phase), tetragonal or orthorhombic, and cubic).

The experiments were carried out on the W/HfO<sub>2</sub>/Si (100) and HfO<sub>2</sub>/Si (100) structures formed by the RF magnetron sputtering (SCR-651 “Tetra”, Alcatel). Four pure HfO<sub>2</sub> tablets with the diameter of 16 mm disposed symmetrically about the circle with the diameter of 45 mm were used as a target. The distance between the target and the Si-substrate was 100 mm. The Si-substrates were phosphorus doped *n*-type wafers with the resistivity of 20 Ω cm. During the sputtering process, the temperature of the Si-substrate was fixed at 200 °C. The residual pressure in the chamber was equal to  $7.5 \times 10^{-7}$  Torr. The film growth was carried out in both Ar (pressure was equal to  $7.5 \times 10^{-3}$  Torr) and Ar/O<sub>2</sub> (partial pressure of oxygen was equal to  $7.5 \times 10^{-4}$  Torr) plasma. It was determined that the value of the HfO<sub>2</sub> film growth rate in O<sub>2</sub> atmosphere was 1.5 nm/min and of the same procedure in Ar/O<sub>2</sub> atmosphere was 0.25 nm/min. The W films were grown at 0.67 nm/sec (~0.01 nm/min). The thickness of the films and the surface morphology of the samples were determined by means of the SUPRA-40 (Zeiss) scanning electron microscope (SEM). The same microscope with the energy-dispersive X-ray (EDX) attachment “Energy” (Oxford Instrument Analytical) was used for testing the chemical composition of the films. Structural studies of the samples were carried out with the help of X-ray diffraction (XRD) analysis done on the DRON-3M X-ray diffractometer with a CuKα X-ray source ( $\lambda_{K\alpha 1}=1.5405$  Å,  $\lambda_{K\alpha 2}=1.5443$  Å) at 30 kV beam energy and 25 mA beam current. A pyrolytic graphite was used as a monochromator. The XRD-spectrum was collected in normal (Bragg-Brentano) incidence geometry over the range  $20^\circ < 2\theta < 100^\circ$  with a step of  $0.1^\circ$  and a scan speed of  $2^\circ/\text{min}$ . A Si (400) crystallographic plane ( $2\theta=69.2^\circ$ ) was chosen for the tuning. The collected XRD pattern was compared to the reference pattern in the Joint Committee for Powder Diffraction standards (JCPDS) Powder Diffraction File (PDF). The HfO<sub>2</sub> films were treated by the rapid thermal annealing process (RTP) at 500, 700 and 900 °C for 60 sec in N<sub>2</sub> ambient. The RTP was held with the help of the SHS 100 (AST) equipment.

Fig. 1 presents the SEM image of the investigated samples in their initial state on the example of the W/HfO<sub>2</sub>/Si (100) structure. The results of the XRD investigations (Fig. 2) are illustrated using the diffraction profile of the HfO<sub>2</sub>/Si (100) structure built before and after RTP at 500 °C in N<sub>2</sub> ambient.

As follows from Fig. 2 we can clearly identify a strong peak corresponding to Si (400) in both the diagrams. Also there is a weak Si (200) peak, which is forbidden for the diamond structure indicating the presence of the slight HfO<sub>2</sub>/Si interface strain. After annealing at 500 °C, the diffraction line of the sample differs from that before RTP. Besides the Si (200) and Si (400) reflexes, there are peaks of the diagram corresponding to the HfO<sub>2</sub> monoclinic crystal standard. There is a monoclinic (11-1) reflex at  $2\theta=28.5^\circ$ , which is the most often identified reflex for the analogous growth compositions [3]. According to the amount and characteristics of the other reflexes, it is obvious that HfO<sub>2</sub> films are polycrystalline after the thermal process. It is known that the tetragonal and the cubic structures are high-temperature structures, normally existing only above 1700 °C and 2800 °C, respectively [1]. So, they are even less likely to be seen at lower temperature, which is typical for the monoclinic phase. Furthermore, it should be noted that (111) reflex ascribed to the monoclinic phase has the higher value of *d* spacing (2.885 Å) in comparison with the same characteristic taken from the PDF (2.825 Å). This fact is in agreement with both the phenomenon of the dependence of the lattice parameter behavior upon the annealing process temperature described in [1] and the fact of the influence of the substrate temperature to the HfO<sub>2</sub> film crystallization state without annealing and after it [2].

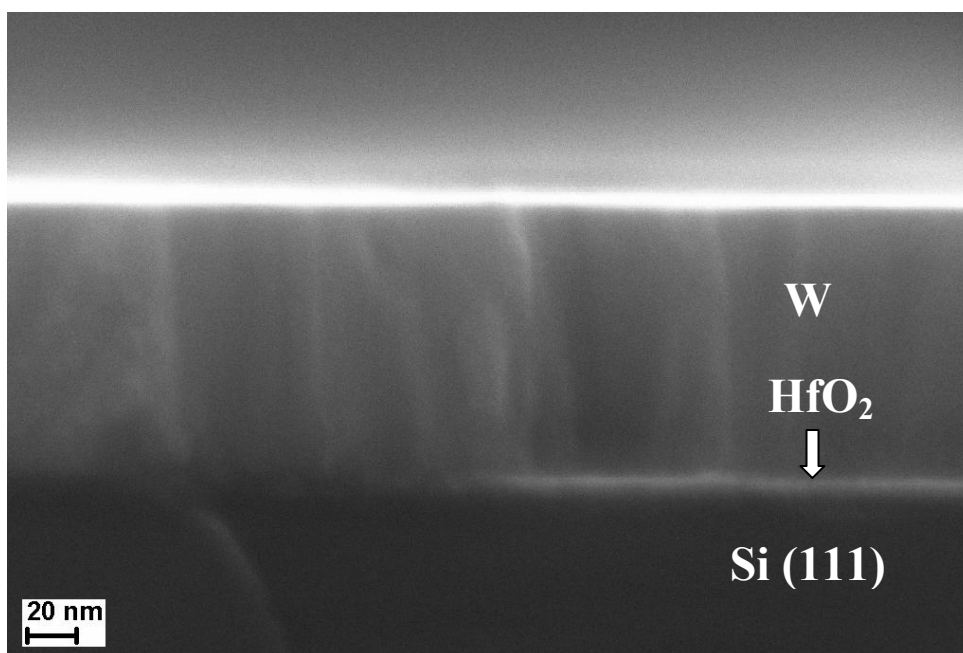


Fig. 1. The SEM image of the W/HfO<sub>2</sub>/Si (100) structure.

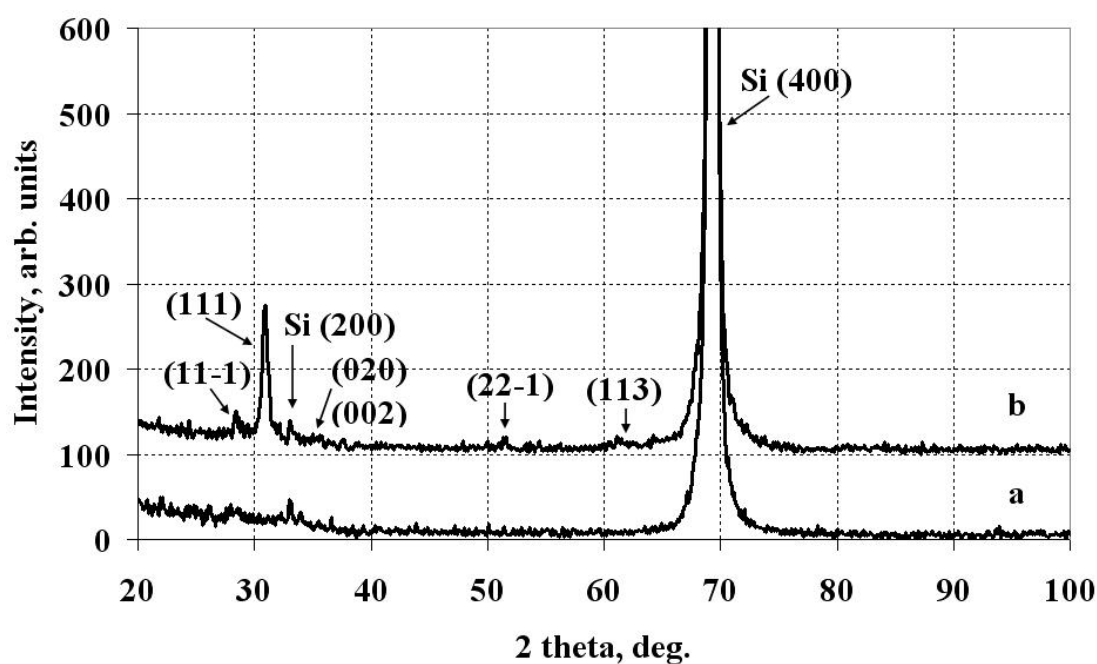


Fig. 2. The XRD spectrum of the HfO<sub>2</sub>/Si (100) structure before (a) and after RTP at 500 °C (b) in N<sub>2</sub> ambient.

1. X. Luo, A. A. Demkov *et al.* "Combined experiment and theoretical study of thin hafnia films", *Phys. Rev. B*, **78**, pp. 245314-1-245314-10, 2008.
2. L. Wang, B. Fan *et al.* "Effects of substrate temperature on crystallite orientation of HfO<sub>2</sub> thin films", *Material Science – Poland*, **27**, № 2, pp. 547-550, 2009.
3. M.-Y. Ho, H. Gong *et al.* "Morphology and crystallization kinetics in HfO<sub>2</sub> thin films grown by atomic layer deposition", *J. of Appl. Phys.*, **93**, № 3, pp. 1477-1481, 2003.

# Electron tomography and STEM investigation of amorphous and nanocrystalline materials CoW-CoNiW systems in external action

O.Voitenko<sup>1</sup>, E.Modin<sup>1</sup>, A.Gluhov<sup>1</sup>, E.Pustovalov<sup>1</sup>, S.Dolzhikov<sup>1</sup>,  
V.Plotnikov<sup>1</sup>, S.Grabchikov<sup>2</sup>, L.Sosnovskaya<sup>2</sup>

1. Far Eastern National University, Vladivostok, Russia, voitenko@lemoi.phys.dvgu.ru.

2. United Institute of Solid-state Physics and Semiconductors, National Academy of Science, Minsk, Belarus

In the view of thermodynamics, amorphous metal alloys represent metastable nonequilibrium systems, which in time transform to equilibrium crystal state. Crystallization of amorphous metal alloys is carried out by transition through a number of metastable conditions at which different on the properties the heterophase structures having nanocrystalline and a polycrystalline structure are formed [1]. The investigation of this process is an important task today.

The structure of amorphous and nanocrystalline alloys CoW and CoNiW systems, obtained by the electrochemical deposition method, was investigated in this work. All samples were deposited in conditions in which amorphous structure organized. Structure investigation was made on transmission electron microscope Carl Zeiss Libra 200 FE in TEM (Transmission electron microscopy) mode and STEM (Scanning transmission electron microscopy) mode with accelerating voltage 200 kV. Also was made electron tomography investigation of amorphous and nanocrystalline structure before and after sample heating.

Amorphous alloys samples CoW and CoNiW systems were heated and cooled to  $-150^{\circ}\text{C}$  in electron microscope column to  $300^{\circ}\text{C}$  with step 2 degree in minute. Specialized double-tilt sample holders Gatan Model 652 and Model 636 were used for sample heating and cooling. Investigation of structure dynamics was made in diffraction mode, which assist in reducing negative electron beam sample heating effect. The structure of sample CoW heated to  $300^{\circ}\text{C}$  in electron microscope column is shown on Fig. 1. In the image center we can see ordered atom structure of nanocrystallite. Initially sample CoW was amorphous. Plane spacing calculated according to the Fourier spectrum data indicates Co cubic phase,  $d_{111}=0,2$  nm. CoW sample structure after heating to  $300^{\circ}\text{C}$  received in STEM mode is shown in Fig. 2. Sample structure after heating became less branchy.

Electron tomography is a powerful method that can investigate the three-dimensional structure of materials. It can be applied to a wide range of samples that can be prepared for transmission electron microscopy. In our case the tomogram reconstruction is performed using a weighted back-projection method. Using a sufficient number of projections, from different angles, the superposition of all the back-projected images will return the original object. 3D models of reconstructed tomograms were made in IMOD [2] software package and Amira software package. Image processing was made using orthogonal wavelet transform and fractal filtration. This work was made with Carl Zeiss grant support.

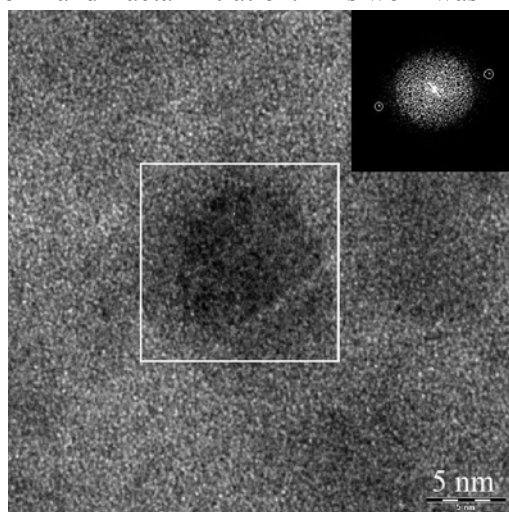


Fig. 1 CoW TEM, 200 kV,  $T = 300^{\circ}\text{C}$

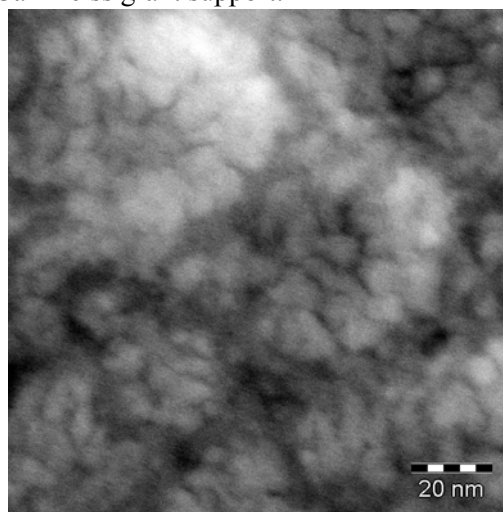


Fig. 2 CoW STEM, 200 kV,  $T = 300^{\circ}\text{C}$

1. Grabchikov S.S., *Amorphous electrolytic deposited metallic alloys*, 6, Publ.center BNU, Minsk, 2006.
2. <http://bio3d.colorado.edu/imod/>

# Structure investigation of electrodeposited CoP-CoNiP amorphous alloys under thermal impact

E.Modin<sup>1</sup>, O.Voitenko<sup>1</sup>, A.Gluhov<sup>1</sup>, E.Pustovalov<sup>1</sup>, S.Dolzhikov<sup>1</sup>,  
B.Grudin<sup>1</sup>, V.Plotnikov<sup>1</sup>, S.Grabchikov<sup>2</sup>

1. Far Eastern National University, Vladivostok, Sukhanova 8 st., 690050.

2. United Institute of Solid-state Physics and Semiconductors, National Academy of Science, Minsk, Belarus

Amorphous and nanocrystalline metallic alloys have unique mechanical and magnetic characteristics and they are of great practical interest. Co- based alloys are soft magnetic materials, so they widely used in magnetic head, magnetic core, electromagnetic shield production[1]. The structure relaxation and crystallization processes of amorphous metallic alloys are investigated for quite long time, but most of work in this matter is devoted to indirect investigation methods[2]. These processes represent the great scientific interest because of the materials physical properties determination. In this work structure relaxation and crystallization processes have been investigated by the direct methods such as high resolution transmission microscopy and diffraction mode observation. Investigated materials are amorphous metallic alloys of CoP and CoNiP. Test samples were prepared by electrodeposition method from sulphuric acid electrolyte. The experiments were held directly in the column of transmission electron microscope Carl Zeiss Libra 200FE, using special double-axis heating holder Gatan Model 652 and liquid nitrogen cooled holder Gatan Model 636. "In-situ" heating of CoP-CoNiP system samples research were carried out in temperature range of -150 °C to 250 °C with constant heating speed about 1-2 °C/min. Some samples were processed with isothermal annealing at temperature 150-200 °C. We used two ways for cooling: with maximum speed about 70 °C/min and second way is stepped with 10 °C/min decrement. Observing the structure dynamics while heating and cooling were held in diffraction mode.

As result of the experiment series of electron diffraction images were obtained. These image series characterize the structure relaxation and crystallization processes. With temperature increasing the first diffuse ring diameter growth can be observed at the electron diffraction images. This diffuse ring on the image below corresponds to the amorphous phase. The increase of amorphous ring diameter shows change in average atomic spacing. Diffraction rings corresponding to polycrystalline phases of Cobalt and Co<sub>2</sub>P ( $d_{122}=2.211$  Å,  $a=5.638$ ,  $b=3.507$ ,  $c=6.603$ , ICSD-43687) also can be observed.

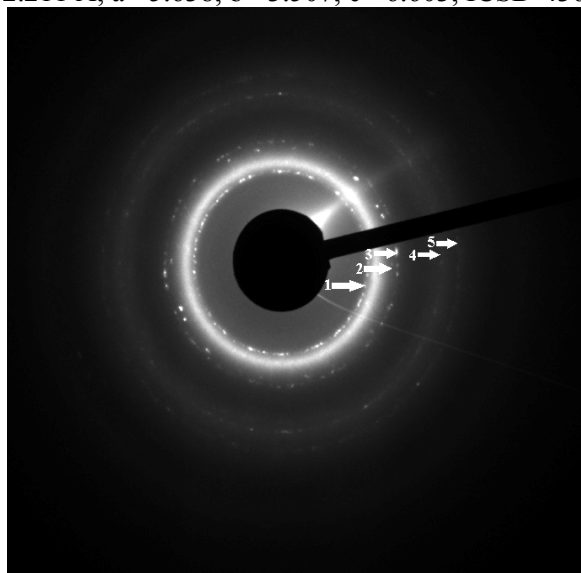


Fig. 1. Electron diffraction image of CoP sample. Rings marked as 1,3,4 show the best correlation with Co<sub>2</sub>P phase, other rings corresponded Co.

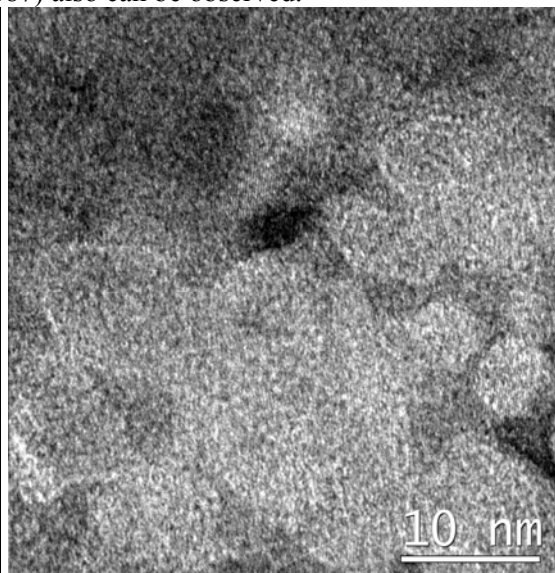


Fig. 2 Electron microscopic image of CoP sample structure after 250 °C annealing.

[1] Grabchikov S.S., *Amorphous electrolytic deposited metallic alloys*, 6, Publ.center BNU, Minsk, 2006.

[2] Khonik S.V., Sviridov V.V., Kobelev N.P. "Kinetics of structural relaxation of bulk and ribbon Pd<sub>40</sub>Cu<sub>30</sub>Ni<sub>10</sub>P<sub>20</sub> glasses determined from electrical resistance measurements", *Physics of the Solid State*, **49**, 8, pp.1345-1351, 2007.

# Application of the phase-field crystal model for materials modeling: metals and colloids

T. Ala-Nissilä

*COMP CoE and Department of Applied Physics, Aalto University School of Science and Technology, FI-00076 Aalto,  
Espoo, Finland*

The recently proposed Phase-Field Crystal (PFC) model [1] can be used to model materials on microscopic length but diffusive time scales. The model can be related to the classical density functional theory of liquids [2] allowing modeling of solidification, phase segregation, grain growth, elastic and plastic deformations in anisotropic systems with multiple crystal orientations. In this talk, I will discuss recent progress on using the PFC model and its extensions to quantitatively model single-component systems such as pure metals (fcc-Fe) and colloidal systems.

\*Work done in collaboration with: A. Jaatinen, C. Achim, K.R. Elder, L. Granasy, and H. Löwen.

1. K.R. Elder, M. Katakowski, M. Haataja, and M. Grant, Phys. Rev. Lett. vol. 88, 245701 (2002); K.R. Elder and M. Grant, Phys. Rev. E vol. 70, 051605 (2004).
2. K.R. Elder, Nikolas Provatas, Joel Berry, Peter Stefanovic, and Martin Grant, Phys. Rev. B vol. 75, 064107 (2007).
3. A. Jaatinen, C.V. Achim, K.R. Elder, and T. Ala-Nissilä, Phys. Rev. E vol. 80, 031602 (2009).

# Phase-field-crystal model for pinning and sliding of adsorbed layers

E.Granato

*Laboratório Associado de Sensores e Materiais, Instituto Nacional de Pesquisas Espaciais,  
12227-010 São José dos Campos, SP, Brasil.*

A driven adsorbed layer on a periodic potential is a fundamental model in the study of sliding friction phenomena between two crystalline surfaces with a boundary lubrication layer<sup>1</sup>. Numerical results are presented for pinning and sliding of adsorbed layers using a phase-field-crystal model<sup>2, 3, 4, 5</sup> and are compared with previous results from particle models. The phase-field-crystal model provides a continuous description of the system allowing for both elastic and plastic deformations of the layer on spatial and time scales much larger than atomic scales. In the absence of driving, the equilibrium phase diagram as a function of lattice mismatch, pinning strength and temperature shows commensurate, incommensurate and liquid-like phases strongly dependent on the ordered structure. With a driving force and inertial effects, the velocity response of an initially commensurate layer shows hysteresis with dynamical melting and freezing transitions for increasing and decreasing applied forces. The main features of the nonlinear response are similar to the results obtained previously with molecular dynamics simulations of particles. However, the dynamical melting and freezing mechanisms are significantly different corresponding to nucleation of stripes rather than closed domains.

Work supported by FAPESP through Grant No. 07/08492-9.

1. B.N.J. Persson, Phys. Rev. Lett. **71**, 1212 (1993).
2. C.V. Achim, M. Karttunen, K.R. Elder, E. Granato, T. Ala-Nissilä, and S.C. Ying, Phys. Rev. E **74**, 021104 (2006).
3. J.A.P. Ramos, E. Granato, C.V. Achim, S.C. Ying, K.R. Elder, T. Ala-Nissilä, Phys. Rev. E **78**, 031109 (2008)
4. C.V. Achim, J.A.P. Ramos, M. Karttunen, K.R. Elder, E. Granato, T. Ala-Nissilä, S.C. Ying, Phys. Rev. E **79**, 011606 (2009).
5. J.A.P. Ramos, E. Granato, S.C. Ying, C.V. Achim, K.R. Elder, T. Ala-Nissilä, Phys. Rev. E **81**, 011121 (2010).

## Diffusion of adatom clusters on metal surfaces: periphery diffusion or concerted motion?\*

T.S.Rahman

*Department of Physics, University of Central Florida, Orlando, Florida, E-mail: talat@physics.ucf.edu*

Coupled with advances in *ab initio* methods for the calculation of activation energy barriers, the kinetic Monte Carlo (KMC) method is proving itself to be an important tool for computational studies of phenomena such as epitaxial growth, surface diffusion and surface morphological evolution. However, despite its ability to carry out simulations for time and length scales that are relevant to experiments, in its nascent form the method has limited predictive power because of its reliance on predetermined atomic events and their energetics as input. To overcome this handicap, we have developed a self learning method (SLKMC) [1], in which we combine standard KMC with automatic generation of a table of microscopic events, facilitated by a pattern recognition scheme. Each time the system encounters a new configuration, the algorithm initiates a procedure for saddle point search around a given energy minimum. Nontrivial paths are thus selected and the fully characterized transition path is permanently recorded in a database for future usage. The system thus automatically builds up all possible single and multiple atom processes that it needs for a sustained simulation. Results of the application of the method to examination of the diffusion and coalescence of 2-dimensional Cu and Ag adatom and vacancy clusters on Cu(111) and Ag(111) will be presented. I will highlight the key role played by specific diffusion processes revealed during the simulation. Of particular interest are multiple atom processes whose presence may have been ignored otherwise. As we will see the importance of such processes is dependent on both cluster size and surface temperature. For adatom clusters varying in size from 2 to 1000, I will discuss the size dependence of the diffusion coefficient and the effective energy barrier. The rate limiting processes will also be discussed for island coalescence. Results will be compared with those from experiments, where available, and with those from KMC simulations based on a fixed catalogue of diffusion processes. I will also provide some details of an extension of the techniques to “off-lattice” case and its application to examine the case of hetero-epitaxial growth. I will focus also on the relative importance of periphery atom diffusion and concerted island motion as a function of cluster size. Of particular interest will be the size at which cross over from the dominance of one type of mechanism over other for the diffusion of Cu and Ag clusters on Cu(111) and Ag(111), respectively..

<sup>1</sup>Work done in collaboration with O. Trushin, A. Kara, A. Karim, G. Nandipati and S. I. Shah.

\*Work supported in part by NSF and CRDF

1. O. Trushin, A. Karim, A. Kara , and T. S. Rahman, Phys. Rev. B **72**, 115401 (2005)
2. A. Karim, A. Al-Rawi, A. Kara, O. Trushin, T. Ala-Nissilä and T. S. Rahman, Phys. Rev. B **73**, 165411 (2006)

# Ordering of 2D binary system with interaction to next nearest neighbors - CCMF method

Z.Chvoj

*Institute of Physics, AS CR, v.v.i., Na Slovance 2, 182 21 Prague 8, Czech Republic*

In recent years there have been extensive studies of the formation of the two-dimensional, surface ordered structures. The description of the phase transformation or ordering is difficult in the interacting many-body systems. Hence, various mean-field (MF) theories have been proposed to get some insight into properties and behavior of such systems and studied phase transitions. The simple MF theory gives not very accurate value for critical points of phase transition. Recently was published new method (see [1]), which works also within mean field concept, but which gives results close to the exact values of critical temperatures of phase transitions. This methods, named Correlated cluster mean-field theory (CCMF), divide the lattice sites into clusters whose size and shape are selected to that the equivalence of all sites in a cluster is preserved. Such division respect the symmetry of structure and must contain all interactions which are in the system considered. The strength of interactions of a cluster with its surrounding clusters is strongly dependent on the configuration of atoms in central cluster itself. Within this concept these interactions are represented by the effective mean field, which depend on configuration of atoms in cluster.

In our contribution we show the suitability of the new approximate methods of the study of interacting many-body systems - the Correlated Cluster Mean Field theory - on the binary systems in lattice gas model. In the case of nearest neighbors interaction the extension is evident. We extend also this model on system with interactions to the next nearest neighbors and investigated critical behavior. After some natural assumptions about effective mean fields we obtain very good agreement with the results of renormalization group theory, concerning critical temperature. It seems, that this new method is powerful and effective in the study of thermodynamic properties of complex systems. In next paper we want to extend our study on the general binary systems  $A_xB_{1-x}$  and find phase diagram with respect the interaction to the next nearest neighbors.

[1] D. Yamamoto, Phys. Rev. B 79, 1444427 (2009).



# Multiscale study of submonolayer growth for Fe/Mo(110)

M.Mašín<sup>1</sup>, M.O.Jahma<sup>2</sup>, T.Ala-Nissilä<sup>2</sup> and M.Kotrla<sup>1</sup>

1. Institute of Physics, Academy of Science of the Czech Republic, Na Slovance 2, Prague, 18221, Czech Republic. 2. Department of Applied Physics, Aalto University School of Science and Technology, P.O. Box 11000, FI-00076 Aalto, Espoo, Finland

We apply multiscale approach to study submonolayer growth for the Fe/Mo(110) system. In particular, we compare results obtained for island size distributions from two methods, namely Kinetic Rate Equation (KRE) approach and Monte Carlo (MC) simulations. This work is motivated by experimental work of Jubert *et al.* [1].

In the MC part of the project we simulate Molecular Beam Epitaxy (MBE) on a lattice with continuous constant flux. We omit adatom desorption, while deposition and diffusion occur via thermally activated jumps. The relevant energy parameters are the activation energy for single-particle jumps

$E_A = E_d + \sum_{i=1}^3 l_i E_{Bi}$ , binding energy to the substrate  $E_d = 0.4$  eV, and attractive nearest-neighbor interactions (bond energies)  $E_{Bi}$ ,  $E_{B1} = -0.329$  eV,  $E_{B2} = -0.072$  eV,  $E_{B3} = -0.079$  eV. The diffusion prefactor (vibrational frequency) has been estimated to be  $\nu = 4 \times 10^{12}$  Hz [2]. Here  $l_i$  is the number of occupied  $i$ -th neighbors. We use the BKL algorithm [3]. We start the simulation at zero coverage and deposit particles up to the so called saturation coverage, where the island density does not depend on deposited coverage or starts to decrease because of coalescence. A deposited particle diffuses around the surface until it is attached to an existing island or creates a new island with another diffusing particle. Detachment and breaking of islands is allowed. We consider a flat surface without any steps, defects or impurities. Islands can move via edge diffusion, but collective moves are not included. Mobility of islands depends on size and temperature – at low temperatures only monomers diffuse.

In the second part we use the KRE approach combined with the Particle Coalescence Method [4] to compute the island size distribution. The rate equation giving the time evolution of island size distribution  $n_s$  for a system undergoing diffusion driven aggregation and with incoming flux  $\Phi$  of adatoms per monolayer is given by [4]

$$\frac{dn_s(t)}{dt} = \sum_{i+j=s} K(i,j)n_i n_j - \sum_{i=1}^{s-1} K(i,s)n_i n_s + \Phi \delta_{1s}, \quad (1)$$

where  $K(i,j)$  is called aggregation kernel defined as

$$K(i,j) = D_i + D_j. \quad (2)$$

$D_i$  is the diffusion coefficient of an island of size  $i$ . The diffusion coefficients are nontrivial functions of the island size [5]. We use values obtained from independent Monte Carlo simulations, where the same energies as mentioned above have been used. We use the transition dynamics algorithm (TDA) [6].

In the case of KRE we use two aggregation modes, namely adatom-island and island-island aggregation modes and two temperatures  $T=500$  K and  $T=1000$  K. In the case of MC we consider the case  $T=500$  K only. Comparing results obtained with both the KRE and MC methods, for temperature  $T=500$  K we can see that we have good agreement for MC and adatom-island aggregation mode. For comparison we use the scaled island density function  $g(x)$  as a function of normalized island size  $x=s/\bar{s}$  [5]. In the case of island-island aggregation  $g(x)$  decreases for small islands and at  $x \approx 0.1$  starts to grow with maximum at  $x=1$  followed by a rapid decrease. In the case of MC and adatom-island aggregation  $g(x)$  grows monotonically for small islands with a global maximum at  $x=1$ .

[1] P.O. Jubert, O. Fruchart and C. Mayer, Phys. Rev. B **64**, 115419 (2001).

- [2] Unpublished data from *ab initio* has been provided by Mark Asta.
- [3] P.A. Maksym, Semicon. Sci. Technol. **3**, 594, (1988).
- [4] M. Rusanen, I.T. Koponen, and J. Asikainen, Eur. Phys. J. B **36**, 567 (2003).
- [5] M.O. Jahma, M. Rusanen, A. Karim, I.T. Koponen, T. Ala-Nissilä and T.S. Rahman, Surf. Sci. **598**, 246-252 (2005).
- [6] T. Ala-Nissilä and J. Kjoll and S.C. Ying, Phys. Rev. B **46**, 846 (1992).

# Effect of misfit dislocation on surface diffusion

O.Trushin<sup>1</sup>, M.Aminpour<sup>2</sup>, T.S.Rahman<sup>2</sup>

1. Yaroslavl Branch of the Institute of Physics and Technology, Russian Academy of Sciences, Yaroslavl, Russia, oleg\_trushin@lenta.ru. 2. Department of Physics, University of Central Florida, Orlando, FL, USA

It is well known that strain fields in crystal lattice affect surface diffusion. Several works were devoted to the effect of homogeneous strain on diffusion barriers [1,2]. However in real systems presence of defects makes strain fields strongly inhomogeneous. It is particular case of misfit dislocations in heteroepitaxial systems. As far as we know there were no systematic studies of the effect of strain fields near dislocation core on surface diffusion. In this work we use molecular dynamics and molecular static methods to study the effect of misfit dislocations in heteroepitaxial system on adatom diffusion in the close proximity to dislocation core. We created misfit dislocation inside Cu/Ni(111) by metallic structure with core located at the interface between Cu film and Ni substrate using method of Repulsive Bias Potential described elsewhere[3]. Presence of defect inside the structure leads to formation of strain field on the surface. This strain field affects adatom diffusion on the surface. To make quantitative estimates of the effect we compare two cases of adatom diffusion on the surface with defect underneath and on the surface without defect.

The model system consists of crystal substrate and Cu adatom on top of it. The substrate itself is represented by heteroepitaxial structure Cu/Ni(111) with isolated misfit dislocation located at the Cu-Ni interface. Typical configuration of the model presented on Fig. 1a. Cu/Ni(111) system is characterized by 5.1 % lattice misfit between Cu ( $a=3.615$  Å) and Ni (3.58 Å). Thus Cu layer is under compressive stress. To create ideal misfit dislocation inside the system we used standard procedure described elsewhere [3]. This procedure allows to activate transition of many atomic system from coherent state (without defect) to relaxed state with defect. The system consists of 10 Ni(111) layers and 3-7 layers of Cu with 250 atoms inside each layer. Periodic boundary conditions were used in the plane parallel to substrate surface to mimic infinitely large system. Two bottom layers of the Ni substrate were fixed to prevent motion of the system as whole.

Embedded atom method potentials used for modeling interatomic forces in the system [4].

First of all we illustrate the effect of dislocation on adatom diffusion by presenting adatom energy maps (Fig. 1b). This map represents adatom binding energy at different positions on the surface.

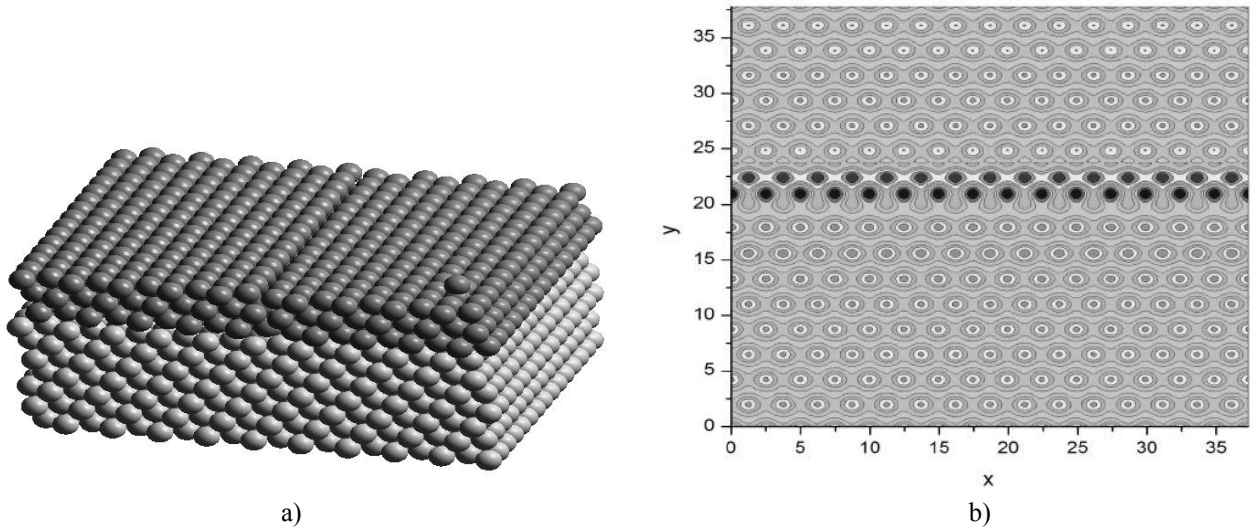


Fig. 1 (a).Side view on the sample Cu/Ni(111) with defect in the middle and adatom walking on the periphery, (b) adatom energy map (binding energy of adatom at different positions on the surface).

We also compare adatom MD trajectories for two systems (system without defect (Fig. 2a) and system with misfit dislocation located underneath the surface (Fig. 2b)). We see that presence of the defect under the

surface strongly affects the trajectory, creating anisotropy in atomic diffusion. We also estimate energy barriers for adatom diffusion in the core region and compare it with defect free sample.

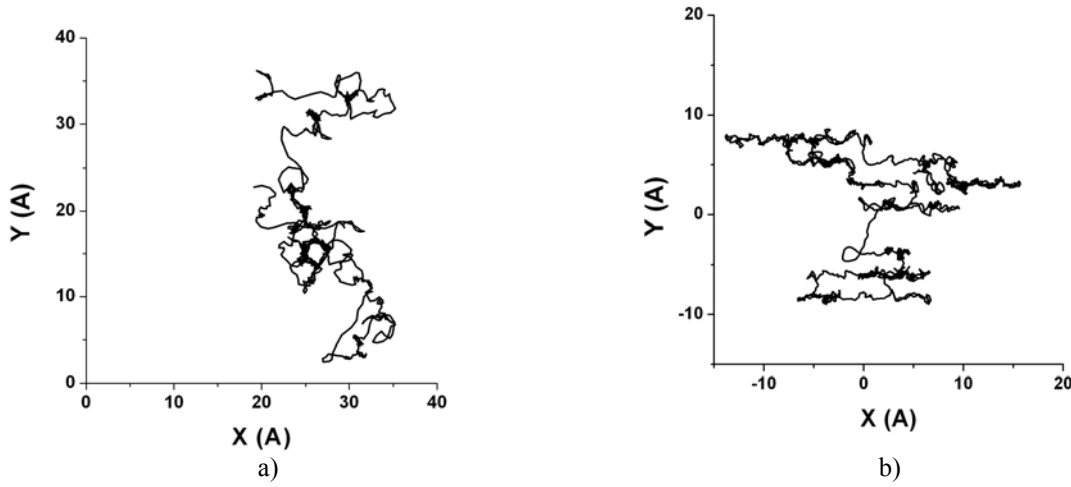


Fig. 2. MD trajectory of adatom moving on the Cu/Ni(111) surface at room temperature (a) sample without defect, (b) sample with ideal dislocation under the surface (dislocation line running along X direction).

In conclusion presence of defect inside substrate has profound effect on surface diffusion. Strain field due to isolated edge dislocation spreads to long distance from dislocation core. It provides anisotropy of surface diffusion near defect. There are trap zones along dislocation line where adatoms prefer to stay. Anisotropy of surface diffusion should lead to modifications of surface morphology during thin film growth.

1. M. Schroeder, D.E. Wolf, "Diffusion on strained surfaces", Surface Science **375**, pp.129 , 1997.
2. C. Ratsch, A. P. Seitsonen, and M. Scheffler, "Strain dependence of surface diffusion: Ag on Ag(111) and Pt(111)", PRB, **55**, p.6750, 1997.
3. O Trushin, J Jalkanen, E Granato, S C Ying and T Ala-Nissilä "Atomistic studies of strain relaxation in heteroepitaxial systems", J. Phys.: Condens. Matter **21**, pp. 084211, 2009.
4. S. M. Foiles, M. I. Baskes and M. S. Daw, "Embedded atom method functions for fcc metals Cu,Ag,Au,Ni,Pd,Pt and their alloys", Phys. Rev. B, **33**, pp.7983, 1986.

# Multiagent approach to adsorption processes modeling by the method of likelihood cellular automat.

N.A.Rud<sup>1</sup>, A.A.Astapkov<sup>2</sup>, P.G.Morozov<sup>3</sup>

1. Yaroslavl Demidov State University, Yaroslavl, Russia, rud50@mail.ru. 2. Yaroslavl Demidov State University, Yaroslavl, Russia, ph4ntom@mail.ru. 3. Moscow Aviation Institute, Moscow, Russia, Pmorozov@bellintegrator.ru

The superficial phenomena are the unique channel for the deep penetration into a crystal. Besides, the properties' modifications of a surface affect volume properties of a firm body by the direct way, especially when the volume and the area are commensurable. Periodic change of dynamic characteristics of process was revealed during anodizing processes of semi-conductor crystals. Oscillation phenomena have been found out during porous silicon etching. Adsorption and desorption the molecules capable to change the kernel, finds out ability of periodic changes of process dynamic characteristics. These facts show the need for development of the theory, capable to explain set of the listed experimental data. Modelling of similar processes is another work target.

Research is based on model representations of adsorption system. That means, there are two various conditions the molecule adsorbed on a surface of the firm body can be - neutral and charged. The model algorithm is constructed on the basis of the likelihood cellular automatic machine method with use of the blocks turn method. The surface of a firm body is presented in the form of the square lattice. It represents a set of energetically identical active centers where adsorbate molecules are localised. One molecule is adsorbed only on one center, i.e. the only one adsorption monolayer is formed during the adsorption process. Adsorption on this centre does not affect adsorption on other centers connected with the model. The considered volume represents some monomolecular layers forming a cubic lattice. Molecules can diffuse both from the outside, and between layers. Each molecule of a firm body is "cell" of the cellular automatic machine. Conditionally, each of cells can be in one of three various conditions: a cage without the absorbed molecule; a cage with the absorbed molecule; a cage with the charged absorbed molecule. Within the model, each of conditions is presented by three various colors: white, grey and black accordingly.

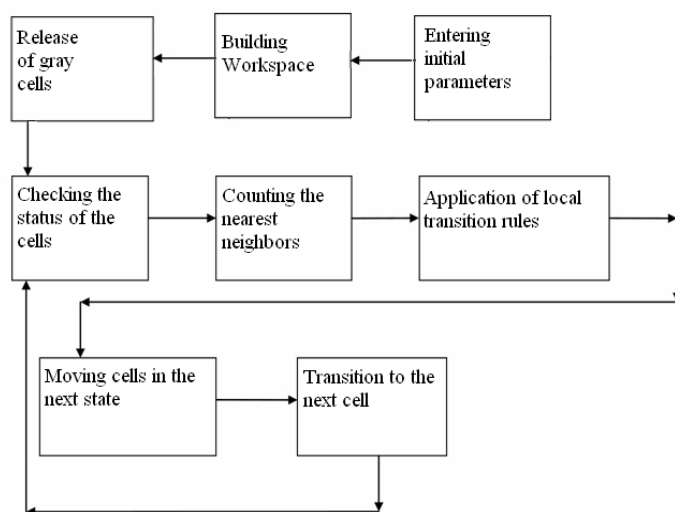


Fig. 1 Schematic block diagram of the algorithm.

The block diagram of model algorithm work is presented on fig. 1. Initial parameters are represented by two three-dimensional matrixes: a matrix life time and a matrix of transition probability. The working area represents some layers of cells modelling a cubic lattice. As said before, "cell" that models a substance molecule, can be in three various conditions. Depending on these conditions and the nearest 'neighbors' in the field of Moore, the transition of "cell" from one condition to another is carried out. Transitions are realized with use of blocks turn method.

The modeling algorithm means recalculation of cell conditions in whole volume on each step. But such decision is not effective. During realization of such algorithm without modification, "in the pure

state" there are problems with shortage of memory and general productivity. For elimination of this problem the algorithm has been modified to reduce "single" recalculation to a minimum. It means recalculation only really changing values of elements. The calculation of independent makes in parallel.

The algorithm is realised in the multiagent system consisting of three kinds of agents: the agent-executor, the paralleling agent and the agent-router. The Agent-executor carries out conditions calculation of the elements in the set segment of a lattice. The paralleling agent breaks a lattice into segments by quantity

of accessible agents-executors and by distributes a problem between them. The Agent-router search new agents-executors located in other applications and machines.

The agents function under the following scheme:

- The paralleling agent interrogates agents-routers and receives names of accessible agents-executors adding them to already existing own list.
- The lattice breaks into segments on number of agents in the list. The information on corresponding segments is dispatched to agents.
- The initialization of segments performs by addition of "grey" cells on a layer.
- On each step the agent-executor having "grey" or "black" cells in segment or border, makes recalculation conditions of segment elements. If "grey" or "black" cells appear on segment border as a result of recalculation the information on these cells is transferring to the agent responsible for the next segment. Those cells should affect calculation of the segment adjoining with the flowing one.

Thus in the received algorithm there is a recalculation only changing segments. Conditions calculation of elements in independent segments makes in parallel. These properties of algorithm allow to reduce calculation time and to lower memory. Multiagent stage was used for realisation of the described approach. It easily allows use agents, placed on the different computers united in a local network, or through the Internet, or even in a cloud. This algorithm allows settle the calculation in several cars at once so raising calculation productivity.

The algorithm is realised in C # machine code with toolkit of construction distributed applications based on multiagent approach and WCF technology. Calculation makes on several computers in a multiline mode. Visualisation of modeling results is realised by Microsoft XNA Game Studio technology. It possesses sufficient productivity and simplicity during workout. There is possibility to regard process on each layer.

# Toroidal moment and current induced transitions in the triangular molecular magnet $V_{15}$

V.V.Kostyuchenko

*Yaroslavl Branch of the Institute of Physics and Technology, Russian Academy of Sciences, Yaroslavl, Russia,  
E-mail: vkqubit@mail.ru*

At present time magnetoelectric phenomena in the molecular magnets systems, the spin states of which can be controlled and manipulated by external fields, attract much interest. A particularly appealing area in the molecular magnetism is that of molecules which have a toroidal moment. The different mechanisms, which may be responsible for the origin of toroidal moment, are actively studied (see e.g. [1, 2] and references therein). In the paper [2] the existence of toroidal moment in the molecular magnet  $V_{15}$  was predicted. It makes the possibility of transition between different spin states of the molecular magnet under the influence of electric current. The present work is devoted the theoretical investigation of these processes.

In the present work the dynamics of spin states in the molecular magnet  $V_{15}$  under the influence of electric current is studied. The toroidal moment of molecular magnet is taking into account. It is shown that electric current creates oscillations of the transition probability between spin states indicated by the quantum numbers  $S_{\Sigma}$  (the total spin) and  $S_z$  (projection of the total spin). The changing of the orientation of electric current with respect to the crystallographic axes can control the character of these oscillations. The dependence of the amplitude of oscillations on the current value has a resonance character. At small current density the amplitude of oscillations increases as the current density is increased. At large current density the amplitude of oscillations decreases as the current density is increased. The resonance value of current is determined by the splitting of ground state doublets and the energy difference between the ground state doublets ( $S_{\Sigma}=1/2$ ) and quartet ( $S_{\Sigma}=3/2$ ). Thus the experimental investigation of spin states dynamics under the influence of current gives additional access to the properties of spectrum of spin states.

As an example the transition between states  $S_z=1/2$ ,  $S_{\Sigma}=1/2$  and  $S_z=1/2$ ,  $S_{\Sigma}=3/2$  which is hardly accessible by another method can be achieved. As a conclusion, the calculations made in present work shows that the existence of toroidal moment in the molecular magnets opens a unique possibilities for control and manipulation of spin states. It may be very useful for the practical realization of quantum computers. It opens a real possibility to turn on (and/or turn off) the exchange interaction between molecular magnet and thus it enables switchable effective interqubit couplings even in the presence of permanent microscopic interactions [3].

[1] M. Trif, F. Troiani, D. Stepanenko, and D. Loss, Phys. Rev. Lett. **101**, 217201 (2008).

[2] A.K. Zvezdin, V.V. Kostyuchenko, A.I. Popov, A.F. Popkov, and A., Phys. Rev. B **80**, 172404 (2009)

[3] S. Carretta, P. Santini, G. Amoretti, F. Troiani, and M. Affronte, Phys. Rev. B, **76**, 024408 (2007)

# Magnetic properties and structure of cobalt films and Cu/Co/Cu/Si heterostructures

A.P.Glukhov, E.V.Pustovalov, B.N.Grudin, V.S.Plotnikov, K.S.Ermakov  
*Far Eastern National University, Russia, gluhov@lemoi.phys.dvgu.ru*

We investigated two types of samples: 1) polycrystalline thin films of cobalt on Si(111) and KCl substrates, with thickness ranging 5 to 20 nm, 2) multilayered poly- and monocrystalline Cu/Co/Cu thin films on Si substrate with thickness of Cu layers up to 2 nm. All samples were fabricated in ultra-high vacuum under following conditions: substrate temperature of 60°C, deposition rates for Co and Cu were 3 and 9 Å per minute respectively.

Arrays of nanodots of various forms and sizes (100-800 nm) were cut in cobalt film using FIB (Focused Ion Beam) system. In this investigation we used such methods as: transmission electron microscopy (TEM), scanning electron microscopy (SEM), electron diffraction. We used Carl Zeiss transmission electron microscope Libra 200FE and dual-beam Carl Zeiss Crossbeam 1540 XB.

Polycrystalline films have grain structure. Grain size was determined using watershed algorithm in ImageJ program using TEM images of the film. Average grain size was 11.9 nm with dispersion of 5.1 nm, Feret diameter was 17.7 nm with dispersion 5.1 nm. The shape of average and Feret diameter's distributions can be approximated by Gaussian distribution. High resolution TEM images as well as microdiffraction patterns reveal cobalt crystallites (Fig.1, Fig.2) with grain-boundary angle ranging 6° to 46°. Grain boundary thickness for large grains is approximately 3-7 nm with 5 nm average.

We also investigated Co films (thickness ~ 20 nm) sputtered on carbon and formvar TEM grids by thermal and magnetron deposition in ultra-high vacuum, in order to exclude any possible substrate effects on the microstructure of the Co film. Fig. 3 shows diffraction pattern of such film. Diffraction pattern shows that this film is a polycrystalline Co-β, without any preferred direction (e.g. no texture). There is also a small amount of cubic Co<sub>3</sub>O<sub>4</sub> (ICSD # 27497) in the film. Grain size was also determined using watershed algorithm. Fig.4 shows TEM image of the area on the surface of the film, which was processed by the algorithm. Average grain size was 6.46 nm with dispersion of 2.08 nm, and average Feret diameter was 9.11 nm with dispersion of 2.90 nm. Thickness of grain boundary itself is about 10 Å.

The nanodots formed by FIB do not have an uniform structure because Ga<sup>+</sup> ions are implanted in the film. The nanodots boundaries have defects in their structure, and consists of unknown Co<sub>x</sub>Ga<sub>1-x</sub> phase. Depending on parameters of focused ion beam sputtering these boundary regions can "swell". Nanodot profile have parabolic form, which complicates further investigations, including research of magnetic properties of the nanodot arrays.

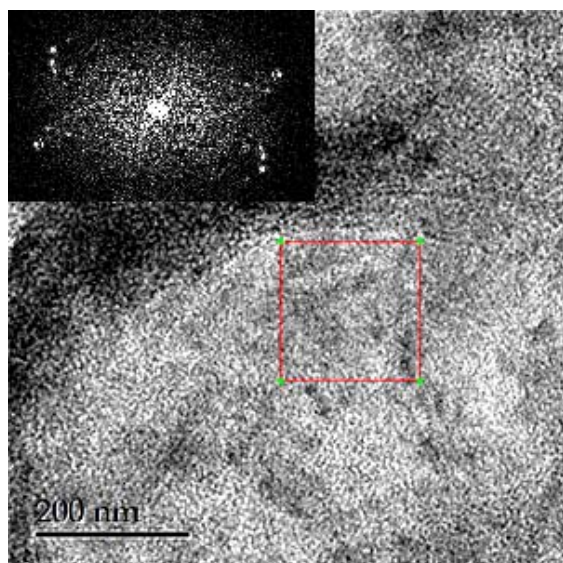


Fig.1. HRTEM-image of Co film and Fast Fourier Transform of red square on the image

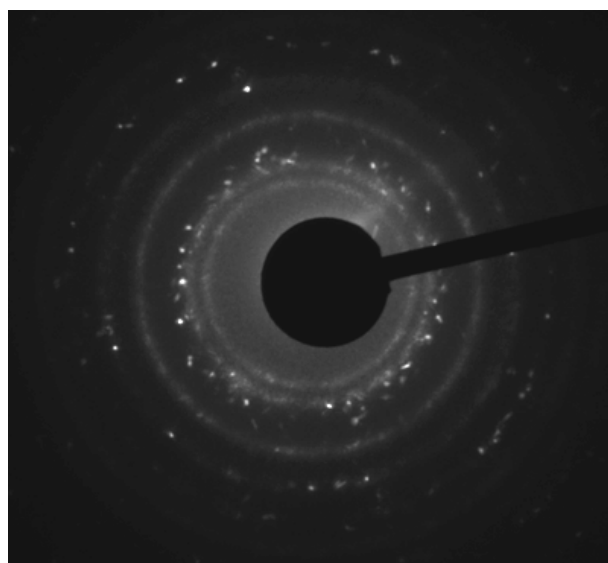


Fig.2. Diffraction pattern of nanocrystalline cobalt film imaged on Fig.1



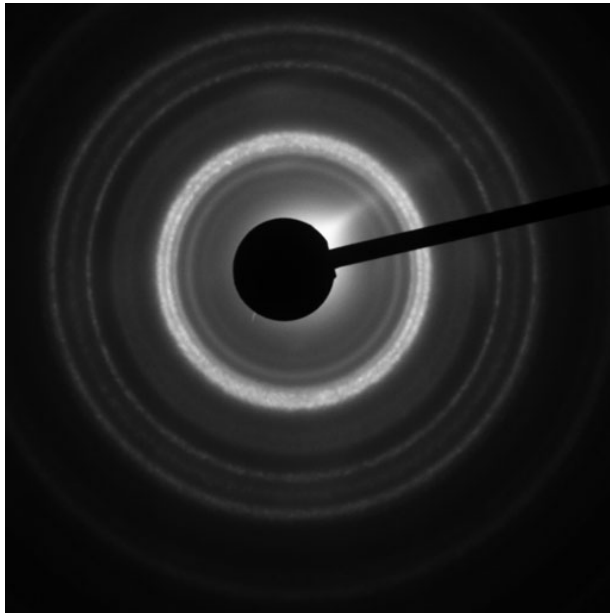


Fig.3. Diffraction pattern of nanocrystalline cobalt film on carbon TEM grid

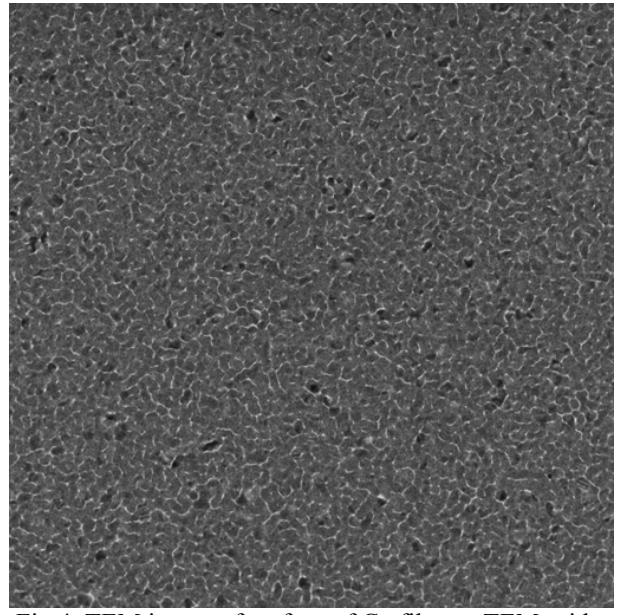


Fig.4. TEM image of surface of Co film on TEM grid

3. P. Kitslaar, M. Strassner, I. Sagnes, E. Bourhis, X. Lafosse, C. Ulysse, C. David, R. Jede, L. Bruchhaus, J. Gierak, "Towards the creation of quantum dots using FIB technology", *Microelectronic Engineering*, **83**, pp. 811-814, 2006.
4. R. Córdoba, J. Sesé, J.M. De Teresa, M.R. Ibarra, "High-purity cobalt nanostructures grown by focused-electron-beam-induced deposition at low current", *Microelectronic Engineering*, **87**, pp. 1550-1553, 2010
5. A. Koblishka-Veneva, M.R. Koblishka, Ion damage during preparation of nanostructures in magnetite by means of focused ion-beam (FIB) milling, *Superlattices and Microstructures*, **44**, pp. 468-475, 2008

# Optimization of spin-valve structures for GMR sensor applications

O.S.Trushin, V.V.Naumov, E.Yu.Buchin, V.F.Bochkarev

Yaroslavl Branch of the Institute of Physics and Technology, Russian Academy of Sciences, Yaroslavl, Russia,  
oleg\_trushin@lenta.ru.

Magnetic field sensors based on Giant Magnetic Resistivity(GMR) effect find wide range of applications in modern technology[1]. High sensitivity at low fields and low cost make these sensors very competitive at a market. The most popular design of these sensors based on spin-valve structures[2]. Modern studies of these structures are aimed on further improvements of its functional characteristics.

In this work we present the results of experimental study of spin-valve structures with exchange bias. Typical example of such structure is shown in Fig.1. It consists of FREE magnetic layer ( $\text{Ni}_{80}\text{Fe}_{20}$  - permalloy), nonmagnetic spacer (Cu) and PINNED magnetic layer ( $\text{Fe}_{80}\text{Ni}_{20}/\text{Fe}_{50}\text{Mn}_{50}$ ). Combining ferromagnetic FeNi and antiferromagnetic FeMn layers provides strong pinning of permalloy layer due to exchange bias effect. There are 2 ultrathin Co Layers placed on the border between magnetic and nonmagnetic layers to enhance GMR effect. Layer of Ta located between Si substrate and permalloy layer provides good conditions for FeNi crystal growth. Another Ta layer on the top of structure is used as a protective coat preventing corrosion of FeMn layer.

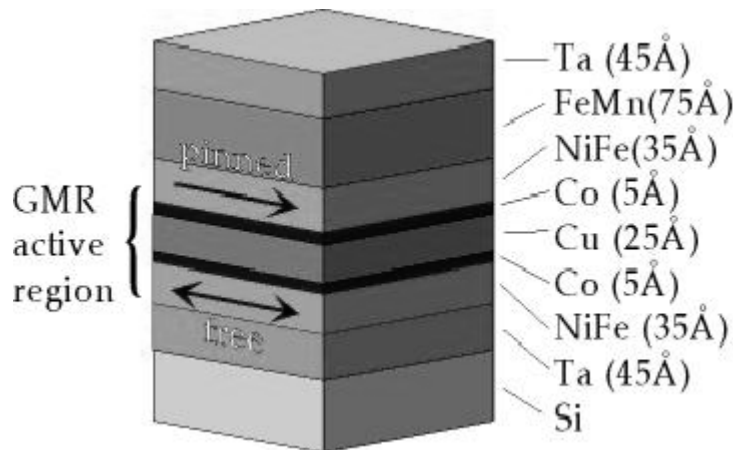


Fig. 1. Typical spin-valve structure with exchange bias.

Multilayer spin-valve structures were deposited by RF magnetron sputtering on TETRA-SCR-600 (Alcatel). Residual pressure at a work chamber was equal to  $8 \cdot 10^{-7}$  mbar. Work pressure during magnetron discharge in Ar was  $2 \cdot 10^{-3}$  mbar. RF power on magnetron was 300 W for FeNi and Co sputtering and 100 W for Cu sputtering. Ferromagnetic films were grown at permanent external magnetic field of 100 Oe.

As deposited structures were used for measurements of magnetic characteristics using magneto-optical Kerr effect and GMR response measurements using home made set-up [3]. The results of such measurements are presented in Fig.2 and Fig.3.

Analysis of these curves shows typical switching characteristics of spin-valve structure. Maximal GMR effect at room temperature achieved up to  $dR/R=3\%$ .

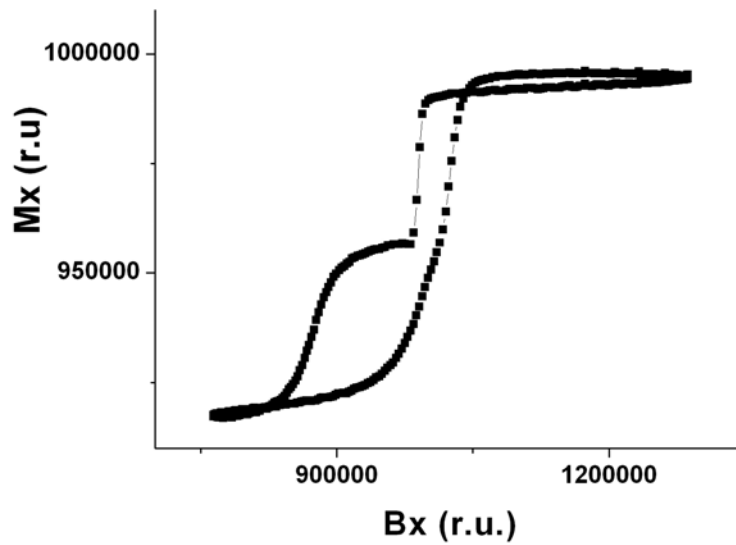


Fig. 2. Magnetization reversal curve of spin-valve structure obtained using Kerr effect measurements

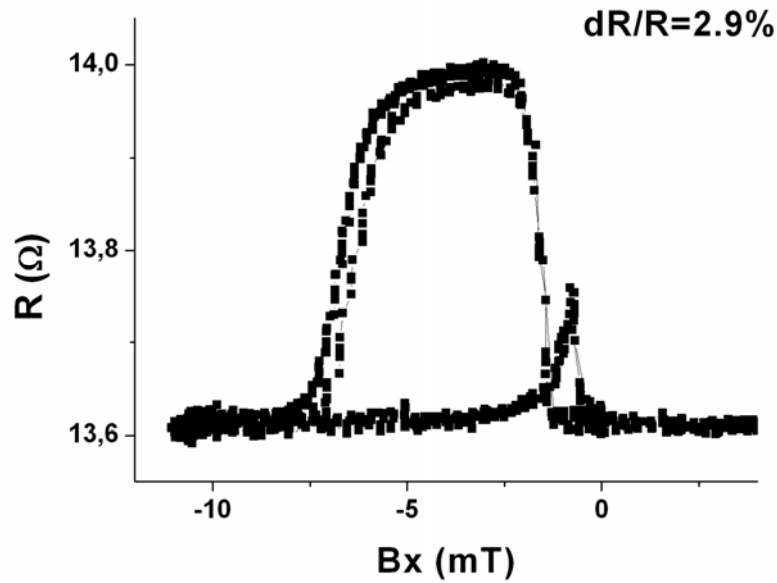


Fig. 3. GMR response curve for Py/Cu/Py/FeMn spin-valve structure.

In summary we present the results of experimental studies of spin-valve structures. As grown structures show typical GMR response and can be used for magnetic field sensors fabrication. We also found strong dependence of spin-valve functional characteristics on technological parameters during deposition process. Thus further improvements in spin-valve performance can be achieved through optimization of the technology.

1. S. Tumanski *Thin magnetoresistive sensors*, IOP publishing Ltd., Bristol, 2001.
2. R. Coehorn "Giant magnetoresistance and magnetic interactions in exchange-biased spin-valves", in *Handbook of magnetic materials*, volume **15**, Elsevier Science, Amsterdam, 2003.
3. O.S. Trushin, D.A. Kokanov, V.F. Bochkarev, V.V. Naumov, E.Y. Buchin, "An automated stand for express-diagnostics of magnetoresistive structures", *Russian Microelectronics*, **38**, pp.257-259, 2009.

# **The possibilities of Mossbauer spectroscopy at research of iron compound in nanostructure (On examples of objects from «natural laboratories» the Earth and Mars)**

A.A.Zalutskii<sup>1</sup>, R.N.Kuzmin<sup>2</sup>

*1. Yaroslavl Technical State University, Yaroslavl, Russia, zalutskii@mail.ru. 2. Physics Department, Lomonosov State University, Moscow, Russia*

In 21 century the number of nanomeasured subject matter works has snowballing increased. So the number of references in various search systems is estimated from hundred thousand to ten millions for nanotechnology subject. However, Internet is searched a few hundred thousand for nanomineral subject. It is easy to explain last years it is clear that unusual nanopartical properties are peculiar not imitation synthesise materials, but also natural soil-mineral objects. The micron and nanomeasured allocations of phases-analogues in studied systems present the greatest information value. Earlier these objects was not studied intently because research equipment of soil scientists and mineralogists was not enough local and absence of change in methodology of scientific researches (intensive transition from highly specialised to interdisciplinary field).

Nanoparticle and nanostructure widespread in Solar system where a different physical processes including unattainable(for example, in vitro the Earth proceed) activate. Recently a new interdisciplinary scientific direction nanomineralogy is formed. Natural nanostructure present a scientific interest not only as an example of a special way of the solid organisation, but also as almost definitively "ready" materials for nanoindustry. So, the clay mineral halloysite which has tubular structure can become natural alternative artificial carbon nanotube.. Cost of the carbon tubes made in laboratory furnace, makes 250\$ for gramme, and halloysite extracted in mines, - no more than 20\$ for 500 gramme. In spite of cheapness Nanotechnology with use of natural systems evidently will move ahead more intensive rates.

Mössbauer spectroscopy (MS) is at present a convenient tool for obtaining information on the macro and microstate features of a substance and is one of the most effective methods for investigating natural systems.

For 50 years which have passed after opening of effect, mossbauer spectroscopy (MS) has come from trial experiments with various soil-mineral objects to regular studying of the fundamental processes proceeding in soils [1]. Research soils of Mars by means of MS only begins [2] whereas for other objects of Solar system (for example, the Moon, meteorites) is observed considerable progress, and there is an extensive information [3, 4]. Exclusive prevalence of iron in the nature allows to make comparative measurements of ferriferous minerals irrespective of a place or character of an origin of the material in Solar system [5].

As a result of the analysis of spectra of all tests of terrestrial and unearthy substance following ferriferous phases have been revealed: paramagnetic phases (olivine, pyroxene, amphibole) and magnetically order phases (magnetite ( $Fe_3O_4$ ), goethite ( $\alpha-FeOOH$ ), hematite ( $\alpha-Fe_2O_3$ ), akaganeite ( $\beta-FeOOH$ )). The magnetic fraction has been allocated for more correct interpretation mossbauer spectra from a part of samples. In addition thermal annealing and modelling experiments (for example, controllable humidifying by steams of water for system  $FeCl_3-FeCl_3 \cdot nH_2O$ ) was made. Thus for the terrestrial samples it was considered a possibility of reception of the additional information with the help X-ray analysis, magnetic measurements, chemical methods etc.

The received results allow to make a conclusion on unity of structure of terrestrial and space bodies, and partially to remove some debatable hypotheses. For example, water existence in the past on a surface of Mars and an origin of the increased maintenance magnetite in top horizons of soils of the Earth.

Observable asymmetry mossbauer absorption lines ( $A = S_{\frac{3}{2}}/S_{\frac{1}{2}}$ ) in our systems can be defined by following reasons: 1) Superposition парциальных spectra from two nonequivalent positions mossbauer kernels; 2) Changes in the nearest nuclear environment mossbauer kernels (for example, hydration of the sample in water steams); 3) Presence of an extraneous phase (for example,  $\alpha\text{-Fe}_2\text{O}_3$ ); 4) Relaxation according to Blum; 5) Structure presence in polycrystalline samples; 6) Goldanskii-Karjagin effect; 7) Diffusion processes.

We established, that foregoing situation are realised as follows. Asymmetry of a line is caused for system  $\text{FeCl}_3 \cdot n\text{H}_2\text{O}$  of laboratory preparation (6). Both the reason (3), and (7) are characteristic accordingly for industrial samples (Russian and French manufacture). Controllable humidifying by water steams leads to essential changes in system that is diagnosed by transformation of the form of a line absorption. Here the reasons (1) and (2) take place. At value of humidity ( $P/P_0 \sim 0.5$ )  $\text{FeCl}_3 \cdot 6\text{H}_2\text{O}$  was stable, the reason (4) can be explain asymmetry mossbauer spectrum. Additional experiments (temperature researches and orientation of the sample under a characteristic corner ( $\vartheta = 54.7^\circ$ )) have excluded a presence of a structure in the sample (5).

Temperature research of artificial orientation sample for system «chloride gland-mineral» has allowed to receive a quantitative estimation of energy of communication the dimmer of iron from mineral surface.

We theoretically also experimentally investigated a temperature dependence of anisotropy fluctuations of atoms  $\text{FeCl}_3 \cdot n\text{H}_2\text{O}$  on a surface of chloride of iron. If we consider a ion  $\text{Fe}^{3+}$  which is found on a surface as a harmonious oscillation (in classical or quantum approach), it is possible to receive a theoretical dependence of the asymmetry parameter

$$A = f(T, \gamma) \quad (1),$$

where  $\gamma$  – the parametre connected with a difference of root-mean-square displacement of atom gland in two perpendicular directions.

It is observed temperature shift ( $\delta_T$ ), which is defined by an oscillatory spectrum of nuclei, because of effect Doppler of the second order along with isomeasured (or chemical) shift ( $\delta_l$ ) mossbauer lines. A temperature shift for dope nuclear which has a mass  $M_{l,k}$  in any lattice of a nonideal crystal can be determined through nuclear power constants of an ideal matrix  $\varphi_{\alpha\alpha}$  and through the change of these power constants caused by introduction of an impurity:

$$\delta_T = \frac{3kT}{2cM_{l,k}} + \frac{\hbar^2}{24cM_{l,k}^2(k_B T)} \sum_{\alpha} \varphi_{\alpha\alpha}(l, k; l', k') - \frac{\hbar^4}{1440cM_{l,k}^2(kT)^2} \cdot \sum_{\alpha, \beta} \frac{\varphi_{\alpha\beta}(l, k; l', k') \varphi_{\beta\alpha}(l, k; l', k')}{M_{l', k'}} + o(T^{-3}) \quad (2)$$

Solving in common the system of the equations (1) and (2) it is possible to define a data about power constants and absolute value of sizes  $\langle x^2 \rangle$  and  $\langle y^2 \rangle$ .

The results which we received can be used in soil science for the solve a problem of division of "exchange" and "structural" iron in clay minerals and soils and for correct diagnostics soil of Mars.

Application of modern physical methods of material research to natural nanostructure leads to occurrence and formation of new scientific knowledge (ideas) which can become a basis for creation of essentially new generations nanomaterials.

1. V. F. Babanin, V.I. Truhin, L.O. Karpatchevkii, et al. *Soil Magnetism*. Moscow, Yaroslavl. 1995.
2. R.V. Morris, et al. «Mineralogy at Gusev Crater from the Mössbauer Spectrometer on the Spirit Rover», *Science*, 305, pp. 833-836, 2004.
3. T.V. Malysheva. *Effect Mossbauer in geochemistry and cosmochemistry*. Moscow, "Nauka". 1975.
4. V.S. Rusakov. *Mossbauer spectroscopy of locally non-uniform systems*. Almaty. 2000.
5. A.A. Zalutskii, et al. «Comparative Mössbauer Analysis of Iron pounds in Soils of Earth and Certain Soils of Mars», *Izvestiya Rossiiskoi Akademii Nauk. Seriya Fizicheskaya*, Vol. 74, No. 3, pp. 410-414, 2010.

# Investigation of surface morphology and magnetoresistance of the granular Co-Cu films deposited by ion-plasmic method

E.Yu.Buchin, V.F.Bochkarev, D.A.Kokanov, and V.V.Naumov

Yaroslavl Branch of the Institute of Physics and Technology, Russian Academy of Sciences, Yaroslavl, Russia,

E-mail: imi.buchin@rambler.ru

The granular magnetoresistance films consist of nanometer-size granules of magnetic material dispersed in nonmagnetic matrix. This structure may be interpreted as a special form of nanometric entities with the resistance controlled by spin-dependent scattering. After applying an external magnetic field magnetizations of the particles are aligned parallel to each other and resistance are decreased. Thus the magnetoresistance effect in granular films and in multilayer structures has a common origin [1]. The magnetic granular films equally with other GMR structures are studied actively in respect to magnetic sensors and computer memory. In the present instance Co-Cu pair considered as the most available. Because of the immiscibility of these metals it is possible to obtain the granular structure. Experimental films fabricated by sputtering deposition from the mosaic material target under HV conditions and 200°C substrate temperature (oxidized siliceous plate). Such process led to spontaneous phase separation. Morphological properties of the samples and location of Co and Cu clusters on the surface of the films were studied using high-resolution scanning electron microscopy (Zeiss Supra-40) with EDX spectrometer. The transfer characteristics of granular films were studied by bridge connection method. Even without annealing samples had thermal stability and tangible magnetoresistance ratio was obtained, exceeding 2% at room temperature. The coercive field was about 300 Oe.

During investigation optimal content of Co (23 at. %) was fixed for this system. In this case films with homogeneous wavy surface were formed. They had a maximum magnetoresistance ratio. On the surface of the films submicron-size pyramids were generated at lower content of Co and whiskers at higher its content (Fig. 1).

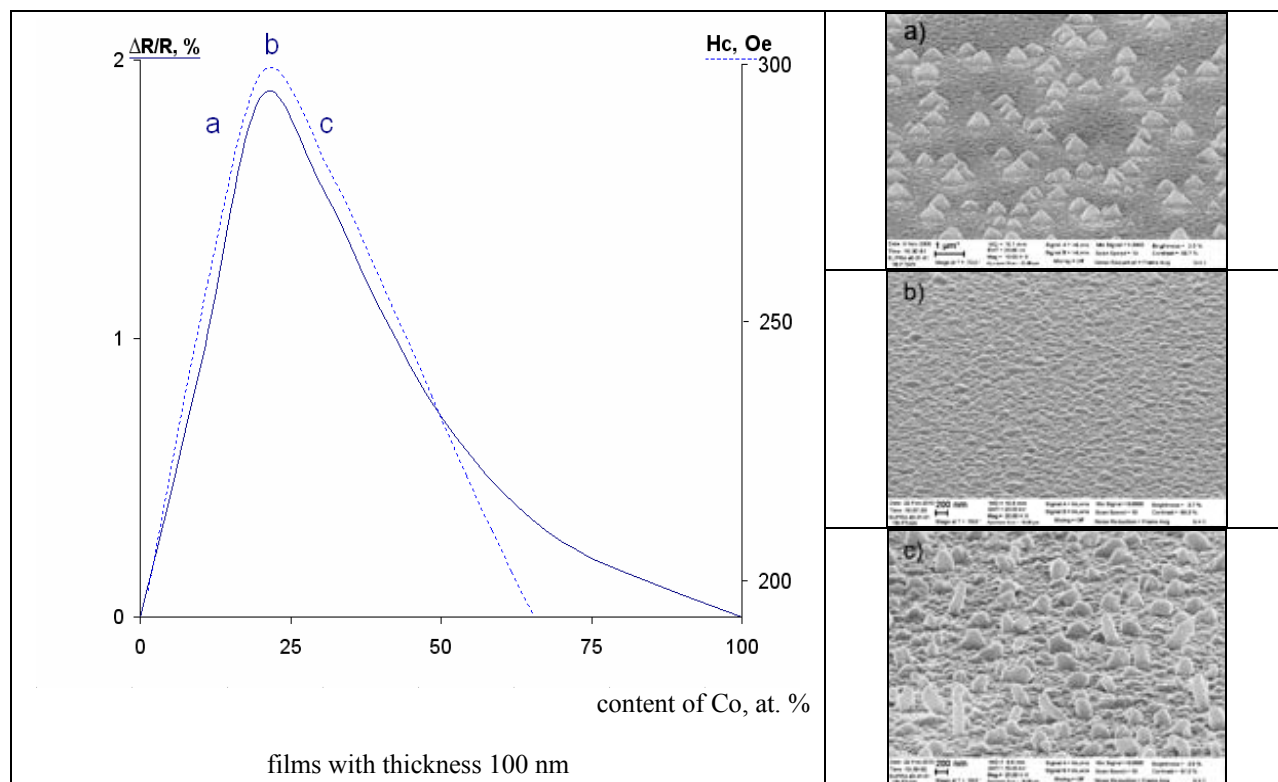


Fig.1. Magnetoresistance ratio, coercive field and SEM images of the surface of granular Co-Cu films obtained with variation of Co content: (a - c) - 15, 23, and 28 at. %, respectively.

The thickness influence on surface morphology and magnetoresistance of granular Co-Cu films at optimal content of Co was studied too. It is known there is limitation in decreasing the thickness of granular layer. The magnetoresistivity significantly drops when the thickness diminishes below several dozen nanometers [2]. During investigation was found that thickness dependence is not monotonous. Below 100 nm this dependence assumes a special character. There are intensive oscillations in magnetoresistance ratio and coercive field. Surface morphology of the films synchronous changes too. Homogeneous films correspond to the maximum level of magnetoresistance ratio and films with detached areas correspond to its minimum level. Heterogeneous films had a greater value of resistance. In addition formation of submicron-size spherical clusters were observed at thickness below 15 nm (Fig. 2). Existence of oscillations is related with change of Co particles diameter and distance between them. For example in the typical thick granular films Co-Ag these sizes are equal 2.5 nm and 8 nm respectively. In the thin films these sizes are changed by force. Cyclicity is connected with reconstruction of Co granules space lattice probably. Similar phenomenon occurs in the sandwich multilayer structures when the thickness of nonmagnetic spacer is decreased [3]. In this case oscillations indicate that the character of coupling between the ferromagnetic films changes with the change of thickness of the spacer – as a periodic sequence from magnetizations of the films aligned parallel to antiparallel. Something similar takes place in granular films. Thus three interesting facts were found during investigation of granular Co-Cu films: optimal content of Co; formation of whiskers and oscillation of thickness dependence.

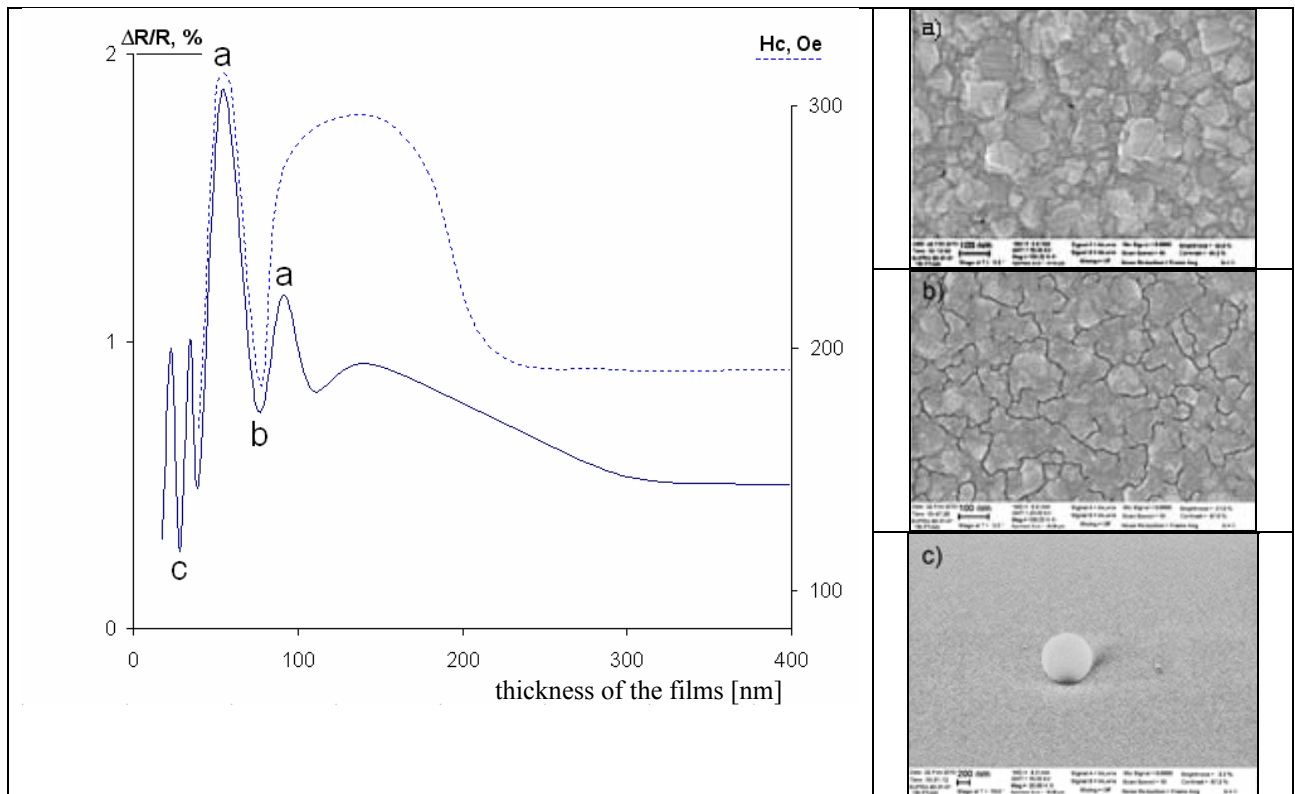


Fig.2. Magnetoresistance ratio, coercive field and SEM images of the surface of granular Co-Cu films obtained with variation of their thickness.

1. A.E. Berkowitz *et al*, «Giant magnetoresistance in heterogenous alloys», Phys. Rev. Lett., **68**, pp.3745–3748, 1992.
2. L.M. Malkinski *et al*, «Thickness dependence of giant magnetoresistance in granular CuCo thin films», Appl. Phys., **85**, pp.4471–4473, 1999.
3. S.P. Parkin *et al*, «Oscillations in exchange coupling and magnetoresistance in metallic superlattice structures: Co/Ru, Co/Cr and Fe/Cr», Phys. Rev. Lett., **64**, pp.2304–2307, 1990.

# Surface modification of oxides by low-energy $\text{Ar}^+$ and $\text{O}_2^+$ ion beams

N.Alov

*Lomonosov Moscow State University, Moscow, Russia, E-mail address: n\_alov@mail.ru*

The irradiation of oxide surfaces by low-energy ion beams, which results in a change in the composition, structure and physicochemical properties, is a promising technique for obtaining of new materials for micro- and nanoelectronics [1]. An advantage of this technique consists in the possibility of controlling the composition and thickness of modified surface layers by changing the irradiation fluence and energy of  $\text{Ar}^+$  and  $\text{O}_2^+$  ions under high-vacuum conditions at room temperature. The aim of this work is to study the influence of low-energy  $\text{Ar}^+$  and  $\text{O}_2^+$  ion bombardment on the surface composition of higher oxides  $\text{Nb}_2\text{O}_5$ ,  $\text{MoO}_3$  and  $\text{WO}_3$  by X-ray photoelectron spectroscopy (XPS).

The  $\text{Ar}^+$  and  $\text{O}_2^+$  ion bombardment of oxides  $\text{Nb}_2\text{O}_5$ ,  $\text{MoO}_3$  and  $\text{WO}_3$  was carried out with energy of 1 or 3 keV, fluence of  $10^{15}$ – $5 \times 10^{17} \text{ cm}^{-2}$  and direction normal to the oxide surface in high-vacuum preparation chamber of *Leybold LHS-10* electron spectrometer. The subsequent determination of surface composition by XPS method was performed *in situ* in high-vacuum analysis chamber of *Leybold LHS-10* electron spectrometer. Fitting of the Nb 3d-, Mo 3d- and W 4f- core level spectra was essential for the estimation of oxidation states. This was done after the subtraction of Shirley background using Gaussian-Lorentzian sum function [2].

It is found from XPS data that under the irradiation by  $\text{Ar}^+$  ions lower oxides  $\text{MoO}_2$ ,  $\text{WO}_2$ , intermediate oxides  $\text{MoO}_x$ ,  $\text{WO}_x$  and unoxidized metals Mo, W are formed in the surface layers of higher oxides  $\text{MoO}_3$  and  $\text{WO}_3$ . Only lower oxide NbO and intermediate oxide  $\text{NbO}_2$  are formed in the surface layers of higher oxide  $\text{Nb}_2\text{O}_5$  under the irradiation by  $\text{Ar}^+$  ions. The irradiation of higher oxides  $\text{MoO}_3$  and  $\text{WO}_3$  by  $\text{O}_2^+$  ions mainly leads to the formation of intermediate oxides  $\text{MoO}_x$ ,  $\text{WO}_x$  with an insignificant content of lower oxides  $\text{MoO}_2$ ,  $\text{WO}_2$ . Only an insignificant content of intermediate oxide  $\text{NbO}_2$  is formed under the irradiation of higher oxide  $\text{Nb}_2\text{O}_5$  by  $\text{O}_2^+$  ions.

The degree of the ion-beam reduction of the surface layers of oxides  $\text{Nb}_2\text{O}_5$ ,  $\text{MoO}_3$  and  $\text{WO}_3$  under the irradiation by inert gas ions  $\text{Ar}^+$  is substantially higher than under the irradiation by chemically active gas ions  $\text{O}_2^+$ , which is associated with the various mechanisms of these processes. Under the irradiation of the surface of higher oxides by  $\text{Ar}^+$  ions the preferential sputtering of oxygen and formation of oxides of lower stoichiometry and metals takes place. Under the irradiation of the surface of higher oxides by  $\text{O}_2^+$  ions along with the preferential sputtering of oxygen the incorporation of oxygen into the surface layers with the subsequent partial oxidation of the reduced layer takes place.

It was revealed that the surface of oxide  $\text{Nb}_2\text{O}_5$  is reduced weaker than the surface of oxide  $\text{MoO}_3$  and considerably weaker than the surface of oxide  $\text{WO}_3$  under the irradiation by  $\text{Ar}^+$  ions and  $\text{O}_2^+$  ions. Earlier using XPS method we have found that in similar experimental conditions the oxidation of surface of metallic Nb under the irradiation by  $\text{O}_2^+$  ions is stronger than the oxidation of surface of metallic Mo and considerably stronger than the oxidation of surface of metallic W [3]. All these results show that the differences in the ion-beam surface reduction of oxides  $\text{Nb}_2\text{O}_5$ ,  $\text{MoO}_3$  and  $\text{WO}_3$  are due to the different values of energy of the metal–oxygen bond in these oxides.

1. G. Betz and G. Wehner, "Sputtering of Complex Materials", *Sputtering by Particle Bombardment*, Ed. by R. Behrisch, 2, pp. 24-133, Springer, Berlin, 1983
2. N.V. Alov, "Determination of Metal Oxidation Degree in Thin Oxide Films by X-ray Photoelectron Spectroscopy", *J. Anal. Chem.*, 60, pp. 431-435, 2005
3. N.V. Alov, "Surface Oxidation of Metals by Oxygen Ion Bombardment", *Nucl. Instrum. Methods Phys. Res. B*, 256, pp. 337-340, 2007



# Ion-beam two-dimensional patterning of silicon subsurface region

M.Yu.Barabanenkov, A.F.Vyatkin, A.I.Il'in, V.I.Zinenko

*Institute of Microelectronics Technology and superpure materials, Russian Academy of Sciences, 142432  
Chernogolovka, IMT RAS, Russia, barab@iptm.ru*

It has been repeatedly demonstrated that ion-beam method is a fruitful technique of chemical composition modification of near surface region of solids. Indeed, synthesis of a buried dielectric layer in silicon wafers by ion implantation is one of the well known examples. Silicon wafers with buried dielectric layer are known as silicon-on-insulator (SOI) structures. Certainly, SOI structures were first introduced for CMOS applications to enhance radiation tolerance and to reduce the parasitic capacitance to the silicon substrate. However, they soon proved equally suitable for the purpose of guided optics. Really, a layer of silicon oxynitride (refraction index  $n = 1.72$ ) sandwiched between two layers of an optically softer silicon oxide ( $n = 1.457$ ) functions as a high-quality planar waveguide in the near-infrared region [1]. SOI devices can compete with those realized using the silica waveguide and polymer technologies. The large index mismatch between the silicon and silicon oxynitride allows for ultra-tight confinement of the optical field. The idea of microphotonics, i.e. a superposition of a dielectric strip waveguide with photonic crystals (PCs), can be readily implemented in practice using SOI like structures. It is also significant that the properties of such integrated planar systems can be locally modified using the ion implantation technique. In particular, periodically arranged, local regions of silicon oxynitride can be created in the silicon layer of SOI structure. These local regions, being formed, for example, as columns of different cross sections penetrating the subsurface silicon region, will produce a dielectric contrast, so that the silicon layer will be able to function as PC (see, for example, [2]).

In the currently presented report we analyze a number of questions arising in the development and ion-beam manufacturing of structured waveguide layers of multilayered microphotonic systems. Considering ion-beam problems, we demonstrate an important role of the silicon surface as a sink for implanted atoms during postimplantation annealing of a sample irradiated with corresponding ions (oxygen and nitrogen) at acceleration energy less than 120 keV. Also, we discuss a possibility of a decrease in the implanted ion dose providing that Si is irradiated through a protective silicon dioxide layer.

Aiming to demonstrate a role of the silicon surface as a sink for implanted atoms we consider a model of simultaneous growth of shallow buried and surface new phase layers in silicon during postimplantation annealing (Fig.1). We start from the conventional point that the radiation-stimulated phase transformation is brought on by the implantation followed by the high temperature annealing of the irradiated sample. Physically at the implantation stage a local phase instability induced by the energy dissipation of the projectiles can develop in the target matrix, in turn causing a small volume of material to differ from its surroundings. In the case of impurity atoms which have a chemical affinity to the target material, nuclei of a new chemical phase are formed as a result of ion implantation (the implanted impurity concentration in the new (synthesized) phase (stoichiometric concentration),  $C_{ph}$ , considerably exceeds it equilibrium value,  $C_s$ , in the silicon matrix, Fig.1). At relatively low irradiation dose, the major fraction of implanted atoms dissolves (see  $C_0(x)$  in Fig.1) and only a small fraction end up as inclusions of new phase (see  $C_{bnd}(x,0)$  in Fig.1). These nuclei can grow at elevated temperature when the impurity atoms become mobile in the matrix. The ensemble of the new phase nuclei function as a spatially distributed sink which competes with a sample outer surface where reagent atoms may out diffuse alternatively. An analytical "diffusion-sink" Cauchy

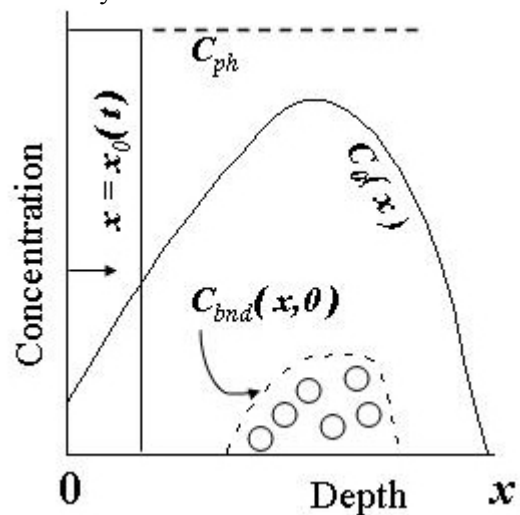


Figure 1. Schematic sketch of the diffusion - alternative - sinks problem. Here  $x_0(t)$  is a coordinate of the growing new phase surface layer versus annealing duration  $t$ .

problem [3] is generalized to describe the decay of the solid solution with simultaneous growth of the new phase flat layer at the outer sample surface when the new phase growth is controlled by interface kinetics.

We suppose that mentioned "diffusion -- sink" problem allows to optimized ion dose for dielectric patterning of subsurface Si region. Figure 2 delivers our first experimental results of ion beam synthesis of a square symmetry photonic structure in Si wafer. Silicon samples (5×5 mm) precoated with an Al layer 0.45 μm thick on the area of 50×50 mcm followed by windows opening with diameter 0.4 μm and period 1 μm (fig.2, (a) and (b)), were irradiated by oxygen ions with fluency of  $5 \times 10^{16} \text{ O}^+/\text{cm}^2$  at ions energy of 40 keV (fig.2, (c)). The samples temperature were at about 300°C during irradiation. The capped Al layer with windows was eliminated after implantation stage (fig.2, (d)).

Fig.2(d) shows weak visual contrast between the irradiated and nonirradiated regions, which can results from small volume fraction of oxide in the irradiated regions of silicon. Besides, the absence of both silicon swelling effect and ion etching of silicon surface (the absence of holes in the irradiated regions) prove insufficiently low ion dose implantation.

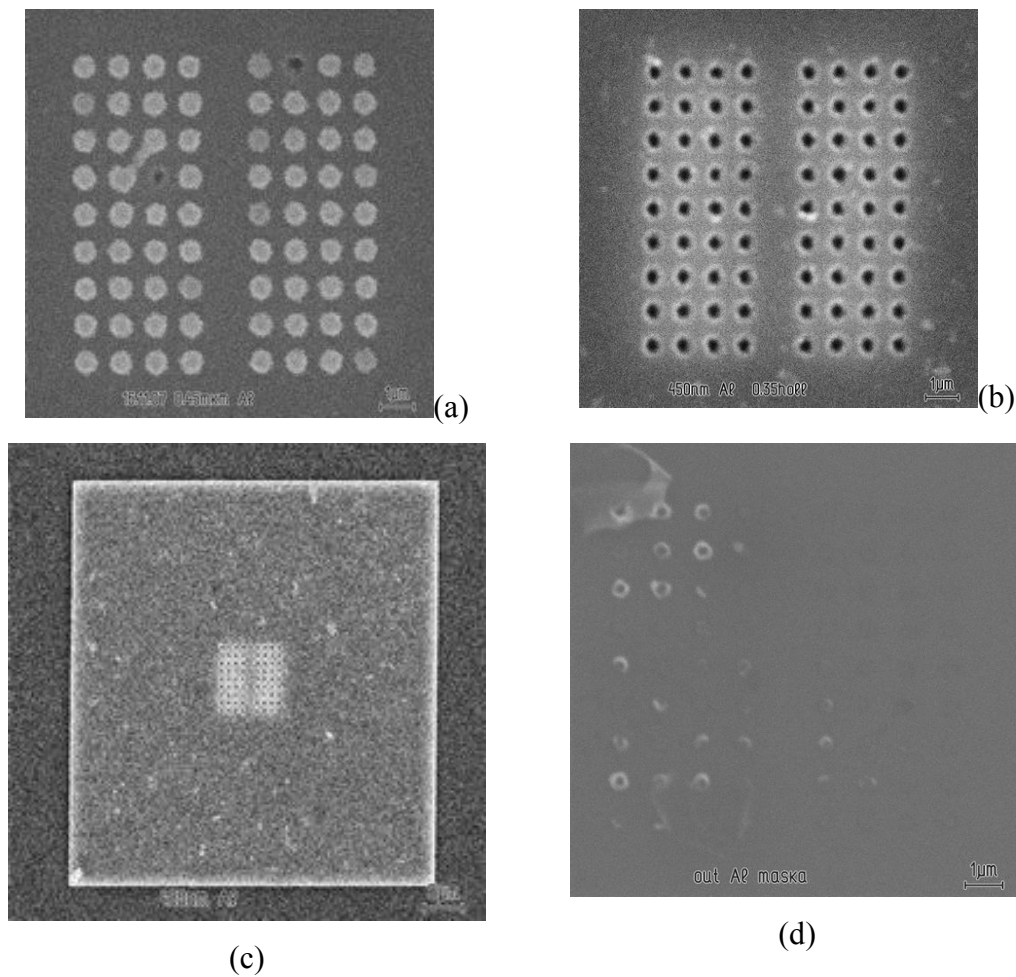


Figure 2. TEM microphotograph (top view) of the silicon structure with periodic (square lattice) dielectric contrast in the form of the silicon oxide rods in silicon: (a) before windows opening in the Al cap layer, (b) after windows opening, (c) the view of whole structure after windows opening, (d) weak visual contrast after Al layer elimination.

1. A. Sayah and Y. I. Nissini, *J. Non-Cryst. Solids* **187**, 473 (1995).
2. M.Yu.Barabanenkov, V.V.Aristov, V.N.Mordkovich, in "Science and Technology of Semiconductor-On-Insulator structures and devices operating in a harsh environment", D.Flandre, A.N.Nazarov, P.L.F.Hemment (Eds), NATO Science Series II: Mathematics, Physics and Chemistry (Kluwer Academic Publishers) **185**, 27 (2005)
3. M.Yu.Barabanenkov, *J.Appl.Phys.* **78**(1995) 2333.

## Redistribution of constituent elements during Co silicidation process in Ti/Co/Ti/Si (100) systems

Yu.Denisenko, V.Naumov, S.Simakin, V.Rudakov

Yaroslavl Branch of the Institute of Physics and Technology, Russian Academy of Sciences, Yaroslavl, Russia,  
E-mail address: den-yur55@mail.ru

Epitaxially grown cobalt disilicide ( $\text{CoSi}_2$ ) on the (100) Si-substrate has emerged as a leading material of contact metallization due to its resistivity, smooth interface and good thermal stability [1]. However, Co presents some difficulties of its usage. The first, it has a high sensitivity to oxygen and water. Even using very high purity inert gas for heat treatment procedure, the resulting cobalt silicides is often oxygen contaminated and its sheet resistance is increased. Another problem is the presence of a very thin native silicon oxide layer between Si and Co. Also Co is neither able to penetrate this oxide layer by the diffusion, no can reduce this oxide to atomic Si. To prevent the cobalt oxidation and reduce the sensitivity of silicidation process to silicon oxidation, the Ti/Co/Ti/Si and Co/Ti/Si schemes can be used. During rapid thermal processing (RTP) in nitrogen  $\text{N}_2$ , cobalt reacts with Si to form  $\text{CoSi} \rightarrow \text{CoSi}_2$ . At the same time Ti migrates to the surface and reacts with nitrogen presenting in the surrounding ambient and in the initial structure in its residual state to form TiN. This process removes the native oxide layers through the reaction as follows:  $\text{Ti} + \text{O} \rightarrow \text{TiO}$ .

The understanding of Co silicidation process in similar multilayer structure needs the study of the elemental depth distributions with nanometer scale depth resolution of all constituents. The secondary ion mass spectrometry (SIMS) allows one detecting secondary current of both atomic and molecular ions, which can provide important information about chemical bond character in the silicide.

The experiment were carried out using initial Ti (8 nm)/Co (10 nm)/Ti (5 nm)/Si (100) structures that had been formed by the RF magnetron sputtering. Silicidation was carried out by the two-step RTP anneal procedures in  $\text{N}_2$ . The first anneal (RTP-1) was performed at 550 °C to form CoSi. Subsequently, (sacrificial) TiN and unreacted Co were removed by the wet etching, after which the sample was dipped into ammonium peroxide mixture (APM :  $\text{NH}_4\text{OH} : \text{H}_2\text{O}_2 : \text{H}_2\text{O}$ ) and sulfure peroxide mixture (SPM:  $\text{H}_2\text{SO}_4 : \text{H}_2\text{O}_2$ ) solutions.

The second anneal (RTP-2) was performed at 830 °C to form low resistivity  $\text{CoSi}_2$  phase. The depth profiles of O, Si, Ti, Co, TiO, TiN in the structure after RTP-1 and RTP-2 were characterized by the time-of-flight SIMS (TOF-SIMS) [2]. ION TOF.SIMS<sup>5</sup> equipment with 0,5 keV  $\text{Cs}^+$  ion primary beam at a beam current of 70 nA was used. The surface morphology and energy-dispersive X-ray (EDX) spectra of the samples were observed with the scanning electron microscope (SEM) SUPRA-40 and EDX microanalysis spectroscopy INCA-X-Act, respectively.

The depth profiles after RTP-1 is shown in Fig. 1. These profiles can be characterized by: a) the formation of a coating on the basis of titanium (oxy)nitride  $\text{TiO}_x\text{N}_y$  with the thickness of 20 nm; b) the penetration of silicon atoms into the cobalt film and formation of a transitional layer from the mixed phase (silicide phase enriched with Co, the elemental Co, Ti-O and Ti-N); c) the displacement of residual elements (C, O and N) from the inner layers of the structure towards the coating. At the initial stage of etching (in the APM solution), the major part of the residual elements can be removed as a part of film of the titanium (oxy)nitride (Fig. 2). The SEM image of the Ti/Co/Ti/Si (100) sample after RTP-1 is presented in Fig. 3. The major part of Co in the transitional layer is removed at a subsequent stage of the etching (in the SPM solution). The depth profiles after RTP-2 is shown in Fig. 4. The admixture of Ti

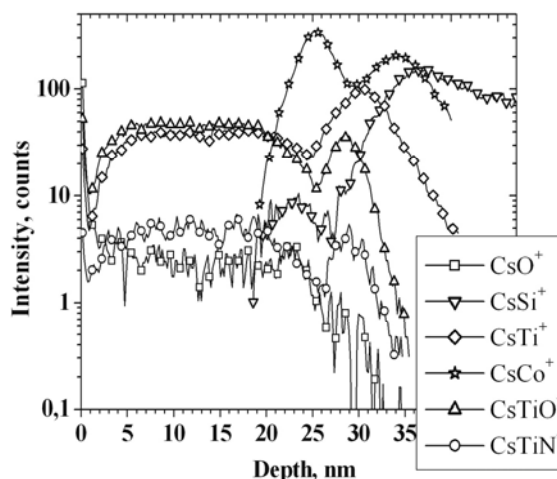


Fig. 1. The TOF-SIMS depth profiles for the samples after RTP-1.

in the final disilicide is presented in much smaller quantities, as it is evidenced of the decreasing in the intensity of  $\text{CsTi}^+$  ions in more than thirty times.

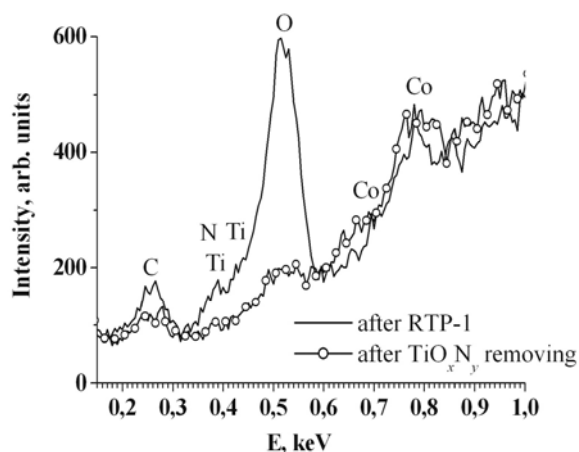


Fig. 2. The EDX spectrum of the sample.

Fig. 3. The SEM image of the  $\text{Ti/Co/Ti/Si}$  (100) sample after RTP-1.

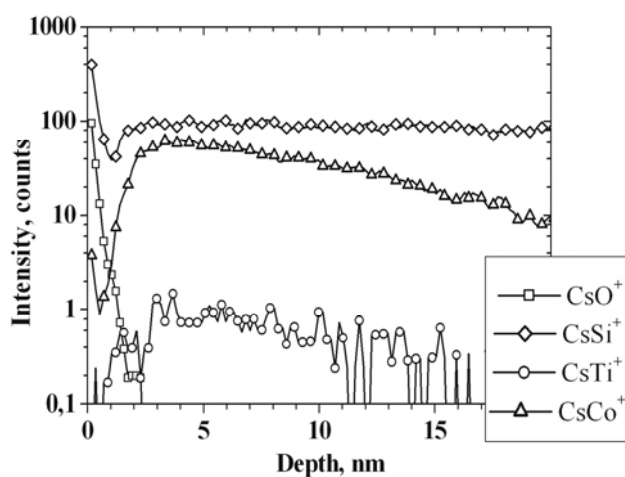
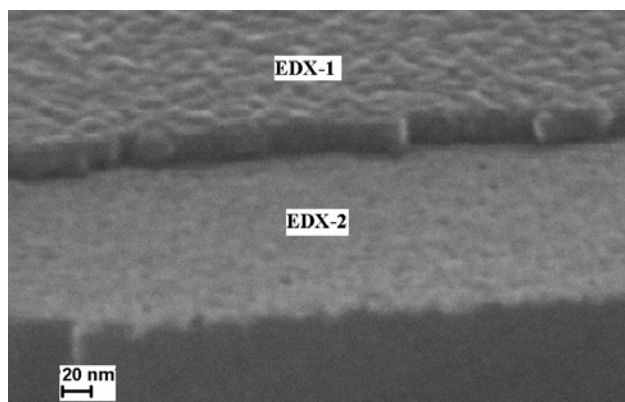


Fig. 4. TOF-SIMS depth profiles for the samples after RTP-2.

1. R.A.Donaton, K.Maex *et al.*, "Co silicide formation on  $\text{SiGeC/Si}$  and  $\text{SiGe/Si}$  layers", *Appl. Phys. Lett.*, **70**, pp. 1266-1268, 1997.
2. T.Wirtz, H.-N.Migeon, H.Scherrer, "Cation mass spectrometer: towards an optimisation of  $\text{MCs}_x^+$  cluster analysis", *Appl. Surf. Sci.*, **189**, pp. 203-204, 2003.

# Etching of high aspect ratio Si nanostructures in the fluorinated plasma

I.I.Amirov<sup>1</sup>, E.N.Zhikharev<sup>2</sup>, V.A.Kalnov<sup>2</sup>, V.F.Lukichev<sup>2</sup>

1. Yaroslavl Branch of the Institute of Physics and Technology, Russian Academy of Sciences, Yaroslavl, Russia, amirov@yftian.ru. 2. Institute of Physics and Technology, Russian Academy of Sciences, Moscow, Russia, Vkalnov@ftian.ru

Creation of high aspect ratio nanostructures is one the main tasks of nanotechnology [1]. Formation of these structures with using etching processes in complex  $\text{SF}_6/\text{C}_4\text{F}_8$  or  $\text{SF}_6/\text{O}_2$  plasmas is performed [2]. Silicon etching at nanoscale dimensions requires quality and precision from etching conditions. The goal of this work was investigation the effects of ion energy and plasma composition on the formation of high aspect ratio ( $A>10$ ) Si nanostructures in fluorine containing  $\text{SF}_6/\text{C}_4\text{F}_8/\text{Ar}$  plasma.

Plasma etching performed in a plasma reactor of RF-inductive (13.56 MHz) low pressure discharge equipped with a RF-electrode. RF bias on the electrode used as a sample holder controlled independently thus determining the ion energy and the ion flux. The average ion energy determined by the negative self bias potential  $U_{sb}$ . The plasma reactor in detail described in [3]. The baseline plasma processing parameters were as follows: 0.3-0.5 Pa pressure, 800 W RF power, 8 sccm Ar, 6 sccm  $\text{C}_4\text{F}_8$ , 3-5 sccm  $\text{SF}_6$ . 0-50 W RF power bias. Plasma Si etching with used 15 nm Cr mask are performed. The mask was produced by “lift-off” technique. The test structures (series line width 30, 50, 100, 150 nm) in electron PMMA resist with the lithograph Raith-150 were received. The characterization of the structures was performed using SEM «Supra-40» (Zeiss).

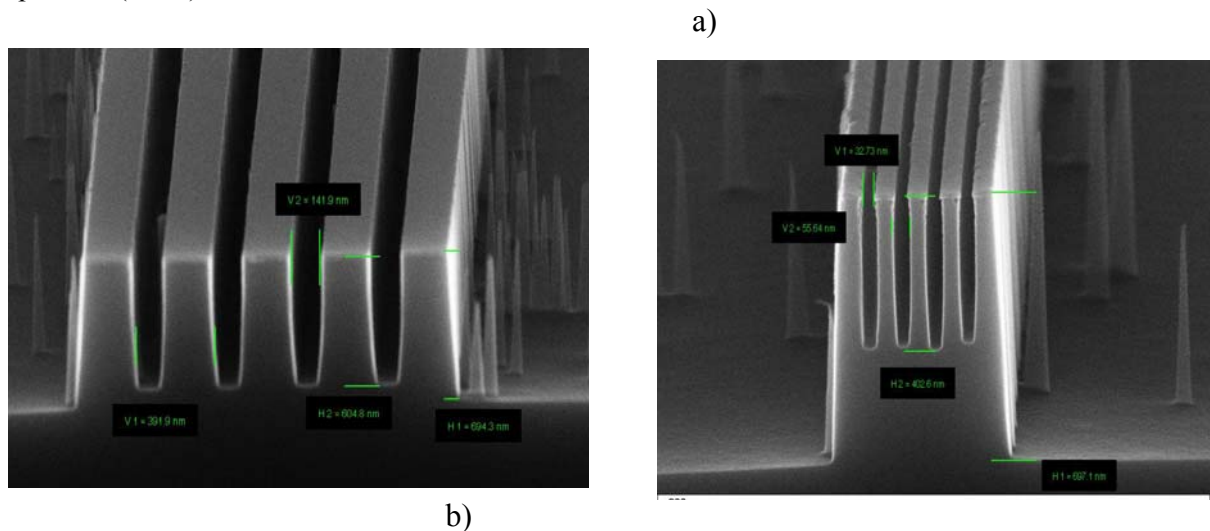


Fig.1. Trenches width 140 and 30 nm and depth 400 and 605 nm, consequently, are received at etching in  $\text{SF}_6/\text{C}_4\text{F}_8/\text{Ar}$  plasma.

In  $\text{SF}_6/\text{C}_4\text{F}_8/\text{Ar}$  (4/6/8) plasma etch Si rate lineally increasing with increasing self bias potential and at the  $-U_{sb}$  is equal 80 V the anisotropic trench etching is observed (Fig.1). At this etching process parameters Si trenches etch rate are decrease with decreasing of the trench width. Trenches with aspect ratio of 8 were received. The aspect-ratio single of silicon nanopillars diameter of 30 nm is equal 24. Anisotropic etch rate of Si nanotrenches was 150-300 nm/min. The mechanism of anisotropic etching of nanoscale dimensions trenches is discussed.

1. T.Lill, O. Joubert. “The cutting edge of plasma etching”. Science. 319, pp.1050-1052, 2008
2. M.D. Henry, S. Walavalkar, A. Homyk, A. Scherer. “Alumina etch masks for fabrication of high-aspect-ratio silicon micropillars and nanopillars”. Nanotechnology, 20, pp. 255305, 2009
3. I.I.Amirov, A.N.Alov. “Formation of Microstructures on Silicon Surface in a Fluorinated Plasma via the Cyclic Etching–Passivation Process”. Khimiya Vysokikh Energii, V. 42, pp. 164–168, 2008

# Mid Infrared tunable whispering gallery modes lasers

V.V.Sherstnev<sup>1</sup>, E.A.Grebenshchikova<sup>1</sup>, M.I.Larchenkov<sup>1</sup>, A.M.Monakhov<sup>1</sup>,  
A.N.Imenkov<sup>1</sup>, A.N.Baranov<sup>2</sup> and Yu.P.Yakovlev<sup>1</sup>

*1. Ioffe Physical-Technical Institute, St. Petersburg, 194021, Russia.*

*2. Institut d'Electronique du Sud (IES), Universite Montpellier 2, 34095 Montpellier, France*

**Abstract:** The technology of fabrication disk cavity of whispering gallery modes (WGM) laser for middle Infrared (MIR) spectral range was developed. The post-growth geometry formation of the disk cavity was performed using selective wet chemical etchant comprised of CrO<sub>3</sub>, HF and H<sub>2</sub>O. The wet-chemical etchant for semiconductor multilayers heterostructure lattice-matched to GaSb was investigated. The application of this technology allow us to fabricate the disk cavity with a diameter of 200 μm and height 15 μm. To enlarge the optical power of emission the disk chip was cleaved up to symmetric half-disk. It was established, that the lasers assembled on the basis of such half-disk cavity are tunable and generate at the wavelength of 2.35 μm at RT.

Advanced measurement techniques that exploit lasers for middle Infrared (MIR) spectral range have become well-established tools for characterizing combustible, exhaust and unhealthy gases. Overtones and combined passages in the molecules of a number of substances (H<sub>2</sub>O, CH<sub>4</sub>, NO<sub>2</sub>, N<sub>2</sub>O, C<sub>2</sub>H<sub>4</sub> and others) lie in the range of (2-4) μm [1]. Therefore the creation of diode lasers for MIR is important task. Such possibility of semiconductor laser as tuning on frequency is the greates advantage. The tunable diode lasers with the resonator Fabry-Perot are reported obtained the tuning range 4-6 Å. It is less than intermode distance for the single mode [2]. In recent years studies on the creation of the whispering gallery mode (WGM) lasers, which generate emission in the MIR [(2-4) μm] spectrum range are intensively developed [3-7]. Such lasers are attractive due to high Q-factor of resonator and the low values of threshold current in comparison with the stripe resonator Fabry-Perot lasers. In the literature there is no information about study of frequency tunable WGM - lasers. This study is devoted to the fabrication of the cavity of electrically pumped WGM semiconductor tunable lasers. These WG mode lasers are attractive because the intrinsically high Q-factor may compensate for the low gain, reduce threshold current, and help to achieve room temperature operation. To fabricate the disk cavity of GaSb-based WGM - lasers we used GaInSbAs quantum well structures, grown by MBE. The post-growth geometry formation of the disk cavity was performed using selective wet chemical etchant, comprised of CrO<sub>3</sub>, HF and H<sub>2</sub>O. The application of this etchant made it possible to prepare the disk cavity with a diameter of 200 μm and height 15 μm. Cavity has the pagoda-like shape, whose convex area is an active region. The ohmic ring contacts with diametr 180 μm and width 30 μm were formed by metal sputtering. The space between contact ring edge and disk edge is about 10 μm. In contrast to Fabry-Perot-laser, where the coherent emission formed in all volume of resonator, in WGM-laser the coherent emission formed only at the periphery. When current increase – coherent emission moving closer to the centre of the disk. This is the argument for the higher working currents and temperature of WGM laser in comparison with Fabry-Perot laser. The main advantage of WGM lasers is a super high Q-factor of the disk cavity. But this good property has a reverse side: it's very difficult to output the emission. To overcome this problem we suggested to cleave disk cavities to half-disk. In the case of half-disk cavities the WG modes were observed too. The disk chip was cleaved up to symmetric half-disk. The photo of chip with cavity is in Fig.1. As can be seen in Fig. (view from above) cavity has the half-disk-like shape.

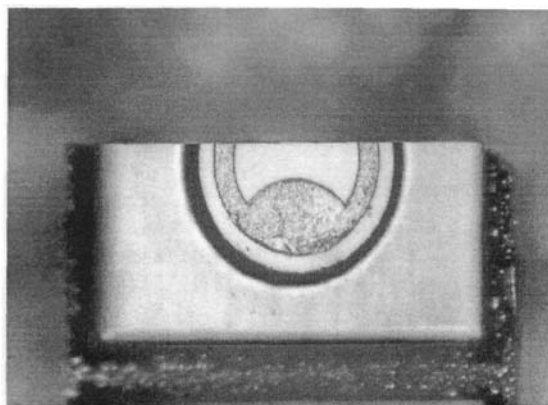


Fig. 1. Photo of the WGM half-disk laser chip (view from above).

The laser, created on the basis of this cavity generated emission at the wavelength of 2.35  $\mu\text{m}$  at room temperature (RT) in the pulsed operation. The smooth tuning of the emission basic mode wavelength to the long-wave side on 30  $\text{\AA}$  have observed. The RT emission spectra of the half-disk cavity WGM laser (presented in Fig. 1), measured at various pumping currents are depicted in Fig.2.

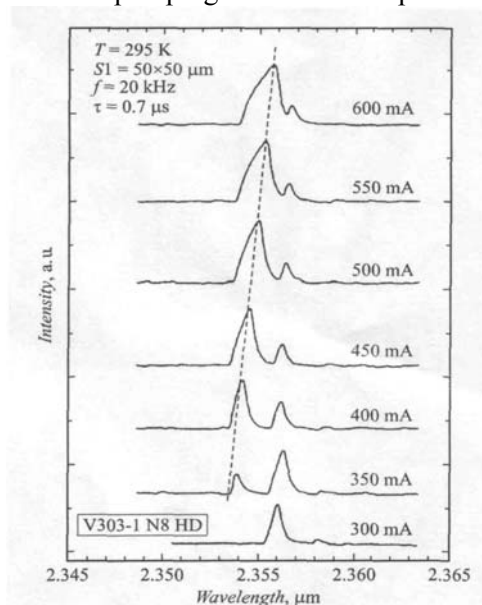


Fig. 2. Room-temperature emission spectra of the half-disk cavity WGM tunable on frequency laser. The measurements were taken at different values of the pumping current, with pulse duration 0.7  $\mu\text{s}$  and repeating frequency 20 kHz. (spectral resolution 2  $\text{\AA}$ )

Fig.2 pointed that the emission spectra have the multimodes periodic structure and tuning towards the long wavelength direction with increasing pumping current. Thus, the process of wet chemical etching in the mixture comprised of  $\text{CrO}_3$ , HF and  $\text{H}_2\text{O}$  was studied and the technology of fabrication half-disk cavity of WGM-laser was developed. The lasers assembled on the basis of such half-disk cavity generated at the wavelength of 2.35  $\mu\text{m}$  in the pulsed operation at RT. The smooth frequency tuning in the process of the flow of current pulse by duration to 1.2  $\mu\text{s}$  was observed. It is shown that the increasing the pulse duration from 0.1 to 1.2  $\mu\text{s}$  shifts the wavelength of the emission to the long-wave direction on 30  $\text{\AA}$ . This study was supported by the project of the Presidium RAS №27 "The bases of fundamental research of nanotechnologies and nano-materials", by Grants 10-02-93110-НЦНИИ\_a, 10-02-00548-a and 09-08-91224-CT\_a.

- [1] A.I. Nadezhdinskiy, The 10<sup>th</sup> Russian seminar on Diod Laser Spectroscopy, 2008. <http://www.dls.gpi.ru/rus/sem/10/Nad.pdf>
- [2] A.P.Astakhova, A.N. Baranov, A.Viset, A.N. Imenkov, N.M. Kolchanova, N.D. Stoyanov, A. Chernyaev, D.A. Yarekha, and Yu..P. Yakovlev "Current and Temperature Tuning of Quantum-Well Lasers Operating in 2.0-2.4  $\mu\text{m}$  Range," Semiconductors, Vol. 37, No 4, 2003, pp. 485-490.
- [3] Sherstnev V.V., Krier A., Monakhov A.M., Hill G. "Mid-infrared ring laser"//Electron. Lett. 2003. V.39, Iss.12, pp.916-917.
- [4] Sherstnev V.V., Monakhov A.M., Astakhova A.P., Kislyakova A.Yu., Yakovlev Yu.P., Averkiev N.S., Krier A., Hill G. /"Semiconductor WGM Lasers for the Mid-IR Spectral Range", Semiconductors, 2005, Vol.39, No. 9, pp.1087-1092
- [5] Monakhov A.M., Sherstnev V.V., Astakhova A.P., Yakovlev Yu.P., Boissier G., Teissier R., Baranov A.N. "Experimental observation of whispering gallery modes in sector disk lasers," Appl. Phys. Lett, 2009, V. 94, P. 051102.
- [6] Yarekha D.A., Glastre G., Perona A., Rouillard Y., Genty F., Skouri E.M., Boissier G., Grech P., Joullie A., Alibert C., Baranov A.N. "High Temperature GaInSbAs/GaAlSbAs Quantum-Well Singlemodecontinuous wave Laser Emitting near 2.3  $\mu\text{m}$ ," //Electron. Lett. 2000, V.36, N. 6, P. 537-539.
- [7] Averkiev N.S., Sherstnev V.V., Monakhov A.M., Grebenshchikova E.A., Kislyakova A.Yu., Yakovlev Yu.P., Krier A., Wright D.A. "Physical Working Principles of Semiconductor Disk Lasers," Low Temperature Physics, 2007. V. 33. N. 2-3, P. 283-290.

# Nanoscale storage elements based on the $\text{TiZrPb}_2\text{O}_3$ films using the atomic force microscopy methods

A.Avachev, K.Mitrofanov, N.Klimov

*Ryazan State Radioengineering University, Ryazan, Russia, rcpm@rgta.ryazan.ru*

Nowadays, it is important issue to improve the parameters of storage devices. The most important characteristics of the storage elements are informational capacity and high-speed performance. Digital information is stored in two main types of storage devices - hard disk drives and solid-state drives. The are rotating magnetic disk and a set of transistors (transistors and capacitors) used to store information there. Also optical media widely used – it is a storage device in which recording and reading information uses optical emission. There are other types of storage devices appears with the development of nanotechnology [1].

The electrical modification of the surface of semiconductor films is a new principle of information recording, which allows to store information as an electric (charge) state changing of the surface local areas. It is possible to use an atomic force microscope probe to the modification of the electric surface topography. In this case, the local charge state is modified by interaction of the probe with the electric potential applied and the structure surface. This process is called electric lithography [2]. This principle allows to achieve a high information capacity limited only by the size of the probe tip. But an urgent task is to improve high-speed performance. The solution is the probes array using (millipede).

In the following work the electric lithography of  $\text{TiZrPb}_2\text{O}_3$  thin films with 100 nm thickness using scanning probe microscopy was carried out. Topography measurements were obtained, the Kelvin probe method was used to show the distribution of surface potential. The electric lithography and the surface potential changes distribution was identifying. The surface potential changes distribution over the time were considered. Measurements were performed at room temperature and atmospheric pressure in air. The surface potential before the lithography does not exceed 35 mV. The surface area with a low-level relief was selected and electric lithography was carried out. The series of lithographic operations at different applied voltage (from 0,1 V to 9 V) were carried out. The result of each operation was observed using distribution of surface potential quantifications in the area of lithography by Kelvin probe method. Lithography process at a voltage equal to 9 V was made a change in the distribution of surface potential at the investigated surface. The lithographic potential was 300 mV. The additional studies of the surface area with the lithographic pattern were carried out and the process of the surface potential reducing over the time was reviewed. The surface potential for the 2 hours after the electric lithography was 65 mV, after 6 hours was 45 mV, and 24 hours was 35 mV. Surface potential was 35 mV in the following 10 days after the electric lithography.

The dependence of the surface potential on the time since the beginning of the surface area lithography process. The next step of the research is electric lithography in a vacuum to implement the conservation of charge on the surface.

1. C. P. Poole, F. J. Owens «Introduction to Nanotechnology», Wiley-Interscience, 2003, p. 400.
2. W. Shen, Y. Chen, Q. Pei «Electric lithography by electrochemical polymerization», Appl. Phys. Lett. **87**, 2005.



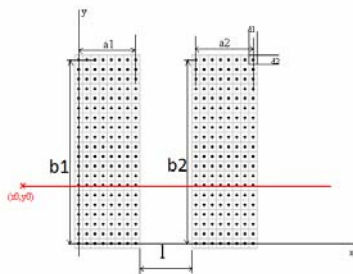
# Simulation of the 100-40 nm transistor gate formation process by EB lithography for 950K PMMA – Si substrate system

M.Alexandrova

*Moscow Institute of Physics and Technology (SU); Institute of Physics and Technology, Russian Academy of Sciences  
Moscow, Russia E-mail: malexandrova@bk.ru*

Focused electron-beam lithography (FEBL) makes it possible to form solid state nanoelements of any configuration. In order to create the required topology, this technology applies sharply focused electron beam controlled by a processor. Determination of optimal exposure parameters for available FEBL units like highly automated E-beam writer RAITH -150 is currently one of the central problems. It can be done by computer simulation for the lithography technology under consideration.

The simulation to optimize the technological processes of transistor gate microfabrication (gate width 100 - 40 nm) was performed for FEB lithography, the targets being 950K PMMA resist on silicon substrate. The used simulation tool [2] was upgraded by adding the new module “Lito\_sum” developed by us. It allows to calculate the spatial distribution of the absorbed energy density in the resist film under linear scan and to determine the obtained latent image during the EBL exposure process.



The software allows also to vary topology design from simple (one or two lines) to more complicated ones (one or two rectangle), spacing between the exposed elements can be variable as well (see Figure).

The software tool includes three steps: (i) simulation of the full electron trajectories, (ii) calculation of the discrete absorbed energy distribution in the resist film due to a point beam for single exposure dot, and (iii) calculation of the spatial distribution of the absorbed energy due to counting of the absorbed energy amount within the line scan. The program takes into account many essential features of real process, for example, a type and chemical properties of resist, substrate and resist thickness etc.

The tool allows varying the main exposure parameters such as electron beam diameter and accelerating voltage over a wide range. The software package is capable of applying the different physical models of electron scattering, on which the numerical algorithms are based on, so one can verify the modeling results rather easily.

The “Lito\_sum” module calculates the energy contribution of exposed resist dots (red line), which are within the effective radius of electrons scattering determined accordingly to the step (ii) for single dot.

As a result of modeling experiments the exposure doses for FEBL microfabrication of the specific 100-40 nm transistor gates were obtained. Currently the results are under experimental verification.

The author would like to express deep gratitude to T. Makhviladze and M. Sarychev for the consultations and helpful discussions during the Modeling Lab workshops.

## References:

- [1] <http://www.raith.com/?xml=solutions\Lithography+%26+nanoengineering>
- [2] D. Drouin, A. Couture CASINO V2.42—A Fast and Easy-to-use Modeling Tool for Scanning Electron Microscopy and Microanalysis Users SCANNING VOL. 29, 92–101 (2007)(C)
- [3] K Vutova, G. Mladenov. Modeling of exposure and development process in electron and ion lithography Modeling Simul. Mater. Sci. Eng. 2 (1994) 239-254
- [4] Vutova, G. Mladenov Simulation of the energy absorption and the resist development at sub-150 nm ion lithography Microelectronic Engineering 78-79 (2005) 533-539
- [5] K Vutova, G. Mladenov Process simulation at electron beam lithography on different substrates J. of Mater. Proc. Tech. 184 (2006) 305-311
- [7] K. Valiev Physics of Lithography (1990) 137-180

# Synthesis of Cu nanoparticles in solutions and its studies with X-ray absorption spectroscopy and X-ray photoelectron spectroscopy

S.Saykova<sup>1</sup>, S.Vorobyev<sup>1</sup>, Y.Mikhlin<sup>2</sup>, A.Romanchenko<sup>2</sup>, M.Likhatski<sup>2</sup>

1. Siberian Federal University, Krasnoyarsk, Russia, ssai@mail.ru. 2. Institute of Chemistry and Chemical Technology, Russian Academy of Sciences Siberian Branch, Krasnoyarsk, Russia, yumikh@icct.ru

Cu-based nanomaterials can be widely used as catalysts, gas sensors, solar energy transformation, lubricants, semiconductors, negative electrode material for lithium ion batteries, in preparation of high-temperature superconductors. Chemical approach for Cu<sup>0</sup> nanoparticles (Cu NPs) synthesis is the most suitable; it is need the simple equipments, the short technology processes, the low investment, and the convenient for industrialization. Besides it is capable of controlling the size and morphology of the products by adjusting the reaction parameters. Though reliable synthesis of Cu NPs remains a challenge because of the ready oxidation of as-synthesized metallic nanoparticles in aqueous media and ex situ. It is required efforts for its stabilization. Moreover, the problem of the Cu NPs characterization still persists as the data obtained by different techniques are often contradictory. Here we describe several procedures developed for the synthesis of Cu NPs varying from 7 nm to 30 nm in diameter and Cu<sub>2</sub>O NPs by using different reducing agents (hydrazine hydrate, borohydride, glucose, and some others), complexants, capping agents, and by tuning the reaction conditions. In particular, a method for the feasible fabrication of stable colloidal Cu NPs via the reduction of Cu<sup>2+</sup> ions by hydrazine hydrate in the presence of sodium citrate or tartrate has been proposed. The production of metallic copper NPs was proved by UV-viz spectroscopy (plasmon peak at about 580 nm) and ex situ TEM, electron diffraction, XRD.

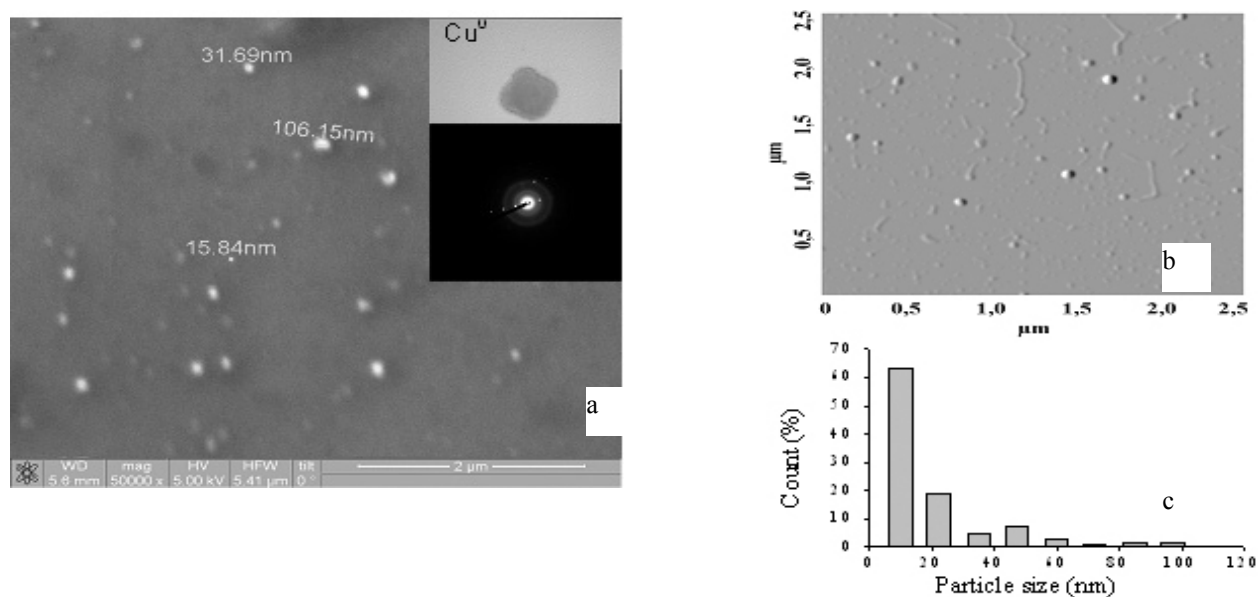


Figure 1. TEM image (a) and SAED patterns (inset), AFM image (b), particle size distribution histogram (c) of Cu Nps (hydrazine hydrate reduction)

At the same time, XPS analysis (fig.2) found Cu(I) oxide with an overlayer of Cu(II) species, while Cu(0) was not definitely specified from Cu 2p and Cu L<sub>3</sub>MM patterns. The Cu L-edge XANES spectra acquired in the TEY mode are indicative of Cu (II) species which occur in the surface layer and usually can be removed by Ar<sup>+</sup> etching, then a Cu(I) oxide layer and metallic Cu underneath (fig.3). Interestingly, the spectra of the Cu(I) species differ in many cases, especially after Ar<sup>+</sup> bombardment, from those of Cu<sub>2</sub>O, probably due to the formation of oxygen-deficient Cu<sub>2</sub>O<sub>1-x</sub> suboxides. The Cu K-edge XANES and EXAFS data obtained in the transmission mode suggest the formation of metallic copper. We have studied the effect of the sample preparation on the XPS and XAS results and arrived at conclusion that the signals from metallic copper in transmission XAS and XRD are often due to comparably large Cu(0) particles (even when Cu<sub>2</sub>O NPs are the major product, for example, with ascorbic acid as a reducing agent) which preferentially

precipitate on a support and are resistant to oxidation. At the same time, intended Cu NPs essentially oxidized in the course of the synthesis rather than the ex situ handling, or Cu<sub>2</sub>O NPs remain in the colloidal solutions. Methods for the sample preparation eliminating the artifacts are proposed.

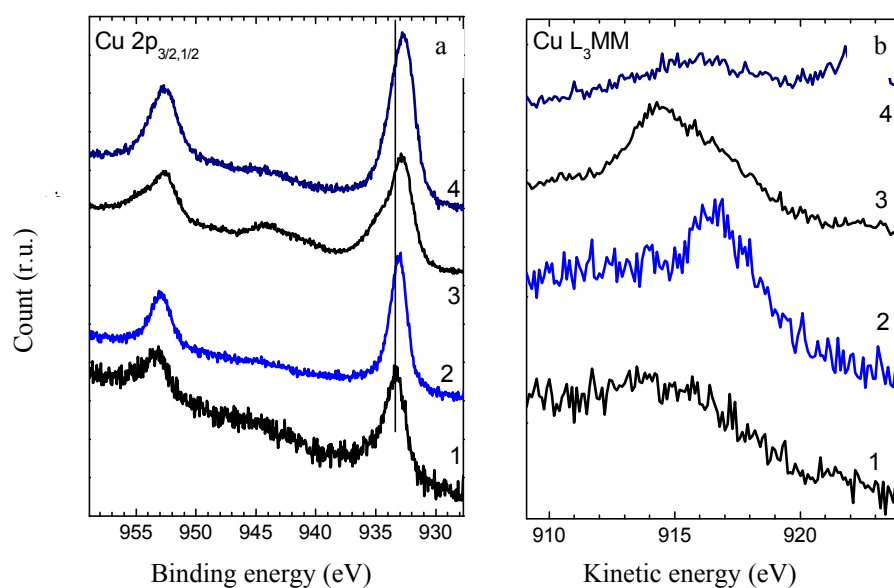


Figure2. XPS Cu 2p (a) and Auger-electron Cu L<sub>3</sub>MM (b) spectra of Cu Nps (hydrazine hydrate reduction with (1,2) ore without (3,4) sodium tatrare additive) before (1,3) and after (2,4) Ar<sup>+</sup> ion beam etching (5 KeV, 30 μA, 2 min)

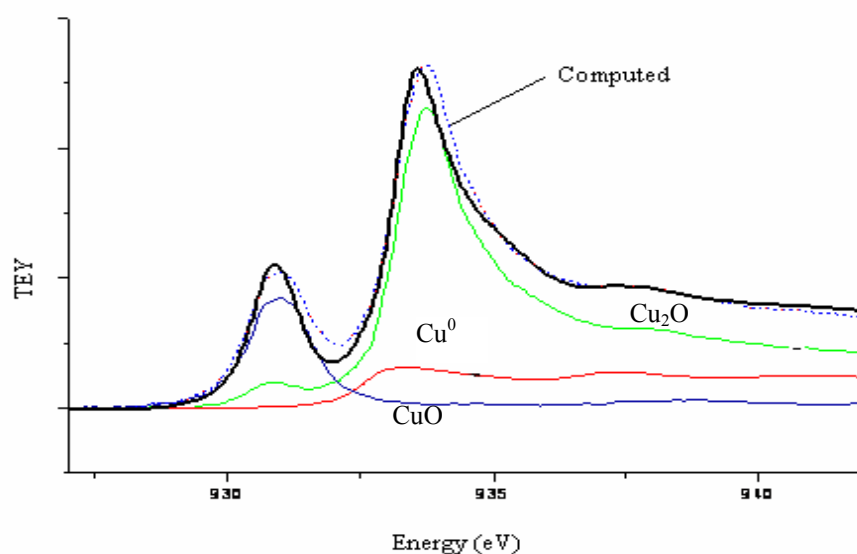


Figure3. TEY XANES Cu L-edge spectra of Cu Nps (hydrazine hydrate reduction)

This work is supported by the grants from Ministry of Education and Science of RF (02.740.11.0269) and from RFBR (09-03-98002-R- Sibir).

# Investigations of morphological and structural properties of porous nanostructured lead chalcogenide films fabricated with the variation of anodic electrochemical treatment conditions

S.P.Zimin<sup>1</sup>, V.M.Vasin<sup>1</sup>, E.S.Gorlachev<sup>1,2</sup>, V.V.Naumov<sup>2</sup>, E.Yu.Buchin<sup>2</sup>

1. Yaroslavl Demidov State University, Yaroslavl, Russia, E-mail: zimin@uniyar.ac.ru.

2. Yaroslavl Branch of the Institute of Physics and Technology, Russian Academy of Sciences, Yaroslavl, Russia

Fabrication of porous nanostructured semiconductor materials with modified properties using low-temperature top-down one-step anodic electrochemical etching process is an extremely promising field of research with applications in nanoelectronics, optoelectronics, chemical sensing. Investigations of porous silicon are widely reported and more recently a new porous semiconductor materials (IV-IV, II-VI, III-V compounds) were studied. However, IV-VI semiconductors, which are widely used in infrared optoelectronics, still are not reported to be successfully obtained in a porous form. The main attractive property of these materials, primarily lead chalcogenides PbX (X = Te, Se, S), is the possibility of the fabrication of nanostructures with outstanding properties and controlled parameters. In this work the results of the fabrication of porous nanostructured lead chalcogenide films using anodic electrochemical etching in a Norr solution and the investigations of their morphological and structural properties are presented.

PbTe and PbSe epitaxial films with n-type conductivity were grown with molecular beam epitaxy on Si(111) substrates with 2 nm thin CaF<sub>2</sub> buffer layers. Thickness of lead salt films was from 2 to 3.5  $\mu\text{m}$ . The films were divided into two groups depending on their initial surface morphology: PbTe and PbSe films with a flat surface with 2-3 nm high nanoterraces and PbSe films with a developed granular surface morphology. A vertical type electrochemical cell was used to perform anodic electrochemical etching of PbX/CaF<sub>2</sub>/Si(111) structures according to a novel technique that was previously developed in our work [1]. The cell had a teflon base containing a circular platinum cathode in its upper part and a flat metallic anode at the bottom, where the samples were placed. Etching was carried out in a Norr electrolyte based on the aqueous solution of potassium hydroxide, glycerol and ethanol, which was originally proposed for electrochemical polishing of PbTe crystals. Anodizing current density  $j_{\text{an}}$  was varied in the range of 2-8 mA/cm<sup>2</sup>, treatment duration time  $t$  was 10-20 min. Morphological properties of the samples were studied using high-resolution scanning electron microscopy (Zeiss Supra-40), crystal structure was studied with x-ray diffractometry (DRON-3M,  $\lambda = 1.54 \text{ \AA}$ ).

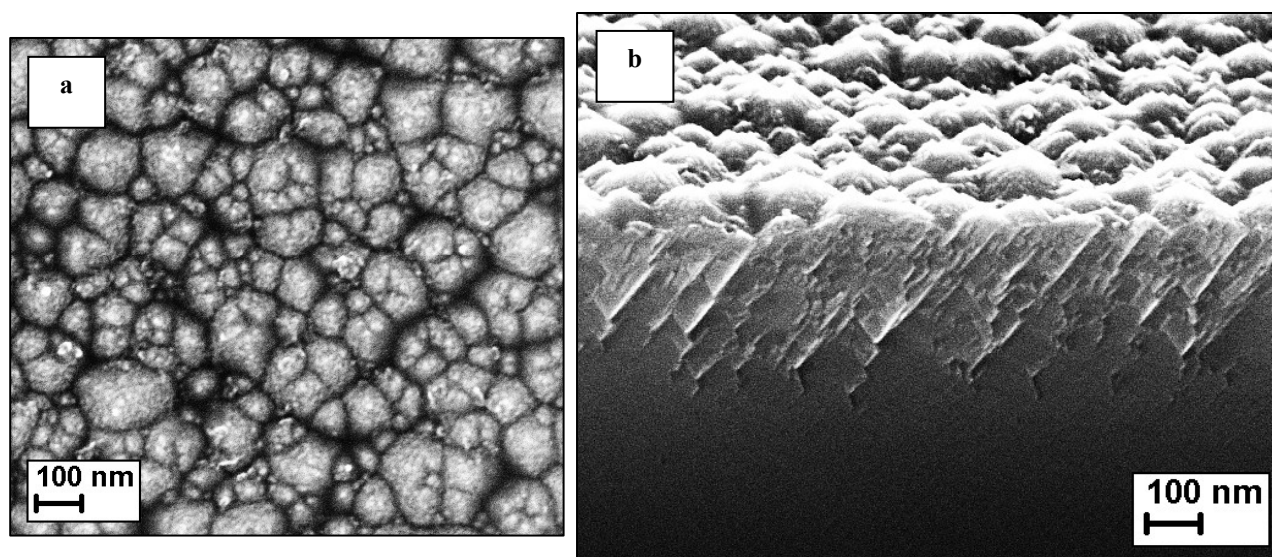


**Fig. 1.** Scanning electron microscopy image of the surface of the anodized porous PbTe epitaxial layer (for  $j_{\text{an}} = 4 \text{ mA/cm}^2$  and  $t = 10 \text{ min}$ ) (a) and a cross-section of this layer with visible mesopores (b).

A domain surface morphology was observed for all of the investigated PbTe films after anodic electrochemical etching (Fig. 1a). The lateral dimensions of the domains were 40-300 nm with an average

value of 130 nm and their surface density was  $\sim 1 \cdot 10^{10} \text{ cm}^{-2}$ . On a cross-sections of PbTe layers obtained with a cleavage of substrate along natural direction [110] the columnar mesopores inclined to the surface at the angle of  $\sim 35^\circ$  were observed (Fig. 1b). The pore diameter was 7-26 nm and the depth of the pores was 150-180 nm as determined both with electron microscopy and x-ray investigations. Therefore, the porous layer occupies only the top region of the anodized film. Porosity value of the porous PbTe layers was 41-68% with the maximum porosity corresponding to the longer anodizing durations. It is well known that in (111)-oriented semiconductors preferential pore propagation corresponds to two main directions:  $\langle 100 \rangle$  or  $\langle 113 \rangle$ . In former case the inclination angle from the surface normal of the pore array is  $35^\circ$  and we can assume that the crystallographic  $\langle 100 \rangle$  directions play a major role in the pore propagation in PbTe films on Si(111). It was also shown that for the longer treatment durations due to surficial material removal during anodic etching it is possible to obtain fully mesoporous PbTe layers with a thickness of 150-300 nm.

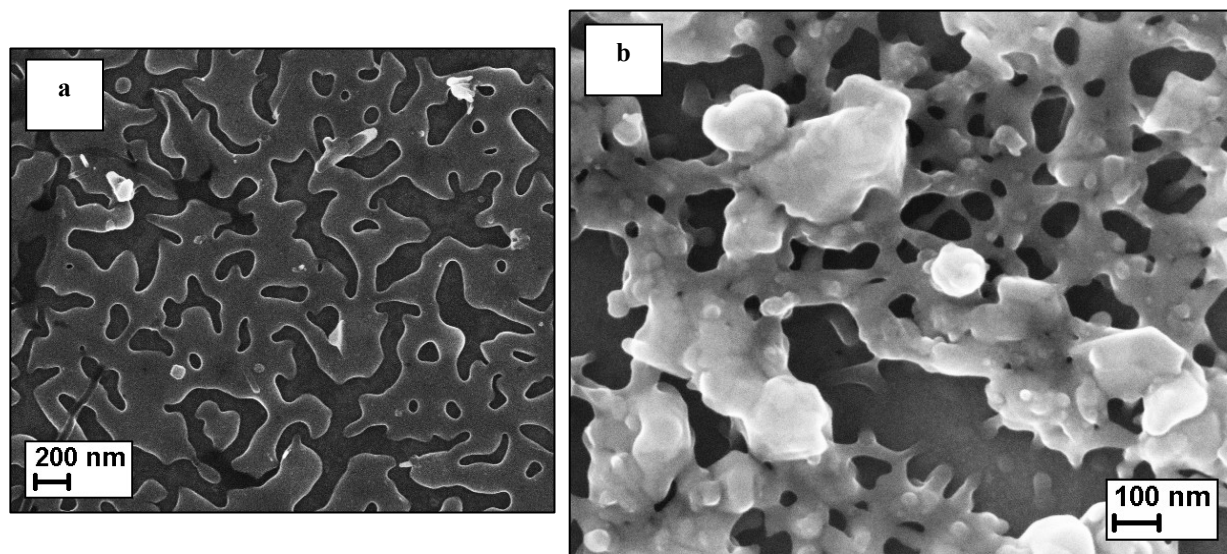


**Fig. 2.** Surface of the anodized PbSe film ( $j_{\text{an}} = 4 \text{ mA/cm}^2$ ,  $t = 20 \text{ min}$ ) with a flat initial surface morphology (a); surface of the anodized PbSe film ( $j_{\text{an}} = 8 \text{ mA/cm}^2$ ,  $t = 10 \text{ min}$ ) with a granular initial surface morphology (b).

PbSe anodized films showed a significantly different results, which depended on the initial film surface morphology. A surface modification for the anodized PbSe films with initial flat surface resulted in a discontinuous surficial film morphology formation (Fig. 2a). Interconnected maze-like pattern, which was located on the surface of electrochemically etched PbSe film, consisted of structures with 80-400 nm lateral sizes and 70 nm average separating gaps. It was possible to fabricate isolated PbSe nanoislands directly on Si substrate for the initial epitaxial films with lower thickness of 2  $\mu\text{m}$  and a longer treatment duration of 20 min. On the other hand, for the films with an initial granular surface morphology a hierarchical porous near-surface layer with large open macropores (100-250 nm), smaller secondary macropores (50-75 nm), and mesopores (15-20 nm) was obtained (Fig. 2b). The most possible reason for the observed pore formation in this case is the non-uniformity of the electrical field for the anodized films with prominent initial surface relief.

In conclusion, an approach to fabricate porous PbTe and PbSe layers on silicon substrates based on anodic electrochemical etching in a Norr electrolyte was presented. Different types of morphology were observed for the anodized films and the techniques to fabricate mesoporous PbTe layers and PbSe nanoislands on Si were proposed. The applied method is promising for the formation of local nanostructured porous areas of IV-VI semiconductors on Si for various practical applications, such as light-emitting layers, thermoelectric devices.

Authors are thankful to H. Zogg for the supplied PbX films on Si substrates and to A.P. Petrakov for the porosity value determination. This work was performed with the financial support of the “Scientific potential development of higher school” Program (project 2.1.1/466).

1. S.P. Zimin, E.A. Bogoyavlenskaya, E.Yu. Buchin, A.P. Petrakov, H. Zogg and D. Zimin, “Formation of porous nanostructured lead telluride films by an anodic electrochemical etching method”, *Semicond. Sci. Technol.*, **24**, pp. 105008-1-6, 2009.

# Mechanical pressure influence on sulfide zinc nanocrystalline films structure

P.N.Krylov, E.A.Romanov, I.V.Fedotova

Udmurt State University, 426036, Izhevsk, Street University, 1, ftt@uni.udm.ru

In work mechanical pressure influence on ZnS nanocrystalline films structure is investigated. The films were obtained at negative condensational temperatures on substrates NaCl, KЭФ-4,5 and SiO<sub>2</sub> [1]. It is shown that mechanical pressure in films on silicon and quartz much less than mechanical pressure in films on NaCl substrates (fig.1). Besides, mechanical pressure in films on NaCl differs from mechanical pressure in films on quartz and silicon on a sign. Compression pressure are characteristic for structures ZnS-NaCl, the given pressure lead to occurrence hexagonal phases. The hexagonal phase crystal sizes increase with fall of condensational temperature. Films on quartz and silicon substrates after heating to room temperatures are subjected compression, and films on NaCl – to a stretching (fig. 2).

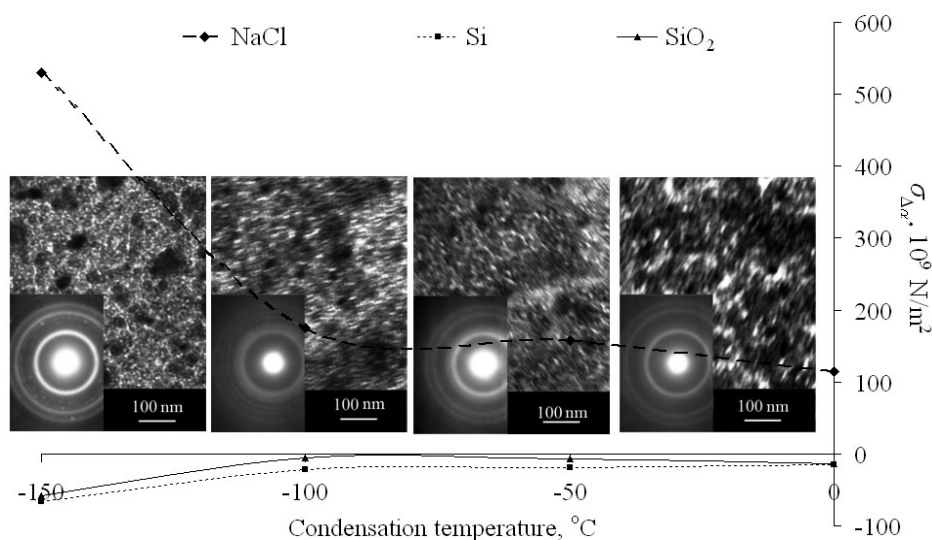


Fig. 1.  
Microstructure of  
films and mechanical  
pressure in zinc  
sulfide films on NaCl  
substrates

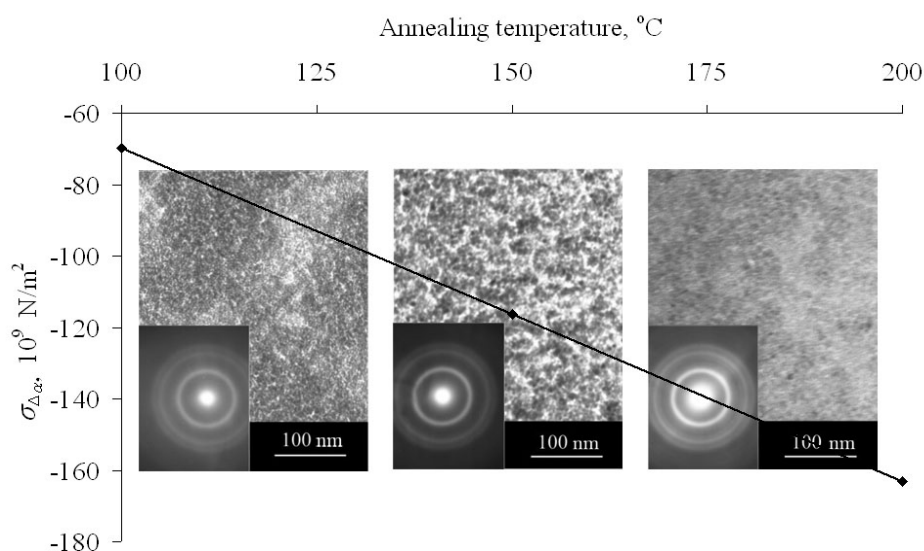


Fig. 2.  
Microstructure of  
films and mechanical  
pressure in zinc  
sulfide films on NaCl  
substrates after  
annealing

1. V.M. Vetrochkin, P.N. Krylov, E.A. Pomanov, I.V. Fedotova, "Super-high-vacuum installation for the synthesis of semiconductor compounds", Vacuum technique and Technology, 10, pp. 75 – 80, 2008.

## Forming methods of island structures

Yu.V.Panfilov, S.V.Sidorova

*Moscow State Technical University n.a. N.E. Bauman, 5, 2<sup>nd</sup> Baumanskaya str., Moscow, 105005, Russian Federation,  
E-mail: sidorova\_bmstu@mail.ru*

Normally growing of thin films on flat surfaces consists of following steps [1]: nucleation centers forming of critical and overcritical sizes, islands forming, islands coalescence, tunnels forming and thin film growing. Islands forming processes in case of thin film growing sequence is one of the most interesting part for modern research and development applications. The result of island forming part are island films or island structures. Different types of electric conductivity could be observed depending of the distance between islands. If the distance is 100 nm and more we have thermoelectronic conductivity. But if the distance is about 2...5 nm it will be tunneling of electrons. R&D applications of island structures could be find in many fields of technique: optics, optical electronics, mico- and nanoelectronics, biomedicine etc. The most interesting structures for such applications are those with the size of 6...10 nm.

The island structures forming methods classification is introduced in the following table. The classification consists of three parts [2]: relief surfaces application, lithography methods and self-assembly methods. The most important parameter in any case is the minimum size of the structure. There are size limitations (20...30 nm) during island structures forming on relief surfaces and in porous of porous materials. The lithography methods (X-ray lithography, electron-beam lithography, lithography based on scanning probes, nanoimprint) allow to receive structure sizes about 10...50 nm. In addition for this technology the application of mask is necessary. Further researches are concentrated on self-assembly methods.

Table – Island structures forming methods classification

Methods group	Title of method	Minimum dimension, nm	E, eV	v, μm/sec	t, sec	Repeatability level
<b>Self-assembly methods</b>	Molecular beam epitaxy	~6...10	0,2...0,3	0,0003	10000...3600	High
	Vapor-phase epitaxy	~10...15	0,1...10	0,01...10	200...0,5	Middle
	Thermal evaporation	~10...20	0,1...0,3	0,1...1,0	20...5	Middle
	Magnetron deposition	~10...15	3...5	0,001...0,5	200...10	Middle
	Ion-beam etching	~10...15	—	-(0,014...0,5)	80...10	High
	Arc discharge method	~10...15	0,1...10	0,1...50	20...0,1	Middle
	Film melting on the surface	~10...50	—	-(0,1...1,0)	20...5	Low
<b>Relief surfaces application</b>	Thin films technology (TFT)	It depends of TFT	It depends of TFT	It depends of TFT	It depends of TFT	Middle
<b>Lithography methods</b>	X-ray lithography	~50	It depends of TFT	It depends of TFT	It depends of TFT	High
	Electron-beam lithography, lithography based on scanning probes, nanoimprint	~10	It depends of TFT	It depends of TFT	It depends of TFT	High

The group of methods which is called self-assembly methods include: molecular beam epitaxy, vapor-phase epitaxy, thermal evaporation, magnetron deposition, ion-beam etching, arc discharge method, film melting

on the surface. The listed methods have number of technological parameters, which exert influence on geometrical sizes of island structures.

The thermal evaporation method and magnetron deposition method are chosen for further researches. Till this moment all researches have been done only for thermal evaporation method. All the samples are produced using copper as an evaporated material. The ceramic and silicon substrates were applied. The recipe parameters of island structures forming are the results of the researches.

1. Leon I. Maissel, Reinhard Glang. *Handbook of Thin Film Technology*. New York: McGraw-Hill, 1970. 1200 p.
2. Yu.V. Panfilov, S.V. Sidorova. "Vacuum methods of quantum dots manufacturing review". Vacuum Science and Technique. Moscow: MIEM, 2009. P. 159–163.



# Effect of arsenic molecular form (As<sub>2</sub> or As<sub>4</sub>) on the composition of solid solutions GaP<sub>x</sub>As<sub>1-x</sub>, GaSb<sub>x</sub>As<sub>1-x</sub> during the molecular-beam epitaxy

E.Emelyanov, M.Putyato, B.Semyagin, A.Vasilenko, V.Preobrazhenskii  
Institute of Semiconductor Physics, SB Russian Academy of Sciences, Novosibirsk, Russia,  
E-mail address: Bagatir@yandex.ru

One of the most important characteristic of A<sup>III</sup>B<sup>V</sup> solid solutions molecular-beam epitaxy is the embedding coefficient of V-group elements ( $S_V$ ) – the ratio of atoms embedded in the growing layer, to the total number of atoms, coming on the growth surface per unit time. Information on the dependence of the coefficient  $S_V$  on the growth conditions and molecular form of the V-group elements in the incident beam is not only of practical importance. It serves as a basis for modeling the growth as A<sup>III</sup>B<sup>V</sup> binary compounds, and V-group substitutional solid solutions.

During epitaxy of stoichiometric A<sup>III</sup>B<sup>V</sup> compounds factor  $S_V$  is not dependent on the substrate temperature ( $T_s$ ), and completely determined by the flux ratio ( $J_{III}/J_V$ ) and the surface reconstruction.

The factor ( $S_V$ ) for some compounds depends on the molecular forms of matter in the V-group flux, for others - no. So factor  $S_{Sb}$  during MBE of GaSb(001) from the flux of molecules Sb<sub>4</sub> strive for unity in a wide range of growth conditions [1]. Factor  $S_{As}$  during MBE of GaAs(001)(2x4) is close to 0.75 and does not depend on the molecular form of arsenic in the incident beam (As<sub>2</sub> or As<sub>4</sub>) [2,3]. In the case of phosphorus, the  $S_P$  during MBE of GaP(001) from the P<sub>2</sub> molecules flux is significantly higher than from the flux of P<sub>4</sub> molecules.

During A<sup>III</sup>B<sup>V</sup> solid solutions MBE with the substitution of the fifth group, such as GaAs<sub>x</sub>P<sub>1-x</sub> and GaAs<sub>x</sub>Sb<sub>1-x</sub>, the factor  $S_V$  is a function of a much larger number of parameters. In this case, the  $S_V$  depends on the ratio  $J_{III}/J_V$ ,  $T_s$ , the growth rate  $V_g$  and other growth conditions. Molecular form of V-group elements in the incident beam also has a significant impact on factor  $S_V$ . This influence is still poorly understood. The aim of this work was experimental investigation of the influence of the arsenic molecular form in the incident flux on the composition of solid solutions GaAs<sub>x</sub>P<sub>1-x</sub> and GaAs<sub>x</sub>Sb<sub>1-x</sub>, during MBE.

Two groups of structures was grown on GaAs(001) substrates. One group consisted of two samples with films of GaAs<sub>x</sub>P<sub>1-x</sub> solid solution, and another of two samples with films of GaAs<sub>x</sub>Sb<sub>1-x</sub> solid solution. In each group one sample was grown using the As<sub>2</sub> flux, and the other using the As<sub>4</sub> flux, which in atomic terms was equal to the As<sub>2</sub> flux. Other growth conditions within the group did not change. The thickness of the grown films was 300 nm. Samples with a GaAs<sub>x</sub>P<sub>1-x</sub> solid solution grown at  $T_s = 500^\circ\text{C}$ , and  $V_g = 1$  monolayer per second, which corresponds to the flux density of Ga atoms equal to  $6.26 \times 10^{14} \text{ cm}^{-2} \text{ s}^{-1}$ . Flux densities of As<sub>2</sub> and As<sub>4</sub> in atomic terms were equal, and amounted to  $1.75 \times 10^{15} \text{ cm}^{-2} \text{ s}^{-1}$  (i.e.  $2 \times J_{As2} = 4 \times J_{As4} = 1.75 \times 10^{15} \text{ cm}^{-2} \text{ s}^{-1}$ ). The P<sub>2</sub> flux density for both samples was the same ( $2 \times J_{P2} = 2.24 \times 10^{15} \text{ cm}^{-2} \text{ s}^{-1}$ ).

GaAs<sub>x</sub>Sb<sub>1-x</sub> films were grown at  $T_s = 400^\circ\text{C}$  and the Ga flux density, equal to  $6.26 \times 10^{14} \text{ cm}^{-2} \text{ s}^{-1}$ . As<sub>2</sub> and As<sub>4</sub> flux densities in atomic terms were equal, and amounted to  $1.9 \times 10^{15} \text{ cm}^{-2} \text{ s}^{-1}$ . In both cases  $4 \times J_{Sb4} = 1.7 \times 10^{14} \text{ cm}^{-2} \text{ s}^{-1}$ . The composition of grown films was determined by X-ray analysis. It seems more conveniently to analyze the relations  $S_{As2}/S_{P2}$  and  $S_{As4}/S_{P2}$  ( $S_{As2}/S_{Sb4}$  and  $S_{As4}/S_{Sb4}$ ) behavior when solid solutions MBE with fifth group substitution are realized. Table 1 shows the composition of the solid solutions layers and values of  $S_{As2}/S_{P2}$  and  $S_{As4}/S_{P2}$  ( $S_{As2}/S_{Sb4}$  and  $S_{As4}/S_{Sb4}$ ) relations for GaAs<sub>x</sub>P<sub>1-x</sub> and GaAs<sub>x</sub>Sb<sub>1-x</sub> solid solutions.

Table 1

Solid solution	Arsenic molecular form	Arsenic portion in solid solution	$\frac{S_{As2}/S_{P2}}{(S_{As4}/S_{P2})}$	$\frac{S_{As2}/S_{Sb4}}{(S_{As4}/S_{Sb4})}$
GaAs <sub>x</sub> P <sub>1-x</sub>	As <sub>2</sub>	0.87	8.56	
	As <sub>4</sub>	0.75	3.84	
GaAs <sub>x</sub> Sb <sub>1-x</sub>	As <sub>2</sub>	0.88		0.66
	As <sub>4</sub>	0.86		0.55

As shown in Table 1, the influence of arsenic molecular form on solid solution composition is more expressed for GaAs<sub>x</sub>P<sub>1-x</sub> than GaAs<sub>x</sub>Sb<sub>1-x</sub>. Our calculations indicated that during GaAs<sub>x</sub>P<sub>1-x</sub> MBE the  $S_{As}$  value is on 15% higher for growth from As<sub>2</sub> flux than from As<sub>4</sub>. These data suggests that the efficiency of As<sub>2</sub> and As<sub>4</sub> embedding is higher than P<sub>2</sub>, but less than Sb<sub>4</sub>.

1. J.R. Waterman, B.V. Shanabrook and R.J. Wagner, J. "Vac. Sci. Technol". B, 10 (1992) 895.
2. V.V. Preobrazhenskii, R.I.Nizamov, M.A. Putyato, B.R. Semyagin, D.I.Lubyshev, O.P. Pchelyakov, Inst. of Physics Conference Series № 155, IOP Publishing Ltd., 1997, ch.3, pp. 311-314.
3. M.A. Putyato, B.R. Semyagin, A.V. Vasev, V.V. Preobrazhenskii, Russian Physics Journal Series: Physics (in Russian) 9/3, (2008) pp. 23-28.

# Local composition analysis of Ge:Mn, Si:Mn и Si:Co magnetic semiconductor thin films by XPS and SAM

D.Nikolitchev<sup>1,2</sup>, E.Demidov<sup>1,2</sup>, V.Podolskii<sup>1,2</sup>, V.Lesnikov<sup>2</sup>,  
A.Boryakov<sup>1</sup>, A.Vihorev<sup>1</sup>, S.Zubkov<sup>1,2</sup>, S.Levchuk<sup>1,2</sup>

1. N.I.Lobachevsky State University of Nizhni Novgorod, Nizhni Novgorod, Russia, nikolitchev@phys.unn.ru.

2. Physico-Technical Research Institute of N.I. Lobachevsky UNN, Nizhni Novgorod, Russia

For spintronic structures there IV group semiconductors (Ge, Si) diluted with elements of iron group (Mn, Fe, Co) act as a materials additionally to semiconducting characteristics modification the possibility to control the carriers spin is present. It was shown [1, 2] that diluted magnetic semiconductors (DMS) grown by impulse laser deposition (ILD) reveal the ferromagnetic features at temperatures up to 310 – 320 K that is confirmed by observation of ferromagnetic resonance, abnormal Hall effect and nonlinear magnetooptic Kerr effect.

The goal of this work is to study the composition of DMS thin films and defects appeared during ILD using methods of scanning Auger microscopy (SAM) and X-ray photoelectron spectroscopy (XPS) in order to understand a connection between composition, electrical and magnetic properties and growth parameters for DMS structures.

The samples were grown by ILD on the semi-insulating GaAs or Si substrates at the 200-450°C. To sputter Si, Ge, Mn or Co targets the impulse YAG:Nd laser with 1.06 mkm wavelength, 0.2 J impulse energy and 12 ns impulse duration was used [3]. Thickness of DMS layers was 30 – 60 nm. Samples were analyzed at ultrahigh vacuum ( $10^{-11}$  mbar) system Omicron Multiprobe RM which included the apparatus for SAM and XPS. For layer-by-layer analysis films were etched by  $\text{Ar}^+$  ions with 1 keV energy. The surface morphology of grown layers was controlled by atomic force microscopy before spectroscopic measurements.

The composition of surface drop-shaped defects organized during film ILD were studied using scanning Auger-microscopy. It was discovered that defects could be formed at any moment of deposition process and could consist fully of either main semiconducting material (Ge or Si) or diluent alloy material (Mn or Co). The example of elemental map for cobalt recorded in Co LMM Auger-line for single drop is shown on Fig. 1. The parameters of deposition from laser plasma that led to increase of defect formation were found.

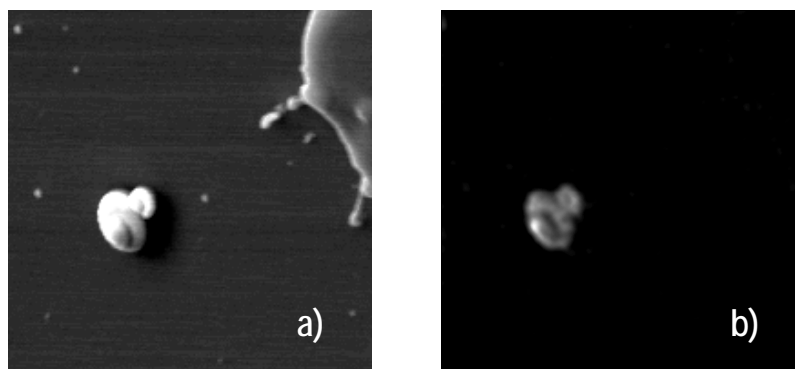


Рис. 1. SEM-image in secondary electrons (a) and surface elemental map for cobalt (b) of DMS-film with Co drop. Image size  $10 \times 10$  mkm.

On the Mn concentration profiles in depth received for Ge:Mn samples the pits near the surface (8 – 10 nm) were observed that can be due to the segregation process. Such effect was more intensive for the Ge:Mn samples that were investigated after more than 1 year since growth and the pit's minimum were shifted toward to the surface into 4 – 5 nm position. During near-surface layers analysis for Si:Mn structures it was determined that Mn segregation is also evidently presented but Si:Co DMS are free from this effect.

To clarify the nature of high temperature ferromagnetism in nanosize Si:Mn layers with homogeniously doping (random alloys) it is of interest to investigate periodic structures or Si/Mn digital alloys (DA). Sputtering depth and so etching rate was determined using atomic force microscopy data. Profiles of concentration depth distribution for Si/Mn DA on Fig. 2 are the evidence of possibility to obtain antiphase modulation of Si and Mn concentration by laser deposition.

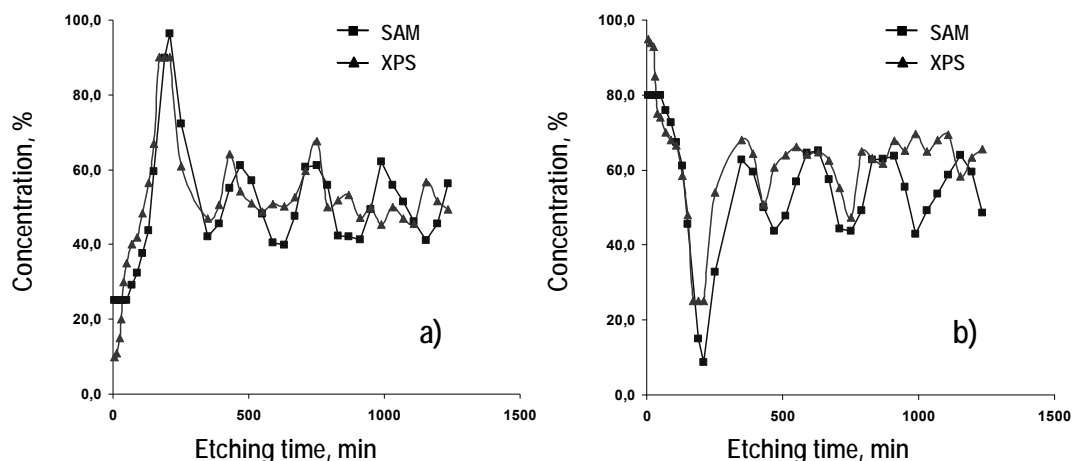


Рис. 2. Профили распределения марганца (а) и кремния (б) по глубине многослойной структуры Si/Mn.

Both XPS and SAM methods have a similar resolution in depth. In the case of SAM more sharp composition depth profile recorded due to the small area of electron beam which can be localized down to 20 nm and set between drops on the surface of discrete alloys structure. During XPS profile acquisition photoelectrons are emitting from area of about 3 mm which is much larger than average distance between drop-shaped defects. Profile obtained by XPS is smoothing because of difference between composition of drops and main DA structure in layer bound-areas. The second case of profile unsharpness can be the non-uniformity of ion etching crater in radial direction.

The main problem during quantitative XPS analysis of Si:Mn and Si:Co films consisted in fact that binding energy of the most intensive photoelectron lines (2p<sub>3/2</sub>) of manganese (639,1 eV) and cobalt (778,4 eV) is strongly differ from binding energy of silicon most intensive lines (2s – 150,5 eV and 2p – 100,1 eV). With regard to this determination of concentration using the relative sensitivity factors (RSF) become problematic. To solve the problem of quantitative analysis by method of RSF photoelectron lines of Mn (3p – 47 eV and Co (3s – 59 эВ) lying near the Si lines were used. After this the concentrations of DMS films obtained independently by XPS and electron Auger spectroscopy methods were coherent.

Investigation of chemical states for main components germanium or silicon doped with manganese or cobalt atoms can help comprehend the mechanism of ferromagnetism in diluted magnetic semiconductors and reveal optimal growth conditions for making spintronic devices on the basis of DMS in future.

1. E.S. Demidov, Yu.A. Danilov, V.V. Podol'skii et al. "Ferromagnetism in epitaxial germanium and silicon layers supersaturated with manganese and iron impurities", JETP Lett., 83, pp. 568 - 571 2006
2. E.S. Demidov, V.V. Podol'skii, V.P. Lesnikov et al. "Ferromagnets based on diamond-like semiconductors GaSb, InSb, Ge, and Si supersaturated with manganese or iron impurities during laser-plasma deposition", JETP, 133, pp.132 – 139, 2008
3. E.S. Demidov, S.Yu. Zubkov, V.P. Lesnikov et al. "X-ray photoelectron and auger spectroscopy analysis of Ge:Mn-based magnetic semiconductor layers", J. Surf. Investig., N. 7, pp.36 – 41, 2008

# Self-organization of atoms into nanosystems

D.B. Titorov

Physical-Technical Institute, Ural Branch RAS 426000, Izhevsk, Russia, titorov@fti.udm.ru

In a condensed substance, the place of each atom among others is exactly determined. During structural and phase changes each atom moves in certain direction and over a certain distance. At the end of 20th century, the experimenters had found a way to move separate atoms [1]. Because of a principle of indeterminacy, the quantum-mechanical approach is not sufficient to predict the structure of a condensed substance and the travels of atoms during formation and transformation of the substance. The model of a pair interpenetration of spheres allows one to form various atomic spatial structures of condensed substances which have different lattices and interatomic bonds (metal, covalent, ionic and others) by simple classical geometrical method [2]. The self-organization of atoms in a condensed substance is a travel of atoms to positions where interatomic forces are balanced. The interatomic attractive forces move interpenetrating atoms closer to each other. The interatomic repulsive forces restrict depth of interpenetration.

Classical atoms are neutral. The shells of atoms isolate atoms from external electric charges. Hence, when distance between atoms is larger than sum of their radii there is no any electrostatic force between them (atom **a** and the rest in Fig.). Suppose an atom from a surrounding medium (atom **b** in Fig.) penetrates into a surface atom of a growing centre (one of four atoms at the bottom of Fig.). The part of a shell (cap) of the surrounding-medium atom, that penetrates, and the core of the atom, in which the cap penetrates, attract each other (the force  $-F$  in Fig.). Shells isolate atoms from external charges. Charges inside an atomic shell interact among themselves only.

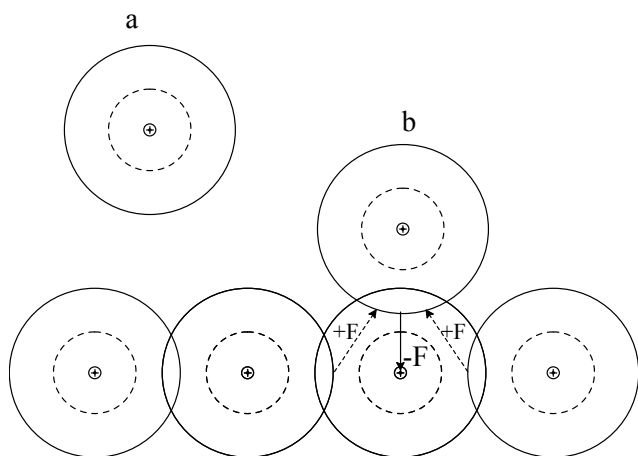


Fig. Adsorption of atom (**b**) to atom on a surface of a growing centre.

The electrostatic repulsive force between the caps that penetrate into one atom (the force  $+F$  in Fig.) prohibit from the caps movement to each other.

Besides, there are repulsive forces which operate between atoms and can be called thermal. Their values can be estimated by division of energy that is spent for increase of interatomic distance at heating, by value of this increase. To determine the thermal repulsive forces (are not shown on Fig.), the data on heat capacity, thermal expansion, and structure, which are known for monoatomic crystals, are used.

Oscillations of atoms are taken into account.

From an equilibrium condition between the repulsive and attraction forces, computed are the sizes of interpenetrating atoms Au, Ag and C, the magnitude of the thermal repulsive forces and, then, the interatomic distances in alloys  $Au_xAg_{1-x}$  and the distance between planes in graphite (between graphenes). The last calculated data coincide with experimental values with precision 0.1 % and better. For example, the prognostic evaluation of  $c/2$  for graphite yields the value of 0.3357nm which differs from the known experimentally one only by 0.0003nm.

In the report presented, mechanical, electrical and other properties are analyzed with application of the model of interpenetrating atoms. The model of self-organization of interpenetrating atoms can be useful for designing and manufacture of nano-sized crystalline and noncrystalline objects and not only.

1. Christian Joachim. *Nanosciences, la révolution invisible* Etude (broché). Paru en 01/2008
2. D.B. Titorov "Formation of planar and space lattices from spherical bodies with mutually penetrating shells" Crystallography Reports, 46, № 1, pp. 19-20, 2001.

# Development of the atomic force microscopy research technique for the nanostructures on the vertical edge of thin insulating film

E.S.Gorlachev, V.M.Mordvintsev, V.L.Levin

Yaroslavl Branch of the Institute of Physics and Technology, Russian Academy of Sciences, Yaroslavl, Russia,  
E-mail: Mordvintsev-Viktor@yandex.ru

Development of a new generation nonvolatile memory devices is one of the most crucial problems of the modern micro-, nanoelectronics. Recently, a nonvolatile electrically reprogrammable memory matrix based on nano-MIM (metal-insulator-metal) diode cells was developed and manufactured showing a full set of memory functions with outstanding stability [1]. This memory device consists of open sandwich W/SiO<sub>2</sub>/Si structures with 10-20 nm thin insulating SiO<sub>2</sub> film. Its functioning is based on the process of electroforming – the self-organization of an insulating nanogap in the active conductive medium on the open insulator edge surface via electric current impact [2-3]. In order to study in detail physical processes of the electroforming it is important to directly investigate conductive nanostructures and insulating nanogap on the surface of the vertical edge of thin insulating film. The aim of the present work was to develop atomic force microscopy (AFM) research technique, which would allow us to solve such task.

Surface topography research was carried out on scanning probe microscope Omicron UHV AFM/STM in contact mode using standard CSG11/TiN (NT-MDT) probes in high vacuum of  $1 \cdot 10^{-8}$  Torr. The particular feature of this instrument was a limited scan range of  $6 \times 6 \mu\text{m}^2$  and availability of only one direction of the coarse sample positioning, which significantly limited the measurement capabilities. The elaboration of the AFM measurement technique was firstly carried out using TGQ1 (NT-MDT) calibration grating arrays of SiO<sub>2</sub> square mesas with 21.5 nm height. Frequently met artifacts (distortions), such as broadening, edge overshoot, blurring, external noises, and tip artifacts due to tip contamination and wear were revealed and excluded. Several factors limiting the AFM performance were established: the inherent piezoelectric scanner nonlinearity, hysteresis, creep. In particular, presence of creep in the vertical direction introduced artificial ridges and grooves near sidewalls, therefore its removal was crucial. Optimum values of scanning speed (50 nm/s), loop gain (1%), and a feedback force set-point (0 nN) were experimentally determined. Also, scanning was conducted with the cantilever mount tilt of 15°, which oriented the tip towards the sidewall. As a result, the AFM measurement optimum regime was obtained [4], which allowed us to observe real morphology of SiO<sub>2</sub> film vertical edge. For the next series of experiments specially fabricated non-electroformed W/SiO<sub>2</sub>/Si open sandwich MIM-structures were used, which had a special topology complying with the abovementioned instrument restrictions in a way that a part of the perimeter of SiO<sub>2</sub> open edge was getting into the scanning area. For the carrying out of AFM measurements the top tungsten electrode was removed in order to provide access of the scanning tip to the edge of SiO<sub>2</sub> film. Using the optimum regime a satisfying results for the sidewall profiles were obtained, which corresponded well to the electron microscopy data, but provided a significantly higher resolution. Fig. 1 shows a typical AFM image of the section of the perimeter of the open edge of SiO<sub>2</sub>/Si sandwich structure.

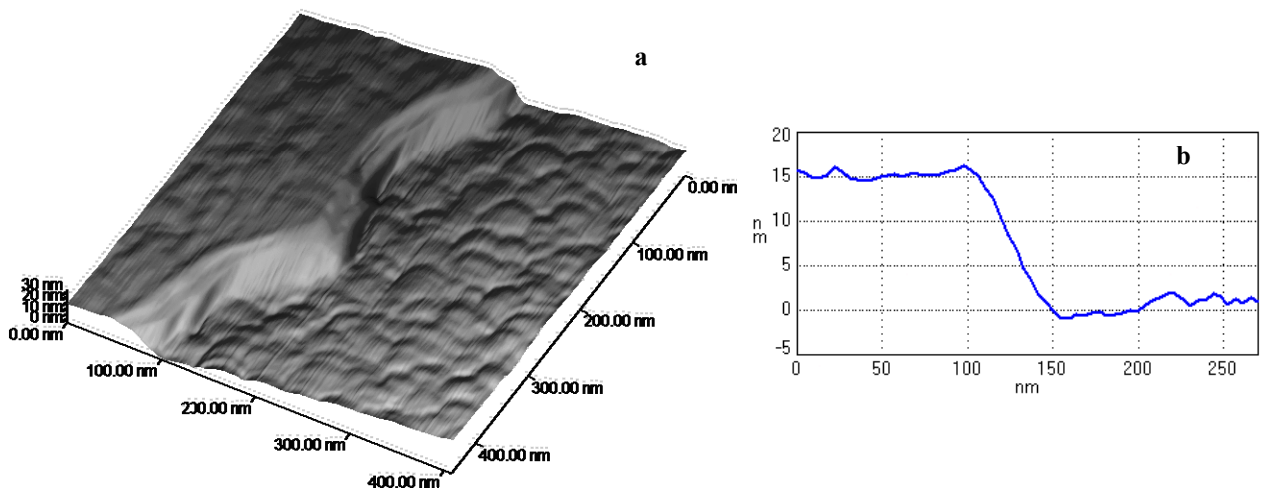
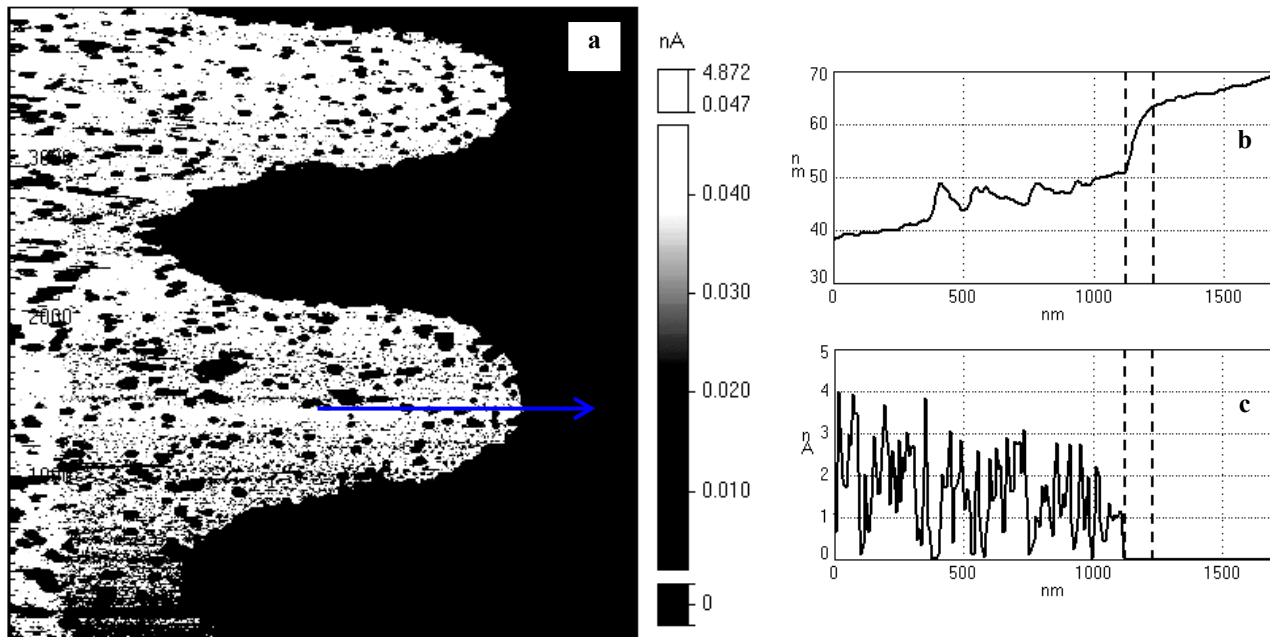


Fig. 1. AFM image (a) of an open SiO<sub>2</sub>/Si structure and typical profilogram (b) of the open edge of the insulating layer.



**Fig. 2.** Typical AFM image of SiO<sub>2</sub>/Si sandwich structure in the spreading resistance measurement mode (a); profilogram of the open edge of insulating layer (b) and corresponding current signal (c).

At the next stage of this work AFM investigations in spreading resistance measurement mode were carried out, when simultaneously with microrelief a current map of the surface area was measured permitting to estimate local surface conductivity of the sample. Fig. 2a displays AFM image of a specially fabricated SiO<sub>2</sub>/Si sandwich structure investigated in spreading resistance measurement mode. Here, black color on the image corresponds to a zero current and consequently to the absence of conductivity (silicon dioxide insulating film area). The most important experimental result is the observation of a sharp transition from insulating to the conductive layers of sandwich structures with nanometer-scale resolution (see Fig. 2b and Fig. 2c). Hence, AFM research is highly promising from the standpoint of the observation of conducting nanostructures on the SiO<sub>2</sub> vertical edge of electroformed nano-MIM-diodes.

The results of this work show that under developed optimum regimes, even considering the limitations of the current Omicron instrument, it is possible to provide sufficient sidewall information using a conventional AFM technique and to carry out local conductivity characterization of MIM-structure SiO<sub>2</sub> film edge with nanometer resolution. The work in progress is to perform modification of Omicron AFM/STM microscope using integrating ultrasmall piezoelectric linear motor (SQL-1.8) with 0.5  $\mu\text{m}$  resolution and 6 mm travel range in order to obtain second lateral scanning direction. This would allow us to perform measurements directly on the electroformed nano-MIM-diode cell structures of the electroformed memory matrix chips in order to detect insulating nanogap and conductive nanostructures on the surface of the vertical edge of thin insulating SiO<sub>2</sub> film.

1. V.M. Mordvintsev, S.E. Kudryavtsev and V.L. Levin, "High-stable nonvolatile electrically reprogrammable memory on self-formed conducting nanostructures", *Nanotechnologies in Russia*, **4**, No. 1-2, pp. 129-136, 2009
2. V.M. Mordvintsev and S.E. Kudryavtsev, "Highly doped Si-SiO<sub>2</sub>-W sandwich structures with an exposed insulator edge: electrical transport and electroforming", *Russian Microelectronics*, **36**, No. 6, pp. 371-383, 2007
3. V.M. Mordvintsev, S.E. Kudryavtsev and V.L. Levin, "Electroforming as a process in the self-formation of conducting nanostructures for the nonvolatile electrically reprogrammable memory elements", *Nanotechnologies in Russia*, **4**, No. 1-2, pp. 121-128, 2009
4. E.S. Gorlachev, V.M. Mordvintsev and V.L. Levin, "Problems of AFM-investigations of open sandwich MIM-structures", *Proc. Int. Conf. "Micro- and nanoelectronics – 2009 (ICMNE-2009)"*, p. O3-20, 2009

# The scalable up process production of carbon nanotube CNT by means of catalytic pyrolysis ethanol on heterogeneous catalyst

N.Savinski<sup>1</sup>, M.Gitlin<sup>1</sup>, A.Rusakov<sup>2</sup>, V.Naumov<sup>1</sup>

1. Yaroslavl Branch of the Institute of Physics and Technology, Russian Academy of Sciences, Yaroslavl, Russia, E-mail: Savinski1@yandex.ru. 2. Yaroslavl Demidov State University, Yaroslavl, Russia

Perhaps the most significant potential impact for CNTs is in future electronics. Depending on their structure, nanotubes can exhibit either metallic or semiconducting electronic properties. There has been significant effort to use nanotubes as components in integrated circuits including :

- metallic interconnects between adjacent layers in the device architecture, and (2) the semiconducting gate material in field-effect transistors (FETs). Metallic nanotubes display low resistivity in the range of  $10^{-4}$  to  $10^{-3}$   $\Omega$ -cm and can withstand enormous current densities as high as  $109 \text{ A/cm}^2$ .
- Field emission and electrochemical devices have been manufactured from arrays of nanotubes to take advantage of these electrical properties, as well as the high aspect ratio and large surface area. Individual metallic nanotubes have been applied as field emission electron sources and tips for scanning probe microscopy.
- Semiconducting nanotubes are being integrated into nanometer-scale electronic devices, such as single electron FETs and switches, and as nanotweezers and chemical sensors.

At present, the most commonly used method for CNT growth is catalytic decomposition of carbon precursors characterized by a metal nanoparticle that is involved in several key steps during nanotube nucleation and growth.

Our groups have introduced the catalysts by

- (Fig 2 a, c ,d) in situ formation of floating catalyst particles from organometallic vapors in furnace reactors ;
  - injection of catalyst particles prepared by either wet chemical routes Fig 2 b,
  - or gas-phase synthesis techniques including metal nano particles on catalyst support Fig 3
- . The experimental setup for CNT growth is shown bellow. The substrate was inserted into a quartz tube, which was evacuated to  $1 \times 10^{-4}$  Pa by a vacuum pump. The tube was then heated up to the growth temperature (973K) under 3 kPa of flowing Ar/H<sub>2</sub> (3% H<sub>2</sub>). When the growth temperature (600 –800 °C) was reached after about 15 min, the Ar/H<sub>2</sub> gas flow was stopped and the quartz tube was evacuated again until the pressure reached  $1 \times 10^{-4}$  Pa. The downstream valve was then closed, and ethanol vapor with or without Ar/H<sub>2</sub> gas was introduced into the tube. When some initial growth pressure was reached, the upstream valve was also closed. Initial growth pressure and growth time were varied from 1.3 to 2.7 kPa, and from 5 to 10 min, respectively. The growth of CNTs was terminated by opening the down stream valve.

In all of these methods, it is necessary to carefully control the metal particle size in order to nucleate and grow well-defined CNTs. While the formation of catalyst particles directly in a furnace reactor is convenient, uncontrolled particle nucleation and agglomeration lead to broad size distributions and poor control of nanotube diameter. Colloidal synthetic approaches (wet chemistry) have demonstrated that catalyst particles with narrow size distributions can be synthesized for controlled CNT growth. However, the injection of these colloidal dispersions into a gas-phase reactor is complicated, and the CNT nucleation and growth can be terminated due to the deactivation of the catalysts by the presence of stabilizer molecules or oxide on the particle surface. High-purity catalyst particles can be produced by gas-phase techniques but the broad particle size distributions of the as-produced catalyst particles make post-synthesis size selection unavoidable.



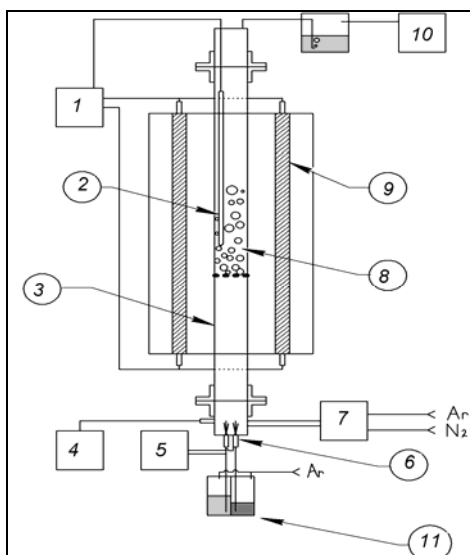


Fig 1 CVD reactor for growth CNT

1-PID control block, 2 - thermocouple probe, 3 - quartz tube, 4 - pressure control unit, 5 - electronic controller of blast atomizer, 6 - blast atomizer, 7 - gas mass flow controllers, 8 - catalyzer, 9 IR - carbon lamps, 10 - bellow gas lift valve, 11 - pressure tank with EtOH.

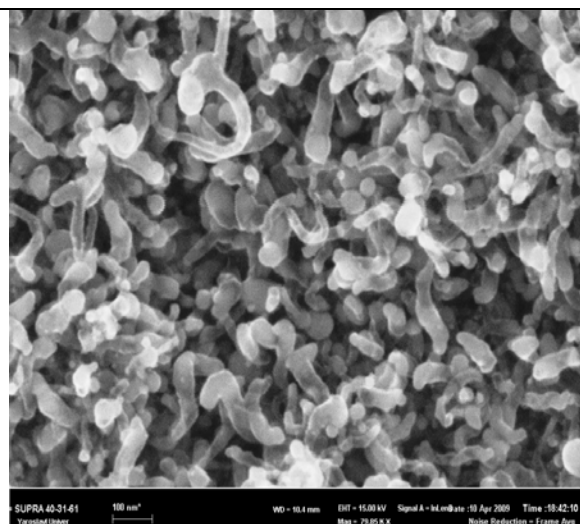


Fig 2a FESEM image of the SNT  
n-Pentan -1 % Ferrocene 800°C

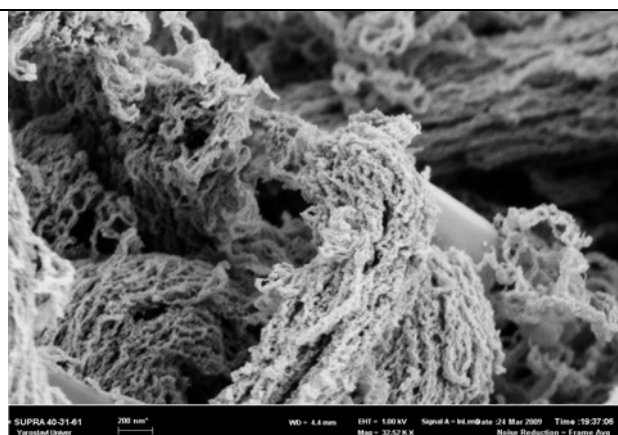


Fig 2b FESEM image of the SNT  
colloidal dispersions  $\text{Co}(\text{NO}_3)_2$  in EtOH 800 °C

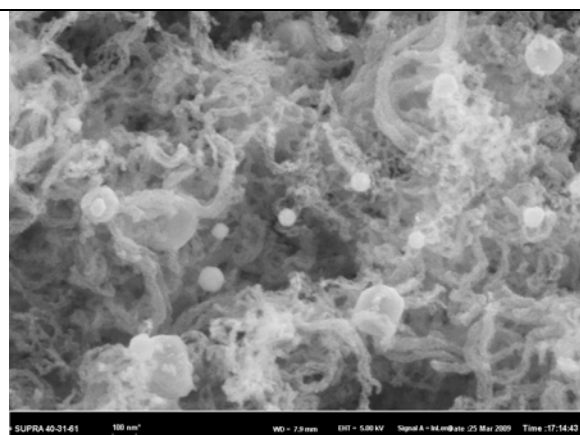


Fig 2c FESEM image of the SNT  
EtOH AACCo- 05%-AAC Fe 0.5% 800 °C

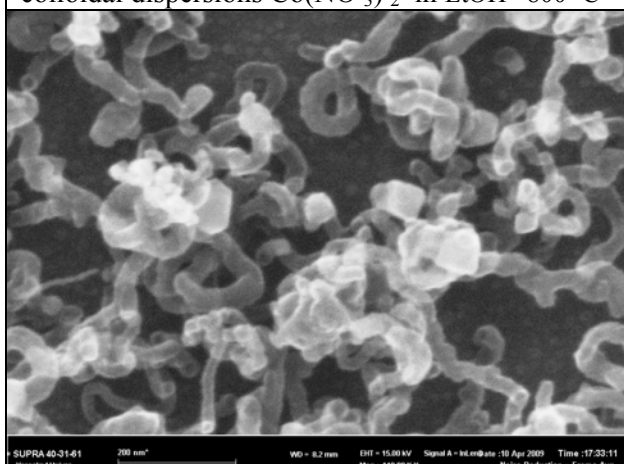


Fig 2d FESEM image of the SNT  
1% AAC Fe in benzene 800°C

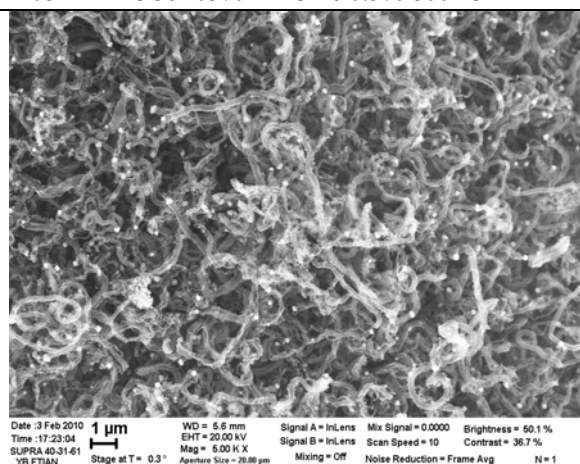


Fig. 3 FESEM image of the SNT  
EtOH Np Co, Mn on catalyst support MgO 750°C



# SOI doping and its influence on a wafer temperature during RTA

V.Prigara, V.Ovcharov, V.Rudakov

Yaroslavl Branch of the Institute of Physics and Technology, Russian Academy of Sciences, Yaroslavl, Russia,

E-mail: vprigara@rambler.ru

In the process of rapid thermal annealing it is an important problem to take into account the influence of radiative properties of a heated wafer on its temperature [1]. In present investigation a numerical simulation of the temperature of the silicon wafer with SOI (silicon-on-insulator) structure at its rapid annealing is made. To carry out the calculations the reactor of RTA is modeled by radiation-closed thermal system consisting of three infinite plane-parallel plates. One of the plates is an absolutely black body (ABB, emissivity equal to 1) serving as a heater. The second investigated wafer of silicon with SOI structure facing the heater has a complex dependence of radiative properties on the wave length of imposed radiation and on the temperature. And the third plate is also ABB wafer with a fixed temperature. It provided heat removal in the considered system. Only the radiation component of heat flux between the plates was taken into account. The higher temperature of the heated wafer the better is the approximation. Let's write down the balance of the heat which is radiated and absorbed by the wafer in infinitesimal spectral interval  $d\lambda$  corresponding to the wave length  $\lambda$ . The heat flux absorbed by the wafer is [2]:

$$dq_{p,abs} = \alpha_{SOI,\lambda}(\lambda, T_p) e_{\lambda b}(\lambda, T_r) + \alpha_{back,\lambda}(\lambda, T_p) e_{\lambda b}(\lambda, T_a). \quad (1)$$

The heat flux radiated by the wafer is as follows

$$dq_{p,rad} = e_{\lambda b}(\lambda, T_r) [\varepsilon_{SOI,\lambda}(\lambda, T_p) + \varepsilon_{back,\lambda}(\lambda, T_p)]. \quad (2)$$

Here,  $e_{\lambda b} = \frac{2\pi C_1}{\lambda^5 [\exp(C_2/\lambda T) - 1]}$  is the Planck spectral function of distribution of emissive power;

$C_1 = hc^2$ ;  $C_2 = hc/k$ ;  $h$  is the Planck constant;  $c$  - velocity of light in vacuum;  $k$  is the Boltzmann constant;  $\varepsilon_{\lambda}(\lambda, T_p)$ ;  $\alpha_{\lambda}(\lambda, T_p)$  are hemispherical spectral emissivity and absorbtivity of a wafer. (The radiative characteristics have subscriptive index "SOI" for the working side having SOI and "back" for the side without SOI.) In accordance with Kirchhoff's law [2] the equality is true

$$\alpha_{\lambda}(\lambda, T_p) = \varepsilon_{\lambda}(\lambda, T_p). \quad (3)$$

Then the following relations are fulfilled for the working and back sides of the wafer

$$\alpha_{SOI,\lambda}(\lambda, T_p) = \varepsilon_{SOI,\lambda}(\lambda, T_p), \quad (4)$$

$$\alpha_{back,\lambda}(\lambda, T_p) = \varepsilon_{back,\lambda}(\lambda, T_p). \quad (5)$$

Using (1),(2),(4) and (5) we write down the integral flux of resulting radiation, connected with the wafer as follows:

$$q_p = \int_0^{\infty} (dq_{p,abs} - dq_{p,rad}) d\lambda = \int_0^{\infty} \varepsilon_{SOI,\lambda}(\lambda, T_p) [e_{\lambda b}(\lambda, T_p) - e_{\lambda b}(\lambda, T_a)] d\lambda - \int_0^{\infty} \varepsilon_{back,\lambda}(\lambda, T_p) [e_{\lambda b}(\lambda, T_p) - e_{\lambda b}(\lambda, T_a)] d\lambda \quad (6)$$

In the stationary case the heat equation for the silicon

$$c\rho b \frac{dT_p}{dt} = q_p \quad (7)$$

can be expressed as follows

$$\int_0^{\infty} \varepsilon_{SOI,\lambda}(\lambda, T_p) [e_{\lambda b}(\lambda, T_r) - e_{\lambda b}(\lambda, T_p)] d\lambda = \int_0^{\infty} \varepsilon_{back,\lambda}(\lambda, T_p) [e_{\lambda b}(\lambda, T_p) - e_{\lambda b}(\lambda, T_a)] d\lambda. \quad (8)$$

In accordance with eq.(8) the temperature of SOI Si wafer is defined by the temperature of the heater  $T_r$ , the absorber  $T_a$ , the functions of  $\varepsilon_{SOI,\lambda}(\lambda, T_p)$ ,  $\varepsilon_{back,\lambda}(\lambda, T_p)$  and also by the wafer parameters such as thickness, doping level and the roughness of its surfaces. The spectral emissivities for both surfaces of the wafer are simulated with the help of software called Rad-Pro [3,4] based on Microsoft Excel programming in the

heater temperature range from 300 K to 1500 K in increment of 10 K and in spectral range from 0,5  $\mu\text{m}$  to 20  $\mu\text{m}$  in increment of 0,05  $\mu\text{m}$ . Eq. (8) was done numerically. The obtained results are represented on fig. 1(a). As can be seen from the figure, the temperatures of the Si wafers with SOI structures doped by boron do not depend on the impurity concentration at the wafer temperature higher than 755 K (the curves are coincided). There is the temperature interval between 300 and 640 K at which the temperature of silicon wafer is higher the SOI (negative values of  $\Delta T_p$ ). The temperature of SOI is higher than Si in interval from 640K to 1200 K (positive values of  $\Delta T_p$ ). Maximum temperature difference  $\Delta T_p = 27$  K is achieved at silicon wafer temperature  $\sim 780$  K. For thorough understanding of the results obtained by numerical simulation the radiation system was modeled in gray body approximation by use of the Chrystiansen formula for the description of radiation exchange. (This approximation neglects spectral dependence of radiative characteristics). This model allows passing from numerical to analytical equation for radiance flux and approximating integral emissivities for working and back sides of SOI Si wafers. The obtained figure 1(b) has the same shape but the value meanings are different. The rapid thermal annealing requires exquisite control of wafer temperature. For example, dopant activation by RTA requires controlling diffusion to a 1% tolerance, thus causing control of a 1000 K temperature to better than  $\pm 1$  K [5]. The temperature difference of  $\sim 15$  K between Si and SOI Si wafer corresponds to half as large diffusion coefficient (see insert in fig.1(a)) by boron in silicon at the  $10^{18} \text{ cm}^{-3}$  boron concentration and the annealing temperature 1120  $^{\circ}\text{C}$ . Such an increasing of diffusion coefficient corresponds to the displacement of diffusion profile on  $\sim 7$  nm for anneal time 27 s [6]. It is a critical in forming of ultra-shallow p-n junctions. The necessity of using exact methods of estimation of wafer temperature is shown for SOI RTA process.

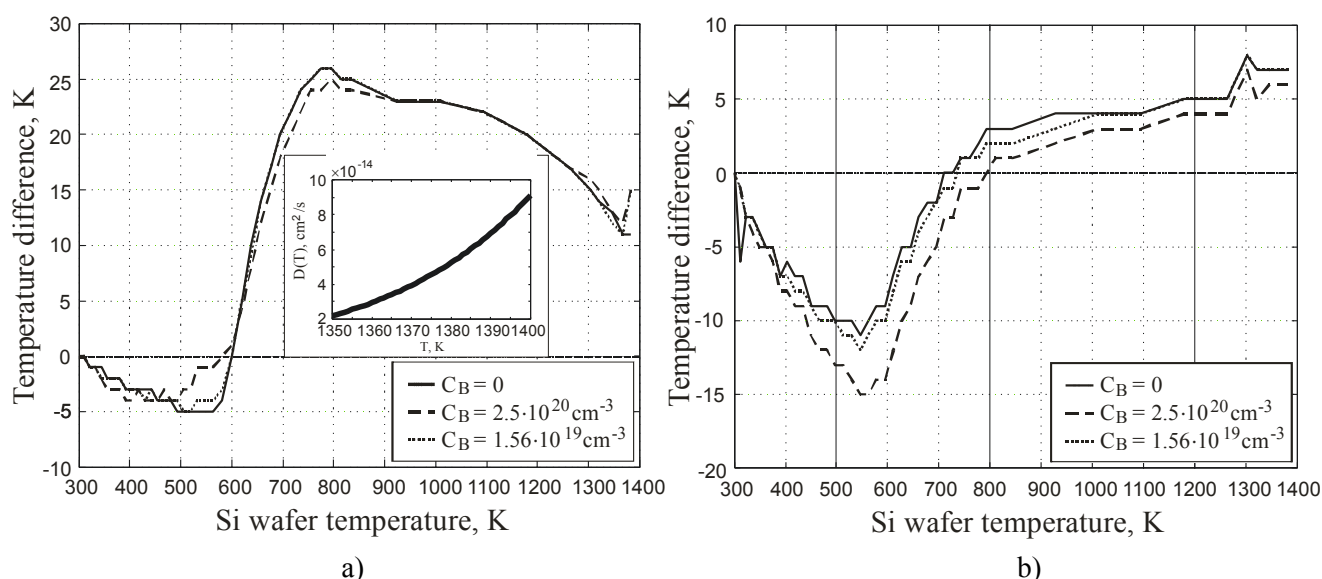


Fig.1. Temperature difference between SOI/Si and Si wafers (Si  $10^{15} \langle P \rangle \text{ cm}^{-3}$  700mkm; SOI/Si:  $\text{SiO}_2$ -135 nm, Si on  $\text{SiO}_2$  – 55nm  $10^{15} \langle P \rangle \text{ cm}^{-3}$ ) vs. Si temperature estimated by:

a) eq.(8) using the spectral dependence of emissivities; b) Chrystiansen's law using the gray body approximation.

1. Z.M.Zhang. *Nano/Microscale Heat Transfer*. McGraw-Hill, New York, 2007.
2. R.Siegel, J.R.Howell. *Thermal Radiation Heat Transfer*. Hemisphere, New York, 1981.
3. [www.me.gatech.edu/~zzhang](http://www.me.gatech.edu/~zzhang)
4. B.J.Lee,Z. M.Zhang, "Rad-Pro effective software for modeling radiative properties in rapid thermal processing". In *Proc. 13<sup>th</sup> IEEE Annu.Int.Conf.Adv.Thermal Processing of Semiconductors (RTP'2005)*. P.275-281. Santa Barbara. CA, October 4-7, 2005.
5. A.T.Fiory, "Recent Developments in Rapid Thermal Processing", JOM, p.1-26, June 2005.
6. V. Ovcharov, V. Rudakov, A. Kurennya, S. Simakin. "Diffusion simulation during RTA of plasma immersion ion implanted boron in SOI structure". In *Proc. International Conference "Modern problems in the physics of surfaces and nanostructures (ICMPSN2010)"*. Yaroslavl, June 8-10, 2010.

## Switching conductivity effect is promising direction of non-volatile memory devices creation

A.Berdnikov<sup>1</sup>, A.Popov<sup>1</sup>, V.Alekseev<sup>2</sup>, A.Perminov<sup>1,2</sup>

1. Yaroslavl Branch of the Institute of Physics and Technology, Russian Academy of Sciences, Yaroslavl, Russia.

2. Yaroslavl Demidov State University, Yaroslavl, Russia, E-mail: Avperminov@inbox.ru

Improvement of memory is one of the main factors in the development of information technology. The special importance has the development of fundamentally new types of memory. The success of technology of nonvolatile Flash memory has stimulated researches in the field of new physical principles of recording and storing information. Number of companies has started practical works in the area of the development of devices with different principles of information storage, because the existing memory devices (DRAM, Flash) are very close to the limit of scaling. One of the most promising effects allowing implementing the memory structure is the effect of conductivity switching under applied electric field. The idea to create a storage unit based on the change in conductivity was proposed nearly five decades ago, when the phenomenon of abrupt change in conductivity of chalcogenide glassy semiconductor was discovered.

One of the advantages of memory devices based on the effect of conductivity switching is that devices can use the topology type of cross-bar. It differs by the presence of two electrodes, whereas the majority of existing memory elements consists of three electrodes. As a result cross-bar topology reduced area needed for 1 bit memory cell.

Cross-bar structure consists of two perpendicular sets of parallel conductors, which are separate by a layer of material that has the effect of switching of conductivity. Structures, which can be switched from a conducting state to the non-conducting and vice versa [1], are obtained at the crossing points of the conductors. Simplicity of topology allows get dense packing elements and large capacity storage devices.

The effect of switching is abrupt and reversible transition the semiconductor from high-resistance state in low-resistivity state under an applied electric field. This effect is called monostable when to maintain the low-resistivity state should pass through the semiconductor is sufficiently large current, and bistable when the state structure remains after removing the voltage.

Effect of switching is also divided into unipolar and bipolar. Current research mainly interested by bipolar and bistable effects. Originally discovered in chalcogenide glassy semiconductors (CSM), a switching effect was later found in the structures based on solid electrolytes, oxides and fluorides of transition metals, silicon based materials and polymer compounds.

Current-voltage characteristics of such structures are identical, but there are few hypotheses, which explain the mechanism of the effect of the bipolar bistable switching conduction. They can be divided into three main categories: thermal, electronic and ionic, although there might be a combination of mechanisms that lead to the switching structures, for example thermo-electronic [2].

Thermal switching mechanism is most probable in the case of a unipolar switching. This switching mechanism is observed in the structure Pt/TiO<sub>2</sub>/P [3]. However, bipolar effect in the case of asymmetric Current-voltage characteristic can be similar phenomena.

Many different structures exhibit switching, corresponding to an ion effects, such as anionic or cationic migration through the dielectric. redox processes, induced by anion migration, often found in transition metal oxides [4].

Switching conductivity by the cation migration. The model of formation and rupture of metallic filament corresponds to this mechanism. Conduction switching by the cation migration occurs, for example in solid electrolytes, concluded between the electrochemically-active and inert electrodes [5]. Switching effect may be explained by structural changes in molecules in case of TiO<sub>2</sub>-based memory devices and devices with amorphous silicon (a-Si).

Electronic mechanism involves charge of structural inhomogeneities (quantum dots) and change the current flowing under the influence of an electric current. Such mechanisms are considered for switching structures based on organic materials [6].

Different effects of switching conductivity show identical current-voltage characteristics. We can supposed, that there is a general theory of these effects of switching. But unified theory of the switching effect isn't developed in detail currently. Most of the experimental facts can be consistently described in any of the models of the switching effect. However, the absence of an adequate model of the effect of switching the

conductivity prevents obtaining structures with optimal parameters and the introduction of mass-storage devices based on the effect of switching conduction in mass production. Therefore, investigation of mechanisms of conduction switching represents considerable practical interest.

We have studied this effect in MOS-like structures, based on nonstoichiometric silicon oxide with different nanoscale inclusions.

1. J. R. Heath, P. J. Kuekes, G. S. Snider, R. S. Williams, "A Defect-Tolerant Computer Architecture: Opportunities for Nanotechnology", *Science* 280, pp 1716–1721, 1998.
2. R. Waser, M. Aono, "Nanoionics-Based Resistive Switching Memories", *Nat. Mater.* 6, pp 833-840, 2007.
3. D.S. Jeong, H. Schroeder, R. Waser, "Coexistence of bipolar and unipolar resistive switching behaviors in a Pt/TiO<sub>2</sub>/Pt stack", *ESL* 10 pp 51-53, 2007.
4. Y. Ogimoto, Y. Tamia, M. Kawasaki, Y. Tokura, "Resistance switching memory device with a nanoscale confined current path", *Appl. Phys. Lett.* 90, 143515-1-3, 2007.
5. K. Terabe, T. Hasegawa, T. Nakayama, M. Aono, "Quantized conductance atomic switch", *Nature* 433 pp 47-50, 2005.
6. L.D. Bozano, B.W. Kean, M. Beinho, K.R. Carter, P.M. Rice, J.C. Scott, "Organic materials and thin-film structures for cross-point memory cells based on trapping in metallic nanoparticles", *Advanced Functional Materials, Adv. Funct. Mater.* 15 pp 1933-1939, 2005.

# Technology for obtaining nanocrystalline inclusions in the matrix $\text{SiO}_2$

A.A.Dedyukhin, V.F.Kobzev, P.N.Krylov, I.V.Fedotova  
Udmurt State University, 426036, Izhevsk, st. Universitetskaya, 1, ftt@uni.udm.ru

It is designed, manufactured and tested in thermal vacuum deposition process module for the magnetron sputtering "Cathode-1M" installation. The module allows making a single technological process sequence of alternating cycles of magnetron [1]. sputtering of a material (dielectric) and thermal deposition of another material.

Investigation of the samples showed a decrease of grain sizes in GaAs, obtained in  $\text{SiO}_2$  matrix by alternating repetitive cycles of thermal deposition of GaAs and magnetron sputtering  $\text{SiO}_2$ , as compared with films GaAs, obtained only through thermal spraying. Depending on the thickness ratio of layers of gallium arsenide and quartz in the structures appear rounded educations (Fig. 1). In the transmission spectra of these structures have the additional absorption in the wavelength range 700 - 800 nm (Fig. 2).

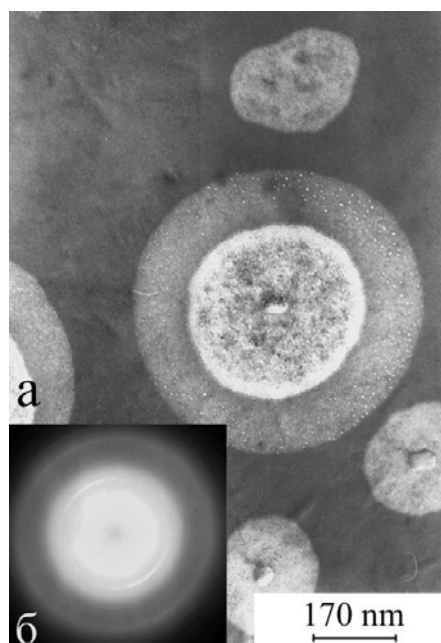


Fig. 1 Electron-microscope investigation of GaAs/ $\text{SiO}_2$  structures obtained in power discharge quartz evaporation 200 W: a – particle in matrix; б - electron diffraction pattern of round inclusion

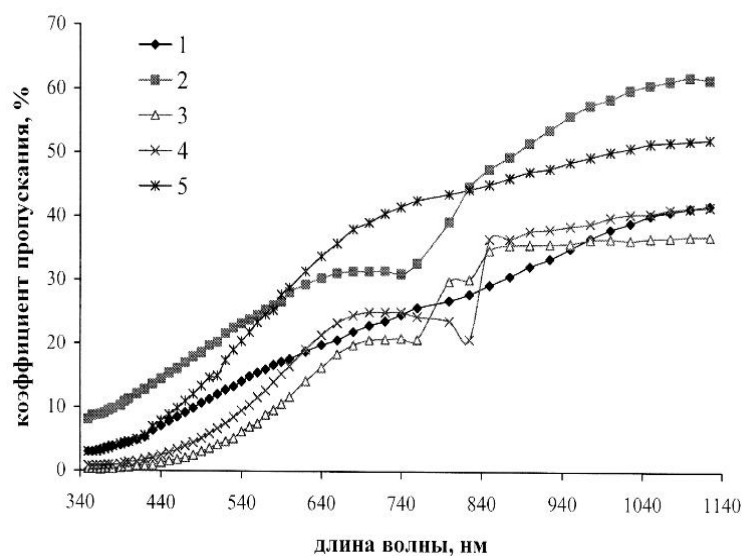


Fig. 2 Transmission spectrum of GaAs/ $\text{SiO}_2$  structures obtained in equal conditions of gallium arsenide evaporation but obtained in different power quartz evaporation: 1 – 100 W; 2 – 200 W; 3 – 300 W; 4 – 400 W; 5 – 500 W.

1. V.M. Vetochnik, A.A. Dedyukhin, P.N. Krylov, I.V. Fedotova, "Technological module of thermal evaporation for magnetron sputtering equipment "Cathod" ", Vacuum technique and Technology, 19, № 1, pp. 33 – 36, 2009.

# Study of the amorphization effects in silicon surface layer at PAI step for process of ultra shallow boron doping

V.Boyadzhi<sup>1,2</sup>, A.Starosek<sup>1,2</sup>, and K.Rudenko<sup>2</sup>

1. Institute of Physics and Technology, Russian Academy of Sciences, Moscow, Russia.

2. Moscow Institute of Physics and Technology, Dolgoprudny, Russia

Ultra shallow and high dose doping of the source/drain and extensions regions of CMOS devices made by ULSI technology are governed by scaling laws. The requirements on 32 nm node for parameters of this doping are following: the depth is less than 20 nm; the dopant concentration is order of solubility level at doping region, sharp impurity profile in the region of p-n junction; the silicon recess after implantation process should be less than 1 nm [1]. Nearest future of CMOS technology will results in more severe demands. Most difficulties are occurs with Boron ultra shallow doping due to known channeling effects and transient enhanced diffusion of small boron atoms in silicon lattice. From these reason the pre-amorphization of surface silicon layer is important procedure defining the following formation of implanted impurity profile and its behavior during post annealing process (RTA).

The ions Si<sup>+</sup>, Ar<sup>+</sup>, He<sup>+</sup> are conventional pre-amorphizing implants (PAI). We have revealed earlier [2] that He<sup>+</sup> as PAI atoms can substantially influence on the implanted boron behavior during RTA. The experiments with high dose ( $D \sim 2 \times 10^{15} \text{ cm}^{-2}$ ) BF<sub>2</sub><sup>+</sup> implantation (0.5 keV energy, plasma immersion mode) with He<sup>+</sup> pre-amorphization ( $E = 3 \text{ keV}$ ,  $D \sim 2 \times 10^{16} \text{ cm}^{-2}$ ) have shown abnormal evolution of boron profile tails in silicon (reverse and forward tail movement) during RTA (Fig.1). That effect didn't observed when ions Ar<sup>+</sup> were used as PAI.

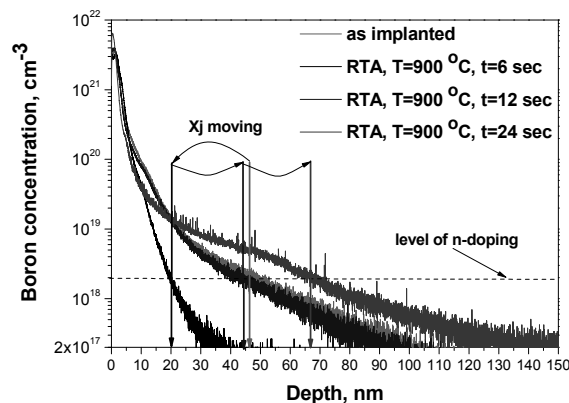


Fig.1. SIMS data for implanted Boron concentration profiles evolution in silicon during RTA. PAI step made by He ions.

We suggest such anomalous profile tail evolution is due to specific defects produced by He ions in silicon during pre-amorphization and their dynamics and interaction with Boron atoms under RTA.

Therefore current investigation is focused on the comparative study of amorphized silicon layers produced by different PAI – argon and helium ions. We've made Si samples with pre-amorphized layers implanted with ions ( $E = 0.5\text{-}3 \text{ keV}$ , exposure dose  $D \sim 2 \times 10^{16} \text{ cm}^{-2}$ ) in experimental plasma immersion ion implanter [2].

Using fast electron diffraction technique we've noticed that surface of Ar PAI sample has structure as conventional amorphous Si layer, and that surface layer in He PAI sample has lost near order in crystal lattice (Fig.2).

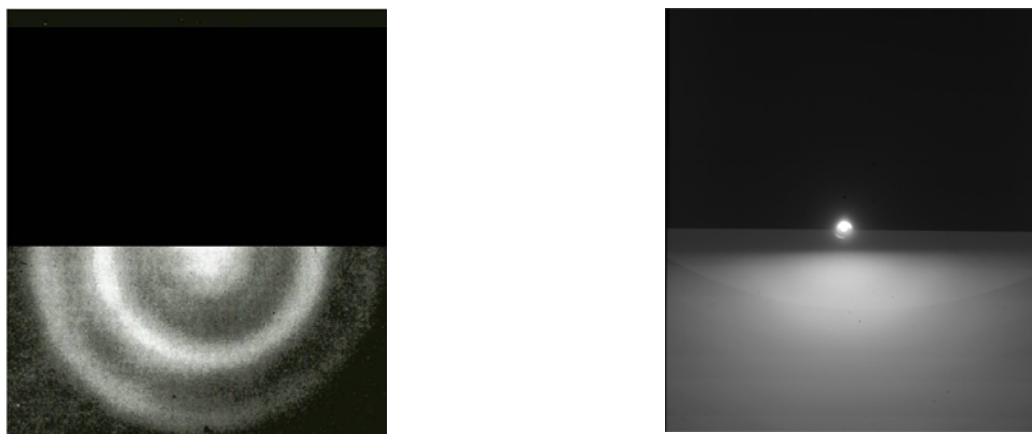


Fig. 2 Electron diffraction images from Ar(left) and He(right) amorphized samples.

Surface relief of He and Ar PAI samples were analyzed by optical white interference analyzer Zygo New View 5000 with vertical resolution  $\sim 1$  nm, by AFM, and by spectral ellipsometry.

We've found that properties of He and Ar PAI amorphous layers differs significantly depending on three main causes: peculiarities of phase transition in amorphous state, the mechanisms of defects formation in silicon crystal lattice in the EOR region, and physical sputtering. It was showed that changing in level for Ar PAI silicon surface was about 13-16 nm downward (Fig. 3, left) relatively to origin value due to sputtering and increasing the density of amorphous layer. In opposite case of He PAI the irradiated silicon surface was about 3-5 nm upward (Fig. 3, right). The last can be explained from the vacancy mechanism of silicon disordering and its final amorphization by light Helium atoms and due to the absence of physical sputtering.

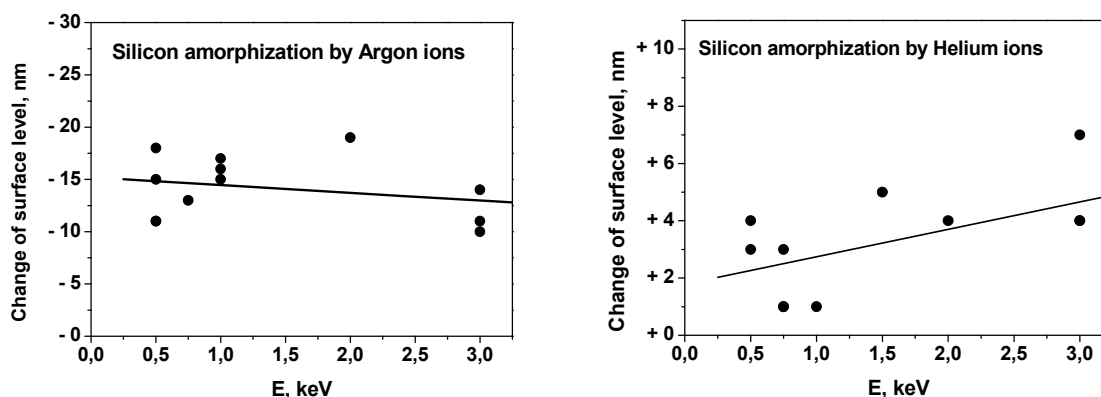


Fig. 3 Height step in Ar (left) and He (right) irradiated Si surface depending on ions energy.

Comparative ellipsometric study have revealed different optical properties and thicknesses for amorphized and disordered silicon layers prepared with Helium and Argon amorphization techniques. This investigation shows that He pre-amorphization of ultra thin silicon layers is preferable for ultra-shallow Boron implantation due to preventing of silicon recess and possibilities for following implanted profile engineering.

## References

1. International Technology Roadmap for Semiconductors. 2008 Update Edition.
2. V. Lukichev, K. Rudenko, A. Orlikovsky et al. Boron profile sharpening in ultra-shallow  $p^+-n$  junction produced by plasma immersion ion implantation from  $BF_3$  plasma. Proc. of 17<sup>th</sup> Intern. Conference on Ion Implantation Technol. (IIT-2008), Monterey, California, USA, June 8-13, (2008).
3. A. Orlikovsky, K. Rudenko, S. Averkin. High Energy Chemistry, Vol. 40, No. 3, (2006).

# Photoluminescence and photoexcitation transport in silicon-rich nitride films with *a*-Si nanoclusters

V.Stuchinsky<sup>1</sup>, T.Korchagina<sup>1</sup>, V.Volodin<sup>1,2</sup>, A.Popov<sup>3</sup>, M.Vergnat<sup>4</sup>

1. Institute of Semiconductor Physics, Russian Academy of Sciences, Novosibirsk, Russia, E-mail address: stuchin@sibmail.ru. 2. Novosibirsk State University, Novosibirsk, Russia. 3. Yaroslavl Branch of the Institute of Physics and Technology, Russian Academy of Sciences, Yaroslavl, Russia. 4. Nancy-Université, Vandœuvre lès Nancy, France

In the present study, we examined the temperature dependence of the photoluminescence (PL) intensity  $I$  in silicon-rich nitride ( $\text{Si}_{3+x}\text{N}_4\text{:H}$ ) films deposited onto Si substrates from a flow of silane-ammonia mixture diluted with nitrogen. The films were of different stoichiometries ( $x=0.08\text{--}3.7$ ), and they were grown at two different temperatures,  $T=100$  and  $380^\circ\text{C}$  (sample series 611-615 and 621-625, see Table 1). Different values of  $x$  were achieved by varying the silane/ammonia flow ratio in the PECVD process. According to Raman scattering data, the films contained amorphous Si nanoclusters (*a*-Si nc's). With increasing  $x$ , the PL spectra taken from the samples at different temperatures in the range from 80 to 350 K exhibited a red shift of PL maxima, this shift being indicative of an increase of nc sizes with increasing the amount of excess silicon in the samples.

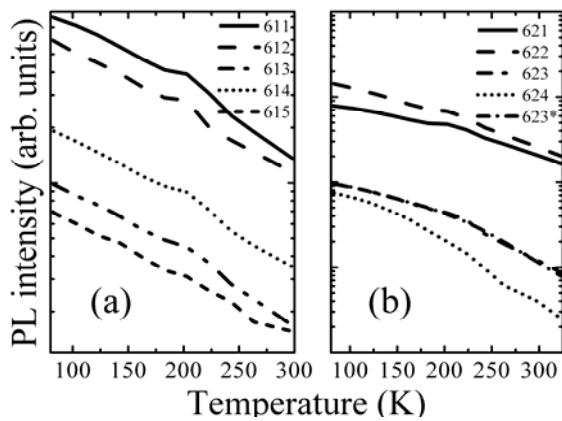


Fig. 1. Maximum PL intensity versus temperature in the spectra of samples grown at temperatures  $T=100^\circ\text{C}$  (a) and  $380^\circ\text{C}$  (b). The fitting quality ensured by the developed model is illustrated by curve 623\*, which was calculated by formula (1) to fit the experimental data for sample 623.

The curves of  $I(T)$  plotted in semi-log scale displayed a distinct change of their slope at  $T^*\approx 200$  K, thus suggesting that two different nonradiative processes were involved in the PL thermal quenching phenomenon (Fig. 1). By fitting our  $I$ -vs- $T$  data with the expression

$$I \propto \frac{1}{1 + f_1 \cdot e_r^{-1}(T) \cdot \exp(-\frac{E_{a1}}{kT}) + f_2 \cdot e_r^{-1}(T) \cdot \exp(-\frac{E_{a2}}{kT})} \quad (1)$$

in which the Calcott formula for the temperature-dependent radiative recombination rate  $e_r(T)$  was used [1], we were able to evaluate the thermal activation energies  $E_{ai}$  and the frequency factors  $f_i$  ( $i=1, 2$ ) of the two processes. Since the activation energy of the process which accelerated the rate of PL thermal quenching at  $T > 200$  K,  $E_{a2} \approx 0.13\text{--}0.15$  eV, was close to the binding energy of a Si nanoparticle confined exciton, this process was identified as the thermally stimulated exciton dissociation proceeding in the system when the most mobile carrier (hole) hopped into a neighboring *a*-Si nc to subsequently migrate into more remote *a*-Si particles. The activation energy of this process was interpreted as the polarization energy due to partial exciton dissociation. The low-temperature process with relatively low thermal activation energy,  $E_{a1} \approx 0.03\text{--}0.04$  eV, was identified as exciton recombination at nonradiative sites in the system, mediated by tunneling migration of excitons as complex particles without (or with negligible) electrical polarization. The proposed identification of the two nonradiative processes was supported by an observed correlation between the ratio of the frequency factors of the two processes,  $f_2/f_1$ , and the value of  $E_{a2}$  in individual samples, and also by the fact that quite reasonable values of typical tunneling distances  $R_t$  in the examined films (in the nanometer range) could be extracted from this identification. In our model, the ratio  $f_2/f_1$  is assumed to be defined by the tunneling rates of holes and excitons making hops between neighboring *a*-Si clusters:

remote *a*-Si particles. The activation energy of this process was interpreted as the polarization energy due to partial exciton dissociation. The low-temperature process with relatively low thermal activation energy,  $E_{a1} \approx 0.03\text{--}0.04$  eV, was identified as exciton recombination at nonradiative sites in the system, mediated by tunneling migration of excitons as complex particles without (or with negligible) electrical polarization. The proposed identification of the two nonradiative processes was supported by an observed correlation between the ratio of the frequency factors of the two processes,  $f_2/f_1$ , and the value of  $E_{a2}$  in individual samples, and also by the fact that quite reasonable values of typical tunneling distances  $R_t$  in the examined films (in the nanometer range) could be extracted from this identification. In our model, the ratio  $f_2/f_1$  is assumed to be defined by the tunneling rates of holes and excitons making hops between neighboring *a*-Si clusters:

**Table 1.** Specifications, growth conditions, thickness  $d$ , and stoichiometry parameter  $x$  of examined  $\text{Si}_{3+x}\text{N}_4$  films.

Sample	$T, ^\circ\text{C}$	$\text{NH}_3/\text{SiH}_4$ flow ratio	$d_{\text{film}},$ nm	$x$
611	100	5	~240	~0.08
612	100	2.6	~400	~0.33
613	100	1.5	~400	~1.0
614	100	0.9	~450	~2.7
615	100	0.5	~450	~3.7
621	380	5	~280	~0.08
622	380	2.6	~430	~0.33
623	380	1.5	~430	~1.0
624	380	0.9	~510	~2.7
625	380	0.5	~510	~3.7



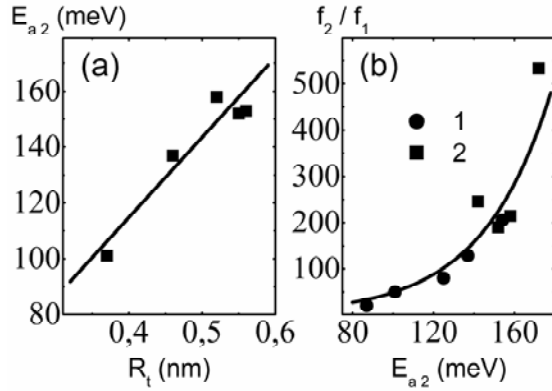


Fig. 2. a) The activation energy  $E_{a2}$  versus the tunneling distance  $R_t$ . The values of  $R_t$  are values obtained assuming  $m/n=1$ . b) The ratio  $f_2/f_1$  versus the energy  $E_{a2}$ . 1 and 2 - data for sample series 611-615 and 621-625, respectively. The curve is the dependence calculated by the developed model with  $m/n=1$ ,  $R_{nc}=1.4$  nm, and with PL emission energy  $E_{PL}=2.52$  eV.

quite realistic, falling into the range from 0.3 to 1.7 nm. As it could be expected, the experimental values of  $E_{a2}$ , if plotted against  $R_t$ , varied in proportion to  $R_t$  (see Fig. 2a). This function, available (for  $m/n=1$ ) in the interval  $0.37 \text{ nm} < R_t < 0.57 \text{ nm}$  could be fitted with a straight line, going through origin, whose slope gave a proportionality-factor value  $2.87 \cdot 10^6 \text{ eV/cm}$  comparing well (within a factor of ten) to the coefficient  $(4q/\pi\epsilon\epsilon_0 R_{nc}^2) \approx 1.6 \cdot 10^7 \text{ eV/cm}$  ( $R_{nc}$  is the nc size) that appears in a simple electrostatic formula relating the electrostatic energy in a plane capacitor formed by two circular capacitor plates of diameter  $R_{nc}$  charged with charges  $\pm q$ . Since the polarization energy  $E_{pol}$  between the parting hole and electron grew in value with increasing the electron-hole separation, it could be expected, in view of the strong dependence of the right-hand side of (2) on  $R_t$ , that some correlation could also be traced between the experimental values of  $f_2/f_1$  and  $E_{a2}$ . As it is demonstrated by Fig. 2b, such a correlation is indeed exhibited by our experimental data. The curve in Fig. 3b was calculated by formula (2) with  $m/n=1$ ,  $R_t[\text{cm}] = E_{pol}[\text{eV}]/2.87 \cdot 10^6$  and with the values of  $R_{nc}$  and  $E_{PL}$  fixed to 1.4 nm and 2.52 eV, respectively. [The PL emission energy  $E_{PL}$  in our calculations was used to determine the value of  $R_{nc}$  (see [2]).] The deviation of the experimental points from the calculated curve is presumably a result of the difference between the actual values of  $m/n$ ,  $R_{nc}$  and  $E_{PL}$  in individual samples and the (fixed) values of  $m/n$ ,  $R_{nc}$  and  $E_{PL}$  used in calculating the curve, and also from disregard of resonance phenomena and finite-size effects for tunneling excitons. Although the values of  $f_2$  and  $f_1$  (and also  $f_2/f_1$ ) in the examined samples showed no regular tendency, or a universal behavior common for both sample series, if considered as function of  $x$ , a clear correlation between the experimental values of  $f_2/f_1$  and  $E_{a2}$  in all samples, quite consistent with the adopted model, is evident. This correlation provides further impressive support for the proposed interpretation of our experimental data.

Thus, the data obtained in the present study strongly suggest that it is the quantum-confinement rather than band-tail PL model [2, 3] that should to be accepted for  $a$ -Si nc's embedded within silicon-rich nitride films grown by the present PECVD process. If considered in a more general context, these data provide a clear picture that shows in which form photogenerated electrons and holes exist and migrate in nanoscale systems formed by 'weakly amorphous' Si nanoparticles hosted in a wide-gap dielectric matrix. Generally, the transport processes of optically generated excitations in such systems involve nondissociative and dissociative migration of excitons to nonradiative recombination sites.

$$\frac{f_2}{f_1} \approx \frac{n^{-1} \cdot v_h \cdot \exp \left[ -\frac{2}{\hbar} \cdot \int_0^{R_t} \sqrt{2 \cdot m_h^{Si_3N_4} (V_b^h - E_{a2} + E_{pol} \frac{x}{R_t})} dx \right]}{m^{-1} \cdot v_{ex} \cdot \exp \left[ -\frac{2}{\hbar} \cdot \sqrt{2 \cdot (m_h^{Si_3N_4} + m_e^{Si_3N_4}) \cdot V_b^{ex}} \cdot R_t \right]} \quad (2)$$

In (2),  $v_h$  and  $v_{ex}$  are the characteristic frequencies of the internal motion of the thermally excited hole and ground-state exciton inside  $a$ -Si nc's;  $n$  is the mean number of hops into neighboring  $a$ -Si nc's the holes makes prior to the complete dissociation of exciton;  $m$  is the mean number of hops the tunneling exciton makes prior to its nonradiative recombination in one of nearby  $a$ -Si nc's;  $E_{pol} \approx E_{a2}$  is the electrical polarization energy;  $R_t$  is the width of the tunnel barrier, or distance, between neighboring nc's; and  $V_b^h$  and  $V_b^{ex}$  are the tunnel barriers for holes and excitons in zero electric field. The right-hand side of (2) was a sharply increasing function of  $R_t$ ; this allowed us, with some values of  $n$  and  $m$  assumed, to evaluate the typical distance between neighboring  $a$ -Si nc's in our films. The obtained values of  $R_t$  proved to be

1. P.D.J. Calcott, K.J. Nash, L.T. Canham, M.J. Kane, and D. Brumhead, "Identification of radiative transitions in highly porous silicon", J. Phys.: Condens. Matter, **5**, pp.L91-L98, 1993.
2. Nae-Man Park, Chel-Jong Choi, Tae-Yeon Seong, and Seong-Ju Park, "Quantum confinement in amorphous silicon quantum dots embedded in silicon nitride", Phys. Rev. Lett., **86**, pp.1355-1357, 2001.
3. M.J. Estes and G. Modell, "Luminescence from amorphous silicon nanostructures", Phys. Rev. B, **54**, pp.14633-14642, 1996.

# Magneto-optical investigation of exchange interacting in Py/Cu/Co structure

E.Fedorov<sup>1</sup>, V.Naumov<sup>2</sup>, V.Paporkov<sup>1</sup>, N.Zvezdin<sup>1</sup>

1. Yaroslavl Demidov State University, Yaroslavl, Russia, pva@uniyar.ac.ru. 2. Yaroslavl Branch of the Institute of Physics and Technology, Russian Academy of Sciences, Yaroslavl, Russia, vvnau@rambler.ru

Hysteresis loops were measured using transverse magneto-optic Kerr effect for some multilayer films of permalloy /copper/cobalt. Sign and value of exchange interaction magnetic field were defined.

There is exchange and magnetostatic (magnetodipole) interaction between layers in ferromagnetic sandwiches. This interaction may be exhibited at biased hysteresis loops (HL) of layers. Measuring of these loops usually implements using magneto-optical methods [1, 2, 3] and from field dependence of magnetoresistance [4] or by superconducting quantum interference device [5]. Meanwhile only the value of interlayer exchange field is identified, but the sign of exchange field is not. The last one is very important because an exchange integral may oscillate, while distance between layers increases [2, 6, 7, 8].

This paper represents the measuring technique allowing to define a sign and value of exchange interaction. Multilayers with surface area  $S = 10 \times 10 \text{ mm}^2$  and different coercive force  $H_c$  of layers were used as samples in present paper:

- 1) Py(5nm)-Cu(3nm)-Co(3.5nm)-SiO<sub>2</sub>(200nm)-Si,
- 2) Co(3.5nm)-Cu(3nm)-Py(5nm)-SiO<sub>2</sub>(200nm)-Si.

To determine the influence of boundary conditions on value  $H_c$ , samples tested were fabricated with different sequence order of magnetic layers. Multilayers were grown using magnetron sputtering with substrate bias, magnetic field of 120 Oe was directed along sample to form an easy magnetization axis.

Hysteresis loops were measured along easy magnetization axis in alternative magnetic field with 30 Hz frequency. In Fig. 1 HL are represented for magnetization reversal of both magnetic layers.

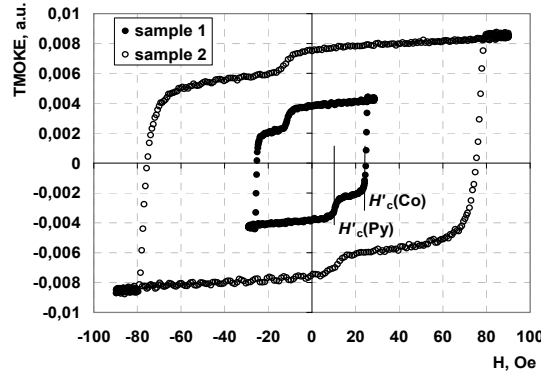


Fig. 1. Magnetization reversal of both magnetic layers in multilayer films.

Fig.1 shows that Co and Py layers magnetization reversal appears at different magnetic fields. This result may be used to measure only Py hysteresis loop. It was found that loops are shifted relative to origin of coordinates. Multiple repetition of these measurements shows that the value of this bias field and its sign are different every time. That result can be explained by high-coercivity Co layer random magnetization and its partial demagnetizing with the decrease of alternating magnetic field during measuring of Py layer minor hysteresis loop. To exclude this effect and to form Co layer fixed magnetic state the direct magnetic field was turned on in addition. It allowed to switch magnetization Py layer, keeping Co layer magnetic state. The

results of these measurements for  $H_0 > 0$  are represented in fig 2. Figure 2 displays that Py hysteresis loops are shifted along opposite site of  $H_0$ . That can be explained in the following way. Whereas film thicknesses are much less than their lateral dimension, we may consider magnetodipole interaction of uniformly magnetized layers as negligible. Thus interlayer field will be only exchangeable. With positive interlayer exchange the layers tends to keep unidirectional magnetization (ferromagnetic interlayer ordering) and with

negative the magnetization is opposite (antiferromagnetic (AF) ordering). Therefore with Co layer positive magnetization in the first case Py layer HL should shift to the left by  $H_{ex}$ , notably,  $H_{c1} = -H_c(\text{Py}) - H_{ex}$ ,  $H_{c2} = H_c(\text{Py}) - H_{ex}$ , where  $H_c(\text{Py})$

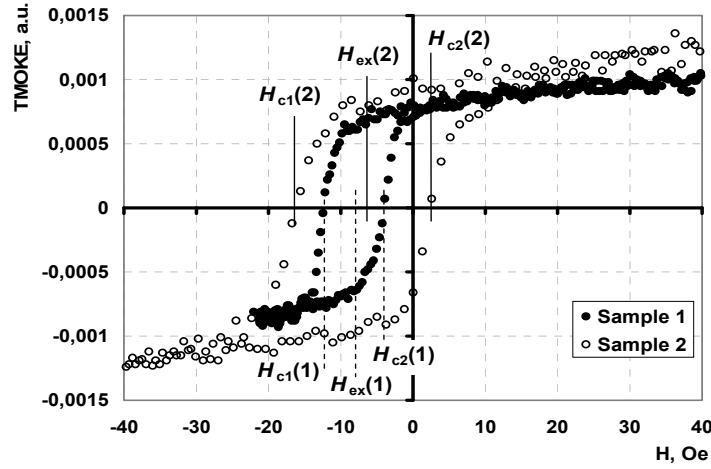


Fig. 2. Py layer magnetization reversal HL for samples №1 and №2 with additional direct magnetic field  $H_0 > 0$  ( $H_0 = 17$  Oe for sample №1 and 45 Oe for sample №2).

Py layer coercive force without interaction with Co layer,  $H_{ex}$  – interlayer exchange field ( $H_{ex} > 0$ ). Meanwhile coercive force of only rising branch of HL is changed. In second case Py layer shift should move to the right (only descending branch of HL shifts,  $H_{ex} < 0$ ). The width of displaced Py layer HL should coincide with the width of HL without interaction with Co layer. It corresponds to Fig. 2 results. Thus, in our case interlayer interaction is positive.

With symmetrical magnetization reversal of both layers their coercive forces  $H'_c$  should be determined as  $H'_c(\text{Py}) = H_c(\text{Py}) + H_{ex}$ ,  $H'_c(\text{Co}) = H_c(\text{Co}) - H_{ex}$ , where  $H_c(\text{Co})$  – Co layer coercive force without interaction with Py  $H_c$  Py layer increases and  $H_c$  Co layer decreases for  $H_{ex} > 0$ .

If only  $H_c$  of soft magnetic material (Py in our case) were equal to 0 then with positive exchange interaction would be  $H'_{c1}(\text{Py}) = -H_{ex} < 0$ ,  $H'_{c2}(\text{Py}) = H_{ex} > 0$ . With negative exchange interaction or strong magnetodipole interaction  $H'_{c1}(\text{Py}) > 0$ ,  $H'_{c2}(\text{Py}) < 0$ . It means that in the case of Co and Py symmetrical magnetization reversal the rising branch of Co layer HL and the descending branch of Py layer HL lie in the positive field ( $H'_{c2}(\text{Co}) > 0$ ,  $H'_{c1}(\text{Py}) > 0$ ) even if  $H_c \neq 0$  the interlayer ordering is AF. These loops are presented in articles [3, 5].

In these films  $H_c$  values depend on layer sequence ordering in samples. However,  $H_{ex}$  values ( $H_{ex} = 8.2$  Oe for sample №1,  $H_{ex} = 9.2$  Oe for sample №2) are insignificantly distinguished.

1. Z.Q. Qui, J. Pearson, S.D. Barder, Phys. Rev. B **46**, 13, pp.8659-8662, 1992.
2. M.T. Johnson, S.T. Purcell, N.W.E. McGee, R. Coehoorn, J. aan de Stegge, W. Hoving, Phys. Rev. Lett. **68**, 17, pp.2688-2691, 1992.
3. M.T. Johnson, R. Coehoorn, J.J. de Vries, N.W.E. McGee, J. aan de Stegge, P.J.H. Bloemen, Phys. Rev. Lett. **69**, 6, pp.969-972, 1992.
4. Peter A. Grunberg, Rev. Mod. Phys. **80**, pp.1531-1540.
5. Z.Y. Liu, S. Adenwalla, Phys. Rev. Lett. **91**, 3, pp.1-4, 2003.
6. J. Mathon, M. Villeret, R.B. Muniz, J. d'Albuquerque e Castro, D.M. Edwards, Phys. Rev. Lett. **74**, 18, pp.3696-3699, 1995.
7. P. Bruno, C. Chappert, Phys. Rev. Lett. **67**, 12, pp.1602-1605, 1991.
8. P. Bruno, J. App. Phys. **76**, 10 pp.6972-6976, 1994.

# Micromagnetic simulations of spin-valve structure

O.S.Trushin<sup>1</sup>, N.Barabanova<sup>2</sup>, V.P.Alexeev<sup>2</sup>

1. Yaroslavl Branch of the Institute of Physics and Technology, Russian Academy of Sciences, Yaroslavl, Russia, oleg\_trushin@lenta.ru. 2. Department of Physics, Yaroslavl Demidov State University, Yaroslavl, Russia

Magnetic field sensors based on Giant Magnetic Resistivity (GMR) effect find wide range of applications in modern technology[1]. High sensitivity at low fields and low cost make these sensors very competitive at a market. The most popular design of these sensors based on spin-valve structures. Such structure consists of three thin film layers of magnetic and non-magnetic materials [2]. Very important problem in designing GMR sensors is the optimization of spin-valve structure with the purpose to improve its functional characteristics. There were many different variants of spin-valve structures discussed in modern literature [1]. Computer simulations using micromagnetic modeling plays an important role in a search of optimal layer thicknesses and composition.

In this work we are using micromagnetic simulations to study magnetic reversal of spin-valve structure. The model system consists of 3 layers: free layer – Py ( $\text{Ni}_{80}\text{Fe}_{20}$  - 3 nm), spacer – Cu (3 nm), fixed layer – Py( $\text{Ni}_{80}\text{Fe}_{20}$  - 3nm) with exchange bias due to contact to  $\text{Fe}_{50}\text{Mn}_{50}$  antiferromagnetic layer. Presence of antiferromagnetic layer is simulated by permanent external filed (500 Oe) acting on Py fixed layer. Sensor element has rectangular shape with fixed length (long side) equal to 500 nm and width (short side) equal to 250 nm.

We used OOMMF code [3] for these simulations. It became very popular tool in micromagnetic studies. We have already tested this program before for single layer Py nanostructure [4].

Typical magnetization reversal curve obtained for three layer spin-valve sensor element with exchange bias is shown in Fig.1. Two loops structure corresponds to magnetic reversal in two magnetic layers (free layer at low magnitude of external field and fixed layer at large values of external filed).

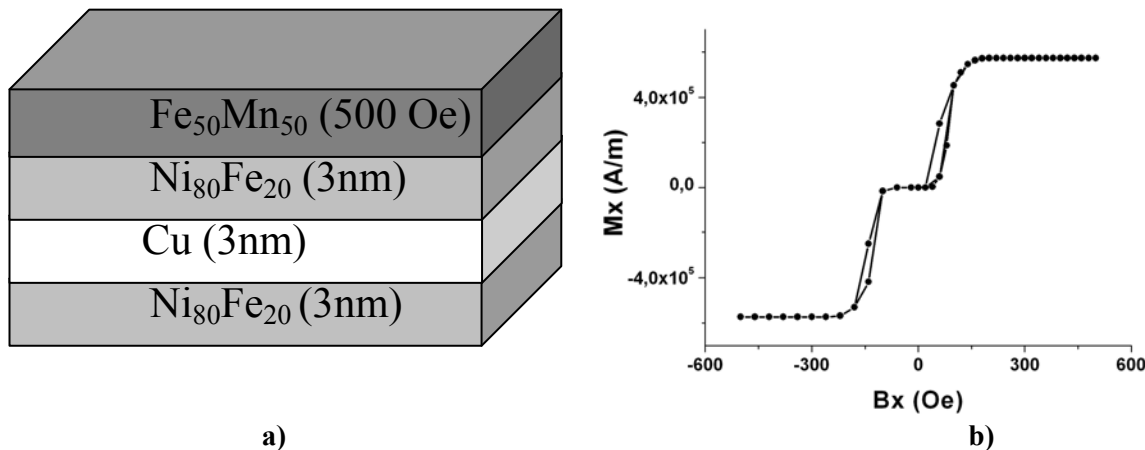


Fig.1. a)Spin-valve structure used in the modeling, b)Magnetization reversal curve calculated with OOMMF package for Py/Cu/Py/FeMn spinvalve sensor with lateral dimensions: width 250 nm, length 500 nm.

In conclusion we performed micromagnetic simulation of spin-valve structure with exchange bias. As the result we have obtained hysteresis loop which agrees well with available experimental data.

1. S. Tumanski *Thin film magnetoresistive sensors*, IOP publishing Ltd., Bristol, 2001.
2. R. Coehorn “Giant magnetoresistance and magnetic interactions in exchange-biased spin-valves”, in *Handbook of magnetic materials*, volume 15, Elsevier Science, Amsterdam, 2003.
3. M.J. Donahue and D.G. Porter, “OOMMF User's Guide, Version 1.0”, Interagency Report NISTIR 6376, National Institute of Standards and Technology, Gaithersburg, MD, 1999.
4. O. Trushin, N. Barabanova, and V.P. Alekseev, “Study of magnetic characteristics of permalloy nanostructures by micromagnetic modeling”, *Russian Microelectronics*, 38, pp. 198, 2009

# Influence of filler size on the mechanical failure of a polymer nanocomposite

A.Kutvonen, G.Rossi, T.Ala-Nissilä

*Department of Applied Physics, Aalto University School of Science and Technology, P.O. Box 11000 FI-00076 Aalto, Finland*

Nanoparticles are known to influence the mechanical properties of glassy polymer materials. Applications range from automotive, mobile phones, coating technologies to membranes, fuel cells, semiconductor technologies. In most cases, the dispersion of nanoparticles into polymer resins enhances the mechanical strength of the polymeric material [1-3]. Still, open questions concern the optimization of parameters such as filler-polymer interaction, filler size, concentration and shape.

In this work we use Molecular Dynamics (MD) to simulate a bead-spring polymer system where colloidal nanoparticles are added to form a nanocomposite. The melt is confined between two sticky walls, and equilibrated well above its glass transition temperature. Nonequilibrium MD is then used to simulate the stretching of the polymer system, by pulling apart the sticky walls along their normal direction. Periodic boundary conditions are applied in the other two directions.

The ability of the nanoparticles to increase the work to failure is studied by varying the size of the nanoparticles and keeping the total loading of nanoparticles constant and close to typical experimental values. Smaller nanoparticles are noticed to increase the work to failure. Void formation in the polymer melt is also studied and compared to stress as a function of wall displacement.



A snapshot of the polymer nanocomposite (red filler, grey polymer chains) during fast pulling of the sticky walls.

## References

1. D. Gersappe, "Molecular Mechanisms of Failure in Polymer Nanocomposites", *Phys. Rev. Lett.* 89, 058301, 2002
2. A. Tuteja, P. M. Duxbury, and M. E. Mackay, "Multifunctional Nanocomposites with Reduced Viscosity", *Macromolecules*, 40, pp. 9427-9434, 2007
3. H. Yagyu, T. Utsumi, "Coarse-grained molecular dynamics simulations of nanofilled crosslinked rubber", *Comp. Mater. Sci.* 46, pp 286-292, 2009

## **Eighth order fitting method for the phase field crystal model**

A.Jaatinen<sup>1,2</sup>, C.V.Achim<sup>1</sup>, T.Ala-Nissilä<sup>1</sup>, K.R.Elder<sup>3</sup>

*1. Department of Applied Physics, Aalto University School of Science and Technology, P.O. Box 11000, FI-00076 Aalto, Finland. 2. Department of Materials Science and Engineering, Aalto University School of Science and Technology, P.O. Box 16200, FI-00076 Aalto, Finland. 3. Department of Physics, Oakland University, Rochester, MI, 48309-4487*

Phase field crystal (PFC) model is a continuum field method for modelling materials science phenomena that takes place on diffusive time scale and atomic length scale. One of the challenges to these models has been incorporating the relevant physical properties of the material under study. We have risen to this challenge by presenting an eighth order fitting method (EOF) that enables us to incorporate the most relevant bulk and surface properties of body-centered cubic metals near their melting point in the PFC model[1]. The EOF-PFC model is applied to study symmetrically tilted grain boundaries of iron, and the results agree relatively well with previously published experimental and molecular dynamics simulation results.

1. A. Jaatinen et al., Phys. Rev. B 80, 031602 (2009)

# Path integral hyperdynamics for systems with internal degrees of freedom – Kramers escape problem for polymers

T.Ikonen<sup>1</sup>, J.Shin<sup>2</sup>, M.Khandkar<sup>1</sup>, T.Ala-Nissilä<sup>1,3</sup>, S.-C.Ying<sup>3</sup>, W.Sung<sup>2</sup>

*1. Aalto University School of Science and Technology, Espoo, Finland, timo.ikonen@tkk.fi. 2. Pohang University of Science and Technology, Pohang, Republic of Korea. 3. Brown University, Providence, Rhode Island, USA*

Many phenomena in, e.g., physics, chemistry and biology can be described by Brownian motion of a particle in an external potential. Often the key task in such a model is to solve the crossing rate of the particle across the barrier. Typically the rate is very small, making the numerical modeling of the system challenging. It is, however, possible to artificially accelerate the dynamics of the system using hyperdynamics, making the evaluation of rare event probabilities feasible.

Until very recently, it was not possible to apply hyperdynamics methods to entropy dominated activation barriers. In 2007, however, a novel path integral hyperdynamics (PIHD) method was introduced [1]. The method is based on a functional integral form of the Langevin equation, giving an analytical formula for correcting the accelerated dynamics of the system. With this method the modeling of systems with entropic activation barriers – polymer escape in particular – is possible.

Here, we study the dynamics of flexible, semiflexible and self-avoiding polymer chains under the Kramers metastable potential. Due to thermal noise the polymers, initially in the metastable well, can cross the potential barrier, but these events are rare at low temperatures. To speed up the slow rate processes in computer simulations we employ the hyperdynamics method using the path-integral representation of the relevant Langevin dynamics [1]. In this study, we extend the method for many-particle systems with internal degrees of freedom, such as the polymer chain.

We study the regime where the well size is comparable to chain length. We find that the flexible, semi-flexible and self-avoiding chains exhibit qualitatively different behavior. For the flexible chain, the crossing rate decreases monotonically with the polymer length ( $L$ ), while for the semi-flexible chain the rate saturates at a level that depends on the chain stiffness. For the self-avoiding chain, on the other hand, the rate varies non-monotonically with  $L$ . For  $L$  less than  $L_m$ , the rate decreases as  $L$  increases, while for  $L > L_m$ , the rate increases with  $L$ . We attribute this behavior to the coil-to-stretch transition of the chain and the confinement of the self-avoiding chain in the potential well, which both lower the effective free energy barrier and enhance the crossing rate. This effect can be instrumental in efficient separation of biopolymers.

1. L. Y. Chen and N. J. M Horing, “An exact formulation of hyperdynamics simulations”, J. Chem. Phys., 126, pp.224103-6, 2007.

# **A data bank approach to multiscale modeling of microstructure formation in polymer casting**

T.Pitkänen, M.Majaniemi, T.Ala-Nissilä

*Department of Applied Physics, COMP center of excellence, Aalto University School of Science and Technology,  
P.O. Box 11100, FI-00076 Aalto, Espoo, Finland, timo.pitkanen@tkk.fi*

A data bank approach to multi-scale modelling of polymer solidification under flow and holding conditions is presented with applications to injection molding. The solidification of supersaturated polymer melt can be described via the time-dependent Ginzburg-Landau formalism. A phase field model called Model C under the classification of Hohenberg and Halperin [1] is applied in the present work.

The latent heat of solidification, which acts as an input parameter for large scale simulations, is determined as a function of different process dependent parameters such as the flow speed, supersaturation and geometric properties including the seed density of emerging spherulitic microstructures. Supersaturation and flow velocities are obtained from the larger scale simulation code as input values. The released latent heat can be obtained from the pre-computed data bank as function of the supersaturation and flow velocity thereby offering a possibility to circumvent the spatial and temporal coarse-graining problem associated with large scale simulations.

The results [2] demonstrate the plausibility of the data bank approach to multi-scale modelling of polymer solidification using 2D phase field simulations. It is noted that increasing seed density at constant supersaturation causes a collapse of the time dependent latent heat production onto a single master curve thereby making the velocity a redundant parameter at high enough densities where sufficient self-averaging takes place. These types of observations can be used to simplify the parametrisation of the data bank.

1. Theory of dynamic critical phenomena, Hohenberg, P. C. and Halperin, B. I., Reviews of Modern Physics, 49 No. 3, 1977
2. Multiscale Modelling of Microstructure Formation in Polymer Casting, T. Pitkänen, S. Majaniemi and T.Ala-Nissilä, accepted to be published in Technische Mechanik in 2010



## Cutting ice: regelation at the nanoscale

V.Heinonen<sup>1</sup>, T.Hynninen<sup>2</sup>, C.L.Dias<sup>3</sup>, T.Ala-Nissilä<sup>1</sup>, A.S.Foster<sup>2</sup> and M.Karttunen<sup>3</sup>

1. Department of Applied Physics, Aalto University School of Science and Technology, P.O.B. 11000, FI-00076 Aalto, Finland, E-mail: vili.heinonen@tkk.fi. 2. Department of Physics, Tampere University of Technology. 3. Department of Applied Mathematics, the University of Western Ontario

Regelation, i.e. the melting of a substance under pressure, is an almost unique property of water and plays an important role in multiple different phenomena of nature. To properly understand regelation it is important to study the microscopic behaviour of water. In this work we present a microscopic model for studying the dynamics of a nanowire cutting through ice. A novel Mercedes-Benz model was used to perform a Molecular Dynamics simulation of the motion of the wire. The motion of the wire can be divided into three different regimes: creep, stick-slip and sliding friction. For all the wires of different sizes used in the simulation a critical force  $f_c$  is witnessed where the wire is subject to a depinning transition  $v \propto (f - f_c)^\alpha$ , where  $\alpha$  is 0.6 for hydrophilic wires of different sizes. This continuous transition changes into a discontinuous one when the hydrophilic wire is replaced by a hydrophobic one. The differences in the dynamics of the system as the wire is changed are explained. It is also witnessed that at high driving forces there is a phase transition of ice that has an impact on the dynamics of the system.

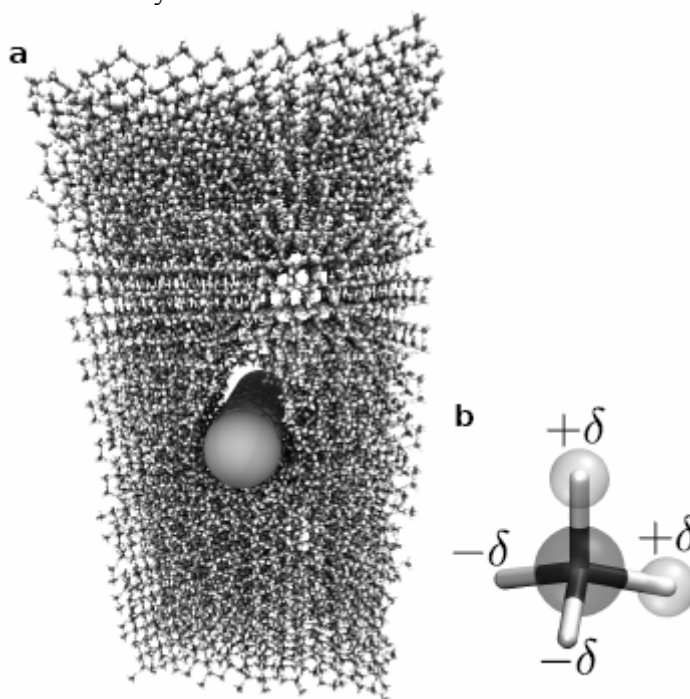


Fig.1 a) The simulation cell showing the nanowire within the ice.  
b) The MB molecule representing water molecules in the simulations.

# Modeling close-packed metallic interfaces with amplitude expansion of the phase-field crystal model

P.T.Kanerva<sup>1</sup>, J.Jalkanen<sup>1</sup>, G.Rossi<sup>1</sup>, K.R.Elder<sup>2</sup>, T.Ala-Nissilä<sup>1</sup>

*1. Department of Applied Physics, Aalto University School of Science and Technology, Espoo, Finland, pekka.t.kanerva@tkk.fi. 2. Department of Physics, Oakland University, Rochester, Michigan, USA*

We study a lattice-mismatched atomic overlayer on a fcc(111) substrate using the phase-field crystal model [1, 2]. In this system the mismatch induces formation of fcc and hcp stacking domains, which are separated by partial misfit dislocations. A well known example of such system is Cu on Ru(1000), where experimental studies have shown four distinct misfit dislocation structures [3]. A recent study has proposed that also Cu on Pd(111) has similar behavior[4].

The amplitude expansion of the phase-field crystal model is well suited for this purpose. It is computationally efficient, which allows us to use realistic system sizes and diffusive timescales. Substrate is modeled by a pinning potential whose minima form a 2D honeycomb lattice. Overlayer is described by the phase-field crystal which prefers triangular lattice with different equilibrium lattice constant than the substrate. We study how the misfit dislocation structure formation is effected by the interfacial energy and energy differences of fcc and hcp sites.

[1] K. R. Elder and Martin Grant, “Modeling elastic and plastic deformations in nonequilibrium processing using phase field crystals”, Phys. Rev. E **70**, 051605, 2004

[2] K. R. Elder, Zhi-Feng Huang and Nikolas Provatas, “Amplitude expansion of the binary phase-field-crystal model”, Phys. Rev. E **81**, 011602, 2010

[3] J. C. Hamilton and S. M. Foiles, “Misfit Dislocation Structure for Close-Packed Metal-Metal Interfaces”, Phys. Rev. Lett. **75**, pp. 882-885, 1995

[4] J. Jalkanen, G. Rossi, O. Trushin, E. Granato, T. Ala-Nissilä and S.-C. Ying, “Stress release mechanisms for Cu on Pd(111) in the submonolayer and monolayer regimes”, Phys. Rev. B **81**, 041412, 2010

# Nonlinear microrheology of dense colloidal suspensions

I.Gazuz<sup>1</sup>, A.M.Puertas<sup>2</sup> and M.Fuchs<sup>3</sup>

*1. Department of Applied Physics, Aalto University, P.O. Box 11000, FI-00076 Aalto, Finland, E-mail: igor.gazuz@tkk.fi. 2. Departamento de Fisica Aplicada, Universidad de Almeria, 04.120 Almería, Spain, E-mail: apuertas@ual.es. 3. Fachbereich Physik, Universität Konstanz, P.O. Box M671, 78457 Konstanz, Germany, E-mail: matthias.fuchs@uni-konstanz.de*

The motion of a colloidal tracer particle, pulled through a colloidal suspension by means an external force is investigated. We are interested in the nonlinear response of the system. We start with the formally exact expressions and adopt the intergration through transients [1] approximation method, developed for sheared suspensions, for our case. The key quantity of the approach is the time and external force dependent density correlator of the tracer. By means of mode-coupling approximations, a self-consistent equation is established for it [2], exhibiting many new properties (e.g. the correlator is, in general, complex) due to the non-hermiticity of the Smoluchowski operator for an open system. The mobility of the tracer strongly changes with applied force as surrounding particles are pushed aside for strong forces. The competition between internal diffusion and external drive leads to the thinning behaviour with increasing external force on the tracer. For a glassy suspension, our approach yields that the tracer can only move if the external force exceeds a certain threshold value. This yielding behaviour is in agreement with experiments and simulations. [2, 3].

- [1] Fuchs M., Cates M. E., J. Phys.: Condens. Matter 17 (2005) S1681-S1696.
- [2] I. Gazuz, A. M. Puertas, Th. Voigtmann, M. Fuchs (2009), Phys. Rev. Lett. 102, 248302 (2009)
- [3] Weeks E. et. al., Europhys. Lett. 67 (3), pp. 4

# Lattice-Boltzmann simulations of colloidal hydrodynamics

S.T.T.Ollila<sup>1,2</sup>, C.J.Smith<sup>2</sup> and C.Denniston<sup>2</sup>

*1. Department of Applied Mathematics, The University of Western Ontario, London, Ontario, Canada N6A 5B8.*

*2. Department of Applied Physics, Aalto University School of Science and Technology, P.O. Box 11000, FI-00076 Aalto, Espoo, Finland, E-mail: [santtu.ollila@tkk.fi](mailto:santtu.ollila@tkk.fi)*

We examine lattice-Boltzmann (LB) methods for incorporating solid moving boundaries within a fluid through a frictional coupling between the fluid and the solid boundary of a colloidal particle. We show that consistency of a hydrodynamic radius determined through measuring Stokes drag, hydrodynamic torques, forces from hydrodynamic interactions, and diffusion is far from assured. However, it is possible to determine an appropriate coefficient of the frictional force by demanding consistency of all these measures, but in many cases this requires a somewhat modified LB algorithm for numerical stability. Choosing our frictional force constant in this way, we show that our particles also obey the expected macroscopic fluctuation-dissipation theorem for the diffusion coefficient of a single particle. We quantify explicitly the range of applicability of the Oseen and Rotne-Prager tensor as tests for speed of propagation of hydrodynamic forces. Somewhat surprisingly, the infinite propagation speed assumed in the Oseen tensor is seen to have serious consequences for some short-range hydrodynamic interactions [1].

[1] S. T. T. Ollila, C. J. Smith and C. Denniston, Phys. Rev E, Lattice-Boltzmann simulations of colloidal hydrodynamics, submitted (2010).

## XPS depth profiling of SiO<sub>2</sub> / HfO<sub>2</sub> / Si thin layers

A.V.Boryakov, A.S.Vihorev, A.V.Ershov, S.Yu.Zubkov, V.V.Karzanov  
*University of Nizhni Novgorod, 23 Prospekt Gagarina, 603950, Nizhni Novgorod, Russia*

The high-k dielectric hafnium dioxide (HfO<sub>2</sub>) is a promising material for application as a gate layer in silicon microelectronics. Having high values of dielectric constant ( $\sim 25$ ) [1] hafnium dioxide allows reducing the thickness of the gate layer and so the size of semiconductor transistors could be decreased. Moreover, the high values of refractive index of HfO<sub>2</sub> films make them possible to apply as an antireflection coating in various optical systems. For example SiO<sub>2</sub> / HfO<sub>2</sub> layers were successfully used as antireflection coating in light emitting heterostructures on the basis of GaAs / InGaAs. Thereby it is necessary to clarify the thermal stability of such layers. There are just a few discrepant reports in the publications referred to the properties of this material.

SiO<sub>2</sub> and HfO<sub>2</sub> thin films were deposited on silicon substrates by electron-beam evaporation method. Firstly silicon substrates were etched with hydrofluoric acid for the purpose to remove a native oxide before film deposition. After the deposition the SiO<sub>2</sub> / HfO<sub>2</sub> / Si structures were thermally annealed in molecular nitrogen flow at the temperatures of 500 – 1100°C. Samples were analyzed by atomic force microscopy (AFM) and X-ray photoelectron spectroscopy (XPS). Depth profiling in XPS method was carried out using sputtering by argon ions (Ar<sup>+</sup>).

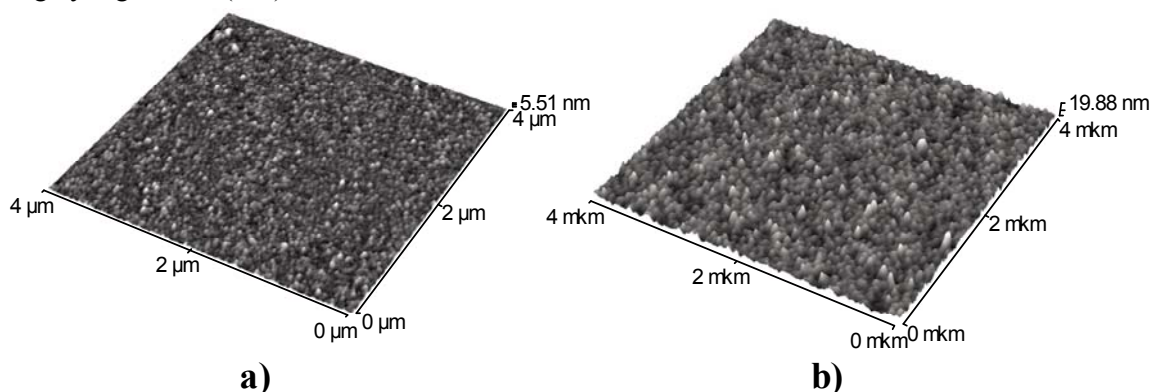


Fig.1. Surface morphology of the structures SiO<sub>2</sub> / HfO<sub>2</sub> / Si: a) before annealing, b) after annealing at 1100°C.

Surface topography study showed that films had a block-droplet structure. It was determined that the nitrogen high-temperature annealing leads to increasing of the film surface morphology heights (Fig. 1). The surface roughness of the original structure was 0.7 nm and it rose up to 2.4 nm after heat treatment.

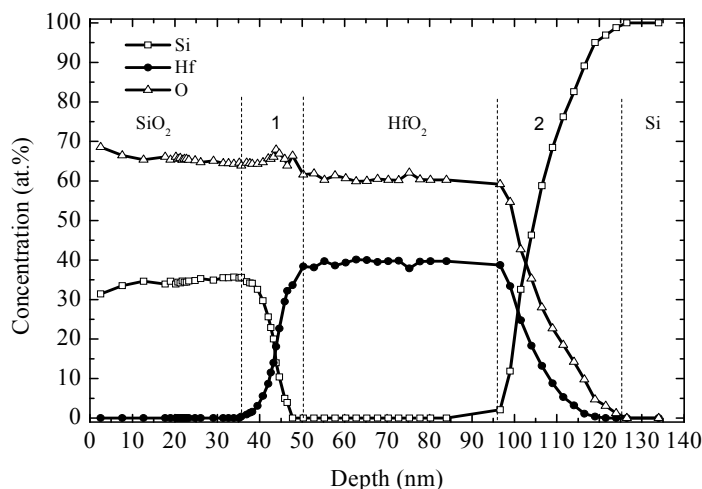


Fig.2. Profile distribution of concentrations of structure SiO<sub>2</sub> / HfO<sub>2</sub> / Si in depth.

The element concentration profiles in depth with the use of X-ray photoelectron spectroscopy (fig.2.) were obtained. The concentration of silicon and oxygen in the SiO<sub>2</sub> film was  $\sim 34$  at.% and  $\sim 66$  at.% respectively. This corresponds to the stoichiometric formula of silicon dioxide. In the hafnium dioxide film the

concentration of oxygen reduced down to 60%, the shape of the photoelectron line 3 on the Fig. 2 changed and the peak corresponded to the metal hafnium ( $\text{Hf}^0$ ) appeared. Changing the stoichiometry of the  $\text{HfO}_2$  film is probably due to the ion sputtering during layer-by-layer profiling.

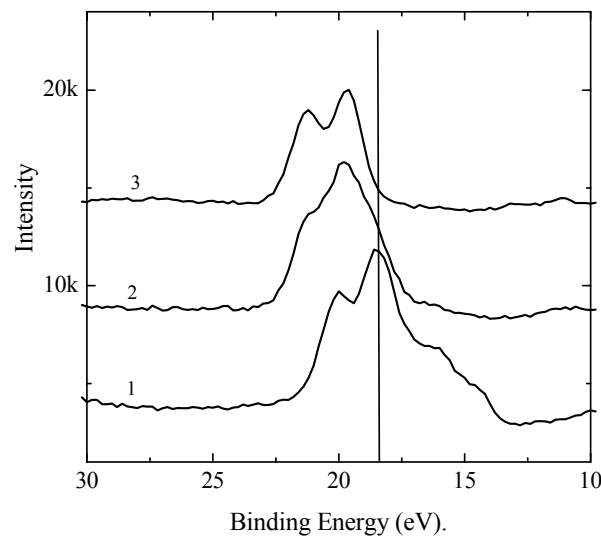


Fig.2. XPS lines with chemical shifts of Hf 4f for the structure  $\text{SiO}_2 / \text{HfO}_2 / \text{Si}$  annealed at  $1100^\circ\text{C}$ : 1- beginning of the  $\text{SiO}_2 / \text{HfO}_2$  heterojunction, 2- intermediate line in the transition layer, 3- end of the  $\text{SiO}_2 / \text{HfO}_2$  heterojunction.

It was observed the shift of the Hf (4f) photoelectron line for the thermal annealed at  $1100^\circ\text{C}$  samples as one approach to the  $\text{HfO}_2$  layer. Hafnium line (4f) recorded at the beginning of the  $\text{SiO}_2 / \text{HfO}_2$  heterojunction was shifted up to 1 eV in the direction of higher binding energies relatively to the same line in the bulk of  $\text{HfO}_2$  film (fig. 2.). Additionally, in the center of the  $\text{SiO}_2 / \text{HfO}_2$  heterojunction the shape change of the Hf (4f) line was observed (fig. 2, line 2). This fact explained by hafnium silicate phase forming within the  $\text{SiO}_2 / \text{HfO}_2$  heterojunction during temperature annealing [2]. For the annealed structures it was also determined the 0.5 eV shift of the  $\text{Si}^{2+}$  (2p) line toward to higher binding energy relatively to the same line for the non-annealed samples. On the heterojunction of  $\text{HfO}_2 / \text{Si}$  the  $\text{Si}^{2+}$  phase was observed for structures annealed at  $1100^\circ\text{C}$ . This can be explained by increasing of the oxygen diffusion to the boundary during high temperatures annealing.

In conclusion, annealing leads to the increase of surface roughness for  $\text{SiO}_2 / \text{HfO}_2 / \text{Si}$  structures and forming the hafnium silicate phase on the border between  $\text{SiO}_2$  and  $\text{HfO}_2$  films.

The work was supported by RFBR # a 08-02-97044.

1. H. T. Johnson-Steigelman, A.V. Brinck, and P.F. Lyman. "Production of a hafnium silicate dielectric layer for use as a gate oxide by solid-state reaction", J. Vac. Sci. Technol., 24, pp. 1218-1222, 2006
2. V.Rangarajan et.al. "Comparison of hafnium silicate thin films on silicon (100) deposited using thermal and plasma enhanced metal organic chemical vapor deposition", Thin Solid Films, **419**, pp. 1-4, 2002

# Three-dimensional modeling of dynamic processes in the crystalline matrix

V.V.Kostin, N.A.Rud

*Yaroslavl Demidov State University, Yaroslavl, Russia, kostin25vitali@rambler.ru*

The paper deals with computer models related to the class of models of controlled gradient of growth. Various algorithms of this class of models allow to obtain a wide range of clusters, characterized by a variety of structures, including fractal.

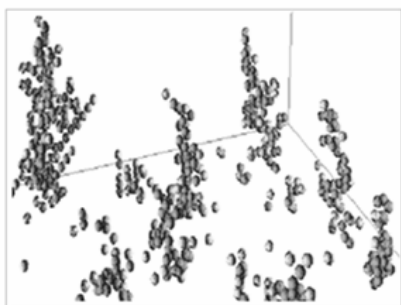
The study of coherent phenomena in stochastic systems is of interest from the standpoint of their application in various physical fields. The phenomena of coherence characterized by the formation of clusters in stochastic systems under certain conditions. Clustering occurs in various models, which in many respects similar to models that describe coherent phenomena in dynamical systems. One of the objectives of this class of phenomena - the clustering of tracer in random velocity fields. The principal feature of the problem is the existence of cluster structure of the field in the impurity concentration. This feature is manifested in the form of caustic structure as a result of the focusing and defocusing in a random environment [1].

Attempts to use computer models to explain the regularities of pore formation were made repeatedly [2]. However, comprehensive model of formation of porous spaces so far not been built, demonstrating the need for further research in this direction.

## Formulation of the problem.

In this paper we investigate the formation of clusters on flat rectangular boundaries of the area covered a square grid. As a result of computer simulation based on the developed software package in a three-dimensional case for certain values of the parameters were obtained by the structure, some of which are presented in this study (Fig 1a). For comparison, presented in a special way the experimentally obtained structure (Fig 1b). To get it into a matrix of porous silicon instilled nickel by precipitation from solution [3]. Silicon substrate itself is then removed by dissolving in caustic potash when heated. It should be noted that the proposed technology fill the pores of nickel not fully penetrated into the pores, so that the structure shown in Fig. 1b is only partially filled the pores of nickel near the openings on the surface.

a)



b)

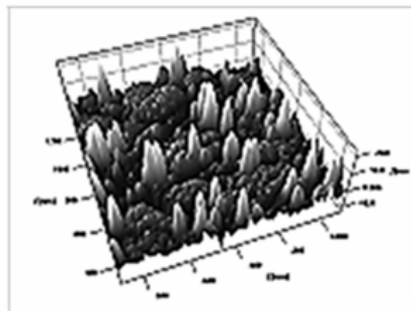


*Fig.1. Three-dimensional structure of the cluster, derived from computer simulation (a). Green spherical structures reflect the structure of the cluster near the beginning of the growth of the cluster, yellow - away from the beginning. Three-dimensional structure obtained by the special technology of metal deposition in porous clusters and subsequent etching of the silicon matrix (b).*

To control the shape of cluster formation, i.e. the influence of random motion of particles in our work we investigated the prevalence of the deterministic components of the velocity determined by the external field, which creates a needle-shaped seed. In the computer simulation used two primers, whose shape is identical hyperboloid of rotation. Primers located at some distance from each other. Calculation of capacity in this case is similar to two-lane hyperboloid. Calculation of potential distribution produced by the method of Lam, which is described in detail in [6].

The developed three-dimensional computer model of the formation of clusters can be regarded as a model for the formation of the porous space in semiconductors for certain values of relevant parameters. The results obtained structures are presented in Fig. 2,a,b. For comparison Fig. 2,c, represented in a special way the experimentally obtained structure deposition of nickel in the matrix of porous silicon with subsequent removal of the silicon substrate by dissolving it in caustic potash.

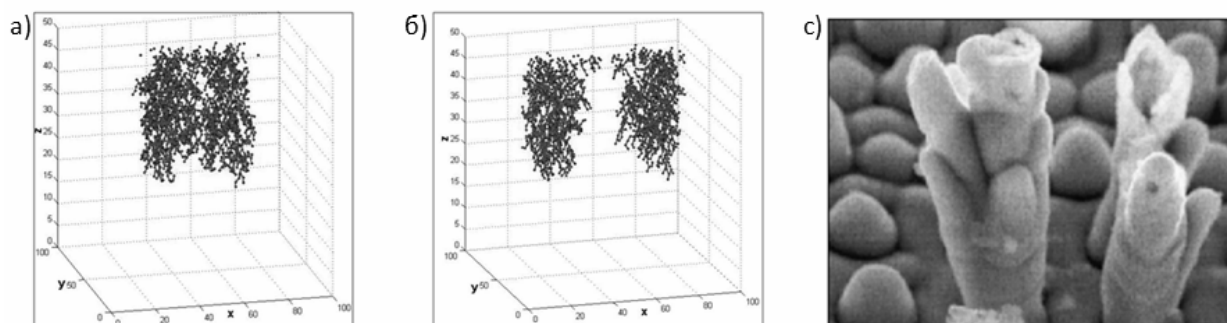


Fig.2. Computer model of cluster formation. The close location of primers reveals their mutual influence on each other (a). Remote location of primers is practically not reveal their mutual influence (b). Experimentally obtained structure (c).

In the simulation revealed the following regularities:

- a) Reduce the thickness of the sample with respect to the density of seeds to each other forms a more extended and more isolated clusters and more tied to the seed
- b) The depth of penetration of particles inside depends on the width of the sample;
- c) The placement of seeds close manifested their mutual influence on each other, which was observed in the constructed model (Fig 2, a).
- d) The remote location of primers revealed little of their mutual influence, which is also observed in the constructed model (Fig 2, b).

In conclusion, we note the following, we have studied computer simulations relating to the class of models of controlled gradient of growth, and also developed a software package in three dimensions, which for certain values of the parameters are calculated and graphically maps out the structure considered previously. Various algorithms of this class of models allow to obtain a wide range of clusters, characterized by a variety of structures, including fractal.

## References

- [1] Kapliy S.A., Prokaznikov A.V., Rud N.A. // GTF. 2004. T. 74. Vol. 5. S. 6-11.
- [2] John G.C., Singh V.A. // Phys. Rep. 1995. Vol. 263. P. 93-151.
- [3] Nikitchuk S.A., Lohanin M.V., Prokaznikov A.V., Rud N.A., Svetovoy V.B. // Technical Physics Letters. 2005. T. 31. Vol. 12. S. 48-55.
- [4] Buchin E.Y., Postnikov A.V., Prokaznikov A.V., Svetovoy V.B., Tchurilov A.B. // Technical Physics Letters. 1995. T. 21. Vol. 1. S. 60
- [5] Winters H., Graves D.B., Humbird D., Tougaard S. // J. Vac. Sci. Technol. 2007. Vol. A25. N1. P. 96-103
- [6] Mirolubov N.N., Kostenko M.V., Levinstein M.L., Tikhodeev N.N. Methods for calculating electrostatic fields. Moscow: Higher School, 1963. 425 p.



# Formation of nanostructured silicon films on glass substrates using femtosecond laser pulse annealings

V.A.Volodin<sup>1,2</sup>, T.T.Korchagina<sup>1</sup>, A.S.Kachko<sup>1</sup>, A.Kh.Antonenko<sup>1</sup>, G.N.Kamaev<sup>1</sup>

1. Institute of Semiconductor Physics of SB RAS, Lavrenteva ave., 13, Novosibirsk 630090, Russia, E-mail address: volodin@isp.nsc.ru. 2. Novosibirsk State University, Pirogova str., 2, 630090, Novosibirsk, Russia

The interest for manufacturing and studies of polycrystalline silicon films and dielectric films with silicon nanoclusters on non-refractory substrates and their crystallization is actual due to application in “giant” microelectronics. For example, the enlargement of sizes of flat panel displays with active thin film transistor matrix can be described as “reverse Moor’s law” [1]. Modern technique of deposition allows producing of a-Si films on substrates with plasticity temperature as low as 100 °C. But for some applications the poly-silicon films have many advantages comparing with a-Si films. So, the development of low thermal budget technology of crystallization of a-Si films is actual, and is of interest up today, especially for femtosecond laser crystallization [2,3].

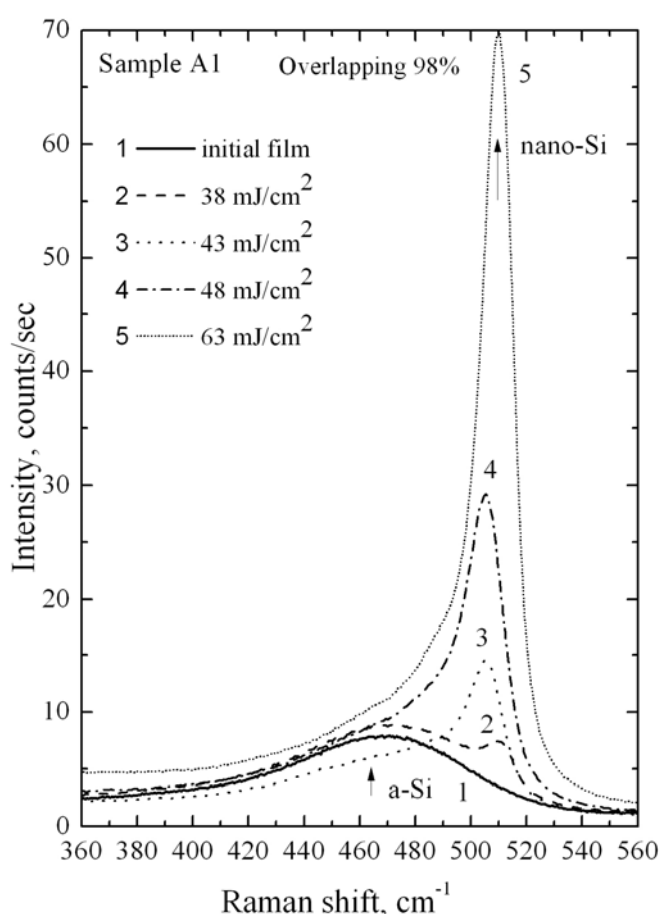


**Fig. 1.** Crystallization of a-Si films under femtosecond laser impact (30 fs).

correspondingly. Due to scattering on optical phonon modes localized in the nanocrystals, the Raman spectrum of nanocrystals is characterized by narrow peak at position between 500-520 cm<sup>-1</sup>. The position and the width of the Raman peaks strongly depend on size and structure of the nanocrystals according to dispersion of the localised modes. The peak width is mainly determined by size dispersion of the nanocrystals. The intensity of the “nanocrystal” peak depends on the contents of nanocrystal phase; so, one can determine the volume part of nanocrystal phase:  $V_{\text{nano-Si}} = I_c / (I_c + \sigma_a I_a)$ , where  $\sigma_a$  is relation between the integral cross sections of crystal Si and a-Si. According to literature data,  $\sigma_a$  can change from 0.1 for large grain polycrystalline silicon up to 0.88 for nano-Si.

The initial thin (50-100 nm) a-Si:H films were deposited on non-refractory glass substrates using low-temperature plasma enhanced chemical vapor deposition (PECVD) technique. According to IR-spectroscopy and light transmission data, the films contain from 10 to 30 atomic percents of hydrogen depending on growth conditions. The initial silicon reach nitride (SRN) films (or SiN<sub>x</sub> films,  $x < 1.33$ ) were deposited using low frequency (55 kHz) PECVD technique. The stoichiometric parameter  $x$  in the SiN<sub>x</sub>:H films was varied from 0.6 to 1.3 using various ratios of SiH<sub>4</sub> and NH<sub>3</sub> gases in reactor during deposition. Some parameters of the films are described elsewhere [4].

Ti-Sapphire lasers with a central wavelength of 800 nm and pulse duration of <30 femtoseconds (fs) and 120 fs were used for laser treatments of initial films. Raman spectroscopy technique was used to identify the structure (amorphous or crystalline) of Si nanoclusters in the films. Raman spectra were recorded in back-scattering geometry. The 514.5 nm Ar<sup>+</sup> laser line was used as a source. Triple spectrometer T64000 Horiba Jobin Yvon with micro-Raman setup was used.

The Raman spectrum of a-Si contains two broad peaks at approximately 480 cm<sup>-1</sup> and 150 cm<sup>-1</sup> appearing as result of effective density of transversal optical (TO) and transversal acoustical (TA) vibration modes

One can see from figure 1 that with growth of density of energy of laser impact (laser fluence) the “nanocrystalline” Raman peak also growth. The volume fraction of nanocrystalline phase in sample treated by femtosecond laser pulse with energy density  $68 \text{ mJ/cm}^2$  is close to 100 %. Microscopic studies have shown that the films scanned by the laser beam with 96-98 % overlapping is homogeneous. So, this treatment can be used for poly-Si films on glass producing.

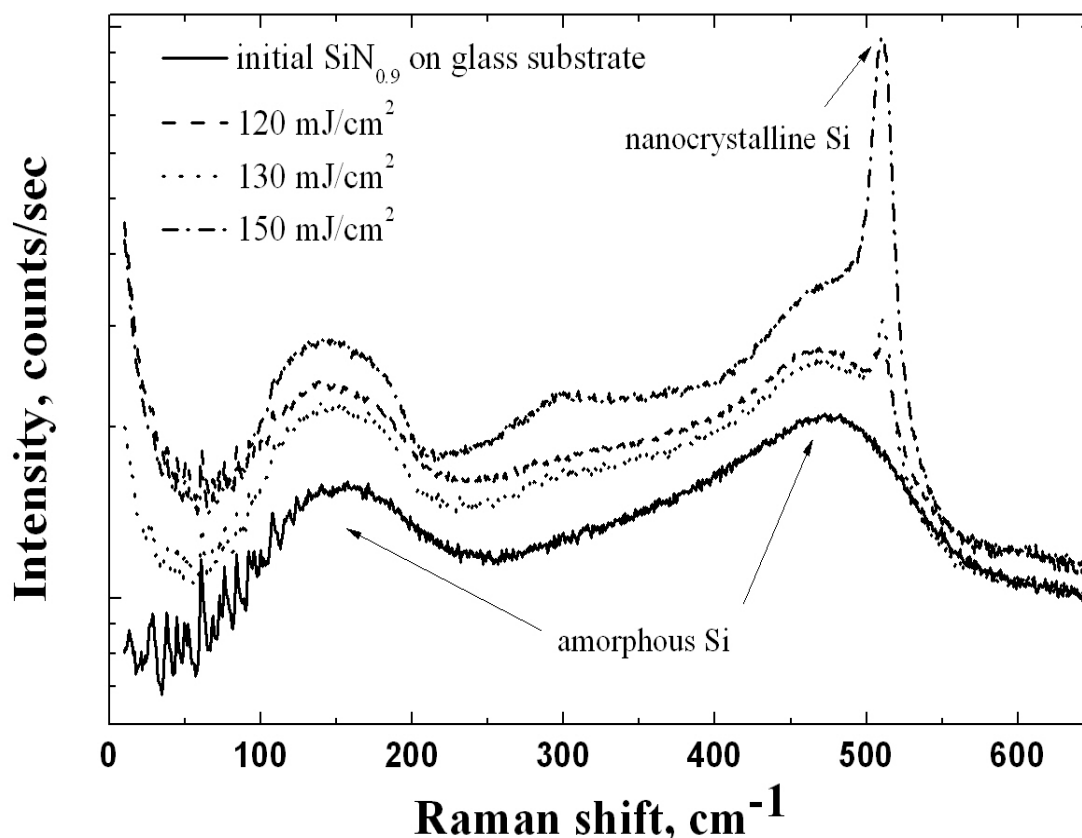


Fig. 2. Raman spectra of initial and laser treated SRN film.

General trend in laser treatments of the SRN films is the more additional Si atoms contains the film – the less laser fluences were needed to crystallize or to modify silicon nanoclusters. It is obvious, because the absorbance coefficient grow with growing of silicon amount in the SRN films. For SRN ( $\text{SiN}_x$ ) films with stoichiometric parameter  $x$  lesser that 1.0 it was possible to crystallize all silicon nanoclusters using laser treatments with fluences  $120 \text{ mJ/cm}^2$  and higher, as one can see from Raman data in figure 2.

In conclusion, the possibility of the femtosecond laser pulses to crystallize a-Si films and amorphous Si nanoclusters in SRN films on glass substrates was shown. The developed approach can be used for formation of nanostructured films on non-refractory substrates. V.A.V is grateful to DAAD and RFBR for support.

## References

1. M.S.Shur, S.L.Rumyantsev and R.Gaska, “Nanostructures on flexible substrates”, *10<sup>th</sup> International Symposium “Nanostructures: Physics and Technology”*, pp. 618-622, Sanct-Petersburg, 2002.
2. G.J.Lee, S.H.Song, Y.P.Lee, H.Cheong, C.S.Yoon, Y.D.Son, J.Jang, “Arbitrary surface structuring of amorphous silicon films based on femtosecond-laser-induced crystallization” *Appl. Phys. Lett.*, **89**, pp. 151907-1-151907-3, (2006).
3. V.A.Volodin, M.D.Efremov, G.A.Kachurin, A.G.Cherkov, M. Deutschmann, N. Baersch, “Phase Transitions in a-Si:H Films on a Glass Irradiated by High-Power Femtosecond Pulses: Manifestation of Nonlinear and Nonthermal Effects”, *JETP Letters*, **86**, pp. 119-122, (2007).
4. T. T. Korchagina, D. V. Marin, V. A. Volodin, A. A. Popov, and M. Vergnat, “Structure and Optical Properties of  $\text{SiN}_x\text{:H}$  Films with Si Nanoclusters Produced by Low-Frequency Plasma-Enhanced Chemical Vapor Deposition” *Semiconductors*, **43**, No. 11, pp. 1514–1520, (2009).

# Optical properties of silicon nanoclusters formed in SiN<sub>x</sub> films: effect of pressure annealing

V.A.Volodin<sup>1,2</sup>, K.O.Bugaev<sup>1</sup>, A.A.Popov<sup>3</sup>, and A.Misiuk<sup>4</sup>

1. Institute of Semiconductor Physics of SB RAS, Lavrenteva ave., 13, Novosibirsk 630090, Russia, E-mail address: volodin@isp.nsc.ru. 2. Novosibirsk State University, Pirogova str., 2, Novosibirsk, 630090, Russia. 3. Yaroslavl Branch of the Institute of Physics and Technology, Russian Academy of Sciences, University ave., 21, Yaroslavl, Russia. 4. Institute of Electron Technology, Al. Lotnikow 46, 02-668 Warsaw, Poland

Semiconductor nanocrystals (NCs) embedded in dielectric films attract much interest due to their optical and electronic properties, which can be modified by varying their sizes. The dependence of energy of optical transition on the NC size is also called quantum-size effect. This effect for Si NCs in the dielectric matrix becomes to be fairly recognizable at room temperature. Because, in some experiments, single NC reveals the delta-function-like photoluminescence spectrum [1], the NCs can be considered to be quantum dots. NCs have shown significant perspectives for a wide range of nanoelectronic and optoelectronic applications. So, the NCs are interesting from both fundamental and applied points of view. Recently, the quantum-size effect was observed not only for Si NCs but also for amorphous silicon nanoclusters [2]. In metal-dielectric-semiconductor structures based on the silicon-rich nitride (SRN) films, an effective electroluminescence was achieved. Red, green and blue light emitting diodes were demonstrated [2]. SRN films are composed from non-stoichiometric SiN<sub>x</sub> ( $x < 4/3$ ). The reproducible, non-expensive, low temperature technologies for deposition of SRN films are available. Additional silicon atoms in some SRN films are randomly distributed in the SiN<sub>x</sub> matrix. They do not form nanoclusters (random bonding - RB model). Some SRN films contain amorphous Si nanoclusters; this depends on the growth condition. Such situation is close to the random mixture - RM model. During thermal annealing, silicon atoms are clustering and form nanoclusters. The influence of enhanced hydrostatic pressure during annealing of silicon oxide and of silicon nitride films was studied earlier [3]. This work concerns further studies of an influence of pressure on the formation of Si nanoclusters in the SRN films.

The initial SRN films were deposited on the Si (100) substrate using low frequency PECVD technique. The films were annealed 5 hrs at temperature 1130 °C at atmosphere pressure (10<sup>5</sup> Pa) and under hydrostatic Ar pressure equal to 1.1 GPa. Optical properties of the as-prepared and of annealed films were studied using photoluminescence (PL) spectroscopy, IR spectroscopy and ellipsometry.

#	NH <sub>3</sub> /SiH <sub>4</sub> flow ratio	d, nm
1	5	240
2	2.6	400
3	0.9	450

**Table.** Characteristics of SRN films.

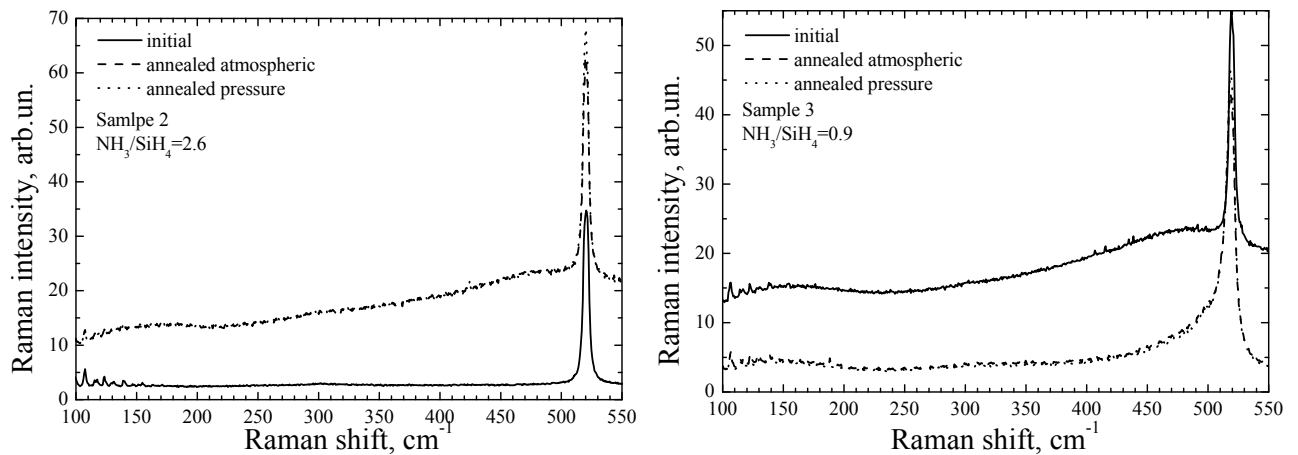


**Fig. 1.** Raman spectra of SRN films 2 (left) and 3 (right).

Raman spectroscopy technique was used to identify the structure (amorphous or crystalline) of Si nanoclusters in the films. Raman spectra were recorded in back-scattering geometry. The 514.5 nm Ar<sup>+</sup> laser line was used as a source. Triple spectrometer T64000 Horiba Jobin Yvon with micro-Raman setup was used. The Raman spectrum of a-Si contains two broad peaks at approximately 480 cm<sup>-1</sup> and 150 cm<sup>-1</sup> appearing as result of effective density of the transversal optical (TO) and transversal acoustical (TA) vibration modes, respectively. Due to the scattering on optical phonon modes localized in the nanocrystals, the Raman spectrum of nanocrystals is characterized by the narrow peak positioned at 500-520 cm<sup>-1</sup>. The position and width of the Raman peaks strongly depend on the size and structure of nanocrystals accordingly to dispersion of the localised modes. The peak width is mainly determined by size dispersion of nanocrystals. One can see from figure 1 that the initial SRN film 2 contains Si nanoclusters in a small concentration. Only the peak at 520 cm<sup>-1</sup> from monocrystalline Si substrate is observed (the films are semi-transparent). Annealing leads to the formation of amorphous Si nanoclusters (the “amorphous” Raman peaks are appeared). The as prepared SRN film 3 contains amorphous Si nanoclusters. Annealing leads to its crystallization – one can see “nanocrystalline” shoulder close to the peak originating from the monocrystalline Si substrate. No apparent difference in the Raman spectra of the SRN films annealed at atmospheric pressure and under 1.1 GPa were observed.

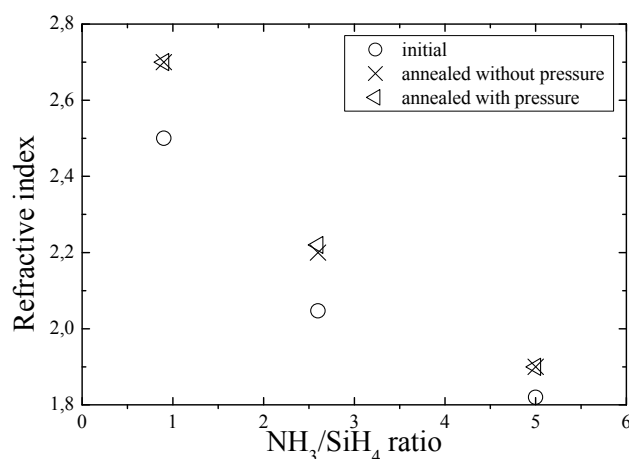


**Fig. 2.** Refractive index of SRN films ( $\lambda=633$  nm).

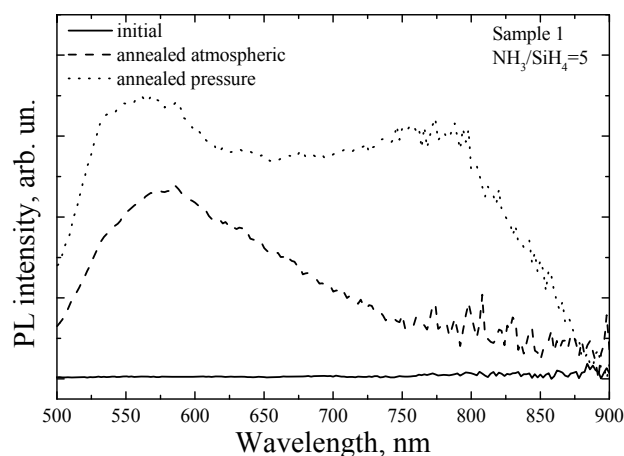


**Fig. 3.** PL spectra of SRN film 1.

Ellipsometric data show that the refractive and absorbance indexes of the SRN films are changed after annealing (figure 2). Annealing leads to clustering of Si atoms and to transformation of the SiN<sub>x</sub> films (situation close to that described by the RB model) to the Si:Si<sub>3</sub>N<sub>4</sub> mixture films (situation close to the RM model), and, according to Bruggemann model, it leads to increase of the refractive index. Another factor leading to changes in the refractive index is dehydrogenization of the films under annealing. According to the IR spectroscopy data, the initial films contain Si-H and N-H bonds. The IR spectra of annealed films shows an absence of hydrogen, but some changes in the Si-N peaks of the annealed SRN films 1 and 2 can be interpreted as the result of crystallization of the silicon nitride matrix. The effect of pressure on optical properties is definitely observable in PL spectra (figure 3). Supposedly, the enhanced pressure affects the formation of defects and probability of the radiative and non-radiative transitions.

V.A.V. is grateful to RFBR for support.

## References

1. I.Sychugov, R.Juhasz, J.Valenta, and J.Linnros, “Narrow Luminescence Linewidth of a Silicon Quantum Dot”, *Phys. Rev. Lett.*, **94**, pp. 087405-1-087405-4, (2005).
2. Nae-Man Park, Tae-Soo Kim, Seong-Ju Park, “Band gap engineering of amorphous silicon quantum dots for light-emitting diodes”, *Appl. Phys. Lett.*, **78**, pp. 2575-2577, (2001).
3. A. Misiuk, A. Iller, L. Rebohle, M. Lukaszewicz, A. Kudla, “Photoluminescence from pressure-annealed silicon dioxide and nitride films”, *Microelectronics Reliability*, **40**, pp. 881-884, (2000).

## Switch conductivity effect in dielectric films with different incorporated clusters

A.E.Berdnikov, A.A.Popov, A.A.Mironenko, V.D.Chernomordick, A.V.Perminov, V.N.Gusev  
*Yaroslavl Branch of the Institute of Physics and Technology, Russian Academy of Sciences, Yaroslavl, Russia,*  
*E-mail: imiraslab4@yandex.ru*

We have found out the conductivity switching effect in films of nonstoichiometric silicon oxide, prepared by method of low-frequency discharge plasma enhanced chemical vapor deposition from gas mixture of monosilane and nitric oxide. This effect allows creation of non-volatile memory devices with cross-bar topology by tradition silicon technology. The effect consists in sharp increasing of MOS-like structure conductivity at supplying of negative voltage on a substrate more then a threshold and sharp increasing of resistance at supplying of positive voltage on a substrate more then a threshold. Between voltage thresholds conductivity remains constant during long time.

In this film there are clusters of silicon, having two various mechanisms of formation. The small size clusters are formed during growth of a film from surplus silicon atoms. Big size clusters arise in a gas phase and transfer to a growth surface. Low size clusters have greater band gap in contrast to big size clusters, because quantum confinement effect increased it.

For improvement of properties of MOS-like elements with conductivity switching effect the technology of embedding of silicon nitride clusters in silicon rich oxide film has been developed. For this purpose before silicon rich oxide deposition, process of silicon nitride deposition by low frequency PECVD from gas mixture of monosilane and ammonia on empty substrate holder was spent. Except a film growth on substrate holder, the particles of silicon nitride appeared in a gas phase. These particles accumulated on inner surface of reactor. At the subsequent growing of a non stoichiometric silicon oxide film on a substrate, particles of silicon nitride get an electrical charge, pass in volume of gas discharge and built in a growing film. During deposition of silicon oxide produced by low frequency PECVD method in a film was appeared also small silicon cluster. The effect of conductivity switching also was found in such material also.

One-step method of formation of silicon nitride clusters has been tested. This method consists in constant adding of a small amount of ammonia during silicon oxide deposition process. Conductivity switching effect has been received in a narrow range of a gas mixture composition. Possibility solid phase separations take place during film deposition. At other contents of gas mixture the switching conductivity effect was not observed.

Other approach to clusters formation in dielectric film consists in consecutive deposition of thin films of various types of dielectrics, which indeed are amorphous semiconductors with various wide bands gaps. Thus there is an alternation of island type growth and level-by-level growth. In particular, during layers deposition with theoretical thickness of 4-5 nanometers silicon oxide and silicon nitride, as a result arise silicon nitride clusters in a silicon oxide film in addition to silicon clusters which formed in gas phase. These materials also have effect of conductivity switching.

Method of clusters formation in a dielectric film has been realised by anodizing of alloy AK1 (aluminium and 1% of silicon). The metal alloy has been deposited on a silicon substrate by method of magnetron sputtering. Further its anodizing was spent. Full oxidation has not occurred nearly to substrate. As a result clusters of not oxidized aluminium exist near silicon substrate. The prepared material also has the effect of conductivity switching. Unlike the previous cases the polarity of effect has changed. Turn on of conductivity occurs at positive voltage on the substrate, and turn off of conductivity occurs at negative voltage on the substrate. When pure aluminium was used to dielectric formation the effect of conductivity switching is not detected. It is possible to assume that silicon from AK1 alloy during anodizing also was agglomerated in a separate phase in a form of silicon clusters.

Thus, technologically different ways of formation of structure “semiconductor – dielectric with included two type of clusters – metal” have been realised. In the all cases the effect of conductivity switching was observed. It is possible to assume that for realisation of such effect formation of dielectric, in which clusters with different band gaps present, between a semiconductor substrate and metal contact is required. Across some clusters current flows while others clusters get, keep and lose an electric charge under applied voltage. The electrical field of these charges blocks the current flow through dielectric.

# Studying of current flow mechanism in structures with conductivity switching effect

A.V.Prokaznikov, A.A.Popov, A.A.Mironenko, A.V.Perminov,  
A.E.Berdnikov, V.D.Chernomordick

Yaroslavl Branch of the Institute of Physics and Technology, Russian Academy of Sciences, Yaroslavl, Russia,  
E-mail: imiraslab4@yandex.ru

We investigated MOS-like structures having conductivity switching effect. There is a numerous class of realization of bistable bipolar effect of the conductivity switching which can use in fabrication of non-volatile memory devices. Various authors explained this effect by various mechanisms. Nevertheless different realizations of this effect show almost identical current-voltage characteristics and have similar memory cell construction. Therefore the studying of current flow mechanism in a conductive state of such cells is very interesting for investigation of structure of such cells in a open state and clarification of the conductivity switching mechanism and the further improvement of memory cell parameters.

The studying of current-voltage characteristics of structures on base of non stoichiometric silicon oxide containing silicon clusters was spent. The structures were produced by method of low frequency discharge plasma enhanced chemical vapor deposition from gas mixture of monosilane and nitric oxide. Well-known conductivity mechanisms in dielectric were checked. Types of conductivity mechanisms and formulas connected current and voltage present in the table 1 [1]. Check of the conductivity mechanism realize by calculation of function  $F(U_{ex}, I_{ex}) \sim U_{ex}$ , where  $U_{ex}$ ,  $I_{ex}$  is a experimental data. It's obvious, that plot of  $F(U_{ex}, I_{ex})$  from  $U_{ex}$  should pass through point 0,0 and must be a straight line. Formulas of functions allow to linearization of experimental data also present in the table 1.

Table 1

Number	Process of current flow	Dependence of current from voltage and temperature	Linearization function (at constant temperature)
1	Schottky emission	$J \sim T^2 e^{\frac{+\alpha\sqrt{U}}{T}}$	$U \sim (\ln J)^2$
2	Poole - Frenkel emission	$J \sim U e^{\frac{+2\alpha\sqrt{U}}{T}}$	$U \sim (\ln \frac{J}{U})^2$
3	Tunneling or fild emission	$J \sim U^2 e^{\frac{-b}{U}}$	$U \sim \frac{1}{\ln \frac{J}{U^2}}$
4	Current limited by volume charge	$J \sim U^2$	$U \sim \sqrt{J}$
5	Ohmic conductivity	$J \sim U e^{\frac{c}{T}}$	$U \sim J$
6	Ion conductivity	$J \sim \frac{U}{T} e^{\frac{-d}{T}}$	$U \sim J$
7	Hopping	$J \sim U f(T) e^{\frac{U}{T}}$	$U \sim \ln \frac{J}{U}$

In fig.1 plots of linearization functions are present. On a horizontal axis voltage in Volt is present. On a vertical axis values of linearization functions calculated as a function of voltage and appropriate experimental current values are present. For convenient of plots placing in one drawing the calculated values of function were multiplied by some constant. Function number on the figure 1 corresponds to function number in table 1.

It is visible that the mechanism of a current limited by volume charge has the best coincidence with linear shape. Besides, similar coincidence is observed in tunneling current [2] in some tunnel configuration.

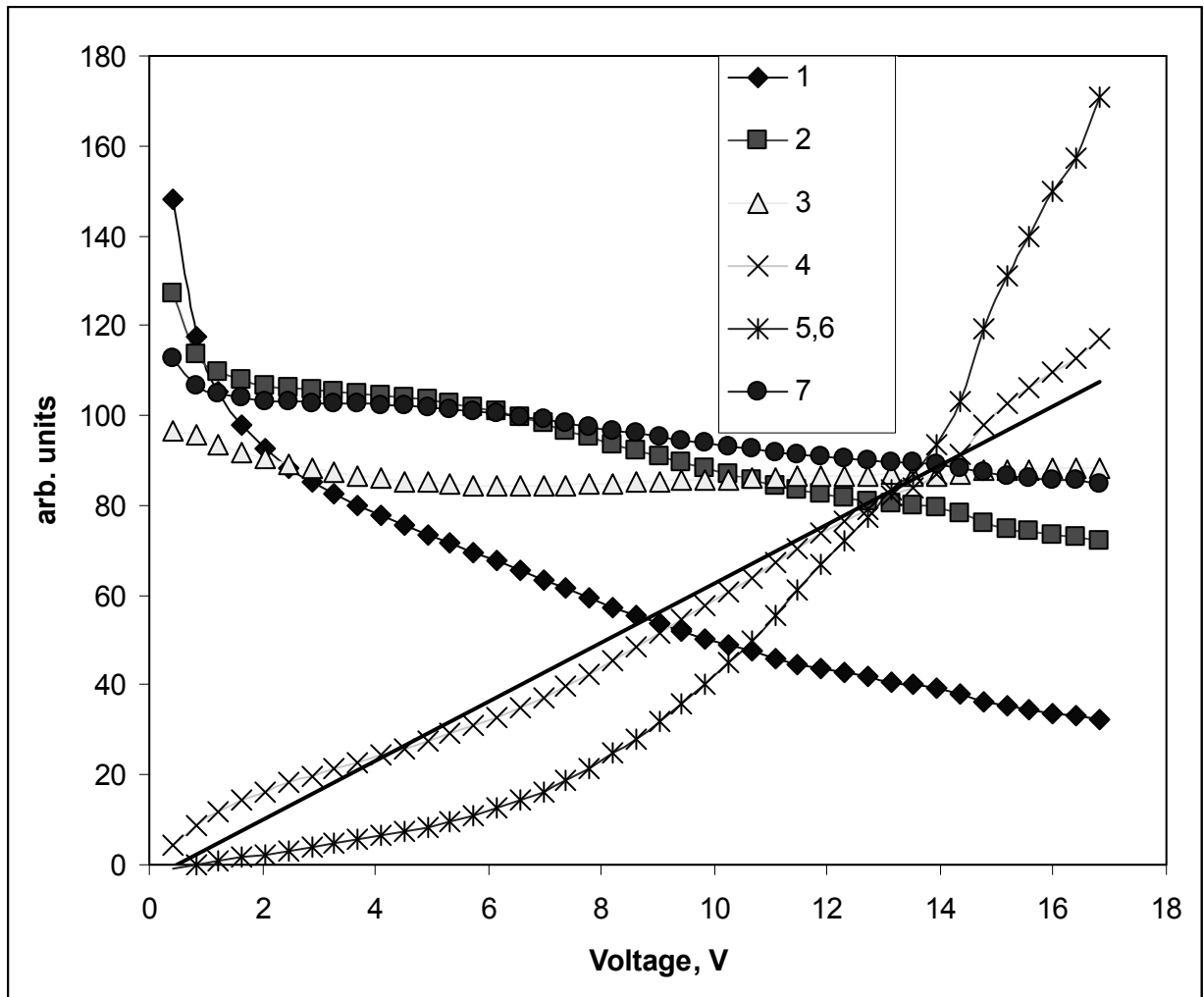


Fig.1. Plots of different linearization functions calculated from experimental data. These functions correspond to different mechanism of current flow in dielectric.

1. S.M. Sze. *Physics of Semiconductor Devices*. John Willey and Sons, New York, 1981
2. Yanson I.K., Vlasenko A.A. "Giant Zero-bias Anomalies and Space Charge Limited Currents in Tunnel Junctions" JETP Letters **V.13**, p.p.294-298, 1971

# Self-formation of microstructures at the deep quartz etching in high density fluorocarbon plasma

M.Izumov, I.Amirov

*Yaroslavl Branch of the Institute of Physics and Technology, Russian Academy of Sciences, Yaroslavl, Russia,  
mikhail-izumov@yandex.ru*

Deep quartz plasma etching have been widely applied in the fabrication of the micro-electro-mechanical system (MEMS). However, the etch rate of quartz is low ( $\sim 0.5 \mu\text{m}/\text{min}$  [1, 2]) and the etched depths of 50  $\mu\text{m}$  and more used in these applications require long time plasma exposure. For the increasing etch rate in the work experiments are performed in the small overall reactor of high density plasma of RF inductive discharge at the high density power ion flux ( $>5 \text{ W}/\text{cm}^2$ ). The etch rate of quartz in  $\text{C}_4\text{F}_8/\text{Ar}/\text{SF}_6$  plasmas achieved  $1.2 \mu\text{m}/\text{min}$ . But at these conditions the array of various form microstructures are observed on the surface quartz (fig.1a). A similar shell-hole-like microstructures generated on the quartz surface are observed early at deep quartz etching [2]. Presence of micro-mask on the quartz plate before etching is considered to be the origin of their self-formation. Defects randomly distributed on the surface. In this work was showed that microstructures self-formation initiated by micro- and nanostructures which formatted on the quartz surface by the lithographic method. In this case regulated self-formatted microstructures (SFM) were received (fig.1b). These SFM were received at the definite conditions. The influence of the plasma parameters, ion energy and flux, plasma composition on the self-formation of microstructures were investigated. The mechanism of self-formation of microstructures on the quartz is discussed.

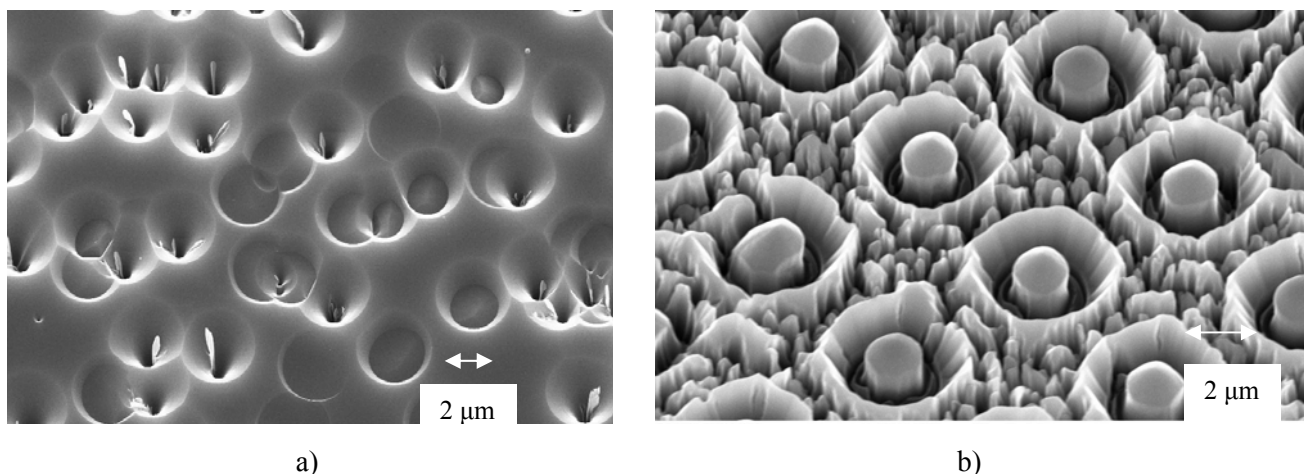


Fig.1. a) Pattern of various form SFM on the quartz surface at the etching during 10 min. b) Pattern of regulated SFM on the quartz surface after 15 min etching.

1. T. Ujiie, T. Kikuchi, T. Ichiki, Y.Horiike. "Fabrication of quartz microcapillary electroforesis chips using plasma etching." Jpn. J. App. Phys. 39, N6A, pp.3677-3682, 2000
2. T. Fukasawa, Y. Horiike. "Deep dry etching of quartz plate over 100  $\mu\text{m}$  in depth employing ultra-thick photoresist (SU-8)". Jpn. J. App. Phys. 42, N6A, pp.3702-3706, 2003



# Cantilever eigenfrequencies control

M.Lokhanin, A.Nikolaev

*Yaroslavl Demidov State University, Yaroslavl, Russia, E-mail address: lokhaninmv@mail.ru*

A cantilever holds many of world records in sensitivity. Detection of single molecule mass or field of single electron, are well-known examples. But a closer look at detection methods show that only two of them are in practical use – registration of static deflection and shift of fundamental frequency. Simple enough methods of movement law registration, such as piezo-sensor, capacitive sensor or interferometer, allows tracking it on angstrom scale. This allows more subtle methods which will maybe provide further progress in sensitivity. We discuss the method based on energy redistribution between vibrational modes due to force applied to cantilever's tip, notably the design of cantilever, fitting this method.

Simple strip cantilever eigenfrequencies form series beginning with 1, 6.267, 17.548 [1] and lying far each other. We are searching the shape for which eigenfrequencies are close enough to interact. Inverse problem – to form series of eigenfrequencies in which the second and following frequencies are by some orders of magnitude greater then the first, have obvious and simple solution – lumped mass on the tip of cantilever. This solution was discussed in details in [2]. Starting with these results we investigate following shapes:

2. beam with variable cross section (exponential, thick at the root thin at the tip)
3. undercut beam
4. two parallel beams with slightly different thickness and common tip
5. strip cantilever with lumped mass in some position between root and tip

It is shown that in the first case there is some convergence of first two frequencies, but the effect is too small. In second case the effect is absent. Only third case gives reasonable result, but cantilever becomes complex enough to fabricate it using standard MEMS process. Fourth case and some other ideas are under investigation.

1. А.Н.Тихонов, А.А.Самарский. Уравнения математической физики. «Наука», М. 1972.
2. М.В. Лоханин, “Возможность реализации метода измерения малых сил”, Вестник ЯрГУ им. П.Г. Демидова , №1, 2009 с.27-30.

# Characterization of electrostatically-actuated metal microbeams

A.V.Postnikov, I.V.Uvarov, I.I.Amirov

Yaroslavl Branch of the Institute of Physics and Technology, Russian Academy of Sciences, Yaroslavl, Russia,  
amirov@yf-ftian.ru

An investigation into the responses of microbeams to electric actuations is presented. Electric actuation uses DC and AC voltages. Electrostatic force drives a mechanical element, a beam or plate, to perform different functions. Microbeam can oscillate and can be implemented in resonant sensors, or it can move back and forth as a switching element in microswitch and transmit signals in electric circuits. Frequency response of a microbeam (the dependence of the amplitude of the oscillation movement of the mechanical element on the frequency of the driving voltage) can give significant information about a microbeam under consideration. It is possible to determine resonance frequencies and quality factors of a microbeam using frequency response. The objective of the present work is to study, how the elastic properties of microbeams, residual stresses in metal films, types of damping sources could be determined using dynamic behaviour of microbeams [1, 2].

The switches were fabricated using surface micromachining technique with a total of four masking levels. No critical overlay alignment was required. The essential process included the following steps: 1) Formation of signal and ground lines. 2) Silicon nitride deposition. 3) Deposition of polysilicon sacrificial layer. 4) Deposition of three layers. 50 nm chromium, 250 nm aluminum, 50 nm chromium; patterning to form switching membranes. 5) Release: removing the polysilicon sacrificial layer by plasma SF<sub>6</sub> to finalize the switch structure.

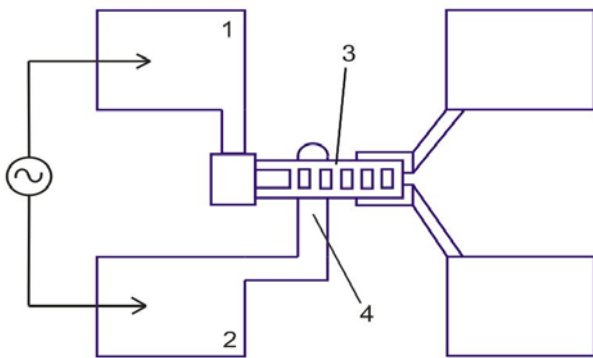


Fig. 1. Electrostatically actuated cantilever (top view, schematic): 1, 2 – contact plates; 3 – cantilever beam; 4 – RF line.

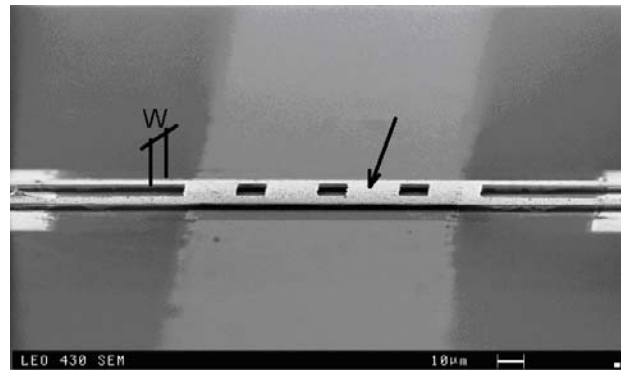


Fig. 2. SEM image of electrostatically actuated bridge.

Two types of microswitches cantilevers and bridges were studied. Top view of the cantilever is shown in fig.1. The cantilever had a beam clamped on one end, suspended over the RF line. The driving voltage was applied using contact plates. SEM photograph of the bridge is shown in fig.2. The bridge had a membrane clamped on both ends. The typical bridge (fig. 2) had the following dimensions: 270 μm length, 60 μm width, 350 nm thickness (50 nm Cr, 250 nm Al, 50 nm Cr), width of the suspension  $W = 10 \mu\text{m}$ , the gap between membrane and RF line beneath was 2 μm. The crucial point of this technology is the formation of switching membranes. Young's modulus of aluminium varies sufficiently depending on sputtering parameters.

At low excitation levels the clamped-clamped beam can be represented as a simple harmonic oscillator under a small signal model. Its principal resonant frequency  $f_0$  can be derived as follows [3]:

$$f_0 = 1.03 \sqrt{\frac{E}{\rho}} \frac{h}{L_r^2} \quad (1)$$

where  $E$  is the Young's modulus,  $\rho$  is the density,  $h$  is the thickness, and  $L_r$  is the length of the beam. The resonant frequency of the clamped-clamped microbeam can be experimentally measured and, therefore, Young's modulus in the metal film can be determined.

The dynamic behaviour of microbeams is affected by residual stresses. In the case of a clamped-clamped microbeam the axial residual stress component  $\sigma_N$  can be computed as follows [4]:

$$\sigma_N = \frac{\gamma_I}{\beta_I^4} \rho l^2 \omega_0^2 - \gamma_I \frac{EI}{Al^2} \quad (2)$$

where  $\beta_I = 4.768$ ,  $\gamma_I = 38.56$ ,  $\rho$  is the density,  $l$  is the beam length,  $\omega_0$  is the first natural structural frequency,  $E$  is the Young's modulus,  $I$  is the inertia moment,  $A$  is the area of the surface of the microbeam. To determine the residual stress components, the natural frequencies of the microbeam need to be measured.

Measurements were performed using the optical method. Laser beam (628 nm) was directed to the top of the microbeam transversely to the microbeam's surface. When the microbeam deflects, the laser beam reflected from the surface of the microbeam deflects, too. The deflection of the laser beam is proportional to the deflection of the microbeam.

Metrology data had shown different dynamic characteristics of MEMS structures. Fig 3a shows the response of cantilever versus frequency of applied sinusoidal voltage (measured for two different positions of the laser beam on the surface of the microbeam, Pos.1 and Pos.2 in fig.3). Structure has strongly pronounced resonances for different modes. Resonance frequencies of this cantilever are 4, 31, 62, 95, 104 and 208 kHz. Fig 3b shows the frequency response of another one cantilever. This structure shows no resonances and low quality factor.

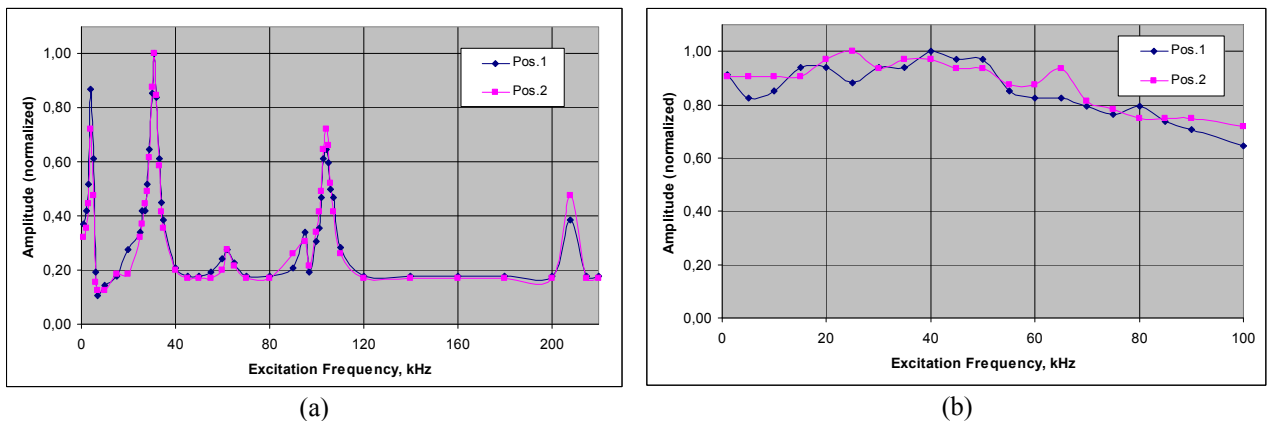


Fig.3. Frequency responses of two different cantilevers.

Such a difference between frequency responses of two cantilevers was caused by properties of aluminium, which was sputtered under different conditions. As a result, cantilever beams had different elastic properties. The structure with low quality factor is suitable for accelerometers and RF switches, structures with a high quality factor could be used as sensors elements.

The MEMS devices with movable membrane fabricated using surface micromachining were tested. The dynamic characteristics were found to be dependent on some technology parameters. Control over sputtering and release processes gives possibilities to obtain stress free membranes with different quality factor for specific purposes such as RF switches and capacitive-type sensors.

Work was supported by RFBR (N 10-07-0047-a).

1. W. Sharpe Jr., *The MEMS Handbook*, Ch3, pp.1-33, 2002
2. Stephen D. Senturia, *Microsystem Design*, Kluwer Academic Publishers, Dordrecht, 2001
3. F. D. Bannon and C. T.-C. Nguyen, "High-Q Hf microelectromechanical filters", *IEEE J. Solid-State Circuits* **35**, pp.1517 – 1517, 2000.
4. Aurelio Soma and Alberto Ballestra, "Residual stress measurement method in MEMS microbeams using frequency shift data", *J. Micromech. Microeng.*, **19**, pp.1-16, 2009

# Growth of carbon nanotubes on multilayers films surface

N.Savinski<sup>1</sup>, M.Gitlin<sup>1</sup>, A.Rusakov<sup>2</sup>, V.Naumov<sup>1</sup>, V.Orlov<sup>2</sup>

1. Yaroslavl Branch of the Institute of Physics and Technology, Russian Academy of Sciences, Yaroslavl, Russia,  
E-mail: Savinski1@yandex.ru. 2. Yaroslavl Demidov State University, Yaroslavl, Russia

Carbon nanotube CNT has attracted much attention since the discovery of its unique property and its potential for application to nanoelectronic devices such as field emission displays FEDs [1]. A growth technique of high quality CNTs directly onto a substrate at low temperature has been required in fabrication process for a FED. Chemical vapor deposition CVD is one of the promising techniques for the growth of CNTs [2,3] because it is possible to grow the nanotubes directly onto substrates at relatively low temperature than other techniques such as an arc discharge method and a laser ablation method. Recently, an alcohol catalytic CVD ACCVD technique, which is a thermal CVD technique using alcohol as carbon feedstock, has attracted much attention because of its ability to yield high quality CNTs and its simplicity in the growth process. Thus if low temperature CNT growth can be possible by the ACCVD method, it can be a high quality CNT growth method at low temperature that is applicable to a FEDs fabrication process. Actually, ethanol decomposes into water and ethylene when kept at the CVD temperature. Hence, the decomposition of some percentage of ethanol is usually expected. Fortunately, ethylene is a carbon source for SWNT growth [4]. In this study, Si<100> single crystal substrates with thermal dioxide silicon (350nm) on which titanium nitride and metal thin films were deposited were used for the CNTs. A Co/Al/TiN three-layered film deposited by RF- magnetron sputtering was formed as a catalyst. The Co layer serves as a catalyst for CNT growth. The Al layer is a buffer layer that prevents silicification of Co film and provides more nucleation sites. The TiN layer is conducting plane (conductor). Then Al was deposited onto the substrate that was followed by Co deposition. The thickness of the Al film was 20 nm and that of Co film was 2 nm. Substrates after the Al deposition were once exposed to air to transfer those into a vacuum evaporation chamber and then Co layers were deposited onto the substrates. After the catalyst deposition, the substrate was introduced into a horizontally fixed quartz tube reactor 37 mm in inner diameter.

The reactor was first evacuated by a mechanical pump and then heated to growth temperature. Ethanol 95% purity, the carbon feedstock used in this study, was then introduced into the reactor and the CNT growth was carried out. The growth time for the CNTs was 10 min. The growth of CNTs by the ACCVD strongly depended on the amount of the ethanol introduced into the reactor.

Thicknesses of the CNT layer are plotted in Fig. 1 as a function of the ethanol pressure. The CNT layer thickness is about 10 nm at 1000 Pa. This graph shows that ethanol supply onto the substrate is a rate-limiting process of this growth process. Vapor pressure of ethanol is 5863 Pa at 20 °C; thus 5332 Pa of ethanol pressure is virtually the upper limit in our CVD equipment. Further increase of the thickness of the CNT layer can be expected by increasing the introduction of ethanol vapor into the reactor. The growth was carried out at a temperature range from 400 to 750 °C. Figure 2 are SEM images of the CNTs grown at this temperature range. The higher growth temperature than 700 °C gives rise to a decrease of the CNT layer thickness. It should be noted that the CNT growth is confirmed at the low temperature as low as 450 °C. Growth of CNTs at 400 °C was also confirmed. The CNTs grown at the temperature less than 500 °C was in a randomly oriented fashion. The growth changes to a vertically aligned fashion at the higher temperature range than 500 °C. The difference in the growth fashion originated from the difference in the amount of CNT growth. A graph plotting a relation between the thickness of the CNTs layer and the growth temperature is shown in Fig. 3. The corresponding Arrhenius plot is also shown in Fig. 4.

In these graphs, three different regions, which show different temperature dependence, can be confirmed: region 1 400–550 °C, region 2 550–700 °C, and region 3 700 °C. Region 1 shows weak temperature dependence on the thickness of the CNT layer (growth velocity 5-6nm/min). The growth velocity steeply increases up to 30nm/min in region 2. The thickness reaches 3,5 μm 700 °C, which is 6 times higher than that at 550 °C. The thickness decreases at the region III. The CNT thickness drops to 10 nm/min at 750 °C. Activation energies of growth reactions for the three regions were estimated from the Arrhenius plot. The activation energies for regions 1 and 2 were 40,5; 79,3 and – 114 kJ/mole, respectively. The value at region II is close to the standard heat of formation for ethanol 235 kJ/mole. This implies that decomposition reaction of ethanol is promoted at this region, and this reaction is a rate-limiting step for a growth reaction of CNTs. The small activation energy seen in region I shows that a growth reaction at this region is remarkably

different from that in region II. A possible explanation for the growth reaction in region I is that a catalyst activity plays an important role for the decomposition of ethanol in this region. Thermal decomposition of ethanol may not be enough in this region due to its low temperature. Thus catalyst-assisted decomposition is a rate-limiting step for the CNT growth in this region. Region III shows negative temperature dependence. This result indicates that an inhibition of CNT growth occurred at this region. A possible mechanism that explains the inhibition is that the high temperature gives rise to a coalescence of catalyst particles and increase of catalyst particle size. The increase of size reduces the growth rate of CNTs.

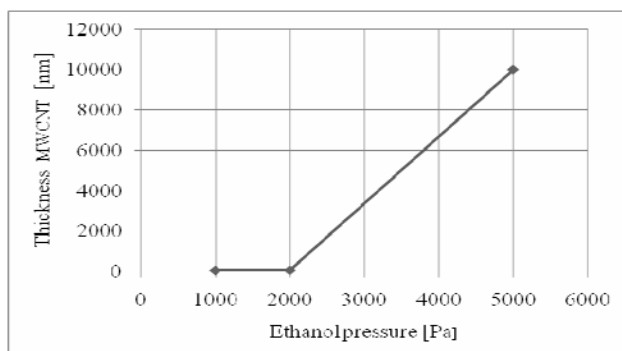


Fig.1 Thicknesses of the CNT layer as a function of the ethanol pressure

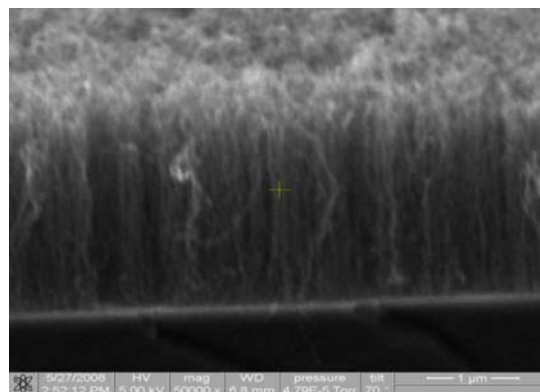


Fig. 2 The growth of CNTs by the ACCVD.

Another mechanism to explain the inhibition is the etching reaction of CNTs. The etching reaction stems from etchant species such as oxygen produced by the decomposition of ethanol. The reaction becomes more active at higher temperature range.

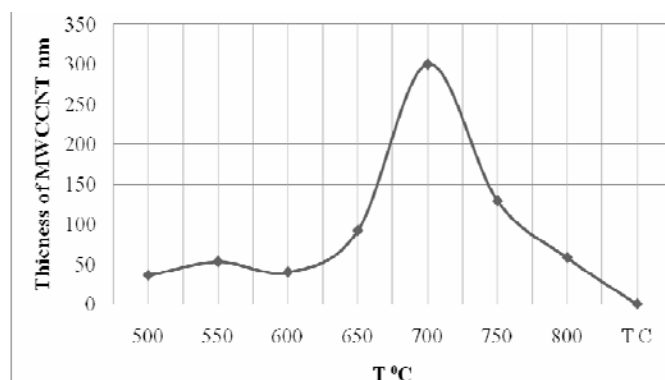


Fig. 5 The thickness of the CNTs layer as a function growth temperature.

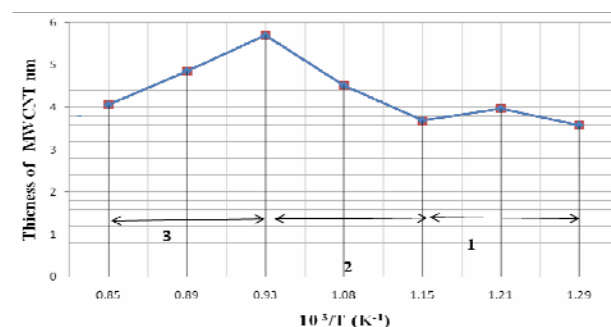


Fig 4 The Arrhenius plot thickness of the CNTs layer as a function growth temperature.

1 Advanced Micro & Nanosystems. Carbon Nanotube Devices., Ed. C. Hierold, Vol. **8**, pp.462, Wiley-vch verlag, 2008

2 Limin Huang, B. White, Matthew Y, Mingyuan Huang, Henry X. Huang, Shalom Wind, J. Hone, and S. O'Brien "Cobalt Ultrathin Film Catalyzed Ethanol Chemical Vapor Deposition of Single-Walled Carbon Nanotubes", J. Phys. Chem. B; V **110** (23) pp. 1103 – 1110, 2006

3 K.B Konravelov, S.V. Sotirchos "Dynamic study of carbon nano-tube production by chemical vapor deposition of alcohol" Rev. Adv. Mater Sci., V.**10**, pp. 243-248, 2005

4 Hisayoshi OSHIMA, Yoshinobu SUZUKI, Tomohiro SHIMAZU, and Shigeo MARUYAMA "Novel and Simple Synthesis Method for Submillimeter Long Vertically Aligned Single-Walled Carbon Nanotubes by No-Flow Alcohol Catalytic Chemical Vapor Deposition" Japanese Journal of Applied Physics, V. **47**, No. 4, , pp. 1982–1984, 2008

# The microwave polyol nano-reactors synthesis of metallic nanoparticles

N.Savinski, V.Naumov

Yaroslavl Branch of the Institute of Physics and Technology, Russian Academy of Sciences, Yaroslavl, Russia,  
E-mail: Savinski1@yandex.ru

Potential applications in electronic, optic, and electrooptical devices and sensors have prompted the development of a large variety of colloid chemical methodologies for the preparation of stable monodisperse nanoparticles [1,2]. Hyperfine metals prepared by chemical method which offers the following principal advantageous : low cost, simple reaction procedure, possible scaling-up, bulk-quantity of product, high chemical purity metals, monodispersed particles, control of particle size from a very small level. The main chemical way is the reduction of metal ions in solution in conditions favoring the subsequent formation of small metal clusters or aggregates. The main disadvantages of chemical syntheses in liquid phase are their relatively low stability that requires the use of organic stabilizers and thus complicates the structure and studies of the properties of the whole system. The particle stability can be significantly enhanced for the chemical synthesis in the media saturated with organic stabilizer. With respect to the mode of particle stabilization, chemical methods may be divided into groups: chemical stabilizers as natural or synthetic polymers and stabilizers forming micellar solutions where aggregation process takes place in the aqueous core of reverse micelles and growing particles are surrounded by the surfactant molecules [3].

## Polyol technique

The ethylene glycol (EG) and polyethylene glycols (PEG) -mediated synthesis is known to be one of the most powerful general methods to prepare uniform nanomaterials . Ethylene glycol (EG) has been widely used in the polyol synthesis of metal nanoparticles because of its physical properties:

- 1) a high dielectric constant, which enhances the solubility of inorganic salts,
- 2) a high boiling point (195°C at atmospheric pressure), which makes it possible to carry out the preparation of inorganic compounds at relatively high temperatures, and
- 3) its strong reducing power.

In the ethylene glycol process, the alcohol served both as solvent and reducing agent for metal ions. However due to slow reaction rate, the synthesis is often carried out at higher temperatures, e.g. 90–160 oC to shorten the reaction time. It is believed that microwave heating offers faster and more uniform heating than conventional heating and thus leads to

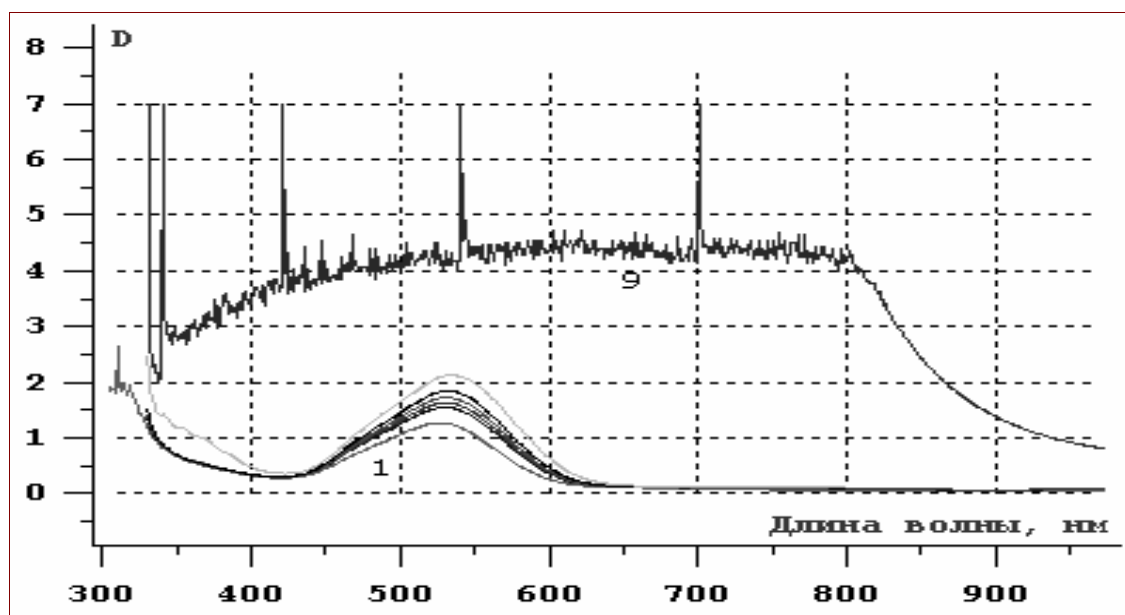


Fig. 1 The time evolution of UV/Vis spectra for solution MPEG of 0.075 M/l  $\text{Co}(\text{NO}_3)_2 \cdot 6\text{H}_2\text{O}$ . The time of exposure MW radiation is 1-0 min, 2-1min, 3-2min, 4-3min, 5-5 min, 6-7min, 7- 10 min, 8-13min, 9- 15min.

more uniform generation and growth of nuclei and avoids the formation of impurity phase. They may have possibly served as nanoreactors for nucleation and crystal growth and inhibited the excess aggregation of particles because the surfactants can absorb on the particle surface. Microwave synthesis is an optimal method for preparing nanoparticles via the polyol method. The metallic particles that are produced during the polyol reaction are excellent receptors for microwave energy which leads to even more rapid heating of the solution.

When these metallic particles are exposed to microwave radiation it can create localized superheated regions in the solvent. The maximum power home microwave oven type “SUPRA” (1500W ; 2.45 GHz) was applied to the microwave cavity until the set temperature was reached. Figure 1 shows the time evolution of the UV/Vis spectra for a methoxy polyethyleneglycol (MPEG) solution of  $\text{Co}(\text{NO}_3)_2$ , and SDBS (sodium dodecyl benzene sulfonate). At the initial stage of reaction, adsorption bands was observed with max at 270 nm and 536 nm. This band can be attributed to the  $\text{Co}(\text{NO}_3)_2$ . The increase in the intensity of the adsorption band 536 nm was observed with exposure MW radiations time. However, a characteristic adsorption broad band from 350nm to 800 nm appeared after 13 minutes exposure MW radiations. This band can be attributed to the localized surface plasmon excitation of cobalt particles. The increase in the intensity of the adsorption band with exposure MW radiations time is due to the increase in concentration of cobalt nanoparticles.

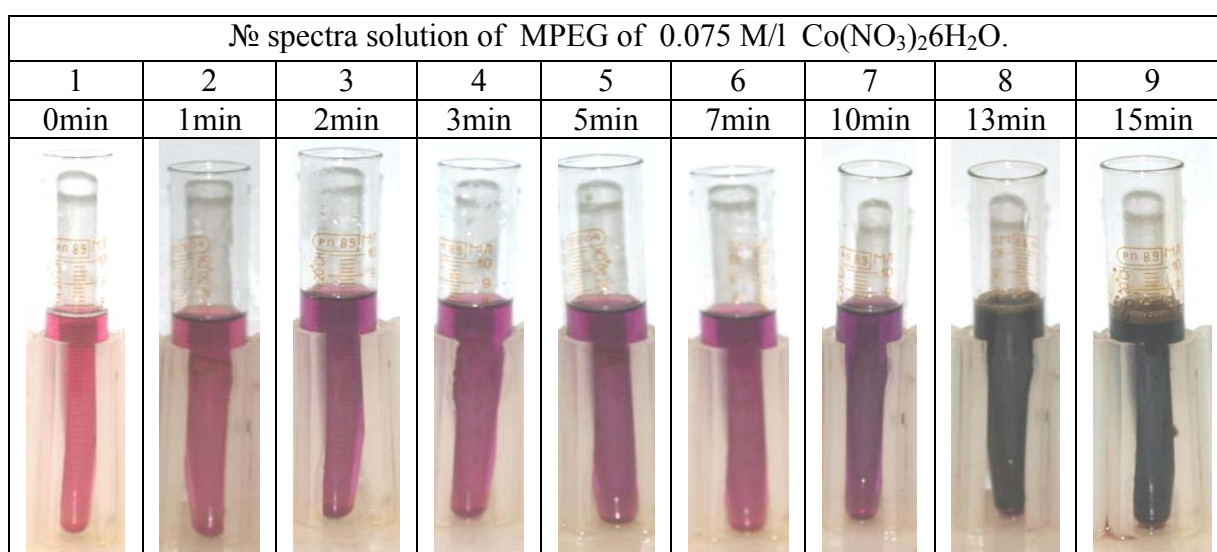


Fig. 2 The samples of solution MPEG of 0.075 M/l  $\text{Co}(\text{NO}_3)_2 \cdot 6\text{H}_2\text{O}$ . The time of exposure MW radiation is 1-0 min, 2-1min, 3-2min, 4-3min, 5-5 min, 6- 7min, 7- 10 min, 8-13min, 9- 15min.

Products were centrifuged in a MLM T24D Centrifuge counter balanced with a centrifuge tube The solutions were typically centrifuged for 240 minutes at 17000 rpm. Washes consisted of sonicating in ethanol three times and a final sonication in n-hexane. The solution fractions were typically discarded after centrifuging leaving a grey powder insoluble in both ethanol and n-hexane. The product was dried under a nitrogen flow. This procedure was repeated using microwave heating. The products from each heat source were compared.

1 Metallic Nanoparticles Volume Editor John, B.V. Elsevier Amsterdam, 2009

2 Plasmonic nanoguides and circuits, editor Sergey I Bozhevolny pp. 441, Pan Stanford Publishing Pte. Ltd, 2009.

3 Nanoparticles: Synthesis, Stabilization, Passivation, and Functionalization ACS Symposium Series Editor R. Nagarajan pp.449, 2008 American Chemical Society Distributed by Oxford University Press



# Solution combustion synthesis of nanooxide catalysts for growth carbon nanotube and nanowire

N.Savinski, V.Naumov

Yaroslavl Branch of the Institute of Physics and Technology, Russian Academy of Sciences, Yaroslavl, Russia,  
E-mail: Savinski1@yandex.ru

Combustion synthesis or fire synthesis is also known as self-propagating high-temperature synthesis (SHS). To generate fire, an oxidizer, a fuel, and the right temperature are needed. All these three elements make up a fire triangle. Fire can be described as an uncontrolled combustion, which produces heat, light, and ash (Fig. 1). The process makes use of highly exothermic redox chemical reactions between an oxidizer and a fuel.

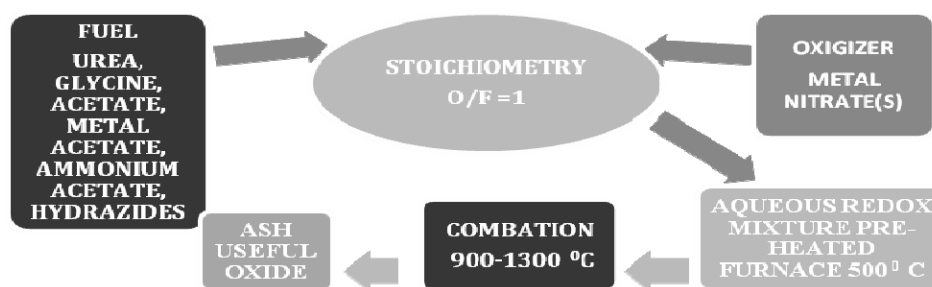


Fig. 1 Scheme SHS process in solution

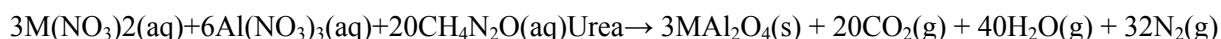
The SHS process pioneered by Merzhanov has been used to prepare a large number of technologically useful oxidematerials (refractories, magnetic, semiconductors, dielectric, catalysts, sensors, phosphors, etc.) and nonoxide materials (carbides, nitrides, borides, silicides) by the solid-state reaction between the corresponding metals and nonmetals. The process requires high-purity fine precursors, which ignite at temperatures >10000 C. The process is highly exothermic (Tad 4000 0C) and self-propagating resulting in coarse products. This process has been successfully used in Russia to prepare hundreds of technologically useful materials, including the preparation of oxide materials in recent times. However, being a solid-state reaction it often does not produce homogeneous products and results in coarse powders. Here, the solution combustion approach is presented to prepare oxide materials of desired composition, structure, and properties. The term combustion covers flaming (gas-phase), smouldering (solid-gas) as well as explosive reactions.

One of the important advantages of solution combustion synthesis is the ease of incorporating any desired amount of impurity atoms or ions in a given oxide matrix. This has been demonstrated by incorporating a variety of metal atoms/ions in alumina and aluminate matrix. As the dopants are of nanosize, they result in the formation of nanocatalysts, nanopigments, and nanophosphors etc.

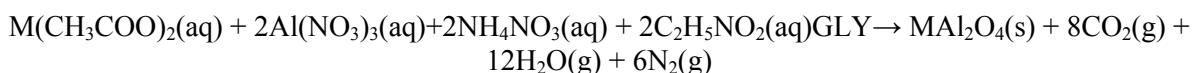


where A = Mg, Zn, Ni, Cu, ...

Typical theoretical equations assuming complete combustion for the preparation of various  $MAl_2O_4$  are given below.



(31mol of gases/mol of  $MAl_2O_4$ ) M = Mg, Ca, Sr, Ba and Zn



(32mol of gases/mol of  $MAAl_2O_4$ ) M = Mg, Mn, Fe, Co, Ni, Cu and Zn



Catalytic CVD methods, in which CNT production is enhanced by metal nano- particle catalysts either suspended in the gas-phase or supported on either substrates or particles, are now widely used to synthesize CNTs. The preparation method of catalyst nanoparticles is critical in the growth of CNTs directly on device substrates. The typical catalyst metals (Fe, Co, Ni) form particles wet partially on a typical support layer ( $\text{SiO}_2$ ,  $\text{Al}_2\text{O}_3$ , or  $\text{MgO}$ ) under equilibrium due to the balance among their surface/interfacial energies and this equilibrium structure makes the latter approach of catalyst preparation effective. The synthesis of vertically aligned carbon nanotubes with submillimeter-order heights was performed using ethanol chemical vapor deposition with Co catalysts supported on  $\text{Al}_2\text{O}_3$  substrates. The effects of  $\text{Al}_2\text{O}_3$  in the form of amorphous alumina and single-crystalline sapphire were investigated through a characterization of the Co catalyst particles on the substrates. An important effect of  $\text{Al}_2\text{O}_3$  was found to be the production of highly dense and nanosized Co particles, owing to a low surface diffusivity[1].



Fig. 2 Cobalt aluminate  $\text{CoAl}_2\text{O}_4$

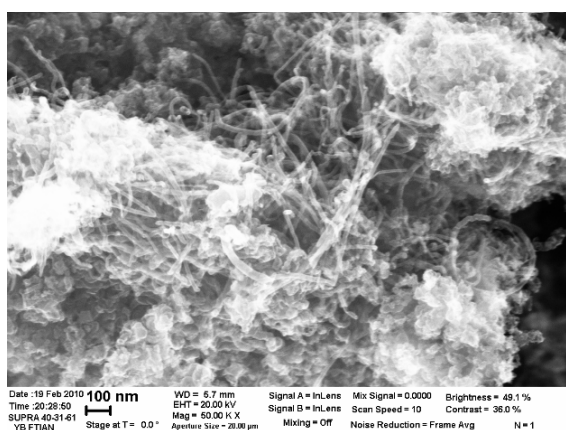


Fig. 3 SEM foto of cobalt aluminate  $\text{CoAl}_2\text{O}_4$

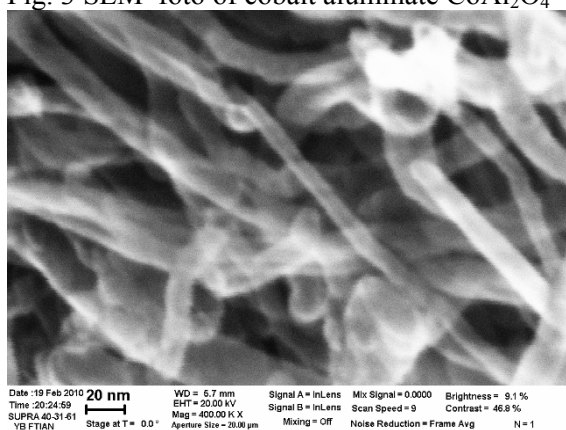


Fig 5 The thick carbon nano ware CVD process on catalyst  $\text{CoAl}_2\text{O}_4$

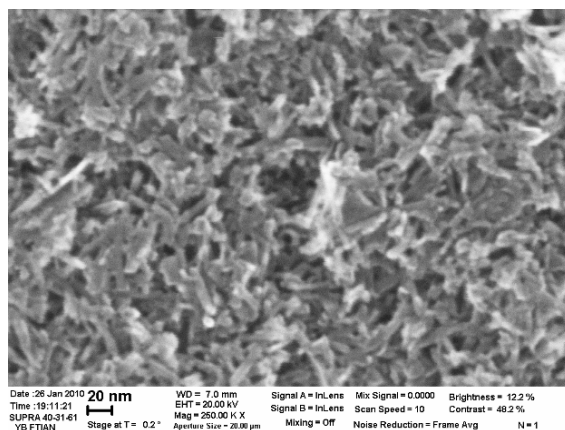


Fig.4 Growth of CVD CNT on catalyst  $\text{CoAl}_2\text{O}_4$

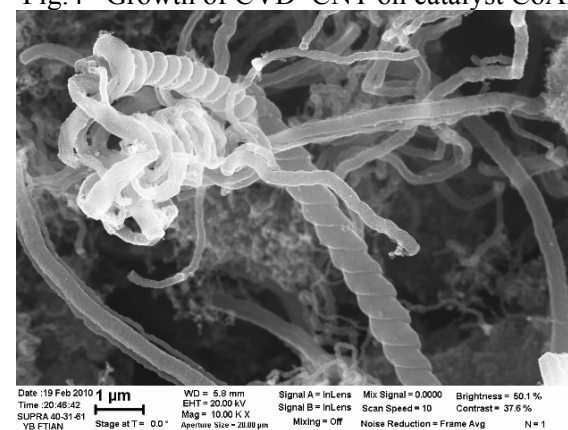


Fig 6The thin carbon nano ware CVD process on catalyst  $\text{CoAl}_2\text{O}_4$

1.Hiroshi OHNO, Daisuke TAKAGI, Kazuki YAMADA, Shohei CHIASHI, Akio TOKURA and Yoshikazu HOMMA “ Growth of Vertically Aligned Single-Walled Carbon Nanotubes on Alumina and Sapphire Substrates”. Japanese J. Appl. Physics, Vol. 47, No. 4, pp. 1956–1960, 2008.

# Template synthesis of water soluble PANI

N.Savinski

Yaroslavl Branch of the Institute of Physics and Technology, Russian Academy of Sciences, Yaroslavl, Russia,  
E-mail: Savinski1@yandex.ru

As a member of the  $\pi$ -conjugated polymers, PANI could be implemented in electronic conductors, light-emitting diodes and chemical sensors, in hyper – capacitor [1, 2]. When exploited as active sensing element, the coupling of ligands to its backbone results in physical distortions, or changes in electronic structure, and thereby modifies conductivity. A PANI–PANI secondary battery system has been built on the basis of the reversible electrochemical doping and undoping (oxidation and reduction) processes of PANI in acidic media [3]. It has been utilized in rechargeable lithium–PANI batteries[4].

PANI- based coatings exhibit anticorrosive behavior and stability in air . A PANI has been shown to have, among other polymeric properties, a high electrical conductivity and that its electronic character also depends on the acidity, redox level and hydration. A PANI can be synthesized chemically giving a precipitate, or electrochemically in the form of thin films, from aqueous solution. The main problem of PANI is that it is poorly soluble in most common solvents, hampering experimental studies and limiting its industrial exploitation. The matrix polymerization of aniline neutralized by polymeric acids is of prime significance as a method of preparing **soluble** materials combining electrophysical and optical properties of polyaniline (PANI) and the mechanical properties of polymer materials. Previously used and poly (2-acrylamino-2-methyl-1-propane) sulfonic acid (PAMPSA) [5], are distinguished by the regular distribution of sulfo acid groups along the main chain of macromolecules. It was assumed that, upon protonation of aniline by the above polyacids, the resulting PANI macromolecules would be located along polyacid macromolecules and form a two-strand macromolecular structure of the interpolymer complex. In this case, the conformations of polyacid and PANI macromolecules are changed to adjust each other.

The PANI is composed of ANI repeat units connected to form a backbone. The existence of a nitrogen atom lying between phenyl rings allows the formation of different oxidation states (doping) that can affect its physical properties. In general, three distinct forms are available, depending on the degree of oxidation of the nitrogens (Figure 1):

- (a) A leucoemeraldine base (LB) is a fully reduced form which contains only benzene rings in the polymer chain.
- (b) An emeraldine base (EB) is a half oxidized form, where both benzene and quinoidal rings are presented.
- (c) A pernigraniline (PNB) is a fully oxidized form.

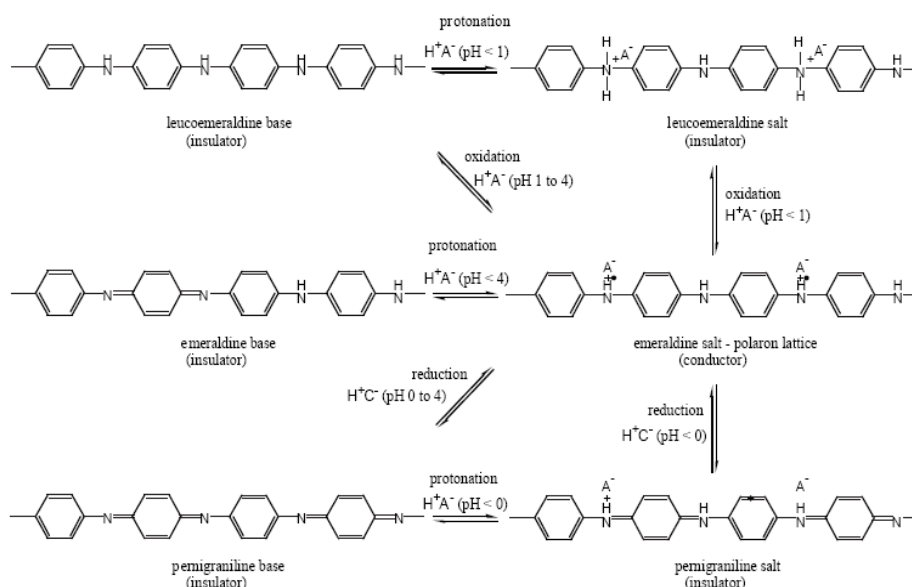


Fig 1 The scheme doping and undoping (oxidation and reduction) processes of PANI in acidic media.

The synthesis was performed at room temperature while successively mixing solutions of PAMPSA, aniline, and ammonium persulfate in water. The ratio of PAMPSA to aniline in the reaction mixture was 1 : 1 mole-unit/mole, and that of aniline to oxidant 1 : 1.25 mole/mole. The concentration of aniline and PAMPSA in the reaction mixture 0.034 M/ L. The conducting emeraldine salt (ES) form can be obtained by oxidative doping of LB, or by protonation of EB. The LB forms are basically insulators characterized by large band gaps and the lack of charge carrier, whereas the PNB forms are considered to be semiconducting. Figure 2 shows the kinetic curves illustrating a variation in the optical absorption of reaction solutions at wavelengths of 450, 650, and 750 nm. As is seen, the optical densities of all these bands simultaneously increase for all polymers. In other words, the polymerization of aniline leads to the simultaneous formation of various electronic structures: cation radicals (450 nm), uinoimine fragments (650 nm), and localized polarons (750nm). The  $\pi^* \leftarrow \pi$  maximum absorption band in the LB form is about 3.6–3.8 eV, which is smaller than that of ANI 4.2 eV, but remains large due to an inhibited connection between the ring and the saturated nitrogen linkage. Thanks to a better conjugation between the ring and imine linkage, the  $\pi^* \leftarrow \pi$  maximum absorption of the PNB form becomes lower, being 1.7–2.3 eV. In the doped ES form, electrical conductivity is greatly increased by the formation of low-energy hole levels. The low band gap of 1.5 eV in ES is interpreted as arising from excitations to the polaron band.

The autocatalytic character of formation of PANI was inferred in from the kinetic measurements of a change in the optical densities of bands corresponding to the absorption of amine and quinoimine forms of PANI and in from the kinetics of a reduction in the optical absorption of aniline during its polymerization in the presence PAMPSA.

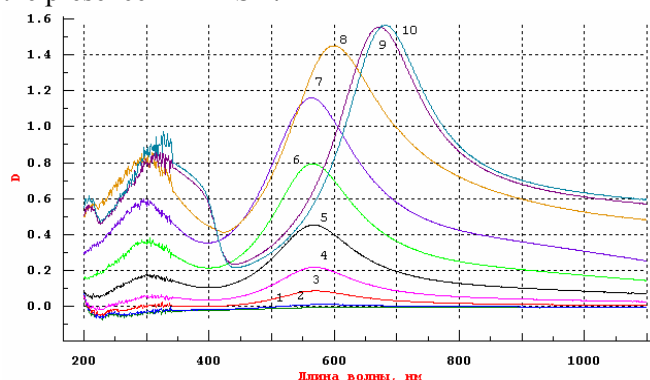


Fig. 2 Variations in the electronic absorption spectra of PANI solutions synthesized in the presence PAMPSA of the time of polymerization is: 1- 0 s, 2 – 240s. 3– 540s 4 – 660s 5 – 795s 6- 925s 7 – 1090s 8 – 1200s 9 – 1335s 10 – 1565s. [Aniline] = 0.7 mM/ L.

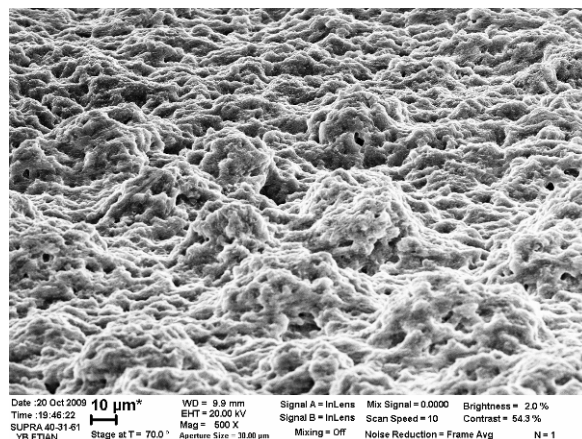


Fig 3 FESEM image of the spin-cast film of PANI–PAMPSA (1:1 M/M)

The electroconductivity of film determined by of polyaniline synthesized by the method of template synthesis with PAMPSA, which was spinning on transparent glass electrode ITO from an aqueous solution at 3500 rpm. An electroconductivity, was measuring by the four-probe method at room temperature, was equal to 0.25 Scm<sup>-1</sup>.

1 Eduardo, H.L.F., Azedado, W. M., “Polyaniline – polyvinyl alcohol composite as an optical recording material.” *Synthetic metals*, v.**128**, pp. 149-154, 2002

2 Koul, S., Chandra, R., Dhawan S.K. “ Conducting polyaniline composite a reversible sensor materials for aqueous ammonia.” *Sensors and Actuators B*; v.**75**, pp.151-159

3 A. J. Epstein, J. A. O. Smallfield, H. Guan, M. Fahlman, “Corrosion protection of aluminum and aluminum alloys by polyanilines: a potentiodynamic and photoelectron spectroscopy study”, *Synthetic Metals*, v.**102**, pp.1374, 1999

4 Morita M., Miyazaki S., Ishika H., Matsuda Y, Tajima, H., Adachi K., “Chage/discharge characteristic of polyamine based polymer composite positives for rechargeable lithium batteries ” *J. Power Sources*; v.**54**; pp. 214-217, 1995.

5 V. F. Ivanov, O. L. Gribkova, K. V. Cheberyako, A. A. Nekrasova, V. A. Tverskoi, and A. V. Vannikov “Template Synthesis of Polyaniline in the Presence of Poly-(2-acrylamido-2-methyl-1-propanesulfonic Acid)” *Russian Journal of Electrochemistry*, Vol. **40**, No. 3, 2004, pp. 299–304. Translated from *Elektrokhimiya*, Vol. 40, No. 3, 2004, pp. 339–345.



# Silver nanoparticles prepared by photo-polyol methods

N.Savinski, V.Naumov

Yaroslavl Branch of the Institute of Physics and Technology, Russian Academy of Sciences, Yaroslavl, Russia,  
E-mail: Savinski1@yandex.ru

Metal nanoparticles can be widely applied in optical, electronic, catalytic, magnetic materials and semiconductors [1] because of their unusual properties and potentials. However, they are hardly useable by themselves since they are poor at dispersion stability and tend to aggregate in the medium. Silver ions have long been known to have strong inhibitory and bactericidal effects as well as a broad spectrum of antimicrobial activities [2]. Therefore, silver has been commercially used to take advantage of its antibacterial properties. Metallic (e.g., Ag, Au, and Cu) nanoparticles have fascinated scientists for several centuries, partly because of the colorful colloidal solution of metallic nanoparticles, in which resonant electron oscillations on the surface of noble metal nanoparticles create the surface plasmon resonance (SPR) that greatly enhances the absorption and Rayleigh (Mie) scattering of light by these particles. The relationship between the SPR absorption spectra and such particle properties as their dimensions or the surrounding environment has been well established [2].

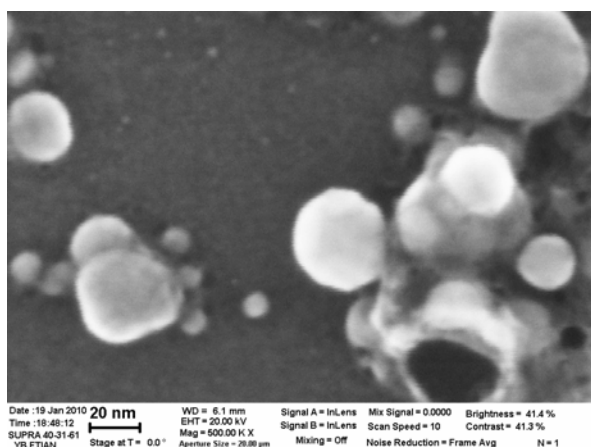


Fig. 1 FESEM image of the silver nanoparticles after were centrifuged from MPEG solution.

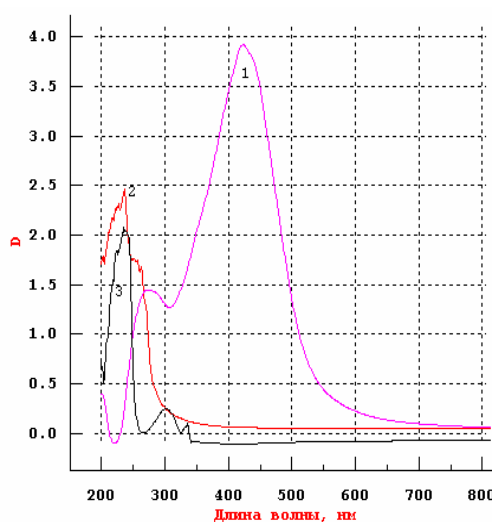
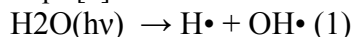


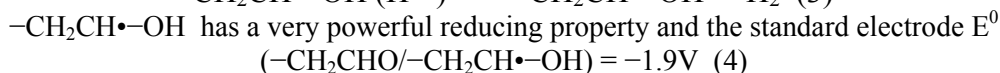
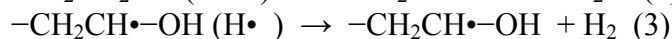
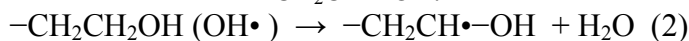
Fig. 2 1)- the UV/Vis spectra for silver nanoparticles surface plasmon resonance (SPR) obtained during photo chemical synthesis with 0.005 M  $\text{AgNO}_3$  in methoxy polyethyleneglycol (MPEG) solution with SDBS (sodium dodecyl benzene sulfonate), 2) - absorption spectra of methoxypolyethyleneglycol (MPEG) solution with SDBS (sodium dodecyl benzene sulfonate), 3) - absorption spectra of electrolyte : aqueous solution of 0.005 M  $\text{AgNO}_3$

The nanosized silver particles have been prepared from an aqueous solution of silver nitrate employing only formaldehyde and trisodium citrate as a reductant and a stabilizer, respectively, which can be easily removed from the resulting nanoparticles by washing. The chemical states of  $\text{Ag}^+$  at the initial stage of reaction, no obvious adsorption band was observed. However, a characteristic adsorption band centered at 420 nm appeared after a few minutes. This band can be attributed to the surface plasmon excitation of silver particles. The increase in the intensity of the adsorption band with electrolysis time is due to the increase in concentration of silver nanoparticles (Fig. 2) The change in color of the solution, from a light yellow at the beginning of experiment, to a dark yellow, and then to brown at the end of experiment, also reflects the formation of more and more silver nanoparticles. The mean diameter of silver particles was 10.1 nm when synthesized using MPEG as the stabilizer and sodium dodecylbenzenesulfonate SDBS, or Oleic Acid as the costabilizer. Furthermore, the concentration of the silver particles increased with increasing the MPEG concentration in the initial reaction solution have a profound influence on the size and size distribution of the resulting silver nanoparticles. In the polyol process methoxy polyethylene glycol (MPEG,

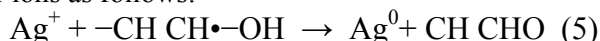
$\text{CH}_3\text{O}(\text{CH}_2\text{CH}_2\text{O})_n\text{H}$  acts as a reducing agent. It generates free radicals by ultraviolet irradiation which reduce the metal ions. MPEG also act as the template of the metal particles. Thus, photolysis of water in presence of a ultraviolet source ( $h\nu$ ) leads to the formation of radicals which then take part in the further steps [3]:



The scavenger of the  $\text{H}\cdot$  and  $\text{OH}\cdot$  radicals is  $\text{CH}_2\text{CH}_2\text{OH}$ , and this yields potential ( $E^0$ ) value is:



which is able to reduce silver ions as follows:



A preparative method for silver particles by taking the advantage of the orientation of polymer methoxy polyethylene glycol (MPEG) in an ultraviolet environment has been reported by Mallick et al. [3]. MPEG generates free radicals which serve as the reducing agent for the silver ions in the presence of ultraviolet irradiation and also act as the template of the silver particles involved in the formation of the silver chain. For the synthesis of metal nanoparticles, the first step involves the reduction of the metal ions in solution. The atoms produced act as nucleation centers and catalyze the reduction of the remaining metal ions present in the bulk matrix. This stage of the process has an autocatalytic nature. The reduction potential of the metalion/metalatom and the metalion/metalcluster systems becomes more negative than that of the corresponding bulk metal. The reduction potential of the Ag ion/Ag bulk (aqueous) system is + 0.79V versus normal hydrogen electrode (NHE), but for the Ag ion/Ag atom (aqueous) system it is -1.8V versus NHE .

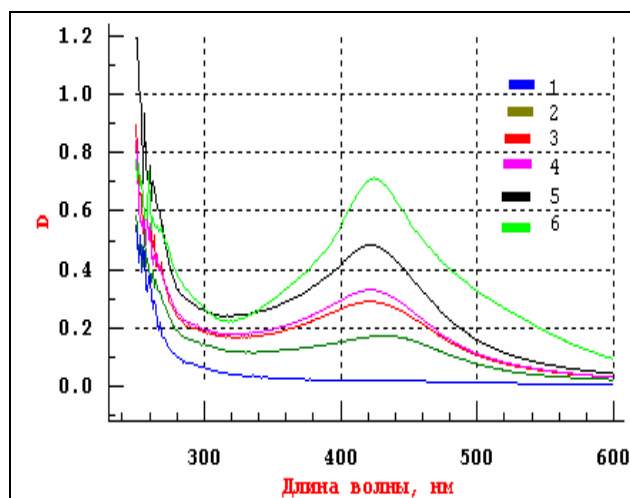


Fig.1 The time evolution of UV/Vis spectra for solution MPEG with SDBS of 0.065 M/l  $\text{AgNO}_3$   
1 - 0 мин, 2 - 9 мин, 3 - 25 мин, 4 - 35мин, 5 - 48мин, 6 - 1260 мин

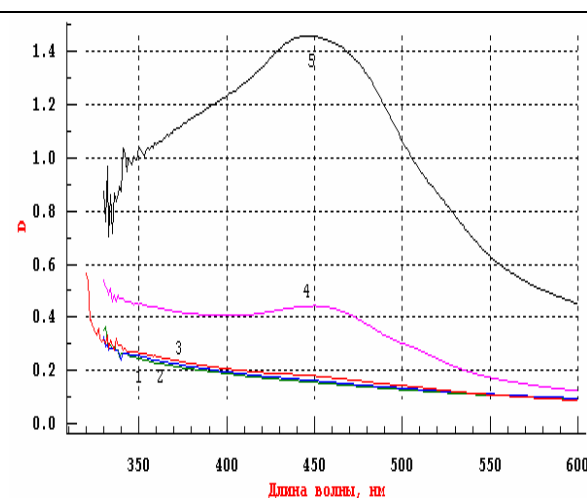


Fig. 2 The time evolution of UV/Vis spectra for solution MPEG with OLA of 0.065 M/l  $\text{AgNO}_3$   
1 - 0 мин, 2 - 18 мин, 3 - 90 мин, 4 - 1380 мин, 5- 14400 мин

1 Ke Xu, Jie-Xin Wang, Xu-Liang Kang, Jian-Feng Chen *Fabrication of antibacterial monodispersed Ag-SiO<sub>2</sub> core-shell nanoparticles with high concentration* Materials Letters 63 (2009)pp. 31-33 ELSEVIER

2 E.Ozbay *Plasmonics: Merging Photonics and Electronics at Nanoscale Dimensions*. Science, Vol. **311**, pp.189-193; January 13, 2006

3 I.Capek *Nanocomposite Structures and Dispersion* Science and Nanotechnology Fundamental Principles and Colloidal Particles pp.299 Elsevier Amsterdam 2006.

# Carbon nanotube emitter matrixs based autoemission devices

N.Savinski, M.Gitlin, A.Shornikov

Yaroslavl Branch of the Institute of Physics and Technology, Russian Academy of Sciences, Yaroslavl, Russia,

E-mail: Savinski1@yandex.ru

Vacuum auto-electron micro-devices AEMD have certain advantages over semiconductor devices. The major are temperature operation range (from  $-130^{\circ}$  till  $+300^{\circ}\text{C}$ ) and resistance to radiation impact. These features are due to the nature of auto-electron emission. The next advantages are related to its super performance as ballistic electron transfer from cathode to anode is a matter of sub-picosecond range. The general trend of vacuum electronics development at recent years is research of ways to shrink low voltage AEMD by design and process means. Following this trend the design based on nanotechnology in general and self-organizing nanostructure process in particular is considered more and more attractive. CNT FEC array is the only functional nanoscale element of device. CNT FEC arrays have excellent features. Along with exciting gain due to self-organizing process CNT within FEC arrays are formed at distances compared with its diameter. Furthermore CNT arrays grow vertically only in case when distance between CNT is so small that Van der Waals interaction takes place. As we already mentioned above emitters at the central area of FEC array are screened, emission current may be unstable as intensively operating edge CNT may burnout. But is each sole CNT-emitter, grid, anode isolate with vacuum surrounding screening problem may be suppressed. This shall cause sufficient emission current density increase because of increase of effective emitter quantity per square unit. Another target is formation of nanoscale vacuum inter-electrode distance which is a matter for device performance limits and power consumption. Such distance shall be not more than CNT diameter. AEMD performance is determined by cathode-anode electron transition along with respective electrodes capacitance. As there is certain electric field non-uniformity at cathode-grid high field level space and grid-anode space with better field uniformity but lower field level, cathode-anode electron transition time  $\tau_{k-a}$  should be determined as a sum of respective times

$$\tau_{k-a} = \tau_{k-g} + \tau_{g-a},$$

where  $\tau_{k-g}$  is transition time for cathode-grid space and  $\tau_{g-a}$  is transition time for grid-anode space

First approximation of cathode-grid electron transition time is determined as

$$\tau_{k-g} = \sqrt{\frac{2m}{eU_g}} (d_{k-g} - h_k),$$

where  $d_{k-g}$  is the distance between electrodes,  $h_k$  is nano-cathode height,  $U_g$  is grid potential,  $e$  and  $m$  are electron charge and mass respectively. Calculating grid-anode transition time it is necessary to take into account certain acceleration of electrons due to grid potential  $U_g$ .

$$\tau_{g-a} = \sqrt{\frac{2m}{e} \frac{(d_{g-a} - h_a)}{\sqrt{U_g} + \sqrt{U_a}}}$$

Let's expect 1V voltage is applied to grid and 4V voltage is applied to anode. Along with estimation of  $(d_{k-g} - h_k)$  and  $(d_{g-a} - h_a)$  about 5nm each we get accordingly. Let's expect 1V voltage is applied to grid and 4V voltage is applied to anode. Along with estimation of  $(d_{k-g} - h_k)$  and  $(d_{g-a} - h_a)$  about 5nm each we get accordingly

$$\tau_{k-g} = 16.85 \cdot 10^{-15} \text{ s} \quad \tau_{g-a} = 5.62 \cdot 10^{-15} \text{ s} \quad \tau_{k-a} = 22.47 \cdot 10^{-15} \text{ s}.$$

Cutoff frequency may be evaluated as

$$f_m = \frac{1}{2\pi\tau} \approx 7.1 \cdot 10^{12} \text{ Hz}$$

Besides electron transition time  $\tau_{k-a}$  inter-electrode capacitance affects nano-triode performance features: input capacitance between cathode and grid ( $C_{k-g}$ ) and output capacitance ( $C_{g-a}$ ). These are actual capacitance of the gaps between electrodes.

For the case of 10nm multi-wall nano-emitter with 20nm anodized aluminum oxide isolation and 10nm inter-electrode distance incoming capacitor may have following capacitance

$$C = \frac{\epsilon_0 \epsilon S}{d}$$

$$C_{k-g} = 8.855 \times 10^{-12} \times 8 \times 236 \times 10^{-18} / 100 \times 10^{-9} = 16.7 \times 10^{-20} \text{ F/m}$$

Let us evaluate inter-electrode capacitance affect upon amplifier performance with  $314 \text{ nm}^2$  active area nano-triode described above. Input and output circuits of the amplifier are considered to be microstrip lines. Input capacitance  $C_{k-g}$  between cathode and grid parallel input circuit. This capacitance mostly effect gain frequency characteristic at high frequency segment. Frequency performance limit at 3dB level may be considered by formula below

$$f_y = 1/\pi ZC$$

where Z is input microstrip line wave resistance (actually it is supposed to equal 50 Ohm). So we get

$$f_y = 1.907 \times 10^{16} \text{ Hz}.$$

This evaluation show that electron transition time is the major factor to define nano-triode performance level.

Residual gas pressure one has in vacuum micro-devices is about  $1-3 \times 10^{-6} \text{ Pa}$ . The main reason to have such high vacuum level in auto-emission micro-devices is to provide stable cathode emission current

Table 1. One-molecule residual gas pressure vs cathode-anode distance when channel diameter is 10nm.

d, nm	5	10	30	50
P, Pa	1910	955	318	190

With these results we get good news that extremely high vacuum is not mandatory factor for efficient performance of nano-triode. Definitely a lot of technological restrictions and difficulties are eliminated.

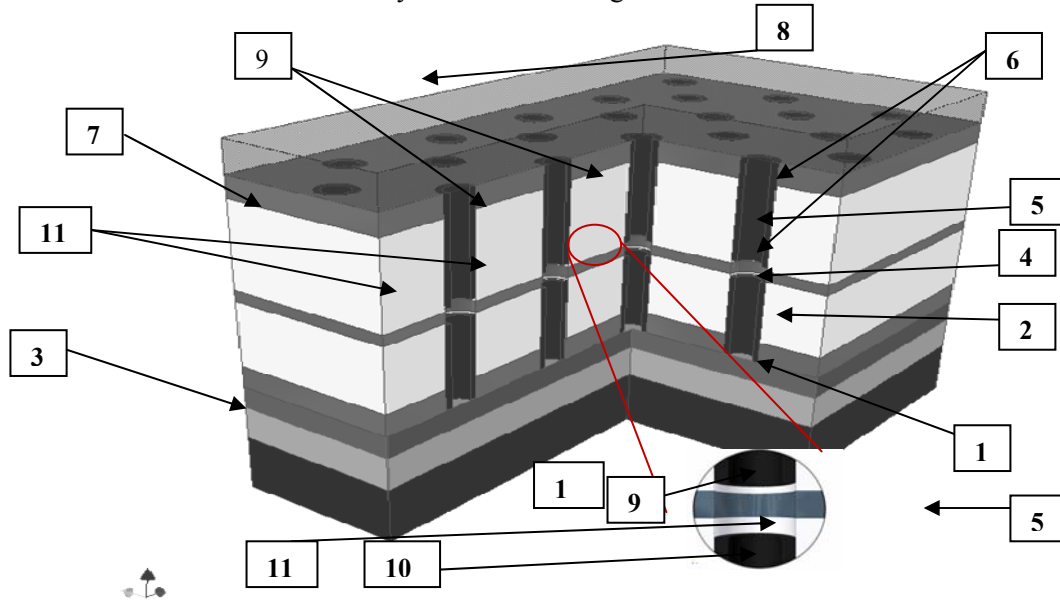


Fig. 1 Design of self-aligned CNT arrays of vertically integrated AEND based on self-organizing catalytic CVD on silicon wafer surface.

1-Silicon substrate; 2 Thermally grown silicon oxide ;3- Cathode catalyst layer CNT; 4- Cathode electrode ;5- Extractor electrode (grid); 6- Inter-electrode dielectric layer ;7- Anode electrode ;8- Capsulation layer; 9 Anode CNT ; 10 Cathode CNT ; 11- Inter-electrode space under vacuum conditions.

# Potential applications of low-frequency noise spectroscopy to the development of flicker-noise gas microsensor

M.I.Makoviychuk

*Yaroslavl Branch of the Institute of Physics and Technology, Russian Academy of Sciences, Yaroslavl, Russia,  
E-mail: makoviychuk@rambler.ru*

In solid-state microsensors the alternate capture and emission of carriers at an individual defect site generates discrete switching in the device resistance – referred to as a random telegraph signal (RTS). The study of RTSs has provided a powerful means of investigating the capture and emission kinetics of single defects, has demonstrated the defect origins of flicker noise in these devices.

During the grows of silicon single crystal and the subsequent technological processes connected to formation of device structures in crystals arise various crystallographic defects and undesirable impurities, that can render negative influence on characteristics and an output of suitable devices. Therefore studying of various aspects of states and behaviour of structural defects and impurities is an extremely actual scientific and technical problem.

The solution of this problem is possible with the help of goal-directed operation of the defect-impurity interaction (DII) ensure required parameters of created structures and devices on their basis. It is a subject of defect-impurity engineering (DIE).

Diagnostic tool-kit of DIE should meet the requirements of operation both in laboratory, in the manufacture conditions when it is necessary to carry out promptly the diagnostic analysis of a plenty of semiconductor structures. To such requirements there corresponds a suggested method of low-frequency noise spectroscopy (LFNS), including the flicker-noise spectroscopy (FNS) and the impurity-level

noise spectroscopy. The methods of low-frequency noise spectroscopy can be used in defect-impurity engineering as rapid and reliable diagnostic tool suitable for laboratory and manufacturing environments alike. We describe the principles and capabilities of each of them in detail in the context of disordered semiconductors.

Method LFCNS combines relative simplicity of technical embodying with high sensitivity to structural damages. The controlled change of a character and degree disordering of a crystalline structure mono-Si was carried out by the method of ion implantation. For solving problems of DIE it is necessary to establish the complete (quality and quantitative) identification of radiation defects and so-called “relict” (background) defects, i.e. structure defects of the semiconductor matrix. The analysis of formation processes of defects and noises is led on the ion-implanted structures of silicon made at various technological conditions.

The application of FNS for a research and analysis of semiconductor ion implanted structures gives obvious advantages in comparison with traditionally used electrophysical methods. The significance of the received results consists in development of a system approach to the problems of fluctuation analysis, enveloping all stages of the ion-doped structures creation and permitting to realize an operating feedback between parameters of quality and technological conditions.

The solution of tasks in view is called to provide making scientific basis for wide and efficient application of the flicker-noise methods of the information analysis in the microfabrication (method FNS) and environmental monitoring (method ADFNS).

In systems with the small geometrical sizes a spectrum of flicker noise at low temperatures have no a view such as  $1/f$ , and represents a line (or total of several lines) Lorentz's of the shape - Lorentzian spectrum. The magnification of temperature or geometrical sizes result ined to thickening of a spectrum and transition it to flicker ( $1/f$ ) spectrum.

Observed facts of flicker-noise parameter  $\beta_s(f)$  in a frequency band  $f = 10 \text{ Hz} \div 2 \cdot 10^4 \text{ Hz}$  here are given at  $P = 10^5 \text{ IIa}$  and  $T = 300\text{K}$  on tests – structures of flicker-noise gas sensor (FNGS), generated on Si, epi-Si and SOI-structures.

It is visible, what even in accordance with diminution only of one geometrical size (thickness of explored test - structure) there is a transition of the shape of a spectrum from flicker such as to the total Lorentzian's.

Now we have already seen that in FNGSs the current fluctuations appear as random telegraph signals (the power spectrum of an RTS is Lorentzian) so that the fundamental question that we now wish to address is the following: what is the relationship between the RTSs observed in small devices and the  $1/f$  spectrum measured in large devices? We shall see that the answer to this question is quite straightforward: RTSs are a



product of the decomposition of the  $1/f$  spectrum into its individual fluctuating components; conversely the  $1/f$  spectrum can be viewed as a superposition of individual trapping events, each generating an RTS in the time domain. The defect origins of  $1/f$  noise have long been suspected, but not definitely proved to the satisfaction of all. On the basis of the work of McWhorter [1], Ralls *et al.* [2] suggested that RTSs were probably the cause of  $1/f$  noise in MOSFETs, but they were unable to demonstrate conclusively the full superposition process to give a  $1/f$  spectrum.

This was due to the fact that in the very small devices which they were studying (about  $0.1 \mu\text{m}^2$ ) it was not possible, even at elevated temperatures, to observe the fluctuations of more than a handful of traps at any particular gate voltage. Studies by Rogers and Buhrman [3] on small-area metal-insulator-metal (MIM) tunnel junctions, Restle *et al.* [4] on small-area silicon-on-sapphire resistors and Uren *et al.* [5] on a range of MOSFETs of different areas provided unambiguous evidence that  $1/f$  noise in these systems is generated through the fluctuation in occupancy of individual defect states modulating the conductivity.

The experiments described in our report provide an elegant demonstration of the full decomposition of the  $1/f$  spectrum into its constituent Lorentzian components and the sample-to-sample variation in the power spectra expected from very small systems.

#### References:

1. McWhorter A.L. – Semiconductor Surface Physics. – Philadelphia: University of Pennsylvania Press, 1957. – P.207.
2. Ralls K.S., Skocpol W.J., Jackel L.D., Howard R.E., Fetter L.A., Epworth R.W., and Tennant D.M. // Phys. Rev. Lett. – 1984. – V.52. – P.228.
3. Rogers C.T., and Buhrman R.A. // Phys. Rev. Lett. – 1984. – V.53. – P.1272; // Phys. Rev. Lett. – 1985. – V.55. – P.859.
4. Restle P.J., Hamilton R.J., Weissman M.B., and Love M.S. // Phys. Rev. B. – 1985. – V.31. – P.2254.
5. Uren M.J., Day D.J., and Kirton M.J. // Appl. Phys. Lett. – 1985. – V.47. – P.1195.

# Adsorption-desorption flicker noise spectroscopy

M.I.Makoviychuk

*Yaroslavl Branch of the Institute of Physics and Technology, Russian Academy of Sciences, Yaroslavl, Russia,  
E-mail: makoviychuk@rambler.ru*

Adsorption-desorption flicker noise spectroscopy (ADFNS) will utilize process of a desorption of adsorbed particles from a surface the semiconductor for carrying out of the complete electrophysical analysis of connection adsorbate - adsorbent (semiconductor substrate). ADFNS - highly sensitive research technique of surface phenomena in gas-sensitive semiconductor structures. Dependence of noise performances on a composition gas phases can be utilized for sensitization and selectivity of detection of gases and steams.

Represents doubtless interest an opportunity of making gas-analysis method combining virtue gas chromatographs (high sensitivity and selectivity) and gas sensors (simplicity of use and efficiency of measuring).

The principle of activity of offered development grounded on set appearance of change of quantities (by a factor of  $10^2$  and more) noise performances of ion -implanted semiconductor structure at adsorption on it surfaces of molecules of different gases. An adsorption capacity (AC) of surfaces depends on a nature of a surface and from that processing, which was the surface is subjected. Perfect affirming to use of ion implantation as effective amplifier of AC are the results for  $^{40}\text{Ar}^+/\text{Si}$ . The radiation defects incipient during an ion implantation, serve by convenient places for adsorption of gas molecules: the adsorption can go mainly on these defects - centers of adsorption. The experimental data confirm presence of two mechanisms of flicker-noise: surface and bulk. In a pressure ranges  $P = 1 \times 10^{-3} - 3 \times 10^{-3}$  the process of desorption from a surface Si of an adsorbate is observed. Surface component of flicker-noise diminishes sharply. At pressure less  $1 \times 10^{-3}$  process of desorption was concluded and now noise level is determined only by volume mechanism of flicker-noise.

Now by most spread method of the check states of a surrounding medium is the gas chromatography. To virtues gas-chromatographic methods it is necessary to refer high selectivity and precision. However these results are obtained for account extremely composite (and, accordingly, expensive!) constructions gas chromatographs, the operation on which requires enormous expenditures of labour the highly skilled personnel.

Features of ADFNS from gas chromatography.

A). Method ADFNS - rapid non-destructive method, i.e. process of measuring and mathematical analysis of observed data occupies no more than 0.5-1 hours, in dependence from quantity of given fixed frequencies, on which happens definition of a noise signal. In that case, when it is possible to do without by small precision and by selectivity, apply gas sensors. The devices grounded on use of gas sensors, differ by relative simplicity of a construction, small price and simplicity in circulation with them that allows using them to the personnel not calls a variety of technical knowledge. To deficiencies of such devices it is necessary to refer their low sensitivity and selectivity. As to selectivity, usually it is required preliminary information on what gas (from group of gases effecting on a sensor control) is present at air, then observed data it is possible to interpret in the terms of his concentration. The principle of activity of such sensors grounded on an appearance of change sheet resistance of the thin-film semiconductor at absorption on its surfaces of molecules of different gases. Than more concentration of molecules in gas, environmental a sensor, the more number absorbed molecules on a surface, and more change of sheet resistance of the thin-film semiconductor.

B). Cost of instrumentation ADFNS is lower than cost of constructions gas chromatographs.

Features of ADFNS from gas sensor.

1. The sensitivity of ADFNS to molecules, adsorbed on a surface, is higher (by a factor of  $10^2$  and more) than sensitivity of a method based on measuring the changing of sheet resistances on gas sensor.
2. In a method ADFNS the definition of noise intensity will be carried out in a wide spectral frequency range that enables to determine presence of different kind of molecules that adsorbed on surfaces.

# Development of 3D-formation on the surface of SIMOX-structure of flicker-noise gas sensor

M.K.Aminov, M.I.Makoviychuk, E.O.Parshin

*Yaroslavl Branch of the Institute of Physics and Technology, Russian Academy of Sciences, Yaroslavl, Russia,  
E-mail: makoviychuk@rambler.ru*

Irradiation of solids with energetic particles leads to the production of lattice defects in the bulk and to sputtered atoms, adatoms, and creators near the surface. Predicting which types of damage prevail in specific situations has been a difficult chore; however, recent developments in computer simulations have greatly facilitated this task [1].

This review provides a fundamental understanding of the damage process in a pure Si. The special role of surfaces on damage production is a central focus of this work.

Surface processes have a great importance for low-dimensional semiconductor structures. Surface-active impurity absorption creates a surface potential that modifies physical processes, especially the carriers transport.

SOI flicker-noise gas sensor with the open base surface can be a good model object for the carrier transport investigations within absorption processes [2, 3]. As the experimental investigation of such processes is a complicated problem, the physical-topological modeling of carrier transport in this structure was provided.

We found that the density, distribution and number of extended defects are strongly dependent upon the oxygen concentration.

The results of electron-microscopy investigation of the growth and development of the 3D-formation on the surface of the SIMOX-structures after high-temperature treatments are presented.

The series of the microphotography's showing the states of the surface sample of the SIMOX-structures on different stages after post-implanted treatments have been received. It was founded the appearance and development "bush-maded" 3D-clusters on the implanted surfaces [4]. It was supposed the source of defects is the SIMOX-structure including  $\text{SiO}_x$ -layer. The treatment environment defines structure, surface density and growth intensity of the defects. It was supposed the observed 3D-formations contain silicon and  $\text{SiO}_x$ -complexes. The appearance of this defects and their development is connected with intensity diffusion processes stimulated by growing of thermoelusticity tension after treatment that is causing of creation of intensity vacancy-impurity fluxes, in the surface melt zone where the 3D-formation growth was observed.

1. R.S. Averback, Mai Ghaly. "Fundamental aspects of defect production in solids". // Proceed. of the Tenth International Conf. on Ion Beam Modification of Materials. – Albuquerque, NM, USA, 1 – 6 September 1996. – Editors J.C Barbour and M.Nastasi. Elsevier Science B.V., North-Holland, 1997.
2. Makoviychuk M.I. Potential Applications of LF-Noise Spectroscopy to the Development of New-Generation Gas Sensors. // Russian Microelectronics. – 2008. - Vol. 37, No. 4. - P. 226–237.
3. Makoviychuk M.I., Chapkevich A.L., Chapkevich A.A., and Vinokurov V.A. Flicker-noise gas sensor. // Biomedical Engineering. – 2009. – V.43, N3. – P.109 – 113.
4. Aminov M.K., Krivelevich S.A., Makoviychuk M.I., Parshin E.O., Pimanov S.Yu., Rekshinskii V.A. Development of 3D-formation on the surface of SIMOX-structures after high temperature treatment. // Proceed. Int. School-Conf. "Physical Problems in Material Science of Semiconductors". - Chernivtsi, Ukraine, 1995. - P.93.

# Annealing temperature dependence of the photo-emf in silicon p-n-junctions with $\text{SiO}_x\text{B}_y$ nanoclusters

S.A.Krivelevich, R.V.Selyukov

*Yaroslavl branch of the Institute of Physics and Technology, Russian Academy of Sciences, Yaroslavl, Russia,  
rvselyukov@mail.ru*

Quantum dots in semiconductors and in insulators are under intensive study in nanoelectronics. Ion synthesis of the nanocomplexes may be proposed as method of the creation of quantum dots in silicon. Coimplantation of oxygen ions and ions of additional element leads to formation of the areas with the clusters which contain atoms of the dopants and of silicon [1, 2]. Some physical properties of these ion synthesized materials depend from kind of additional impurity. Thus implantation of boron allows to create silicon structures with nanoclusters which have the chemical composition like of borosilicate glass. Borosilicate glass is insulator, therefore increasing of energy gap should occur in the areas containing  $\text{SiO}_x\text{B}_y$  clusters. This phenomenon results to change of electrical and photoelectrical properties of considered structures in comparison with silicon. Hence characteristics of p-n-junctions with nanoclusters  $\text{SiO}_x\text{B}_y$  will be differ from characteristics of silicon p-n-junctions significantly. Particularly maximum of spectral dependence of the photosensitivity for considered p-n-junction have to shift towards shorter wavelengths in comparison with analogous silicon photodiode. This feature allows to consider studied p-n-structures as perspective photocells. The main stage in process of ion synthesis of considered nanoclusters is heat treatment of the silicon implanted by oxygen and boron. Variations of the conditions of the annealing allow to vary concentration of the nanoclusters. Consequently possibility to change the properties of ion synthesized material is arises. The aim of present investigation is to find out the influence of annealing temperature and annealing time on magnitude and spectral dependence of the photo-emf of considered structures.

The objects of present research were two kinds of the samples which were prepared as described further. First, implantation of molecular oxygen  $\text{O}_2^+$  into the (100) n-Si wafers was carried out with ion energy 300 keV and with two doses  $1,2 \cdot 10^{17} \text{ cm}^{-2}$  and  $2 \cdot 10^{17} \text{ cm}^{-2}$ . Then samples were annealed at 900°C during 5 minutes in atmosphere of dry oxygen. Afterwards both samples were implanted by boron ions  $\text{B}^+$  with energy 100 keV and dose  $8 \cdot 10^{16} \text{ cm}^{-2}$ . After the second implantation the heat treatment at 900°C during 5 minutes was repeated. Further samples were annealed in temperature range 1000-1050°C and time range 5-60 minutes. All these treatments were carried out in atmosphere of dry oxygen. Implantation and heat treatments lead to the formation of the  $\text{p}^+$ -n-junction with  $\text{SiO}_x\text{B}_y$  nanoclusters in  $\text{p}^+$ -area of the samples.

After annealing spectral dependence of the photo-emf magnitude was measured for two kinds of the samples. These measurements were carried out at open-circuit mode of the p-n-structures. Value of the photo-emf was measured by microvoltmeter without amplifying of input signal. Monochromatization of incident radiation was carried out by monochromator. Incandescent lamp and halogen lamp were the light sources in this experiment. Magnitude of photo-emf was measured in the wavelengths range of incident radiation 360-2000 nm. Obtained dependence of photo-emf magnitude on annealing temperature has maximum nearly 1025°C. P-n-structures produce smaller signal at the lower heat treatment temperatures because these temperatures are not enough for effective synthesis of the nanoclusters. This result can be explained also by the fact that implantation damages are not eliminated at these annealing temperatures. Decreasing of photo-emf at higher temperatures can be explained by dissociation. Thus influence of annealing temperature on photoresponse of the p-n-junctions in silicon with  $\text{SiO}_x\text{B}_y$  nanoclusters is studied. Optimal temperature for the preparation of photoelectrical devices based on considered structures is determined.

1. V.I. Bachurin, S.A. Krivelevich, Yu. I. Denisenko and R. V. Selyukov, "Ion synthesis of buried isolating silica layers", *Izvestiya RAN. Seriya fizicheskaya*, **70**, pp. 883-885, 2005
2. S. A. Krivelevich, E. Yu. Buchin, Y. I. Denisenko and R. V. Selyukov, "Diffusion and phase formation in ternary silicate systems framed by an ion bombardment", *Micro- and Nanotechnologies 2005. Proc. of SPIE*, K. A. Valiev and A. A. Orlikovsky ed., vol. 6260, p. 626007, 2006

# Diffusion simulation during RTA of plasma immersion ion implanted boron in SOI structure

V.Ovcharov, V.Rudakov, A.Kurennya, S.Simakin

Yaroslavl Branch of the Institute of Physics and Technology, Russian Academy of Sciences, Yaroslavl, Russia,  
E-mail: vladovcharov@rambler.ru

Plasma immersion ion implantation is one of the most perspective technologies for dopant introduction at an ultra shallow p-n junction formation [1]. The simulation of the dopant diffusion has to be developed for the optimization of the activating impurities and annealing implantation damage. In present work the model of the evolution of diffusion profile of boron implanted from ion immersion plasma of  $\text{BF}_2$  in a thin layer silicon of SOI structure is developed for a rapid thermal annealing (RTA) carried out in a set-

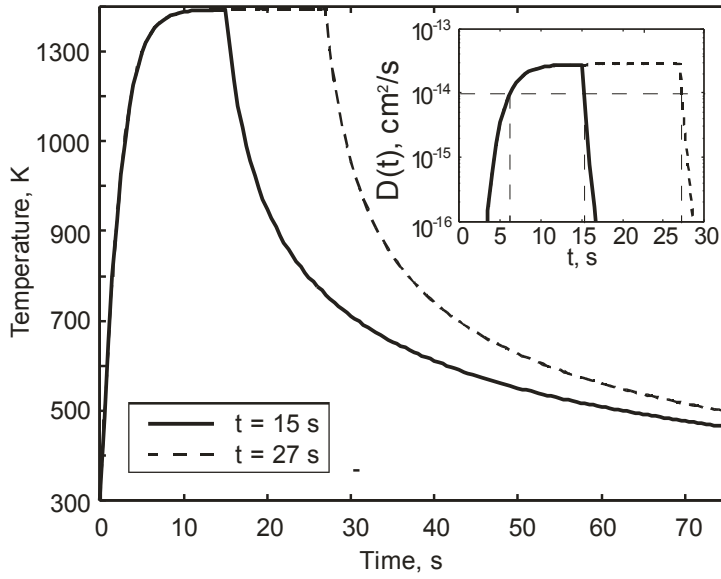


Fig. 1. Time-temperature diagrams of RTA during 15 and 27 s and the calculated dependence of the boron diffusion coefficient in silicon layer vs time, corresponding to the TTD at the stationary temperature of the silicon plate of  $T_s = 1120^\circ\text{C}$ .

up for the temperature-gradient heat treatment of semiconductor wafers [2]. The initial boron profile was modeled by exponential function where  $x$  is the Si layer depth,  $C_s$  is a boron surface concentration,  $g$  is a straggling. The diffusion coefficient is supposed to be a function of the temperature  $T$  and the time  $t$ , i.e.  $D = D[T(t)]$ . A temperature-time diagram of the annealing process and the dependence of the diffusion coefficient on the time are shown on fig. 1. In this case a one-dimensional diffusion equation

$$\frac{\partial C}{\partial t} = D(t) \frac{\partial^2 C}{\partial x^2} \quad (1)$$

by introduction of a new variable

$$\theta(t) = \int_0^t D(\tau) d\tau \quad (2)$$

is transformed to a form [3]

$$\frac{\partial C}{\partial \theta} = \frac{\partial^2 C}{\partial x^2} \quad (3)$$

at the same initial condition

$$C(x, 0) = C_0. \quad (4)$$

Solving the equation (3) for the dopant diffusion in the semi-infinite medium with the initial condition (4) and the boundary condition

$$\left. \frac{\partial C}{\partial x} \right|_{x=0} = 0 \quad (5)$$

(reflecting boundary) is of the form [3]:

$$C(x, \theta) = \frac{1}{2} \exp(\gamma^2 \theta) \left\{ \exp(-\gamma x) \left[ 1 + \operatorname{erf} \left( \frac{x}{2\sqrt{\theta}} - \gamma\sqrt{\theta} \right) \right] + \exp(\gamma x) \left[ 1 - \operatorname{erf} \left( \frac{x}{2\sqrt{\theta}} + \gamma\sqrt{\theta} \right) \right] \right\}. \quad (6)$$

The diffusion process modeling described by the equation (6) in accordance with a temperature-time diagram shown in fig.1 was developed with MatLab programming. As a result of modeling, an approximated activation energy  $E = 3.38$  eV and a frequency multiplier  $D_0 = 0.044$   $\text{cm}^2/\text{s}$  were obtained. The values provided a good coincidence of tails of the experimental and theoretical profiles for diffusion time  $t = 15$  s (fig. 2). The analysis of fig. 1 shows that the max value of the diffusion coefficient, corresponding to the stationary value of the plate temperature  $T_{ps} = 1120^\circ\text{C}$  does not exceed  $3 \cdot 10^{-14}$   $\text{cm}^2/\text{s}$ .

This value is one order less than typical magnitudes of the boron diffusion coefficient for this temperature [4]. Modeling of the experimental profile corresponding to annealing for 27 s did not provide the expected agreement between the theoretical and experimental tails of the profiles. To achieve the acceptable fit of the tails the frequency multiplier  $D_0$  must be doubled. This fact cannot be explained within the framework of the given model by using the difference of the efficient temperatures of annealing as both of the processes were performed practically at the same stationary temperature.

The average boron diffusion coefficients as the functions of an anneal time were found using the formula

$$\bar{D} = \frac{\theta(t_{ann})}{t_{ann}}. \quad (19)$$

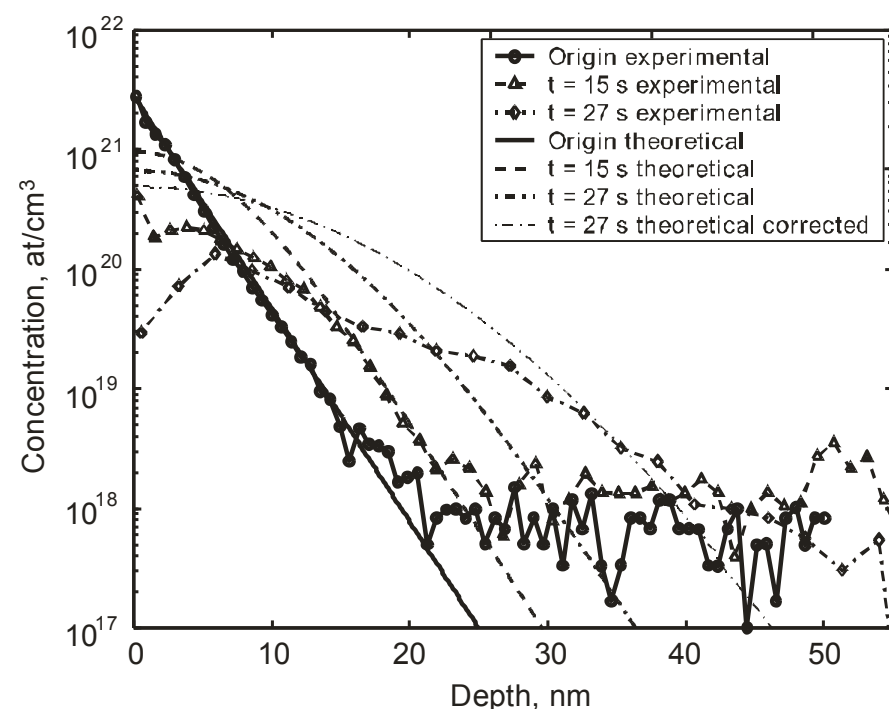


Fig. 2. The experimental and the theoretical concentration profiles of B in silicon layer after implantation from plasma  $\text{BF}_2$  and RTP during 15 and 27 s at stationary temperature of the silicon plate of  $T_s = 1120^\circ\text{C}$

fluorine concentration profiles evolution was investigated for furnace annealing during 15 minutes at  $850^\circ\text{C}$ . The analysis of the profiles shows that the diffusion fluxes of the boron and fluorine atoms are directed to opposite sides. As a result fluorine concentration at the depth of the tails of boron concentration profiles is decreased to a critical value  $\sim 10^{18} \text{ cm}^{-3}$  [5], at which the fluorine atoms slightly suppress the boron diffusion. We come to the conclusion that the boron diffusion coefficient of the profile tails should increase with the increase of annealing time. The conclusion approves of the experimental results for various anneal periods of the implanted boron.

Their values are  $\bar{D}_2 = 1.5 \cdot 10^{-14} \text{ cm}^2/\text{s}$  for  $t_{ann2} = 15 \text{ s}$  and  $\bar{D}_3 = 2.07 \cdot 10^{-14} \text{ cm}^2/\text{s}$  for  $t_{ann2} = 27 \text{ s}$ . Corresponding values of the diffusion length  $L = \sqrt{\theta_{ann}}$  are  $L_2 = 4.7 \text{ nm}$  and  $L_3 = 7.4 \text{ nm}$ .

To explain such small values of the boron diffusion coefficients and the change of the diffusion parameters during the increasing anneal time, the joint diffusion of boron and fluorine has become a necessity. Shano et al [5] in their study have indicated that fluorine atoms presenting in silicon crystalline lattice suppress the diffusion of the boron. The conservative values of the boron diffusion coefficients obtained from the analysis of RTP are attributable to this fact. In the work [1] joint boron and

1. А.Н. Аверкин, А.А. Орликовский, К.В. Руденко, "Плазменно-иммерсионная ионная имплантация бора для создания ультратонких p<sup>+</sup>-n переходов в кремнии", *Труды 3-го Международного симпозиума по теоретической и прикладной плазмохимии*, т. 2, с. 360 – 362, Плес, 2002
2. Б.В. Мочалов, В.И. Рудаков, "Установка для термоградиентной обработки полупроводниковых пластин", *ПТО*, №2, с.155-157, 1996
3. И.Г. Араманович, В.И. Левин. *Уравнения математической физики*. «Наука», Москва, 1969
4. S.M. Sze. *Physics of Semiconductor Devices*. John Wiley and Sons, New York, 1981
5. Shano T., Kim R., Hirose T. et al., "Realization of ultra-shallow junction: suppressed boron diffusion and activation by optimized fluorine co-implantation", in *Proc. IEEE*, p. 131, 2001

# Plasma molding in deep silicon reactive ion etching

O.Morozov

*Yaroslavl Branch of the Institute of Physics and Technology, Russian Academy of Sciences, Yaroslavl, Russia,  
morozov@yftian.ru*

In the time multiplexed deep silicon etching (TMDE) for a microelectromechanical system (MEMS), the typical etch depths are in the range of 10–500  $\mu\text{m}$ . Lateral sizes of etched features can vary from submicron size to millimeters. In this case, the plasma often interacts with features that are comparable to, or larger than the sheath thickness. When the substrate surface contains geometrical features like deep cavity the plasma-sheath boundary will try to wrap around the contour of the cavity. This is called plasma molding. The resulting curved electric field lines can alter the oncoming ion trajectories, greatly influencing the ion impact angle. The important length scales that control behavior are the plasma sheath thickness and the lateral sizes and depth of the cavity [1]. The success of deep silicon etching depends critically on the angular distributions of energetic ions bombarding the substrate. In this work presents the result of the experimental study of the plasma molding effect on etched trench profile. Silicon etching was carried out with ICP TMDE etcher.  $\text{SiO}_2$  and Cr layers were used as the self-aligned etching masks (fig. 1a.) The deep cavities with widths from 200  $\mu\text{m}$  to few millimeters were etched using Cr/ $\text{SiO}_2$  masks (fig. 1b). The cavities depth varies from 50  $\mu\text{m}$  up to 500  $\mu\text{m}$ . After  $\text{SiO}_2$  mask removal the array of narrow trenches was etched (fig. 1c). In such circumstances, plasma molding over cavity influences the slope of narrow trenches. In fig. 2 the SEM image of tilted trenches profiles at the upper corner of the cavity step is shown. Slope angles of trenches were measured as function of the depth and the lateral size of cavities and distance from the corner of the cavity step. If the cavity lateral size doesn't exceed 200  $\mu\text{m}$ , the slope angle of narrow trenches is  $90^\circ$  (vertical). For cavity lateral size of 3000  $\mu\text{m}$  (fig. 2) the slope angle of narrow trenches at the corner of the cavity step is  $84^\circ$ . The cavity depth was 205  $\mu\text{m}$ . The measurement results reveal that a transition point exists between the cavity lateral size-sensitive and lateral size-insensitive areas of the slope of narrow trenches. The increase of cavity depth leads to increasing of trenches slope in lateral size-sensitive area. The tilt of the trenches is maximal at corner of the cavity step and tends to vertical across the distance 500  $\mu\text{m}$ . Having measured trenches slope, the average ion impact angle is determined. The results can be used for new MEMS application and verification numerical plasma mold simulation.

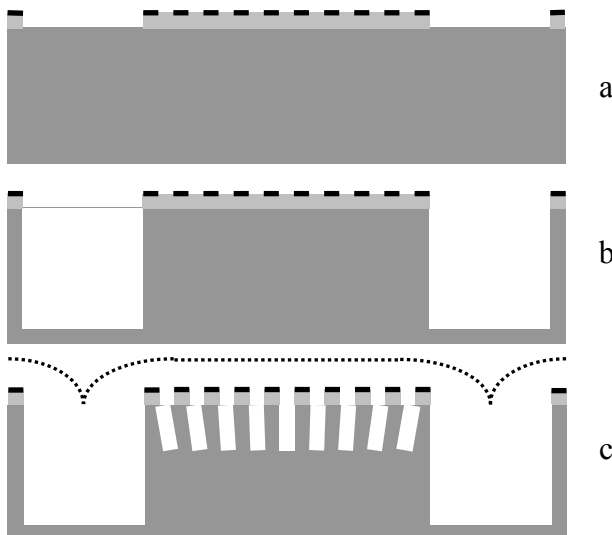


Fig. 1 Experimental process flow. In c) dashed line denotes curved plasma sheath boundary.

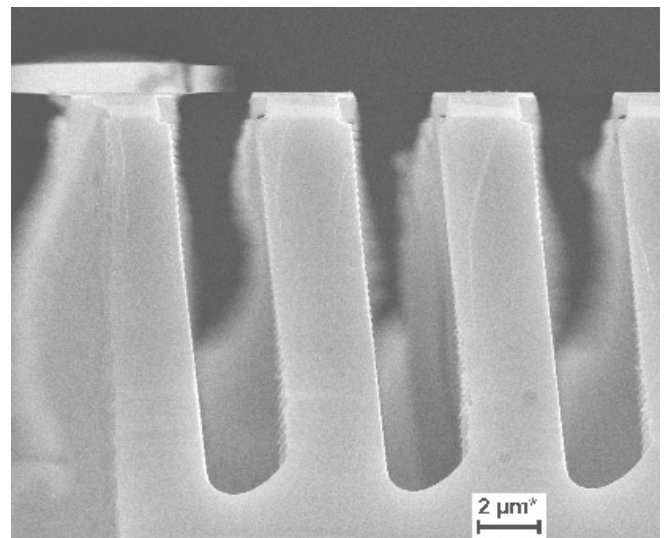


Fig.2 SEM micrograph of etched narrow trenches at the upper left hand corner of the cavity step.

1. Doosik Kim and Demetre J. Economou, "Plasma molding over deep trenches and the resulting ion and energetic neutral distributions", J. Vac. Sci. Technol. B, 21(4), 2003, pp1248-1253.

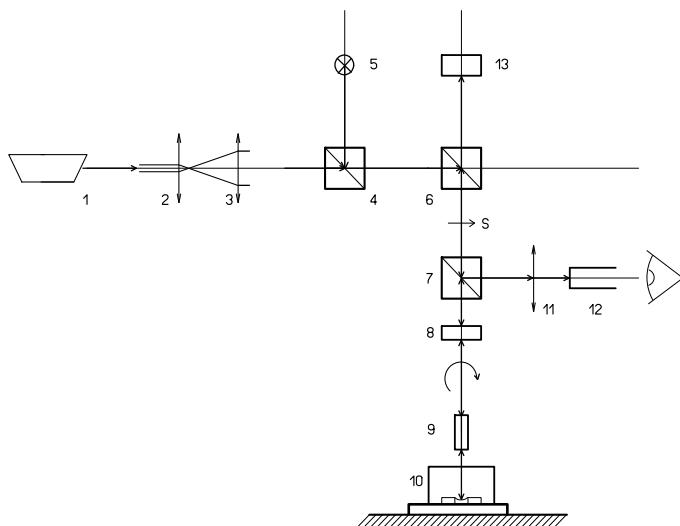
# The test bench for study of dynamic characteristics of MEMS

A.V.Postnikov, I.A.Kozin

Yaroslavl Branch of the Institute of Physics and Technology, Russian Academy of Sciences, Yaroslavl, Russia,  
amirov@yf-ftian.ru

The microelectromechanical systems (MEMS) technology developed a variety of microdevices in the fields of sensors and actuators[1,2] as well as components for radio frequency and optical telecommunications.[3,4] An important class of devices is the movable micrometer sized structures released from the substrate. Microdevices are the surface micromachined mechanical resonators that come in many geometrical configurations, such as laterally movable and vertically movable beam resonators, and torsion resonators. It is important to develop simple tools for measuring micro-switch behavior to verify analytic models. Optical methods with the capability of accurately measuring very tiny movement of the movable element, such as optical beam deflection, optical interferometry, can provide high performance by their subnanometer sensitivity and much less interference from the parasitic signals. Especially the dynamic measurement of out-of-plane vibration can be easily carried out to reveal valuable information on vibration modes, damping mechanisms, and elastic properties, etc. [5,6]

The objective of our work is design the optical test bench for optical testing of MEMS devices in vacuum cell under different temperature conditions fig(1).



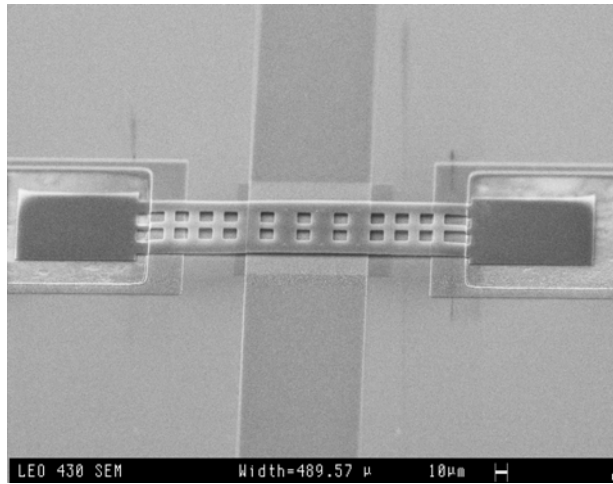
- 1- He-Ne the laser with wave length 628 nanometers.
- 2- Converging lens of the optical expander  $f_1=15\text{mm}$ .
- 3- Converging lens of the optical expander  $f_2=65\text{mm}$ .
- 4- Beam splitting cube.
- 5- Lamp.
- 6- Polarization cube.
- 7- Beam splitting cube.
- 8- Plate  $\lambda/4$ ,  $\lambda=628\text{nm}$ .
- 9- Objective  $F=25\text{mm}$ .
- 10- Vacuum chamber with MEMS structure.
- 11- Image-forming lens.
- 12- Eyepiece.
- 13- Two sell split photodiode S9345.

Fig(1). The apparatus optical scheme.

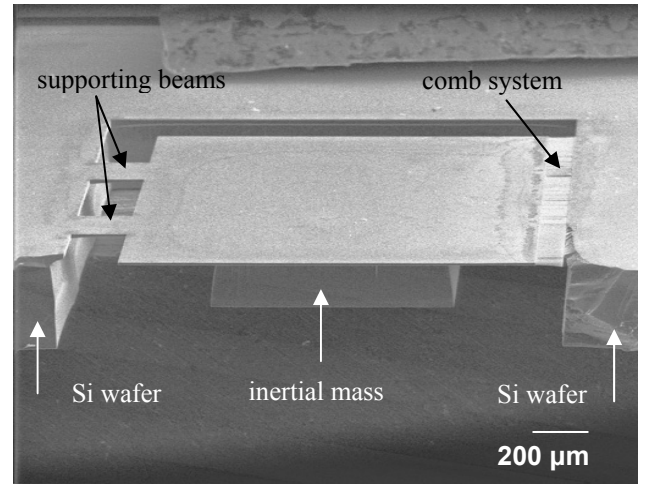
To detect the motion of switch membrane and determine the dynamics characteristics laser beam deflection method was used. A laser beam (628nm) was reflected off the end of a cantilever or periphery area of a device under test. The detector can measure displacements of a light beam, which is equivalent to a displacement of the cantilever in the submicron scale. Laser beam illuminates the 20x microscope objective. The reflected light is collected by a bicell split photodetector, which outputs the differential electrical signal proportional to the vibration amplitude of the beam.

The AC coupled output of the detector was connected to the digital oscillograph. To align the beam with samples a conventional lamp and Eyepiece were combined with laser beam path. The digital oscillograph was connected to a Windows PC using a GPIB interface. A program was developed to save the data to the hard disk but also to adjust the settings of the oscillograph. Functional frequency generator was used to drive the structure under test. The resonator is placed in a vacuum chamber under pressure less than  $10^{-3}$  Torr, the temperature can be varied from  $-10^\circ\text{C}$  to  $50^\circ\text{C}$ . The photodiode amplifier has frequency range up to 1 MHz. Fig (2) shows tested MEMS structures : RF switch - a), and proof mass of inertial sensor - b). The RF switch dimensions are: length 270  $\mu\text{m}$ , width varied from 100 to 40  $\mu\text{m}$ , gap 2-10  $\mu\text{m}$  depends on fabrications conditions. Responses of RF switch, and inertial sensor structures under frequency scanning from 1 to 200 kHz presented in fig.3a) and 3b).



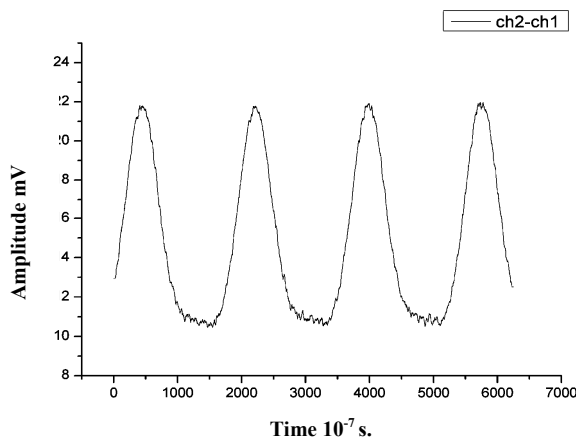


(a)

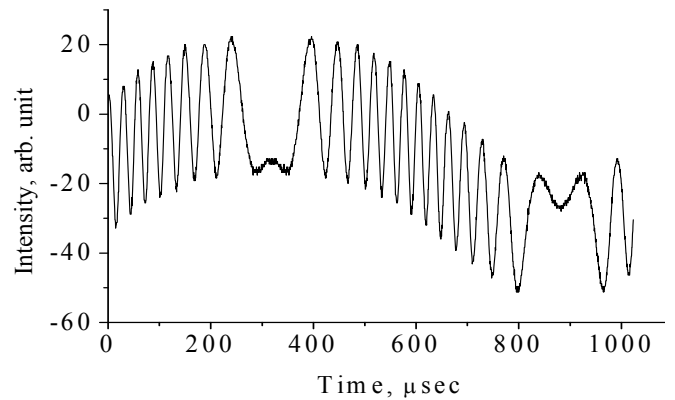


(b)

Fig (2). Tested MEMS structures a) – RF switch, b) – inertial sensor



(a)



(b)

Fig(3). The responses of RF switch, and inertial sensor to the sinusoidal signals.

A simple and efficient technique has been presented to characterize dynamic behavior of the MEMS structures. The apparatus allows test MEMS devices under different pressure and temperature conditions.

1. G. T. A. Kovacs, *Micromachined Transducers Sourcebook* \_McGraw-Hill, Boston, 1998\_.
2. J. W. Judy, *Smart Mater. Struct.* **10**, 1115 \_2001\_.
3. C. T.-C. Nguyen, *Proceedings of the 2000 European Solid-State Device Research Conference, Ireland, 11–13 September 2000* \_IEEE, New York, 2000\_, pp. 2–12.
4. J. Jason Yao, *J. Micromech. Microeng.* **10**, R9 \_2000\_.
5. S. L. Firebaugh *et al.*, *IEEE Trans. Instrum. Meas.* **53**, 1047 \_2004\_.
6. D. W. Carr, S. Evoy, L. Sekaric, H. G. Craighead, and J. M. Parpia, *Appl. Phys. Lett.* **75**, 921 \_1999\_.

# Electron-hole plasma in a one-dimensional parallel wires system

V.Stepanov<sup>1</sup>, A.Churilov<sup>2</sup>

1. Ioffe Physical Technical Institute, Russian Academy of Sciences, St. Petersburg, Russia, stelsxx76@mail.ru

2. Yaroslavl Branch of the Institute of Physics and Technology, Russian Academy of Sciences, Yaroslavl, Russia, abchurilov@mail.ru

According to Earnshaw's theorem, the static electric charge system has not a steady state [1]. Nevertheless, such systems exist in the nature. As example - solitary charged conductors are such systems. To explain the fact of their existence using formal representations of the nonelectrostatic forces in origin. This forces are barriers to charge for the surface of the conductor and provide the required stability of the system of charges.

In this work we calculated electrostatic energy of the Coulomb interaction of opposite electrical charges inside the parallel wires as a function of  $\epsilon$  - medium permittivity. Found that accounting for the forces of nonelectrostatic origin providing one-dimensional motion of electric charges along the wires and preventing the flow perpendicular to the axis, gives rise to a minimum and maximum potential energy of their interaction, which corresponds to the existence of stable and unstable spatial configuration of charged particles. The result of calculation for silicon wires is represented in Fig. 1. The lower branch of the curve corresponds to the stable state of charge (this region on a larger scale is shown in the insert), and the upper - unstable. It is evident that large and may significantly exceed room temperature.

The analog of the considered system unlike charges can serve as a nonequilibrium electron-hole plasma formed by photoexcitation of porous silicon. Such wires can be created using the another materials in base.

Accounting for quantum properties of electrons and holes will provide a more complete and accurate understanding of this condition. In

particular, reducing the distance between the charges in nearby wires can increase the energy of their Coulomb interaction so that the particles can experience the transition to a localized state. On the other hand, it may lead to pairing of particles and the transition of nonequilibrium electrons and holes in a new superfluid state [2].

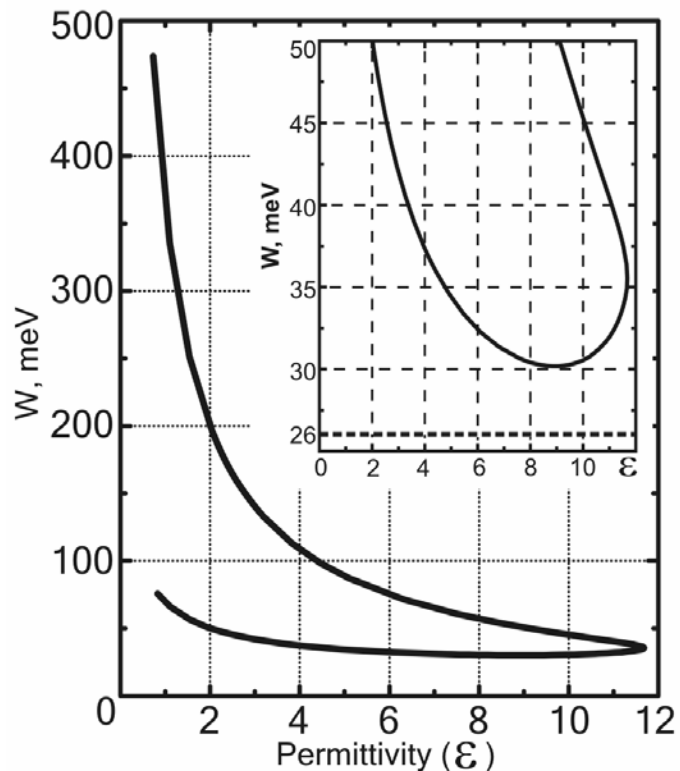


Fig. 1. Energy of the Coulomb interaction of unlike electric charges inside the parallel wires vs dielectric permittivity of the medium.

1. I.E.Tamm. *Electricity Theory Backgrounds*, Fizmatlit, Moscow, 2003. [in Russian]
2. Yu.E. Lozovik and V.I.Yudson, "Feasibility of superfluidity of paired spatially separated electrons and holes; a new superconductivity mechanism", JETP Lett., **22**, pp.274-276, 1975

